Karlsruhe Institute of Technology

Pascal Rietz

On Parallelization Approaches for Two-Step-Absorption 3D Laser Microprinting

2025
Dissertation

ON PARALLELIZATION APPROACHES FOR TWO-STEP-ABSORPTION 3D LASER MICROPRINTING

Zur Erlangung des akademischen Grades eines
DOKTORS DER NATURWISSENSCHAFTEN (Dr. rer. nat.)
von der KIT-Fakultät für Physik des
Karlsruher Instituts für Technologie (KIT)

genehmigte

DISSERTATION

von

M. Sc. Pascal Rietz
geboren in Ruthweiler

Tag der mündlichen Prüfung:	12. Dezember 2025
Referent:	Prof. Dr. Martin Wegener
Korreferent:	Prof. Dr. Carsten Rockstuhl

CONTENTS

PUBLICATIONS

PARTS OF THIS THESIS HAVE ALREADY BEEN PUBLISHED . . .

. . . in scientific journals:

- P. Rietz, P. Somers, S. Kalt, J. L. G. Schneider, P. Kiefer, and M. Wegener, ”Dynamic Multi-Focus 3D Laser Nanoprinting Based on Two-Step Absorption and Computational Holography”, *Laser & Photonics Reviews* **19**, 2500187 (2025).

- J. Weinacker[1], S. Kalt[1], P. Kiefer[1], P. Rietz[1], and M. Wegener, ”On Iterative Pre-Compensation of 3D Laser-Printed Micro-Optical Components Using Confocal-Optical Microscopy”, *Advanced Functional Materials* **34**, 2309356 (2024).

- V. Hahn, P. Rietz, F. Hermann, P. Müller, C. Barner-Kowollik, T. Schlöder, W. Wenzel, E. Blasco, and M. Wegener, ”Light-Sheet 3D Microprinting via Two-Colour Two-Step Absorption”, *Nature Photonics* **16**, 784 (2022).

. . . at scientific conferences (only own presentations):

- P. Rietz, P. Somers, S. Kalt, P. Kiefer, J. L. G. Schneider, and M. Wegener, ”Parallelized Two-Step-Absorption 3D Laser Nanoprinting via Computational Holography using a Digital Micromirror Device” (invited), Proc. SPIE PC13354, SPIE Photonics West, San Francisco, United States of America, January 2025.

ADDITIONAL RELATED WORK HAS ALREADY BEEN PUBLISHED . . .

. . . in scientific journals:

- A. Vranić, S. Wulff, P. Rietz, J. L. G. Schneider, S. A. El Mirate, M. Wegener, and S. Bräse, ”Novel Photoinitiators for Two-Step Absorption based 3D Laser Nanoprinting: From Molecular Design to Printing Behavior”, *ChemPhotoChem* **10**, e202500337 (2026)

- N. M. Bojanowski, A. Vranić, V. Hahn, P. Rietz, T. Messer, J. Brückel, C. Barner-Kowollik, E. Blasco, S. Bräse, and M. Wegener, ”Search for Alternative Two-Step-Absorption Photoinitiators for 3D Laser Nanoprinting”, *Advanced Functional Materials* **33**, 2212482 (2024).

---

[1] These authors have contributed equally.

- V. Hahn, N. M. Bojanowski, P. Rietz, F. Feist, M. Kozlowska, W. Wenzel, E. Blasco, S. Bräse, C. Barner-Kowollik, and M. Wegener, ”Challenges and Opportunities in 3D Laser Printing based on (1+1)-Photon Absorption”, *ACS Photonics* **10**, 1, 24 (2023).

Chapter 1

1 INTRODUCTION

Since its emergence, 3D additive manufacturing has increasingly permeated modern manufacturing [1–4]. At its core, 3D additive manufacturing, or 3D printing as it is commonly referred to, is a digital manufacturing process: a 3D model constructed using computer-aided design software can be directly translated into a physical object through an automated fabrication routine [1]. It is an integrated digital-to-physical workflow, which enables the immediate realization of a 3D design, bypassing the traditional, often lengthy steps of tooling and mold creation. The direct fabrication approach unlocks a suite of powerful advantages. It offers unprecedented design freedom, enabling engineers and designers to create complex internal geometries, functionally optimized lattices, and lightweight structures that were previously prohibitively costly or simply impossible to manufacture [4, 5]. Users can transition from a digital design to a physical prototype quickly, within a single fabrication device and process step, and without the need to consult experts on different fabrication routines. This has made 3D printing a cornerstone of rapid prototyping, dramatically accelerating innovation cycles [1]. Although the predominant impact of 3D printing lies not in replacing entire manufacturing chains, it enables the tailored fabrication of crucial, selected parts. This makes mass customization and on-demand production economically feasible, paving the way for personalized medical implants, bespoke consumer products, and specialized industrial tooling [4–7].

A further trend in modern technology is miniaturization, as it is the foundation of any integrated circuit. This application-side development naturally requires a counterpart development on the side of microfabrication techniques [8, 9]. This development further stimulates the desire to extend 3D manufacturing to the microscale. However, conventional microfabrication methods, such as photolithography, are typically limited to planar geometries or demand complex, multistep processing. Bridging this gap requires methods that combine the digital design freedom of additive manufacturing with the precision of micro- and nanofabrication - leading to the emergence of 3D laser micro- and nanoprinting [10–12].
The currently dominant technology for achieving true 3D fabrication at the micro- and nanoscale is two-photon-absorption 3D laser printing, or two-photon polymer-

ization (2PP) in short [10, 13, 14]. In this approach, a tightly focused laser beam is scanned throughout the volume of a liquid photoresist, inducing solidification of the material with sub-micrometer resolution. This technology enables applications in life sciences [15–17], micro-optics and photonics [18–20], and micro-fluidics [21, 22], where precise 3D structures at the micro- and nanometer scale are required. However, since polymerization initiation in 2PP relies on a nonlinear two-photon absorption process, it requires high light intensities and therefore costly short-pulsed laser sources [11]. Overcoming this limitation is key to expanding the accessibility and scalability of nanoscale 3D printing [23].

A promising alternative is two-step-absorption (2SA) 3D laser nanoprinting [24], which uses a sequential excitation process for polymerization initiation, thereby reducing the required laser intensities by several orders of magnitude. This allows the use of compact continuous-wave (cw) lasers, significantly lowering system cost. These developments first contain new photoresists used for 3D printing. But with new photoresists, also new printing approaches emerge, such that these two branches of research stimulate each other. Based on this, printing approaches have been realized, demonstrating both a compact 3D laser nanoprinter [25] and a largely parallel projection-based approach via light-sheet 3D laser printing (LS3DP) [26]. However, print speeds and/or total build volumes still lag behind the mature technology of 2PP [24–27].

Since 2SA 3D laser nanoprinting is still in its infancy, this work aims to advance and explore new 3D printing approaches to bring the technology closer to the capabilities of established 2PP - while preserving and expanding its inherent advantage of cost efficiency. This overarching goal condenses into three main topics, all focusing on parallelized 2SA 3D laser printing: first, LS3DP, a recently introduced [26, 28], massively parallelized 3D printing technique based on 2SA photoinitiation, offers significant speed advantages over conventional focus-scan printing approaches. Within this work, crucial challenges currently limiting LS3DP's applicability are addressed, and strategies to overcome them are developed. Second, the print speeds of focus-scan 2SA 3D printing are inherently limited by the photochemical properties of the photoresist. To circumvent this, a dynamic multi-focus 3D printing setup was designed and realized. This uses cost-efficient digital micromirror devices (DMDs) and computer-generated holograms for beam splitting and beam steering. By this technique, print speeds are increased through parallelization measures while still relying on compact cw diode lasers. Third, an advanced version of this setup was developed by incorporating 3D laser-beam steering with a novel, fast, and power-efficient spatial light modulator. This micromirror-based phase light modulator (PLM) was therefore evaluated and successfully used for the application of 3D laser nanoprinting. Furthermore, an emphasis was placed on achieving both affordability and versatility of the printing approach.

OUTLINE OF THIS THESIS

In chapter 2, I will discuss the fundamentals of photopolymerization 3D laser printing. This includes an explanation of the workflow and chemistry, which form the basis of many 3D laser microprinting approaches in general, as well as of all the approaches addressed in this thesis. Afterward, the nonlinearity of 3D laser printing is discussed as a key concept in understanding the 3D capability of the printing approaches addressed. A large part then comprises two-step absorption, its chemistry, as well as advantages, challenges, and limitations. The chapter concludes with a summary of variations of 3D printing processes.

In chapter 3, light-sheet 3D laser microprinting, as originally introduced by Hahn et al. [26, 28], is first explained. Challenges and development potential of this technique are identified in the following to overcome the limitations of LS3DP that hinder its application-oriented use. The challenges addressed within this work are picked up in the following. This includes incorporating a fluidics chamber to increase build volumes by mitigating dose accumulation, as well as developing an optical element for power-efficient generation of the light sheet. The chapter concludes with a critical assessment of the taken routes.

In chapter 4, the framework is established for parallelizing one-color 2SA 3D laser printing as a straightforward method to increase print speeds in 2SA 3D printing, thereby circumventing some of the difficulties of LS3DP. Dynamic holographic laser beam splitting and beam steering via micromirror-based spatial light modulators is identified as a suitable technique to accomplish parallelized 2SA 3D laser printing. Based on this, the computational approach to multi-focus holographic laser beam scanning is introduced, laying the foundation for the following chapters.

In chapter 5, the design, realization, and experimental evaluation of a dynamic multi-focus 2SA 3D laser printing setup based on digital micromirror devices (DMDs) is discussed in detail. This includes the optical design as well as the computational and electronic framework. Emphasis is placed on the diffractive properties of the DMD and on how to manage them to achieve the best printing results. The just-mentioned printing results are presented in the following section. The chapter proceeds with an investigation of spatiotemporal proximity effects, which are important for improving the printing quality of the presented setup and for further understanding the specialties of 2SA 3D printing.

In chapter 6, a second version of the prior presented setup is introduced. The emphasis lies on achieving affordable 3D laser nanorprinting, defined as a cost-effective, versatile 3D printing approach. This is achieved by incorporating novel micromirror-based phase light modulators (PLMs) and 3D holographic laser beam scanning. In doing so, multi-focus 3D beam steering is performed via a single device, rendering the overall setup compact and inexpensive. The chapter concludes with a discussion of holographic approaches for 3D laser printing.

In chapter 7, the results of this thesis are summarized and an outlook on future steps is given.

2

Chapter 2

FUNDAMENTALS OF 3D LASER PRINTING

As the scope of this thesis is the discussion of technological advancements particular to parallelized two-step-absorption 3D laser printing, the following chapter will provide a basic understanding of the physics, chemistry, and engineering involved in 3D laser printing. To do so, I will first illustrate the general workflow in 3D laser printing and briefly discuss the chemistry of photopolymerization. Afterward, I will explain the importance of nonlinearities in 3D laser printing and simple approaches to model the printed structure. In line with these universal concepts, I will discuss in more depth the specific photoinitiation mechanism used throughout this work: two-step absorption. Finally, different implementations of 3D printing processes will be shortly debated.

2.1 Workflow and Chemistry of Photopolymerization 3D Printing

Basic Terms and Workflow

What I will refer to as 3D laser printing is also sometimes called direct laser writing (DLW). The latter provides a more graphic description of the general workflow. Very simplistic, one can imagine the fabrication process as "writing with a pen of light" [29]. This basic concept is further illustrated in Figure 2.1.

First, a droplet of a liquid, light-sensitive photoresist is applied onto a glass substrate. Mostly, negative-tone photoresists are used, which are liquid at room temperature, allowing for easy handling, and which solidify during the 3D printing process [30]. Next, the sample is placed in a microscope assembly near the focal plane of the objective lens. Depending on the targeted feature and structure size, objective lenses with different numerical apertures (NA) and magnifications can be used. With the right choice of photoresist and objective lens, feature sizes in the sub-micrometer regime can be achieved. A laser beam is then tightly focused within the volume of the photoresist, triggering a polymerization reaction and thereby solidifying the photoresist. Several configurations are possible: In oil-immersion mode, the light is focused through a layer of immersion oil and through the glass substrate. Looking at Figure 2.1b, the objective lens would be located at the bottom. Alternatively, the objective lens can be immersed in the photoresist, a configuration which is referred to as dip-in mode [31]. Again, when looking at Figure 2.1b, the objective lens would be located at the top. While the oil-immersion mode has several limitations regarding the structure height and the substrate used, the laser beam not propagating through a larger volume of photoresist might also be beneficial. This is especially true for the two-step absorption photoresists used in this thesis, as discussed later.

The smallest volume element that can be controllably polymerized as part of the entire structure is called a voxel [32]. This term is the 3D equivalent of the 2D picture element, the pixel. As the smallest building block and constituent of the structure, the voxel is of great importance for quantifying and comparing the performance of different 3D printing approaches. The printing speed, which one wants to maximize, is commonly measured in units of voxels per second. The voxel size is a measure for the resolution of a printing approach, which one often wants to minimize, however, depending on the specific application targeted [29].

With these definitions in mind, the laser focus is now scanned across the photoresist volume along a predefined path, polymerizing and thereby building the complete structure. For this, the laser focus and the substrate must move relative to each other. A common configuration involves lateral scanning of the laser focus within a single plane, while the substrate is physically moved in the axial direction to

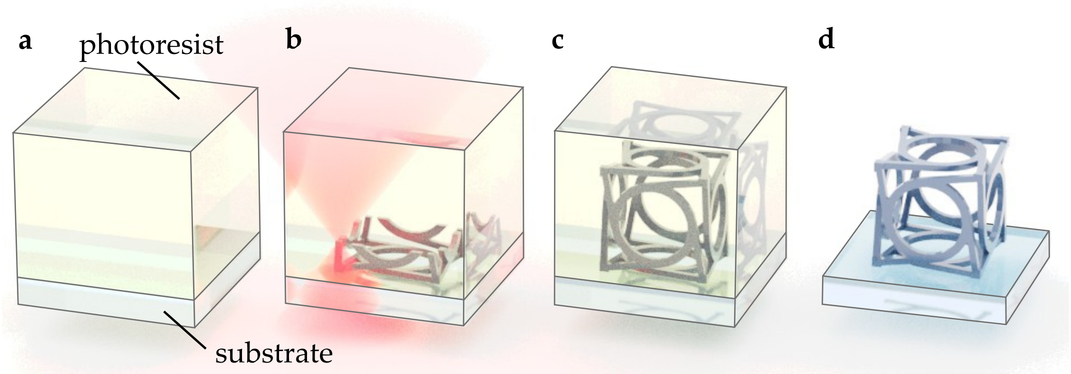

Figure 2.1: General workflow of 3D laser printing. a A droplet of liquid photoresist is placed on a glass substrate. **b** In the close vicinity of a focused laser beam, a volume element, called the voxel, is polymerized. **c** After scanning the laser focus throughout the volume, a solid 3D structure is fabricated. **d** Finally, the unpolymerized, still liquid photoresist is washed away. Figure adapted from [34, 35].

address different planes [11]. This, however, is by far not the only possible configuration for printing 3D structures, as we will see later.

When the printing process is finished, a 3D structure adhering to the substrate but still immersed in the liquid photoresist is the result. In the final step, the sample is immersed in an organic solvent, allowing the unpolymerized photoresist to be washed away. Further UV-curing or post-exposure baking steps [33] are typically not necessary.

The Chemistry of Photopolymerization 3D Printing

The already mentioned photoresist typically consists of two basic components: photoinitiator and monomer molecules. The photoinitiator starts the chemical reaction of polymerizing the monomeric liquid to a solid polymer. The polymerization process for 3D printing employed in this thesis is free-radical photopolymerization [11]. Although other processes, such as step-growth [37] or cationic [10] polymerization, are possible, free radical polymerization is the most commonly used in 3D laser printing. This chemical reaction can be divided into four steps [11, 38], as illustrated in Figure 2.2.

First, the absorption of light by photoinitiator molecules (I) promotes them to an excited state. From this excited state, cleavage of the molecule into two radicals ($R^\bullet$) might occur if the energy supplied exceeds the bond-scission energy. This is called a Norrish type 1 reaction. Alternatively, radical formation occurs via hydrogen abstraction. The latter is called a Norrish type 2 reaction and often comes along

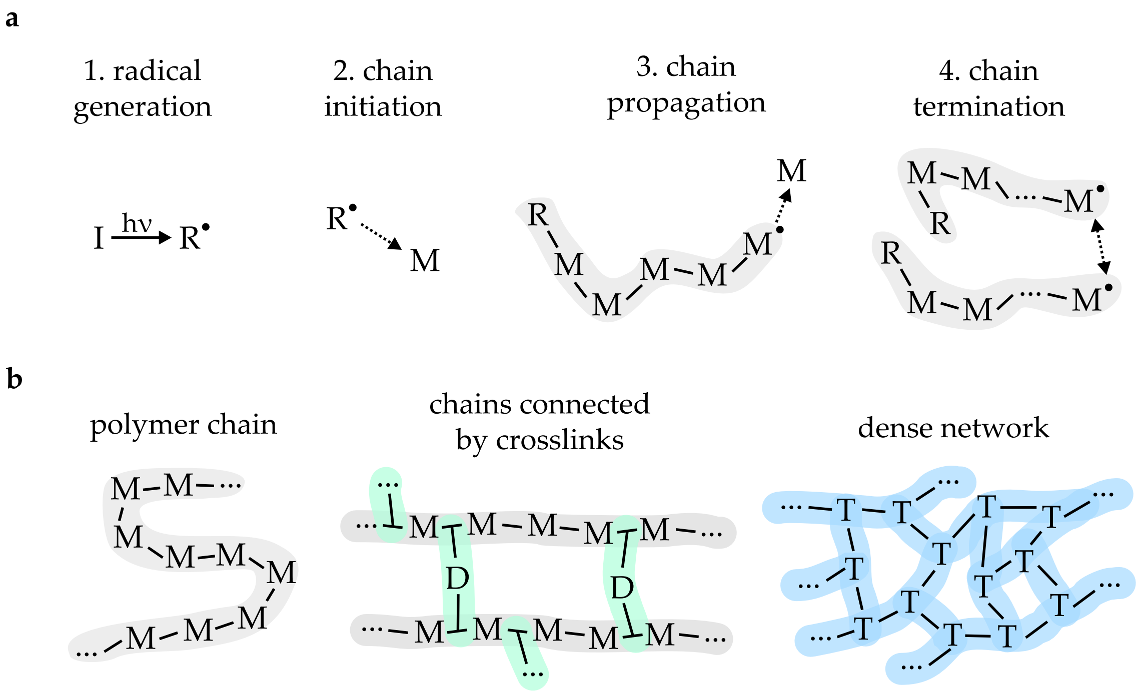

Figure 2.2: Sketch of the photopolymerization chemistry. a The free radical polymerization comprises four steps: light absorption of photoinitiator molecules (I) leads to radical generation. Radicals react with monomer molecules (M) to initiate a radical monomer chain. Further reactions with monomer molecules lead to chain propagation. Several reactions, e.g., a radical recombination, can terminate the chain growth. **b** Depending on the number of functional groups per monomer, the density of the final polymeric network is affected. As an example, mono- (M), di- (D), and tri-functional (T) monomer molecules are considered. Figure reproduced from [36].

with a hydrogen-donating coinitiator [39].

Following the radical formation, the photoinitiator radicals react with functional groups of nearby monomer molecules (M). The photoinitiator radical is attached to the monomer's functional group, creating a radical as the combined molecule. This is the chain initiation step.

Third, this monomer radical can again react with and attach to further monomer molecules. A connected chain of monomers with a radicalic functional group results. This growth of the polymeric network is called chain propagation.

Finally, several possible steps can lead to the chain propagation coming to an end. These are so-called chain termination reactions. Two radicals, either photoinitiator radicals or radicalic monomer chains, can recombine and therefore terminate the chain growth. Alternatively, so-called scavenger molecules can react with radicals, creating molecules that do not contribute to further chain growth. Important radical-scavenging reactions involve atmospheric oxygen, which provides an efficient scavenging pathway via the formation of peroxy radicals [39]. Although

they are radicals themselves, they do not propagate the chain further but quickly recombine. In commonly used monomers, oxygen scavenging is a process that must first be overcome during the polymerization induction period until the oxygen concentration is locally depleted. Only after that, efficient chain propagation can take place, eventually forming a solid polymer.
The monomer molecules used in this work feature acrylate groups. One monomer molecule can have one or more acrylate groups. This property influences crosslinking, since monofunctional monomers only form unconnected long chains. Multifunctional monomers provide better crosslinking, leading to connected chains and dense networks (see Figure 2.2b) [11]. Throughout this work, only multi-functional monomers are used.

2.2 NONLINEARITIES AND THE EXPOSURE DOSE

Summarizing the above, 3D laser printing in the mentioned implementation aims to polymerize small building blocks within the volume of a liquid photoresist. This requires the ability to confine the polymerization reaction volume in 3D space to the close vicinity of a tightly focused laser beam and to steer it along with the laser focus. In this section, I will explain how to achieve this 3D confinement. To this end, I want to start the discussion at a higher level of abstraction by describing the so-called threshold and accumulation model of a photoresist.

Threshold Model and the Exposure Dose

In the threshold model, the outcome of the polymerization reaction is assumed to be binary: either the degree of polymerization is high enough that the polymer network withstands the development routine, or it is insufficient and the loosely connected polymer chains are washed away during development. Furthermore, the complex chemical processes involved will be approximated by a single quantity, the local exposure dose D. If the dose exceeds a certain polymerization threshold D_{th}, the material solidifies [42, 43]. This local exposure dose can be assumed to be proportional to the number of radicals generated, which can be assumed to be proportional to the number of photoinitiator molecules excited [24]. To further refer this to the optics parameters of the laser beam employed, this is assumed to be proportional to the quantity I^N, being I the light intensity and N the nonlinearity exponent. With the exposure time t_{exp}, the exposure dose typically scales linearly. This leads to

$$D \propto I^N \cdot t_{\text{exp}}, \tag{2.1}$$

which gives the local deposited dose for a single point exposure [24]. The nonlinearity exponent N is an expression of the specific photoinitiation pathway employed.

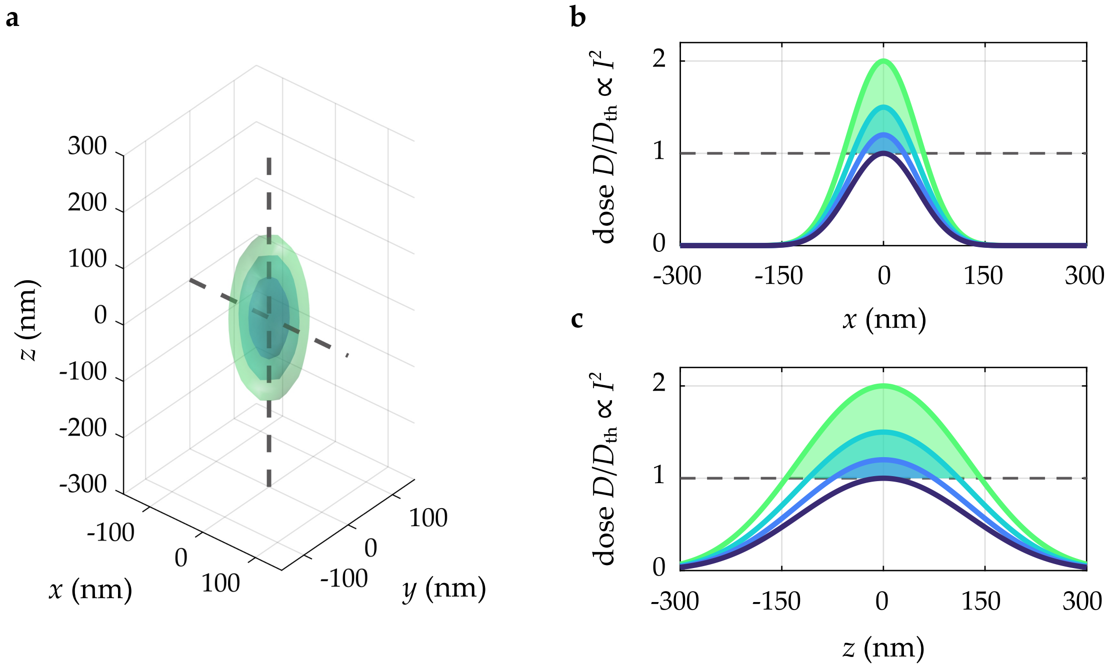

Figure 2.3: Illustration of the threshold model of 3D laser printing. a Schematic of differently sized voxels, i.e., the isovalue surfaces of a constant deposited dose are drawn for different threshold values. **b** Cut along the x-direction. Doses above the polymerization threshold are shown as colored areas. **c** In the same fashion, a cut along the z-direction is shown. The focus is calculated following the formalism of Ref. [40], using a wavelength of $\lambda = 405\,\mathrm{nm}$ and a numerical aperture of $\mathrm{NA} = 1.4$. Figure adapted from [35, 41] under CC BY 4.0.

These pathways will be explained in more detail towards the end of this chapter. An illustration of equation 2.1 is provided in Figure 2.3. Within the threshold model of a single exposure, the polymerized voxel can be arbitrarily small [42]. But, as soon as we want to talk about 3D printing of more than one voxel, the threshold model has to be expanded by the accumulation model.

Accumulation Model and Feature Sizes

The polymerization of more than one voxel at different points in time and space cannot simply be treated as the combination of several arbitrarily small voxels, as the threshold model states for single exposures. This behavior would be observed with an imagined "forgetting" photoresist. However, in reality, photoresists typically exhibit "memorizing" behavior, where exposure doses accumulate [42, 43]. This is an expression of the accumulation model and is illustrated in Figure 2.4a. The deposited dose from exposures at different points in space and time is

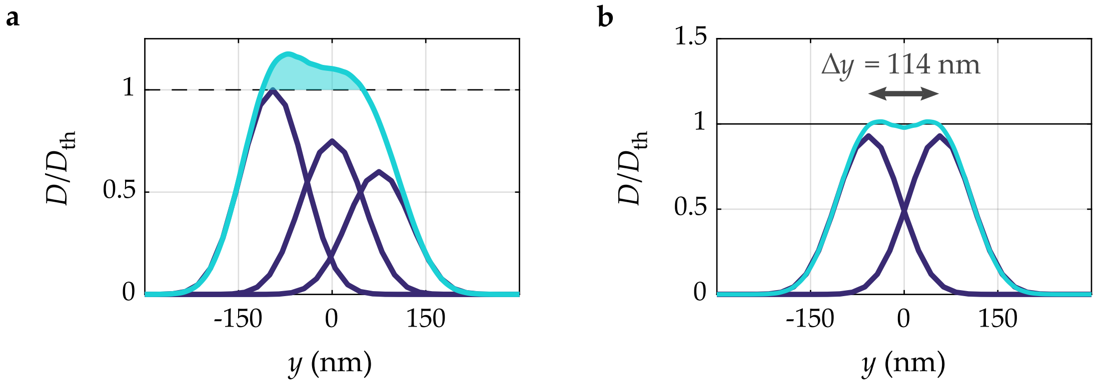

Figure 2.4: The accumulation model and its impact on the minimum feature size. a Illustration of the normalized dose of three subsequent exposures (dark blue), each being below the polymerization threshold D_{th}. The accumulated dose (light blue) is, however, above the threshold, leading to a polymerized structure. **b** Illustration of the Sparrow criterion as a definition of the minimum feature size achievable. For the chosen parameters of $\lambda = 405\,\mathrm{nm}$, $\mathrm{NA} = 1.4$, and two point-like exposures, this is reached at $\Delta y = 114\,\mathrm{nm}$, where the accumulated dose still exhibits a local minimum below the polymerization threshold. Figure adapted from [41, 44] under CC BY 4.0.

summed, regardless of whether the individual exposures are above or below the polymerization threshold. Doing so, two voxels cannot be brought arbitrarily close together - there is a minimum separation distance that depends on the targeted structure. These effects are also called proximity or dose accumulation effects. The total exposure dose resulting from multiple exposures is consequently given by the time integral

$$D(x, y, z) \propto \int I^N(x, y, z, t)\,\mathrm{d}t. \tag{2.2}$$

The chemical rationale for this phenomenological model is the formation of so-called oligomers or pre-polymers [32]. These are chains of monomers, where the radical polymerization reaction terminates before a sufficient degree of polymerization is reached for the material to solidify. But after a further generation of radicals, these oligomers can again participate in the chain-propagation reaction, eventually forming a dense polymeric network. Limitations of the accumulation model, assuming an infinitely long memory of the photoresist, are diffusion processes due to which the still mobile oligomers spread across the photoresist volume [45]. Of course, also an in-situ resist exchange or a continuous flushing of the reaction volume with new photoresist will change the conditions by partly "resetting the photoresist's memory". This will be exploited in section 3.3.

Accompanying the discussion of the accumulation model is the discussion of the minimal reachable feature size or resolution of a 3D laser printing approach. First, the terminology has to be defined. The resolution of a 3D laser printing approach is commonly defined according to the Sparrow criterion. There, the achievable resolution is the distance between two local maxima of the accumulated exposure dose, which still feature a local minimum in between [42]. This is therefore identical to the minimum distance of two disconnected voxels.

Putting this in the context of the optics involved, the resolution depends on the laser focus's numerical aperture NA, the free-space wavelength λ, and the nonlinearity exponent N. An approximation for the lateral resolution Δy is given by [42]

$$\Delta y = \frac{1}{\sqrt{N}} \frac{\lambda}{2\,\mathrm{NA}}, \tag{2.3}$$

which is further illustrated in Figure 2.4b. The axial resolution Δz is calculated as the lateral resolution scaled by the aspect ratio of the laser focus's point spread function (PSF).

Nonlinear Photoinitiation

Already mentioned and tacitly used in the two previous sections, I now want to provide a more detailed explanation of the importance and the physics behind the nonlinearity exponent N, following the description of Ref. [35]. To start, I want to showcase different edge cases and their impact on 3D printing, as illustrated in Figure 2.5. In Figure 2.5a, the normalized dose is depicted along the optical axis z and the perpendicular x-direction for a Gaussian beam ($\lambda = 405\,\mathrm{nm}$ and $\mathrm{NA} = 1.4$) focused to the coordinate origin. It is assumed a strongly absorbing photoresist and a nonlinearity exponent $N = 1$, rendering $D \propto I$. According to the Beer-Lambert law, the intensity, and therefore the dose, exponentially decays as it propagates through the absorbing photoresist. In the right panel of Figure 2.5a, the summation of the dose along the x- and y-direction, and therefore the accumulated dose per z-layer, is shown. This again indicates the exponential decay along z. Replacing the strongly absorbing photoresist with a very weakly absorbing one, the outcome is depicted in Figure 2.5b: the intensity, and therefore the dose, peaks at the coordinate origin for $N = 1$. However, the accumulated dose per z-layer is constant, since the optical power and the number of absorbed photons per z-layer are constant, when assuming the absorption to be negligible. Assuming again a negligible absorption, but a relation of $D \propto I^2$, therefore a nonlinearity exponent of $N = 2$, the situation is different. Still, the dose peaks at the focus position, but the accumulated dose per z-layer does so as well, rather than being constant across all z-layers. This is illustrated in Figure 2.5c.

The implications of this can be understood through a simple thought experiment: consider the case of a weakly absorbing photoresist and the exposure of a single voxel at an arbitrary position within the focal volume. For $N = 2$, the dose per

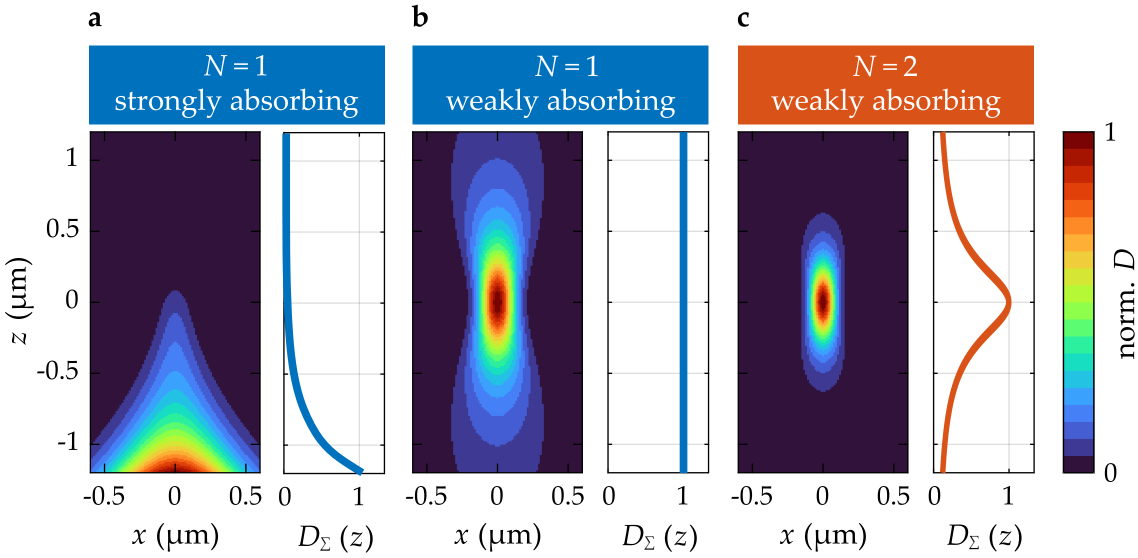

Figure 2.5: Demonstration of the importance of nonlinearities for 3D laser printing. **a** The normalized dose ($D \propto I^N$) is plotted for a Gaussian beam at $\lambda = 405\,\text{nm}$ and $\text{NA} = 1.4$, focused into a strongly absorbing photoresist and assuming $N = 1$. The deposited dose is highest at the interface and decays exponentially. This is further illustrated in the right panel, which shows the accumulated dose per z-layer. **b** Likewise, the case of a weakly absorbing photoresist is shown. The beam is focused inside the volume. However, since the optical power is equal for all z-layers, the accumulated dose is also equal for all z-layers. **c** In case of $N = 2$, the accumulated dose peaks at the focus position, rendering 3D printing inside the volume possible. Figure adapted from [35, 44].

unit volume and the accumulated dose peak at the focus position. For $N = 1$, only the dose per unit volume peaks at the focal position. However, in combination with the photoresist's threshold behavior, a single voxel can still be printed. When polymerizing an extended plane within the photoresist volume, the focus position needs to be scanned across this plane. Therefore, also above and below the targeted plane, the absorbed photons and therefore accumulated dose add up, leading to polymerization above and below the target plane. In the case of an infinitely large plane and an infinitesimally small spacing between exposures, the dose per volume, decisive for local polymerization, approaches the shown summed dose D_Σ, thereby polymerizing the entire volume. The printing of complex and extended 3D structures, therefore, requires a nonlinear process ($N > 1$), where the summed dose is not constant.

A side note should be made to the case of Figure 2.5a, where also D_Σ is not constant. Indeed, the large absorption provides a nonlinearity that can be exploited for 3D printing (see chapter 2.4), but polymerization always takes place at the interface between the photoresist and its surroundings. This contradicts the 3D laser printing approach presented in Figure 2.1, which targets 3D printing within the photoresist volume.

As the concept is generally applicable, all the discussions so far have lacked deeper explanations of the mechanisms underlying the different nonlinearities, which I want to catch up on now. The nonlinearity exponent relates the light intensity I to the deposited dose D. It was mentioned that the dose is proportional to the number of radicals generated. Therefore, it has to be looked at the radical generation and the photoinitiation pathway. This can be mediated by a single photon, which excites a photoinitiator molecule to a higher electronic state from which it decays into radicals. In this one-photon-absorption (1PA) case, the nonlinearity exponent is one. Besides this, there can be a two-photon-absorption (2PA) pathway, in which the simultaneous absorption of two photons, each with half the energy of the electronic transition, excites the photoinitiator molecule. This is the most commonly exploited pathway in 3D laser micro- and nanoprinting, where $N = 2$ [11]. In this nonlinear optical process, the light field creates a so-called virtual state, through which the absorption of two photons can occur [46]. This process, however, is very unlikely, which means that high photon flux densities are needed to make two-photon absorption usable for 3D laser printing. Such high photon flux densities can be provided in the focus of a pico- or femtosecond-pulsed laser beam. Additionally, the energy of the photons should not be sufficient to trigger a reaction via one-photon absorption. In other words, the photoresist should be transparent to the laser wavelength used but absorptive at half that wavelength. This also inherently fulfills the criterion of weak absorption set out at the beginning of this section.

Two-photon absorption as a nonlinear photoinitiation pathway for 3D laser micro- and nanoprinting has matured over almost three decades since its first use in 1997 [14]. Despite being the workhorse enabling a range of applications across different fields, there are conceptual drawbacks: As mentioned, high photon flux densities are required for reasonable print speeds, which necessitates the use of short-pulsed laser sources. These laser sources are relatively expensive and bulky, limiting the affordability and compactness of 3D laser nanoprinters. There are, however, alternative nonlinear photoinitiation pathways that overcome the need for short-pulsed laser sources and rely on continuous-wave (cw) lasers. Among these is two-step absorption [24], which is the photoinitiation pathway employed for all 3D laser printing approaches presented in this thesis.

2.3 TWO-STEP-ABSORPTION (2SA) 3D LASER PRINTING

In the following section, I will introduce the concept of two-step absorption as an alternative photoinitiation pathway to two-photon absorption. This first involves

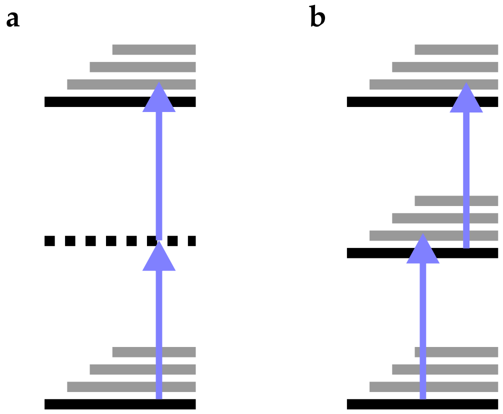

Figure 2.6: Two-photon absorption and two-step absorption. a shows a simplified energy level diagram for two-photon absorption via a virtual state (dashed line). **b** In two-step absorption, two subsequent transitions proceed via a real intermediate state (solid line). Adapted from [44].

explaining how to achieve and maintain the necessary nonlinearity of the 2SA process during 3D printing. Following this, the versatility of 3D laser printing approaches, coming along with 2SA, will be explained in general, as well as for the specific 2SA photoresist systems used in this work.

2.3.1 The Effective Nonlinearity in 2SA 3D Printing

Two-step-absorption photoinitiation is able to provide the same nonlinearity exponent of $N = 2$ as in the two-photon-absorption case. A very basic comparison between these two is provided in Figure 2.6. The schematic energy-level diagram in Figure 2.6a shows the 2PA process via a virtual intermediate state, indicated by the dashed line. The virtual intermediate state, which requires strong light fields to be present and to provide a 2PA pathway, can also be exchanged by a real intermediate state, as shown in Figure 2.6b. This real intermediate state is an always-present electronic energy level of the photoinitiator molecule. Therefore, the intermediate-state lifetimes are vastly different for 2PA than for 2SA. For 2PA, the intermediate-state lifetime is directly connected to the laser pulse duration, which is commonly on the order of several hundred femtoseconds [14]. The intermediate-state lifetime for a real intermediate state is independent of the pulse duration and a parameter of the photoinitiator molecule, as well as the photoresist mixture as a whole. Taking intermediate-state lifetimes of tens to hundreds of microseconds as a reasonable example for the photoresists used in this thesis [24, 26], the intermediate-state lifetime is eight orders of magnitude different. This is accompanied by a drastic reduction in the light intensity required to promote the two transitions, since the probability of a second photon further exciting a molecule in the intermediate state increases with the lifetime of this level.

For the 2SA process to retain the necessary nonlinearity, several significant criteria must be fulfilled [24]. First and foremost, the real intermediate state has to be an inert state. This means that no or only a very small number of radicals should be generated from the intermediate state. If there is a competing radical-generation pathway from the intermediate state, the effective nonlinearity decreases and approaches one if that were the dominant path. Furthermore, the intermediate-state lifetime should neither be too short nor too long. Considering the first case of a short intermediate-state lifetime, 2SA loses its advantage, as the necessary light intensity increases with a shorter lifetime. Considering the extreme other case of an infinitely long intermediate state, which might be an intermediate molecule of a two-step chemical reaction, the initiation pathway loses its nonlinearity. When scanning the laser focus, eventually, all molecules, also in the tails of the laser focus, are pre-excited. The intermediate state can be thought of as the new ground state, and the photoinitiation takes place via a one-photon absorption process. The decay from the intermediate state back to the ground state is, therefore, another prerequisite to be fulfilled.

To find suitable conditions for a nonlinear 2SA photoinitiation, Hahn et al. performed rate-equation calculations on a simple three-level system [24]. This represents a simplified energy-level diagram of the electronic levels of the photoinitiator molecule, depicted in Figure 2.7a. From a ground state A, an optically triggered transition to state B can be performed with the rate coefficient k_1 being proportional to the light intensity I and the extinction coefficient ε_1. Likewise, a transition between B and C can be performed at a rate $k_2 \propto \varepsilon_2 I$. Following this two-step absorption, radicals can be generated (state D). The population of D is assumed to be proportional to the deposited dose. As discussed, a decay from B to A is necessary for a nonlinearity, which is maintained by the decay rate k_D. Based on this model, a nonlinearity exponent N can be calculated following

$$N = \frac{I}{D}\frac{\mathrm{d}D}{\mathrm{d}I}. \tag{2.4}$$

The nonlinearity for various parameter combinations dependent on k_1 and k_2, which are normalized to a certain k_D, is shown in Figure 2.7b. It can be seen that all values between $N = 1$ and $N = 2$ can be addressed, depending on the rate coefficients. Looking at the regime at the bottom left, where $k_1 < k_\mathrm{D}$ and $k_2 < k_\mathrm{D}$, the nonlinearity is the highest. Therefore, a rapid decay from the intermediate state, resulting in a short intermediate-state lifetime, is beneficial for maintaining a high nonlinearity.

Furthermore, these calculations show that, for a given photoresist (i.e., given ε_1, ε_2, and k_D), the nonlinearity depends on the printing parameters. For this reason, one often speaks of an effective nonlinearity, since it is not a fixed parameter. For a given photoinitiator, the ratio of the extinction coefficients at a given wavelength is fixed, such that the diagonal lines in Figure 2.7b can be read as choosing a photoinitiator molecule and/or wavelength. As an illustrative example for the photoinitiator benzil, which will be introduced in the next section and widely used throughout

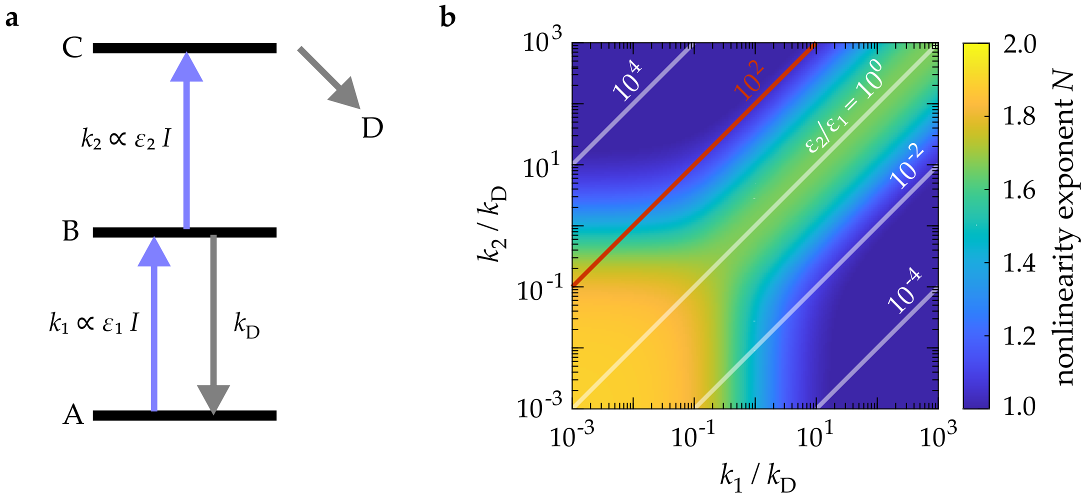

Figure 2.7: Rate-equation calculations on two-step absorption. **a** Three-level model employed for the rate-equation calculations. A two-step absorption takes place from level A to B and from B to C. From C, a fast decay into radicals is assumed. These are assumed to be proportional to the deposited dose D. **b** False-color plot of the nonlinearity exponent N, calculated following equation 2.4. For transition rates k_1 and k_2 smaller than the decay rate k_D, a nonlinearity $N > 1$ is achieved. The diagonal lines depict constant ratios of the extinction coefficients ε_1 and ε_2, which refer to a fixed photoresist system at a fixed wavelength. The red line indicates the ratio corresponding to the photoinitiator benzil at a wavelength of 405 nm. Figure adapted from [24, 44] with the permission of Springer Nature.

this thesis, a red diagonal line at a constant ratio of $\varepsilon_2/\varepsilon_1 = 10^2$ is drawn. When moving along this line from the bottom left to the top right, e.g., the laser light intensity increases while the other parameters remain fixed. At a constant dose, this implies an increase in the print speed v. Therefore, increasing the print speed above a particular value decreases the nonlinearity of the photoinitiation process. This sets a limit to the single-focus print speed and favors parallelization approaches, which are employed in this work.

2.3.2 *One-Color and Two-Color 2SA*

All the above discussions on 2SA are generally applicable but were made for the case of two transitions bridging the same energy gap. Therefore, the same laser light wavelength and the same intensity I were assumed. However, this is not necessarily the case. The subsequent absorption of two photons of different energies can also be exploited for advanced 3D laser micro- and nanoprinting approaches, as will be introduced in this section on one-color and two-color 2SA.

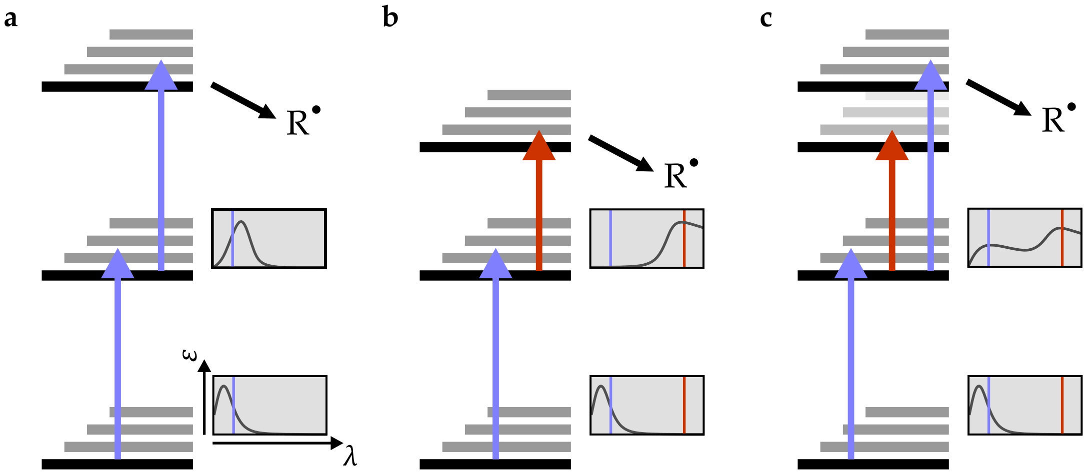

Figure 2.8: Multi-color 2SA processes. **a** One-color 2SA where both transitions are mediated by light of the same wavelength. In the two boxes, schematic absorption spectra for the ground- and excited-state absorption are shown. **b** Synergistic two-color 2SA. Only the simultaneous presence of light of two different wavelengths leads to a radical generation, since the absorption spectra are non-overlapping. **c** Antagonistic two-color 2SA. Radicals are generated after one-color 2SA. However, this process can be inhibited by the absorption of a photon of a different energy.

This has to include a closer look at the absorption spectra of the ground and intermediate states of the photoinitiator molecule. The location of the absorption bands features several possible combinations, where I want to focus on three different cases illustrated in Figure 2.8.

The already discussed case of one-color 2SA is shown in panel a. Although the absorption spectra of the ground and intermediate states are typically different, they must overlap at the employed wavelength, as indicated by the blue line. Tuning the laser wavelength in this case also changes the ratio $\varepsilon_2/\varepsilon_1$, which was discussed in the last section.

Figure 2.8b showcases synergistic two-color 2SA [26, 47, 48]. The two absorption spectra of the ground and intermediate states show no mutual overlap at the two wavelengths indicated by the colored lines. This means that the light of both wavelengths has to be present at the same point in space and within the time interval of the intermediate-state lifetime to accomplish the 2SA process. Such a photoinitiation process can also be called an *AND*-type photoinitiator [28]. Synergistic two-color 2SA allows for a massively parallelized 3D laser printing approach by light-sheet 3D laser printing (LS3DP) [26, 47], which will be as part of the present work discussed in more detail in chapter 3.

A third case, which is exploited for 3D laser nanoprinting, is antagonistic two-color 2SA. There, the absorption bands at a first wavelength, indicated by the blue line in Figure 2.8c overlap, allowing for one-color 2SA 3D printing. Furthermore, a second

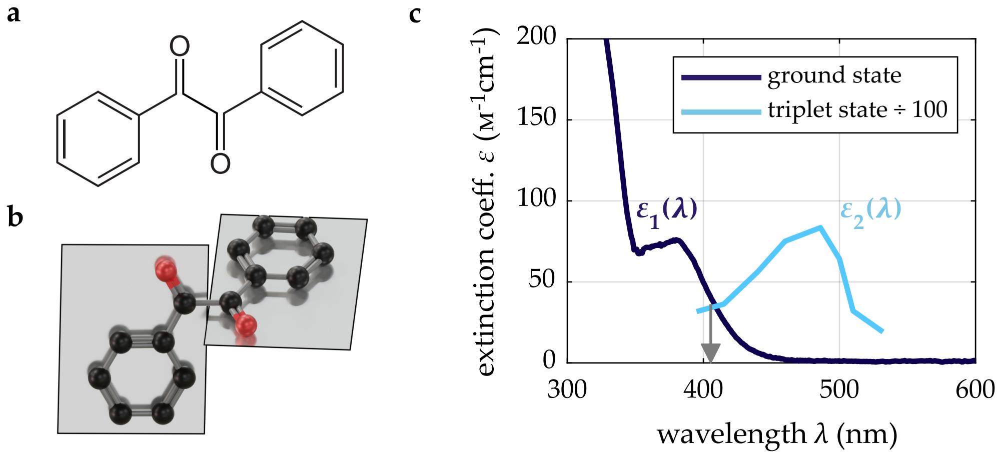

Figure 2.9: Structure and absorption spectra of the photoinitiator molecule benzil. **a** Structure of the α-diketone benzil. **b** In its ground state, benzil shows a skewed conformation, twisted in between the two carbonyl groups. **c** The ground-state molar decadic extinction peaks in the UV region and phases out in the blue. The triplet-state extinction, which is scaled down by a factor of 100, peaks in the blue region. At 405 nm, both spectra overlap at a ratio of $\varepsilon_2/\varepsilon_1 \approx 100$. Figure and data adapted from [24, 44] with the permission of Springer Nature.

wavelength can lead to a reversible depletion of the intermediate state, therefore effectively inhibiting the polymerization reaction. An inhibition pathway can also be used in 2PA 3D printing as STED-inspired 3D laser printing to increase the resolution below the diffraction limit of the optics employed [32, 42]. Also in 2SA, a resolution enhancement over one-color 2SA could be demonstrated by employing antagonistic two-color 2SA [27].

2.3.3 A Benzil-Based One-Color 2SA Photoresist

The search for photoinitiator molecules that meet the criteria for two-step absorption is an active and ongoing area of research [27, 49]. To date, several molecules and photoresist combinations have been reported for each of the three different classes introduced in the last section [27]. The state-of-the-art photoresist system for one-color 2SA, which has been most intensively studied and which is also used for one-color 2SA 3D printing in this work, is based on the molecule benzil [24]. Benzil is one molecule out of the group of symmetric α-diketones [50]. Therefore, the core structure is composed of two adjacent carbonyl groups followed by a phenyl group on either side. At room temperature, benzil is a yellow solid. The structure formula of benzil is shown in Figure 2.9a, whereas in Figure 2.9b, a ball-and-stick model showing the 3D structure in its ground state is depicted. There it can be seen that the two benzoyl groups forming the molecule are twisted by 117°

[51]. In the literature, benzil has been reported as "reluctant", therefore fairly poor, one-photon photointiator [52].
The molar decadic extinction coefficient of benzil in its ground state as well as in its lowest triplet state is shown in Figure 2.9c. The ground-state absorption peaks in the ultraviolet (UV) region below 300 nm (not shown), and phases out towards the visible spectral region [24]. The triplet-state extinction is shown in the blue and green spectral region, where the extinction peaks at around 480 nm [53]. Note that the triplet-state extinction is scaled down by a factor of 100. At 405 nm, a wavelength where a large variety of diode lasers are available, both extinction spectra overlap at a ratio of the extinction coefficients of $\varepsilon_2/\varepsilon_1 \approx 100$. The absorption bands, therefore, fulfill the criterion for one-color 2SA.

Without further explanation, I have considered the lowest triplet state as the intermediate state for two-step absorption. The justification of this should be given now, alongside a more detailed energy level diagram of benzil, which is depicted in Figure 2.10. From its singlet ground state, benzil can be excited via one-photon absorption to an excited singlet state S_1. Although a fluorescent or non-radiative decay back to the ground state is possible, an intersystem crossing (ISC) to the triplet manifold predominantly takes place with a high quantum yield of $\Phi_{\text{ISC}} = 92\,\%$ [54]. The energy of the lowest triplet level T_1 is given as $E_{\text{T}} = 2.3\,\text{eV}$ [55]. This energy is lower than benzil's lowest carbon-carbon bond scission energy, which is on the order of 3 eV [56], rendering the probability of a radical formation from T_1 rather small. Therefore, benzil meets another criterion for good two-step-absorption photoinitiators: an inert intermediate state.
Furthermore, there are decay pathways from the T_1 state back to the electronic ground state S_0 via phosphorescence, reverse intersystem crossing, as well as bimolecular quenching and triplet-triplet-annihilation processes [53, 57]. Therefore, the criterion of a decay from the intermediate state back to the ground state is fulfilled.
Besides spontaneous decay from T_1, benzil can undergo excited-state absorption to higher triplet states. The extinction coefficient of the T_1 state is shown in Figure 2.9a. It peaks at around 480 nm at a value of $\varepsilon_2 = 8 \cdot 10^3\,\text{M}^{-1}\,\text{cm}^{-1}$ [53]. From these higher triplet states, the energy is high enough for a symmetric α-cleavage into two radicals [50, 52, 56].
Despite the predominant fulfillment of the raised criteria for good 2SA photoinitiators, there are processes that counteract the two-step photoinitiation pathway. This is mainly undesired radical generation from the intermediate state, rendering it not completely inert but partly reactive. The main pathways involve hydrogen-abstraction reactions from T_1 [58]. In this reaction, a hydrogen atom is abstracted from nearby hydrogen-donating groups, e.g., of the monomer. This leads to the formation of free radicals [55].

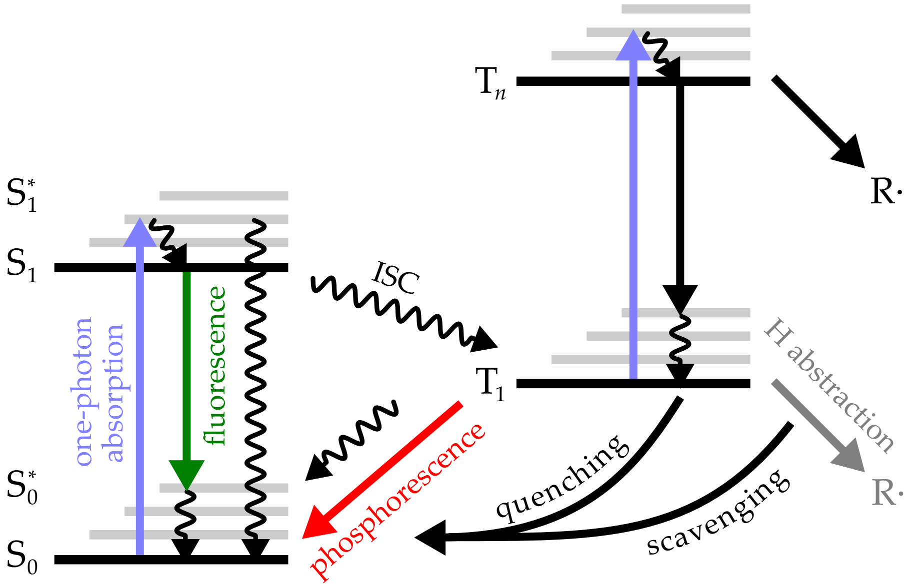

Figure 2.10: Energy level diagram and dominant processes of the benzil-based one-color 2SA photoresist following [57]. Starting from the singlet ground state S_0, benzil can undergo a one-photon absorption to an excited singlet state followed by an intersystem crossing (ISC) towards the triplet manifold. From there, a second absorption can promote the molecule to an excited triplet state, from where a decay into radicals follows. Besides this photoinitiation pathway, there are several radiative (straight, colored arrows) and non-radiative (waved arrows) relaxation pathways. From T_1, undesired hydrogen abstraction can take place, which is reduced by adding additional molecules serving as triplet quencher and radical scavenger. Figure and data adapted from [24, 44, 57] with the permission of Springer Nature.

It is desired to suppress the hydrogen-abstraction reaction. This can be achieved by adding triplet-quencher molecules to the photoresist. These are molecules which provide a relaxation pathway from the T_1 state back to the ground state via an energy transfer to the quencher molecule [55]. Adding such molecules allows for tuning the effective T_1 lifetime of benzil. The lifetime can be reduced, thereby enhancing nonlinearity and making the hydrogen-abstraction reaction less likely. One triplet-quenching molecule is solvated molecular oxygen, which is always present in the photoresist under ambient conditions [59, 60]. Since adjusting the solvated oxygen concentration is, however, cumbersome, additional molecules are added to the photoresist. One molecule that has been proven beneficial for this purpose is bis(2,2,6,6- tetramethyl-4-piperidyl-1-oxyl) sebacate (BTPOS) [24]. BTPOS consists of two (2,2,6,6-tetramethylpiperidin-1-yl)oxyl (TEMPO) moieties connected by an aliphatic chain. In the literature, TEMPO is described as a molecule belonging to the group of hindered amine light stabilizers, which have applications in nitroxide-mediated radical polymerization reactions [61, 62]. TEMPO is a persistent radical

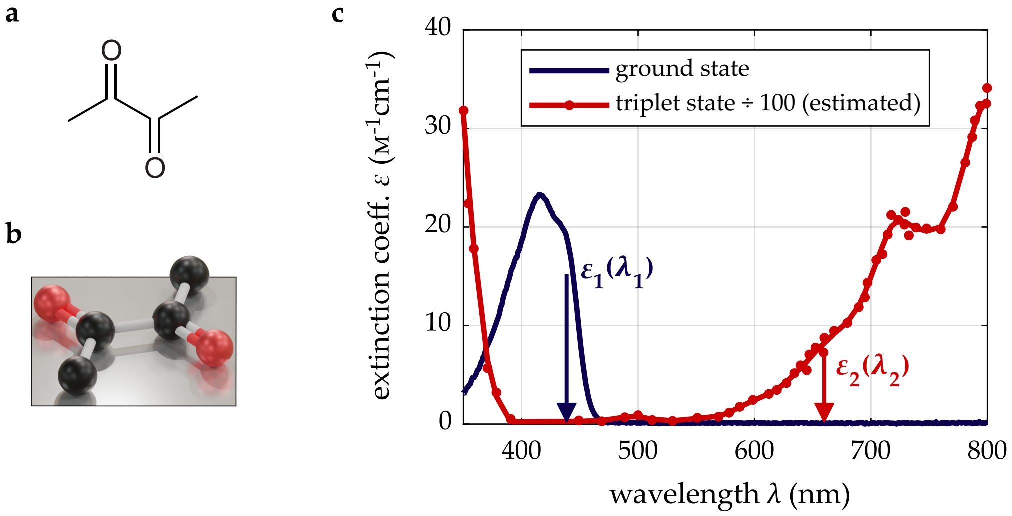

Figure 2.11: Structure and absorption spectra of the photoinitiator molecule biacetyl. **a** Structure of the simplest α-diketone benzil. **b** Ball-and-stick model showing a planar configuration in biacetyl's ground state. **c** The ground-state molar decadic extinction peaks in the blue region. The triplet-state extinction, which is taken from [65, 66], is scaled down by a factor of 100 and shows several peaks in the red and infrared region. At the two wavelengths indicated by the colored arrows, the two spectra do not overlap, fulfilling one necessity for synergistic two-color 2SA. Figure adapted from [26, 44].

that does not self-terminate with other molecules of the same kind. In combination with benzil, TEMPO can act twofold: It quenches the lowest triplet state of benzil at a diffusion-limited rate [63] and suppresses hydrogen abstraction reactions [64]. BTPOS and TEMPO are required ingredients for the 2SA photoresist. However, the predominant supporting pathway is still not fully understood [44]. Therefore, the terms of scavenging and quenching will be used interchangeably throughout this work.

The discussed benzil-based photoresist will be employed for two newly developed one-color two-step-absorption printing approaches presented in the chapters 5 and 6.

2.3.4 *A Biacetyl-Based Two-Color 2SA Photoresist*

Like benzil, which is the state-of-the-art example for a one-color 2SA photoinitiator, biacetyl is the analogue example for a synergistic two-color 2SA photoinitiator [26]. As shown in Figure 2.11, biacetyl (butane-2,3-dione) is the simplest α-diketone. Following the two carbonyl groups are only two methyl groups on either side. At room temperature, biacetyl is a yellow liquid with a significant buttery odor [67].

As can be seen from the ball-and-stick model (Figure 2.12b), biacetyl exhibits a planar configuration in its ground state [68]. Biacetyl is not commonly used as a photoinitiator, but it is widely used as a buttery flavoring agent, though it is simultaneously controversial [67, 69].

In Figure 2.12c, the molar decadic extinction spectra of biacetyl in its singlet ground state as well as in its lowest triplet state are shown [26, 65, 66]. As already discussed in 2.3.2, the prerequisites for a synergistic two-color 2SA photoinitiator are non-overlapping spectra of the ground and the intermediate state for at least two distinct wavelengths. This is the case, e.g, when looking at the two wavelengths highlighted by the blue and red arrows at 445 nm and 660 nm, respectively.

Very similar to the preceding section on benzil, I want to discuss the other criteria for good 2SA photoinitiators alongside the energy level diagram of biacetyl, which is depicted in Figure 2.12c. From its S_0 ground state, biacetyl can be excited via the absorption of a photon in the UV or blue spectral region to the S_1 state. From there, radiative or non-radiative relaxation is possible, however, intersystem crossing to the triplet manifold occurs at a close to unity quantum yield [70]. The lowest triplet state has an energy of $E_T = 2.4\,\text{eV}$ [55, 70, 71]. This is well below its lowest bond-scission energy of 3.2 eV, rendering a decay of biacetyl into radicals from T_1 improbable [72]. Still, similar to benzil, radical generation can occur via hydrogen-abstraction reactions with nearby hydrogen-donating molecules [73–75]. These undesired side reactions can be minimized by adding additional quencher molecules such as TEMPO or BTPOS, again serving as a triplet quencher and a radical scavenger. If done so, biacetyl features a sufficiently inert intermediate state fulfilling one of the criteria for good 2SA photoinitiators.

Third, biacetyl shows a spontaneous decay from its intermediate state back to the ground state via several processes, including phosphorescence, non-radiative internal conversion pathways, as well as triplet-triplet-annihilation processes of two excited biacetyl molecules [76, 77]. From measurements exploiting biacetyl's room-temperature phosphorescence, the triplet-state lifetime can be deduced to be around 200 µs [78].

Although 3D laser printing via co-focusing two cw laser beams of two wavelengths to one focus and scanning this single focus throughout the volume is possible [48], synergistic two-color 2SA can realize its full potential through a massively parallelized light-sheet 3D laser printing approach [26, 28]. The investigation of several strategies for improving light-sheet 3D printing will be discussed in chapter 3.

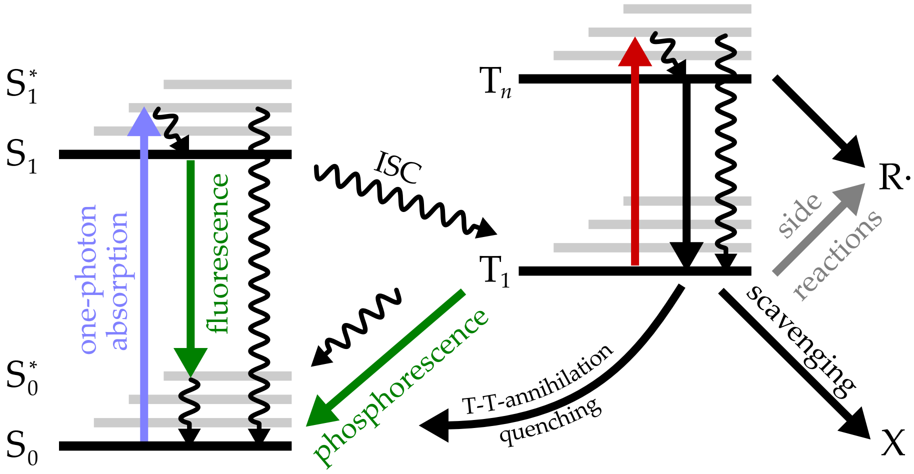

Figure 2.12: Energy level diagram and dominant processes of the biacetyl-based synergistic two-color 2SA photoresist. Starting from the singlet ground state S_0, biacetyl can undergo a one-photon absorption to an excited singlet state followed by an intersystem crossing (ISC) towards the triplet manifold. There, a second red or infrared photon can be absorbed, followed by a decay into radicals. Besides this photoinitiation pathway, there are several radiative (straight, colored arrows) and non-radiative (waved arrows) intramolecular as well as bimolecular relaxation pathways. From T_1, undesired side reactions can take place, which are minimized by adding additional molecules serving as triplet quencher and radical scavenger. Figure adapted from [26, 44].

2.3.5 Discussion on Opportunities and Limitations

Two-step absorption as an alternative photoinitiation pathway for 3D laser micro- and nanoprinting was motivated in its development and therefore starts from the inherent advantage of low-intensity photoinitiation compared to two-photon absorption, which makes the use of cw laser sources possible. Based on the explanations given in the previous sections, I want to conclude the section on two-step absorption by summarizing different opportunities and limitations of 2SA 3D printing, which will be picked up at different points of this thesis.

Low polymerization threshold laser powers and the possibility to use compact and low-cost diode lasers encourage two different targets: one can aim for faster and parallelized printing, which still relies on compact continuous wave lasers, where the use of two-photon absorption would require high-power amplified femtosecond pulsed laser sources [79, 80]. On the other hand, one can aim for a compact and low-cost overall setup relying on small laser diodes and decreasing the total cost and volume by more than an order of magnitude compared to widespread two-photon-absorption 3D printers. Both targets have already been followed [25, 26], whereas one main goal of this work is to bridge the gap between them by

bringing these two distinct goals closer together.
A further advantage that comes together with 2SA is the possibility of higher-resolution 3D laser nanoprinting compared to commercialized 2PA 3D printing [24]. This relies on photoinitiators with absorption bands in the UV and blue spectral region and therefore uses laser sources in the near infrared at around 800 nm. At the same time, 2SA based on the presented photoinitiator molecule benzil uses laser sources in the blue spectral region at, e.g., 405 nm. Considering the same optics, the halved wavelength provides a factor of two increase in resolution, as can be seen from equation 2.3.
Furthermore, 2PA 3D laser printing suffers from micro-explosions during printing [81, 82]. These lead to undesired local defects inside the volume or at the surface of the structure, potentially impairing their functionality. Such micro-explosions can occur at impurities that absorb the pulsed laser beam within the sample, therefore depositing considerable heat. Or they occur through multi-photon-absorption processes inside the photoresist, leading to a photoionization thereof. These effects narrow the process window for 2PA 3D printing. In 2SA 3D printing, however, no such micro-explosions have been observed due to the substitution of the pulsed laser source. Tuning the laser power at values above the threshold, the voxel size changes, which, however, could be exploited at the same time for grayscale 3D laser printing [83].

On the downside, there are also limitations and challenges to tackle with 2SA 3D laser printing. The first and most fundamental limitation concerns the single-focus print speed, which is directly linked to the intermediate-state lifetime. As already shown in Figure 2.7 from rate-equation calculations and discussed in section 2.3.1, the nonlinearity exponent changes for a given photoresist and a given wavelength – therefore given values of ε_1, ε_2 and k_D – when changing the exposure time per focus and consequently the focus velocity for focus-scanning 3D printing. To yield a nonlinear 2SA process, the laser focus exposure time t_exp should be well above the intermediate-state lifetime $\tau = k_\mathrm{D}^{-1}$ [44]. Considering the benzil-based photoresist as an example and taking the optical parameters of $\mathrm{NA} = 1.4$ and $\lambda = 405\,\mathrm{nm}$ for the laser focus, changes in nonlinearity between $N = 1$ and $N = 2$ are present for exposure times in the order of hundreds of microseconds corresponding to single focus scan speeds in the order of hundreds of micrometers per second [24]. Therefore, this establishes an upper bound on the single-focus scan speed. In the experiment, the 3D printing of structures at up to $v = 4\,\mathrm{mm\,s^{-1}}$ has been demonstrated [24]. However, typically single-focus velocities of $v = 1\,\mathrm{mm\,s^{-1}}$ are employed [24, 25, 27]. Such limitations, which set a sharp contrast to 2PA 3D laser printing, hinder the commonly pursued goal in 3D laser printing of increasing print speeds by first of all increasing the single-focus scan speed [29, 84]. It rather directs the efforts to parallelization approaches to increase print speeds, the implementation of which is a major part of this thesis.

A second drawback concerns the maintenance of the desired nonlinearity. As discussed in sections 2.3.3 and 2.3.4, the two most commonly employed photoresist systems exhibit a one-photon-triggered polymerization pathway. This can be significantly suppressed by adding quencher molecules, but it still contributes to dose accumulation, especially for large prints. Furthermore, the added quencher molecules complicate the reaction-diffusion kinetics during the printing process, as their diffusion and consumption must be accounted for to achieve optimal printing results. This said, the one-photon-triggered polymerization is no fundamental limitation of 2SA 3D printing, but a current challenge for the ongoing effort on photoresist development. At this point, I want to draw a comparison to two-photon-absorption 3D printing: following the first reports 30 years ago [14, 85], hundreds of photoinitiators have been reviewed and developed, with state-of-the-art initiator molecules reported only in 2020 [43]. Therefore, also the research on 2SA photoinitiator candidates might still lead to significant improvements in the future.

2.4 IMPLEMENTATIONS OF 3D PRINTING PROCESSES

As this thesis deals with technological advancements specific to two-step-absorption 3D laser printing, I briefly provide a broader overview of different 3D printing approaches described in the literature. This will enhance understanding and serve as a source of inspiration to adapt several approaches.
To date, a multitude of 3D printing approaches have been reported, and a considerable number of different approaches have been commercialized and are used for various applications. Without any claim of completeness, I will therefore only provide further details for some chosen approaches that are the most relevant for the topics to be discussed in the scope of this work. These primarily include light-induced 3D printing techniques with voxel sizes in the nano- and micrometer range.
Judging the relevance of a certain approach can be done based on different criteria. Often, 3D printing approaches are compared based on their peak printing rate in units of voxels per second and their minimum voxel size [29, 84, 86]. Besides this, the total build volume, the versatility of the materials, the device and process cost, and the printer size are other criteria.

Already introduced, two-photon-absorption 3D laser printing (2PP), has been extensively studied and provides print speeds up to 10^8 voxels s^{-1} at voxel sizes below 1 µm [13, 20, 84]. Originating from the printing of acrylic polymers [14], nowadays different polymeric materials [87–89], but also metals [90] and fused silica can be printed [91, 92]. Commercially available instruments already achieve printing rates of up to 3×10^5 voxels s^{-1} by scanning a single laser focus through

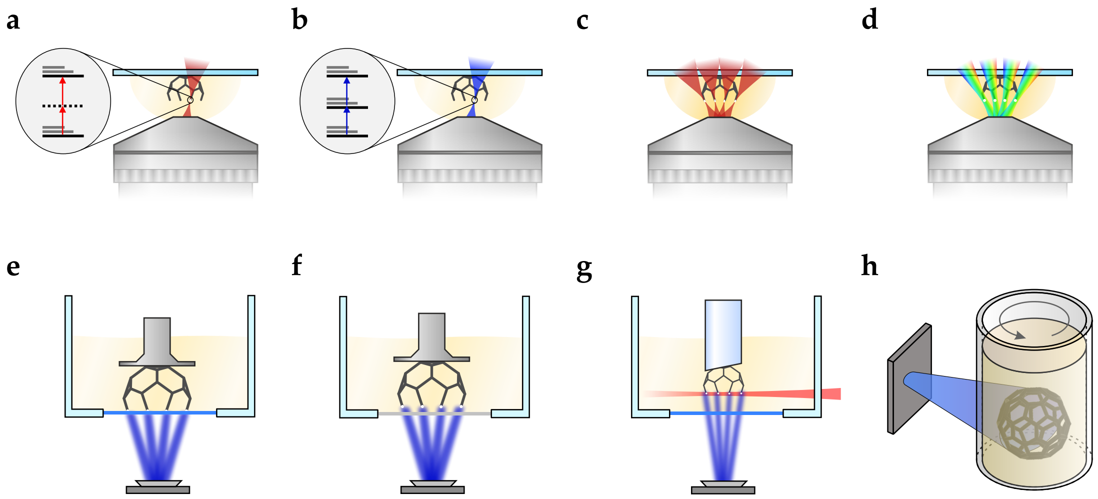

Figure 2.13: Illustration of different 3D laser printing techniques. **a** Two-photon-absorption 3D laser printing (2PP). **b** Two-step-absorption 3D laser printing. **c** Multi-focus two-photon-absorption 3D laser printing. **d** Projection-based 2PP via spatiotemporal focusing. **e** Bottom-up stereolithography. **f** Continuous liquid interface production (CLIP). **g** Light-sheet 3D laser printing (LS3DP). **h** Tomographic volumetric additive manufacturing (TVAM). Figure inspired by [95].

the photoresist volume [83].
Further increase has been demonstrated by different parallelization approaches [29, 79, 80, 84, 93, 94]. Among these are multi-focus 2PP. Using 49 laser foci in parallel, print speeds of up to 10^8 voxels s^{-1} have been shown, and centimeter-scale structures could be printed [84]. Projection-based methods can be considered as a largely parallelized printing with a large number of distinct foci. While a direct projection of an extended plane, however, significantly decreases the resolution along the optical axis (see section 2.2), spatiotemporal focusing methods can be applied to mitigate this problem [79, 93]. There, the frequency components of an ultrashort-pulsed laser beam are separated, thereby stretching the laser pulse in time. This reduces intensity in out-of-focus regions, whereas in the print plane, all spectral components are recombined.

A topic of current research and a potential future alternative to 2PP is two-step-absorption 3D laser printing [24, 25, 27, 96–98]. As explained in section 2.3, 2SA 3D printing relies on a second-order nonlinearity to achieve a focus-scan 3D printing inside the volume of a liquid photoresist. It can also be seen as a representative of the larger class of (1+1)-photon absorption. This term comprises several photoinitiation mechanisms in which the photoresist responds superlinearly to the light intensity, excluding two-photon absorption [49]. Therefore, no ultrashort-pulsed lasers are necessary for (1+1)-photon-absorption 3D printing. Besides 2SA, also other mechanisms have been reported as photoinitiation mechanisms for 3D laser micro- and nanoprinting, like upconversion luminescence [99–102] and triplet-triplet-annihilation [103–105].

In an upconversion luminescence process, an upconversion nanoparticle gets excited via the sequential absorption of two, e.g., red photons. From a higher excited state, the emission of a, e.g., blue photon follows at a rate proportional to the squared intensity of the red light. This blue photon then initiates a radical generation by getting absorbed from a photoinitiator molecule. In this process, the absorption length of the blue photon currently limits the achievable spatial resolution of the printed structures.

A photoresist for 3D printing based on triplet-triplet annihilation (TTA) consists, in addition to the monomer, of three components: sensitizer, acceptor, and initiator molecules. Two sensitizer molecules get excited into their lowest triplet state by the absorption of one photon each. These molecules transfer energy to nearby acceptor molecules, so the sensitizer is de-excited to its ground state, and the acceptor stores the energy in its lowest triplet state. In a further bimolecular process, the two excited acceptor molecules transfer energy, promoting one of them to a higher energy level and de-exciting the other. The combined energy carried by one of the acceptor molecules is then transferred to the initiator, which decays into radicals [103].

The two alternative (1+1)-photon-absorption processes presented rely on bimolecular reactions and energy transfer between molecules, which pose additional challenges to the achievable resolution and printing rate. Current implementations achieve voxel sizes below 1 µm, however at printing rates of 1 voxels s^{-1} to 200 voxels s^{-1} [49, 102]. Still, the continuous development is ongoing, e.g., through the implementation of parallelization measures to increase print rates [106]. With progress across different approaches, (1+1)-photon-absorption techniques are expected to become increasingly significant in the future.

Other approaches, typically relying on one-photon absorption as the photoinitiation mechanism, can be summarized under the term of stereolithography, which was first used in an early realization of 3D printing in 1984 [107]. In stereolithography, a liquid photoresist is photopolymerized typically by blue or UV light emitted from a light-emitting diode (LED) or a laser. This can be done either by scanning a single focus or by projecting an image, therefore polymerizing an entire plane at once. This still yields an axial confinement since the photoresist is highly absorbing at the wavelength used (see Figure 2.5a). The polymerization therefore occurs at the interface of the photoresist to the surrounding material. In stereolithography, two general implementations exist [95]. In the first one, polymerization is induced at the top surface of the photoresist in a vat, i.e., at the interface between the photoresist and air. After polymerizing one layer, the already polymerized structure is lowered into the photoresist, allowing a new layer of liquid photoresist to be exposed on top

of it. In this approach, the photoresist vat has to be as large as the structure build volume, and one has to wait for a new layer of photoresist to flow in and level prior to exposure [108]. Alternatively, the exposure can take place at the bottom of a photoresist-containing vat via a transparent window. After polymerizing one layer, the structure must be delaminated from the window, which slows the printing process.
To overcome the low print rate resulting from the delamination process, several other approaches have been reported to reduce this flaw. One of these is continuous liquid interface production (CLIP) [109]. There, the transparent window is also oxygen-permeable, so an oxygen concentration gradient forms from the window into the photoresist volume. Because oxygen can suppress photopolymerization reactions, there is a "dead zone" where the polymerization reaction is hindered. The polymerization plane is slightly shifted inside the photoresist volume. Therefore, no delamination is necessary and print rates up to 10^7 voxels s^{-1} could be achieved [110, 111]. Remaining challenges in CLIP include heat dissipation from the polymerization volume and the supply of fresh photoresist to it [95].
A further recent advancement is dynamic interface printing [112]. There, the polymerization takes place at an air-photoresist interface between a pressurized tube and the photoresist-containing vat. This interface can be actively controlled by acoustic waves, which support mass transport and thereby address the challenge of rapidly supplying fresh photoresist to the reaction volume. Again, the build platform can be continuously moved, since no delamination is necessary. Using this approach, print rates of 10^8 voxels s^{-1} at voxel sizes of tens of micrometers could be achieved.

Another continuous layer-by-layer 3D printing approach is light-sheet 3D printing (LS3DP). Again, a 2D image is projected into the volume of a liquid photoresist. In contrast to stereolithography and its extensions, no highly absorbing photoresist is used to confine the axial extent of the polymerization plane, but the nonlinear photoinitiation is performed via a synergistic two-color 2SA process. By this process, the polymerization plane can be confined by a second laser beam, forming a flat light sheet. Two implementations have been reported, one relying on the rearrangement of a photochromic molecule as the intermediate state [47] and one relying on the electronic states of the photoinitiator as intermediate state [26, 28]. The further development of the latter is presented in the scope of this thesis in chapter 3.

While in stereolithography and LS3DP the polymerization occurs layer-by-layer, tomographic volumetric additive manufacturing (TVAM, also referred to as computed axial lithography, CAL) is often considered a volumetric printing approach [33, 113]. There, a liquid photoresist is contained in a rotating vial and is exposed to projections of the designed object from different angles. Polymerization commonly occurs via one-photon absorption. As an illustration of TVAM, one can think of this process as the reverse of a tomographic reconstruction of a 3D object by taking images from different angles. Conceptually, one could expose the photoresist from all angles in a single shot [12]. The implementation of a single optical path and a rotating sample is, however, more practical.

An approach that comes closer to single-pulse volumetric 3D printing is referred to as interference lithography, or, more generally, holographic lithography. The goal is to shape the 3D light field so that a complex 3D structure can be printed with a single laser pulse, thereby achieving unprecedented print rates. Early implementations used nanosecond pulses and the interference of four laser beams in the print volume [114, 115]. This, however, severely limits the structures that can be printed to periodic ones. Steps to extend this to arbitrary 3D structures have been undertaken, and research is ongoing [116].

Despite now being around for decades, 3D printing is still a blooming field of research. New technological approaches are reported, novel materials are becoming accessible, and printing rates are still increasing. Furthermore, the intersection with neighboring fields of research and engineering stimulates the development. To name some, this includes the adaptation of techniques from microscopy and imaging [26, 32, 33, 79], the implementation of computational techniques to optimize the printing process [117–119], or the realization of highly specific applications in biology, optics, or engineering [13, 15, 20].
Focusing on the novel field of two-step-absorption 3D laser printing, this work aims at exploring different methods to further develop 2SA 3D printing. Along these lines, the following chapter will discuss some approaches for advancing light-sheet 3D laser microprinting.

Chapter 3

3 ON ADVANCEMENTS FOR LIGHT-SHEET 3D LASER MICROPRINTING

Light-sheet 3D laser printing based on two-color two-step absorption is a largely parallelized, emerging 3D microprinting approach that was experimentally first realized only in 2022 [26]. This chapter discusses the efforts undertaken to improve and expand this original setup. To that end, I will first introduce the method and implementation of light-sheet 3D laser printing. Subsequently, I will discuss current challenges and identify the development potential they create. Two identified topics, which were mainly pursued, are outlined afterwards. This covers a fluidic chamber to mitigate dose accumulation effects, as well as an optical element for the power-efficient generation of a light sheet.

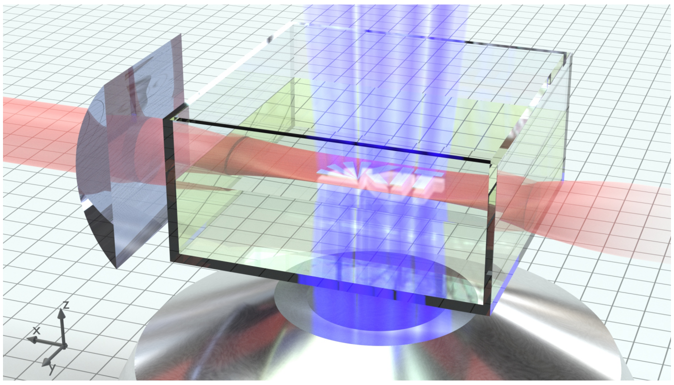

Figure 3.1: Artistic sketch of light-sheet 3D printing. The red light-sheet beam and the blue projection beam are co-focused to the printing plane. That is located inside the volume of the photoresist, which is contained in a small transparent vat. Figure taken from [26].

3.1 INTRODUCTION TO LIGHT-SHEET 3D LASER MICROPRINTING

Light-sheet 3D laser printing, a parallelized, projection-based 3D printing technique, was briefly introduced in section 2.4. This section aims at presenting a specific light-sheet 3D microprinting implementation relying on two-color two-step absorption as well as a setup tailored to the biacetyl-based photoinitiator system introduced in section 2.3.4. The setup was built by Vincent Hahn and is published in Ref. [26].
An artistic illustration of the basic principle of LS3DP is shown in Figure 3.1. From the bottom, slices of the 3D object are projected into the photoresist volume using a blue laser beam. This photoresist is contained in a small transparent vat, the cuvette. From left, a light-sheet beam at a different wavelength, formed by a cylindrical lens, is focused into the cuvette. At the plane of intersection, the two-color two-step photoresist polymerizes, such that the KIT logo is printed in this minimal example.

A schematic of the components and the optical paths of the LS3DP setup is depicted in Figure 3.2. On the left, the blue-light projection beam path is indicated, while on the right-hand side, the red-light light-sheet beam path is drawn. Both focal planes intersect inside the cuvette, shown in the middle of the schematic. A sophisticated explanation of all the components and the design rationale can be found in Ref. [44]. In the following, I will describe the beam paths and the main components.
In the projection beam path, the blue laser light is generated by four multi-mode laser diodes, each with 6 W maximum output power at 440 nm (Lastertack PD-01231). Their output light is coupled into a rectangular-core fiber (Ceramoptec, NA $= 0.22$). The rectangular end facet is imaged onto a liquid crystal display (LCD). This is accomplished via a microscope objective lens (Carl Zeiss EC-Epiplan Neofluar 20×/NA0.5) and an achromatic doublet lens (TL1, Thorlabs AC254-150-A-ML). In between, a polarizing beam splitter (Thorlabs PBS251) and a zero-order

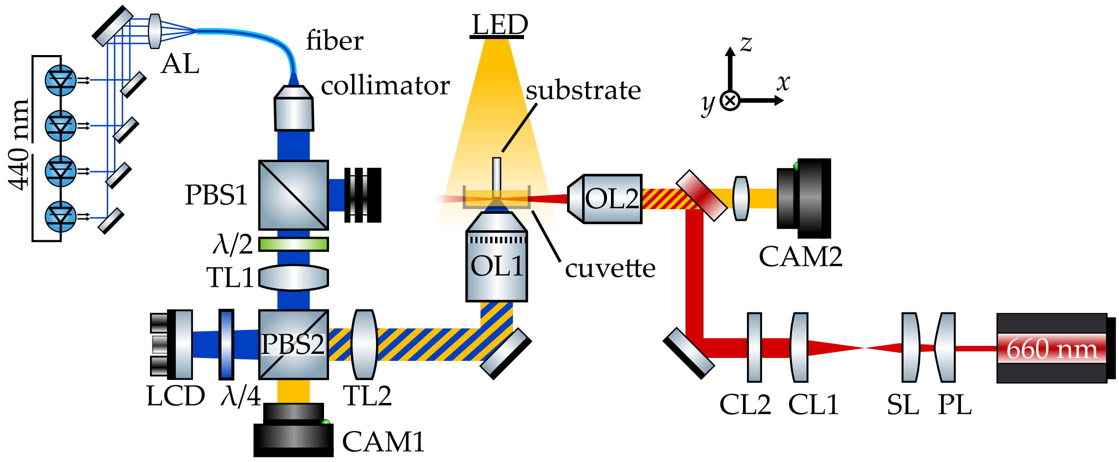

Figure 3.2: Schematic of the light-sheet 3D microprinting setup. The blue-colored projection beam path is shown on the left, the red-colored light-sheet beam path is shown on the right. The following abbreviations are used: AL: aspheric lens, PBS: polarizing beam splitter, TL: tube lens, LCD: liquid crystal display, CAM: camera, OL: objective lens, CL: cylindrical lens, SL: spherical lens, PL: Powell lens. Figure adapted from [44].

half-wave plate (Thorlabs WPQ10M-445) are placed for polarization selection and rotation. Following TL1, the light is reflected at a second polarizing beam splitter (Thorlabs PBS251) and transmitted through a quarter-wave plate (Thorlabs WPQ10M-445) for converting the linear polarization to a circular polarization until it reaches the LCD (Holoeye HED4552, 1920 × 1080 px, 720 Hz frame rate). The reflection-mode LCD reverses the handedness of the circular polarization of light reflected from nominally "white" pixels, while light reflected from "black" pixels retains its handedness. In combination with the quarter-wave plate and the polarizing beam splitter, this translates into an amplitude contrast. Only light from the "white" pixels is transmitted through the polarizing beam splitter, gets collimated by a tube lens (Thorlabs ITL200), and focused by a high-NA objective lens (Carl Zeiss LD LCI Plan Apochromat 63× /NA1.2 Imm Corr DIC) into the photoresist.
For the light-sheet beam path, a 6 W output power, solid-state laser at 660 nm wavelength (Laser Quantum axiom) is used. The laser beam is transferred to a 1° fan angle Powell lens (Laserline Optics Canada LCOP-8.9R01-1.0), which is an aspheric, cylindrical lens generating a diverging laser beam of uniform intensity distribution [120]. The laser beam is focused and again collimated by an arrangement of a spherical and two cylindrical lenses (Thorlabs LA1131-A-ML, LJ1629RM-A, and LJ1267RM-A). Reflected off a dichroic mirror, the beam finally gets focused into the photoresist by a microscope objective lens (Carl Zeiss Epiplan 5× /NA0.13).
The photoresist is confined in a home-built container. This container is assembled from a 85 µm-thick microscope coverslip (Thorlabs CG00C) forming the bottom

surface, and a cut-out from a plastic spectroscopic cuvette (Brand) forming the four 1 mm-thick side walls. Both parts are glued together via an UV-curable adhesive (Norland Products NOA63).
Since the optics of both the projection and the light-sheet beam path are fixed, it is convenient to introduce a movable substrate on which the printed structure adheres. For this, cylindrical glass rods of 1 mm diameter are immersed in the photoresist cuvette from the top. A close-up photograph of this assembly is shown in Figure 3.3a. The glass rods are manually ground and polished to an angle of $\approx 8^\circ$ to prevent the light-sheet beam from propagating through the glass rod, which would lead to undesired diffraction artifacts [44]. A side-view photograph of the angled printing substrate is shown in Figure 3.3b. For visualization, the projection and the light-sheet beam paths are drawn into the photograph in blue and red, respectively. The glass rod is positioned by a set of four single-axis translation stages: A stepper-motor actuated, 13 mm travel-range stage for coarse z-movement; two voice-coil actuated, 20 mm travel-range stages for xy-movement; and a piezo actuated, 250 µm travel-range stage for fast z-movement (all Physik Instrumente, L-306.011112, V-528.1AA, and P-622.ZCD).

Using the presented setup, the printing of various test structures at printing rates of up to 7×10^6 voxels s^{-1} and lateral and axial voxel sizes of 500 nm and 2.2 µm, respectively, has been shown. As an example, Figure 3.3c and d show scanning-electron micrographs of three knot-like structures printed in parallel within 153 ms. Still, a demonstration of applications and widespread use is pending. This is largely due to a currently small build volume and high printing overheads. The current limitations and potential ways to overcome them will be discussed in the next section.

3.2 IDENTIFYING CHALLENGES AND DEVELOPMENT POTENTIAL

The primary target of light-sheet 3D printing is to establish a fast 3D printing approach. This can be quantified to a large extent by the printing rate, measured in voxels per second, which is desired to be as large as possible. In the case of the presented LS3DP setup, two main issues are present: First, besides the printing, which takes only milliseconds to seconds for the structures presented in [26], the overhead time of substrate preparation, everyday alignment, and sample positioning can be significantly larger, namely on the order of tens of minutes. Second, there is a natural application case for fast 3D printing approaches, which is currently limited using LS3DP: the printing of either large structures on a millimeter to centimeter scale or the printing of a large number of disconnected particles. This can also be

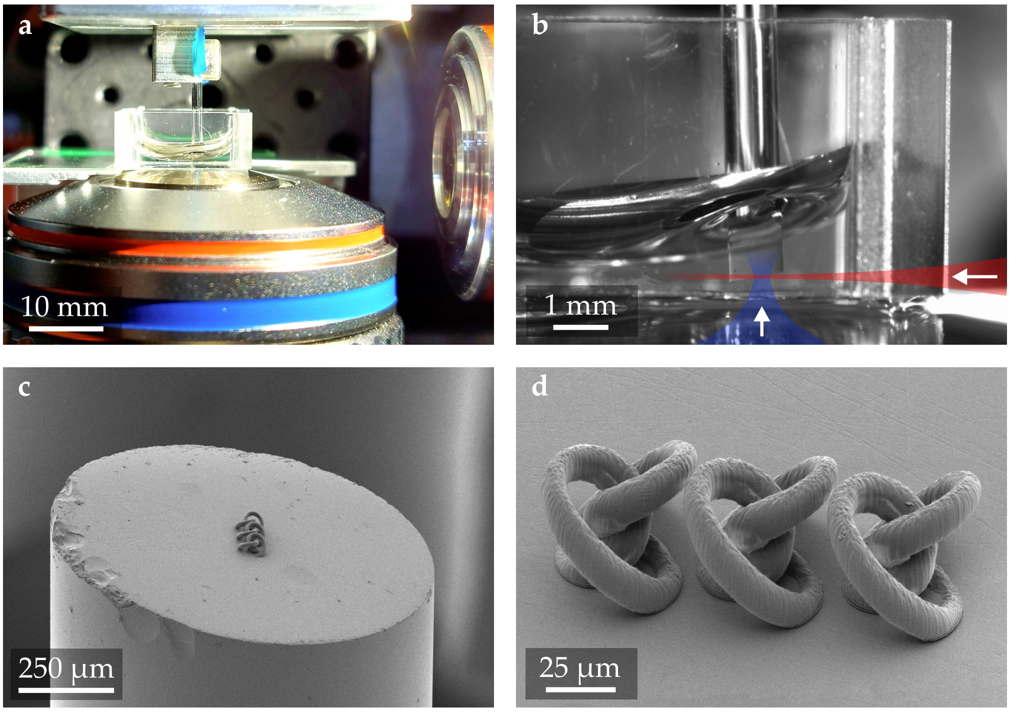

Figure 3.3: Light-sheet 3D printing substrate and printed structures. **a** Photograph of the LS3DP photoresist cuvette and the glass-rod substrate. On the bottom, the projection objective lens can be seen, and on the right, the light-sheet objective lens. **b** Zoom in to the print plane. A blue-colored projection beam and a red-colored light-sheet beam are drawn for visualization. **c** Scanning-electron microscopy (SEM) image of the printing substrate containing three knot-like structures printed by LS3DP. These are shown at a higher magnification in **d**. Panels a, c, and d are adapted from [44].

referred to as a limited build volume. Specific development tasks to overcome the limitations are therefore discussed in the following and are illustrated in Figure 3.4.

Considering the first point of reducing the overhead time, one could first of all think of automation measures to assist the printing preparation and the everyday alignment. The challenge in LS3DP is to co-focus two microscope objective lenses and to position the printing substrate at these intersecting focal planes. These tasks are currently already combined into one process step: For alignment, the light-sheet beam reflected from the glass rod gets collected by the objective lens of the projection beam path and focused on the camera (CAM1). This feedback signal is used to align the objective lens OL2, while OL1 is kept in place. To increase the signal-to-noise ratio, a second, gold-coated, 45°-angled glass rod is used for this process, further increasing the overhead time. Using the already installed cameras and a software-controlled feedback loop, the alignment and positioning of the glass rod could be automated.

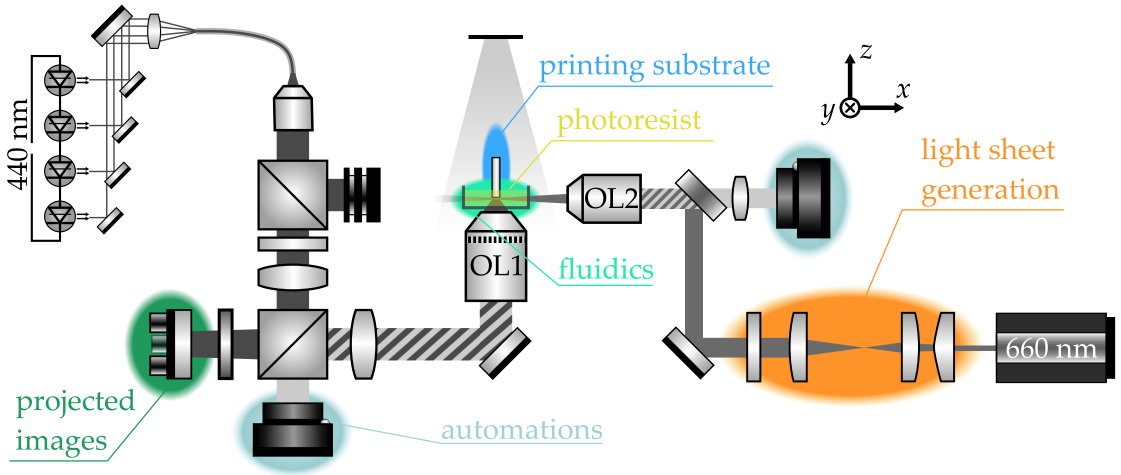

Figure 3.4: Identified topics for further development of LS3DP. A more power-efficient generation of a potentially more uniform light-sheet could reduce the laser powers needed. Changing the printing substrate could ease the printing process and reduce the overhead time. Implementing a fluidic chamber could increase the build volume by reducing dose accumulation effects. A better understanding of the chemical processes and/or the development of new photoresists could reduce the laser power required. Figure adapted from [44].

As is the case for a lot of 3D printing approaches, the printed structure does not necessarily match the designed structure sufficiently in the first print, effectively causing a time overhead due to repeated printing. Iterative pre-compensation loops have been proven to mitigate this problem [121]. Other approaches aim at either in-situ monitoring the printing process [119] and potentially making adjustments based on this or at simulating the printing process beforehand [122]. Since the involved optics and reaction-diffusion kinetics pose a significant hurdle, simplifications are typically necessary. Following a simple model based on the convolution of a 3D Gaussian distribution with the design, adjustments of the design have already been undertaken for some of the structures presented in Ref. [26] and printed by LS3DP. A further developed dose simulation routine was established by Stefano de Giuseppe in the scope of his Bachelor's thesis [123], which was supervised by the author. There, the light sheet and the projection beam were modeled using Gaussian optics. Tailored to LS3DP using a biacetyl-based resist, the dose model, which transfers the intensity of the blue projection and the red light-sheet at every point in space and time to a dose value, was based on rate-equation calculations. These were originally set up by Vincent Hahn [44]. However, with the simplifications made, the dose simulation currently does not provide sufficient quantitative agreement with the printed results. Nonetheless, it still serves as a first step towards a pre-compensation tool. Further discussions on this can be found in Ref. [123].

Besides the time overhead, LS3DP has shown the best printing results with in-

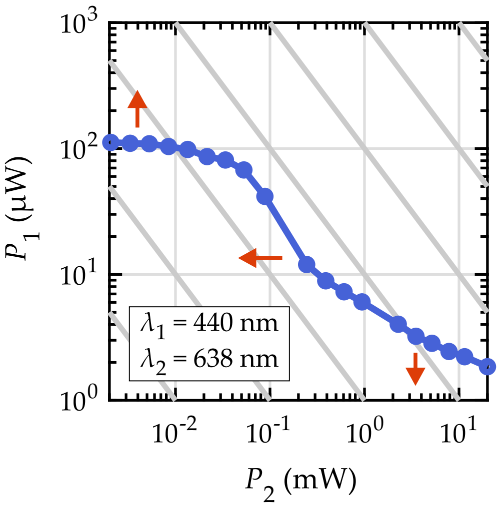

Figure 3.5: Exemplary two-color polymerization threshold. The photoresist (PRA) contains biacetyl and TEMPO, which are dissolved in PETA. Ideally, the blue-only threshold should approach infinity, while the two-color threshold and therefore the threshold contrast should increase with the sigmoid shape, preferably shifted to low red laser powers. These desired directions are indicated via the orange arrows. Figure adapted from [26, 44].

Table 3.1: Description of photoresist (PR) compositions as used in this work. Each resist consists of monomer, photoinitiator (PI), and quencher (Q) molecules. Following the composition of PRi, different photoinitiators are compared. Experimental details regarding the photoresist mixture are given in the respective references.

resist	monomer	photoinitiator	c_{PI} (mM)	quencher	c_{Q} (mM)	source
PRA	PETA	biacetyl	110	TEMPO	11	[44]
PRB	TMPTA	biacetyl	110	TEMPO	11	[44]
PRC	DPEHA	biacetyl	110	TEMPO	11	[44]
PRi	PETA	(varying)	100	TEMPO	50	[27]

creased red light-sheet beam power. At the wavelength of the light sheet, the second absorption step is promoted, such that high rates, therefore a high intensity at a given extinction coefficient, make undesired one-color radical generation processes less probable. Hence, a power-efficient light-sheet beam path is desirable, which will be addressed in section 3.4.

The second raised point regarding a limited build volume is primarily related to the photoresist used. The underlying reasoning and possibilities to overcome this will be presented in the following section.

Discussion on Deficiencies of Current Two-Color 2SA Photoresists

As already discussed in section 2.3.2 on synergistic two-color two-step absorption, an ideal photoinitiator would lead to radical generation only after exposure to light of two different wavelengths. As we have seen for the biacetyl-based photoresist in section 2.3.4, there are, however, single-color, one-photon triggered polymerization pathways. In the context of LS3DP, this leads to undesired radical generation reactions mediated solely by the blue projection laser beam. For prolonged printing times, the deposited dose accumulates, leading to polymerization in out-of-focus regions. This issue can be addressed by identifying a photoinitiator with a completely inert intermediate state.

An assessment and comparison of different photoresists (PRs) can be done by measuring the polymerization threshold power for different combinations of the laser power of the two distinct wavelengths. This was done in a focus-scanning 3D nanoprinting setup by co-focusing two laser beams into the photoresist. Dashed line patterns were printed while the laser powers P_1 and P_2 were independently varied. For each laser power P_2, the minimal laser power P_1 for which a line is printed was determined by darkfield microscopy of the sample after development. In the experiment, P_2 is referring to a red laser beam at $\lambda_2 = 638\,\text{nm}$ while P_1 is referring to a blue laser beam at either $\lambda_1 = 405\,\text{nm}$ or $\lambda_1 = 440\,\text{nm}$. The wavelengths used are stated for each experimental result shown. A detailed description of the focus-scanning setup as well as the experimental routine can be found in [27, 44].

The photoresists investigated and compared in this section differ in their ingredient compositions and concentrations. To give a compact overview, the compositions are summarized in table 3.1.

Exemplary data for the state-of-the-art photoinitiator biacetyl is shown in Figure 3.5. The data is taken from [26] and refers to a photoresist composition of pentaerythritol triacrylate (PETA) as the monomer, biacetyl at a concentration of 110 mM as photoinitiator, and TEMPO at a concentration of 11 mM as quencher molecule (PRA). In the blue, a wavelength of $\lambda_1 = 440\,\text{nm}$ was used. It can be seen that the polymerization threshold is lowest at high red laser powers and increases as red laser power decreases. The ratio of the blue threshold laser power for low red laser powers and the blue threshold laser power for high red laser powers is called the threshold contrast γ. For an ideal two-color 2SA photoinitiator exhibiting an inert intermediate state, γ would approach infinity. In Figure 3.5, the desired directions for how one would like to shift the polymerization threshold curve are indicated by orange arrows: at $P_{2,\text{min}}$, the threshold should increase, at $P_{2,\text{max}}$, the threshold should decrease. Furthermore, it is desired to shift the sigmoid shape towards overall lower red laser powers.

Routes in the direction of finding novel photoinitiator molecules have been taken by Bojanowski et al. [27] and Vranić et al. [124], in collaboration with the author. Different diketones have been synthesized and tested regarding their printability. Data of 14 photoinitiators showing a two-color two-step behavior are shown in Figure 3.6. For comparability, all photoinitiators were dissolved at a concentration of 100 mM together with the quencher molecules TEMPO (50 mM) in the monomer PETA (following PRi in Table 3.1). A blue laser source at $\lambda_1 = 405\,\text{nm}$ was used

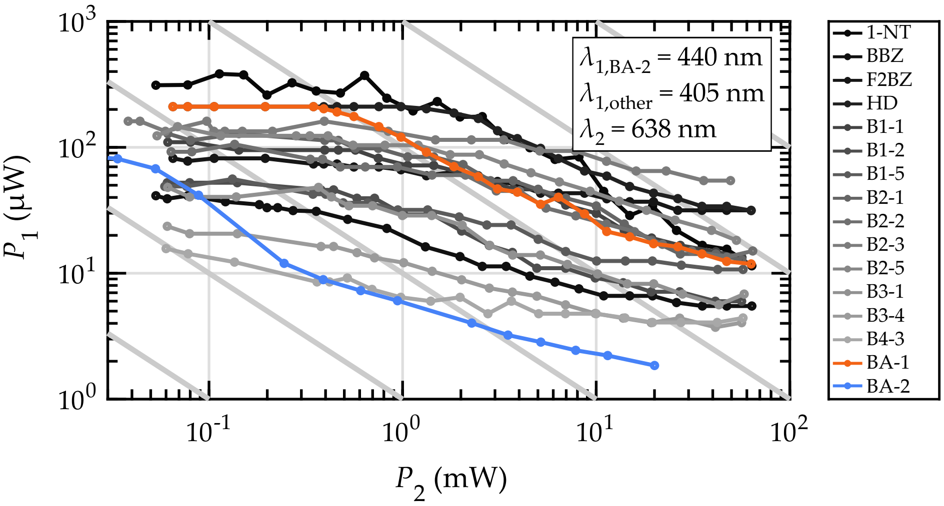

Figure 3.6: Two-color polymerization thresholds for different photoinitiators. 14 different photoinitiators were tested and compared regarding their threshold contrast, their threshold powers, and their printability. All new initiator molecules were dissolved in PETA at a concentration of 100 mM together with TEMPO (50 mM) following the composition of PRi in Table 3.1. These comparative experiments were performed at 405 nm wavelength in the blue region. Compared to biacetyl at the same experimental conditions (drawn in orange), as well as at 440 nm and $c_Q = 11\,\text{mM}$ (drawn in blue), no other initiator significantly outperforms it, rendering biacetyl the state-of-the-art for two-color 2SA. The full name of the initiator molecules can be found in Appendix A.1. The experiments were performed by Maximilian Bojanowski, Aleksandra Vranić, and Vincent Hahn. The data is taken from [26, 27, 124].

for these experiments. Therefore, the comparable curve for biacetyl (shown in orange) exhibits a threshold contrast of $\gamma \approx 18$ under these conditions compared to $\gamma \approx 60$ at $\lambda_1 = 440\,\text{nm}$ and $c_{\text{TEMPO}} = 11\,\text{mM}$ (shown in blue, following PRA). In both cases, biacetyl ranks among the best-performing photoinitiators, according to the criteria stated above. Based on the threshold contrast, 1-Naphtil shows the largest contrast of the novel photoinitiator molecules at a value of $\gamma \approx 28$, but the sigmoid shape starts at higher red laser powers compared to biacetyl. More detailed discussions on how the molecular structure relates to printing results are provided in Refs. [27, 124]. Up to now, biacetyl has remained the state-of-the-art photoresist for two-color two-step absorption.

A way to still increase the build volume while relying on biacetyl as the photoinitiator is to achieve stable conditions for prolonged printing experiments. So far, the dose accumulates during long printing times due to blue-laser-triggered radical generation. Since preventing radical generation via the photoresist formulation has not been successful so far, one could consider technological approaches to mitigate proximity effects. One approach discussed in section 2.3.5 was CLIP.

Figure 3.7: Two-color polymerization threshold under different atmospheres. The photoresist (PRB), as well as the surrounding atmosphere during printing, was either oxygen-enriched or oxygen-depleted (argon-enriched) in comparison with atmospheric conditions. For the two-step pathway, an effect of oxygen concentration was observed despite the high TEMPO concentration, unlike in the one-step pathway at low red laser powers. Figure adapted from [26].

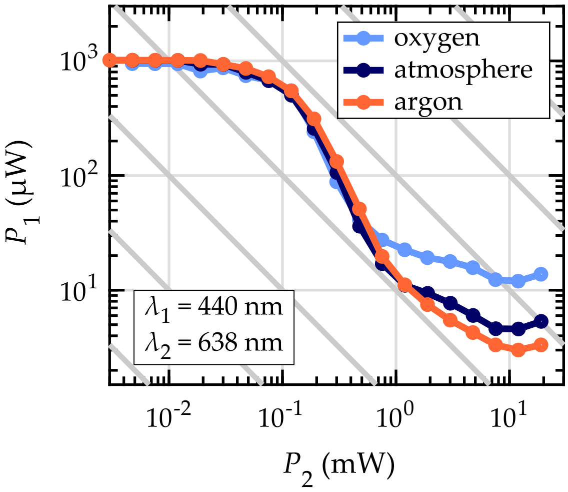

Following this, an oxygen-permeable membrane could be used as the cuvette's bottom window to deliver fresh oxygen to the photoresist. In LS3DP, TEMPO is, however, considered as the primary contributor to quenching reactions since its concentration is 10 times higher than that of oxygen at atmospheric conditions [26]. As a preliminary experiment, the two-color polymerization threshold is investigated in an oxygen-enriched and an argon-enriched (therefore oxygen-depleted) atmosphere. The experimental setting is the same as in the previous experiments. The atmospheric conditions were altered by bubbling the photoresist with the respective gas before printing, and by flushing the printing chamber during printing. As a photoresist composition, PRB in the nomenclature of Table 3.1 was chosen, containing the less viscous monomer trimethylolpropane triacrylate (TMPTA). The result is shown in Figure 3.7. An enriched oxygen concentration increases the polymerization threshold only at higher red laser powers. From this, one can conclude that the two-color two-step process, which is the predominant path for high red laser powers, is indeed significantly influenced by solvated oxygen. For low red laser powers, where the two-step process is less probable, the influence of oxygen seems less pronounced. This could be due to triplet-triplet-annihilation processes being the dominant quenching pathway under the conditions chosen here [26]. Therefore, the possible benefits of an oxygen-permeable membrane on reducing proximity effects would be lowered. An improvement by CLIP-inspired LS3DP should still not be ruled out based on these findings. Dose accumulation in out-of-focus regions in LS3DP occurs on a time scale of seconds, but at rather low blue-light intensities. Both are conditions not covered by the presented experiment. However, it remained unclear whether LS3DP would benefit significantly from an oxygen-permeable membrane. To circumvent this uncertainty, an "active" approach rather than a "passive" membrane was chosen, implemented in a fluidics chamber to provide a steady stream of fresh resist while printing. This will be explained in the next section.

3.3 A FLUIDICS CHAMBER TO MITIGATE DOSE ACCUMULATION EFFECTS

In the following, general considerations for fluidics implementations are discussed and matched to the demands of LS3DP. The implementation developed in this work is explained, and printing results are shown.

Design Considerations

A (micro-)fluidics chamber has already been integrated into various 3D laser printing approaches, serving different purposes. In all cases, photoresist is removed from the polymerization volume and new photoresist is delivered to this volume. Doing so, multi-material printing can be achieved by exchanging the photoresist while the sample is kept in place and aligned [125–127]. This approach can also serve as a fully integrated 3D laser printing platform if the development step is carried out in the same manner [125]. As an additional option, the printing substrate, typically a glass coverslip, can be omitted by printing the desired structures into the volume of a continuously flowing photoresist [128–130]. Therefore, no additional translation-stage movements are necessary to access different print fields. However, printing microscopic structures freely flowing in a liquid is only useful for a limited number of applications, like large numbers of identical particles of often simple shape [129, 131]. Using the fluid flow for sample positioning furthermore requires a meticulous engineering of that movement [128].

The integration of fluidics into 3D laser printing often requires solutions specifically designed for the setup in question [125–127, 132]. As an add-on to a commercial two-photon polymerization system, this can be accomplished by a sealed fluidics cell with at least one transparent window for focusing the laser beam. The liquid can be pumped through this cell, e.g., via a pressure controller which applies an overpressure to the resist containers [125]. A conventional glass coverslip is placed inside the cell, and printing is conducted in a sandwich-like configuration. If printing is performed in a liquid stream, microfluidic chips can also be used directly [130]. In these cases, the fluidics cell is sealed and can be pressurized while printing. This gets more complicated if parts of the optics or the sample need to move inside the fluidics cell. This is the case for stereolithography and variants thereof, for focus-scanning 3D laser printing in a dip-in configuration, and for LS3DP. Implementations have been shown where a fluidics chamber is incorporated as a sealed cell [133], or an open chamber has been chosen [126, 127]. For the latter, care has to be taken to maintain a steady liquid level at the liquid-to-air interface. Nowadays, such solutions are commercially available as add-ons for 2PP printers [134].

The Fluidics Chamber Integrated into LS3DP

Based on the overview given above, I want to describe the experimental realization of a fluidics add-on for LS3DP developed in this work. In the presented implementation, the main objective is to continuously deliver fresh photoresist during printing rather than achieving multi-material or continuous-flow printing. Furthermore, the glass rod, as a printing substrate, is moved out of the photoresist container during printing. To maintain this movement unrestricted, an open-chamber solution is chosen. Therefore, the printing process remains unchanged, and the fluidics is solely a reversible add-on.

The assembly of the fluidics system outside the LS3DP setup is shown in Figure 3.8. The liquid photoresist is contained in a syringe and pumped through the system via a syringe pump (New Era Instruments NE1010). The syringe is connected to the printing container via tubes of 1 mm inner diameter made from fluorinated ethylene propylene (FEP). As printing container, a 10 mm × 10 mm × 5 mm plastic cuvette glued onto a glass coverslip is chosen. Therefore, no changes are made compared to conventional LS3DP in this regard. As inlet and outlet ports, holes are drilled into the sidewalls of the cuvette. Through these holes, the tubing for inflow and outflow of the photoresist is connected to the cuvette and sealed via UV-curing adhesive (Norland Products NOA63). To be able to clean the cuvette, the short inlet and outlet tubings are connected to the rest of the system via standard microfluidic connectors. The cuvette assembly is glued on an aluminum sample holder, which is screwed to manual translation stages for positioning the cuvette in the setup. At the outlet port, a short FEP-tube of 2.54 mm inner diameter is connected to a microfluidic fitting. This can be linked to flexible Tygon® tubing connected to a peristaltic pump (Ismatec REG DIG MS-2/8), which vacuums the excess photoresist from the cuvette to maintain a steady resist level. The output of the peristaltic pump is guided to a waste container.

It should be noted that the presented assembly meets all geometric requirements posed by the LS3DP setup presented in section 3.1. These are further illustrated in Figure 3.8b. Four surfaces need to be transparent and of optical quality for transmission of the light-sheet beam, the projection beam, and for an additional camera beam path. Further space restrictions are posed by the objective lenses and by the multi-axis translation stage assemblies for moving the cuvette, as well as the printing substrate.

As discussed for open microfluidic systems, the liquid level in the cuvette needs to be controlled to avoid overfilling or emptying the cuvette during printing. Since the typically used monomers are relatively viscous and the usable tubing diameter is limited, spontaneous flow from the cuvette to the outflow tube is slow. For this reason, a peristaltic pump is connected to the outlet tubing. For leveling the fluid inside the cuvette without the need to adjust both pumps synchronously, the outlet tubing is placed such that its opening reaches from ≈ 0.8 mm up to ≈ 3.3 mm from

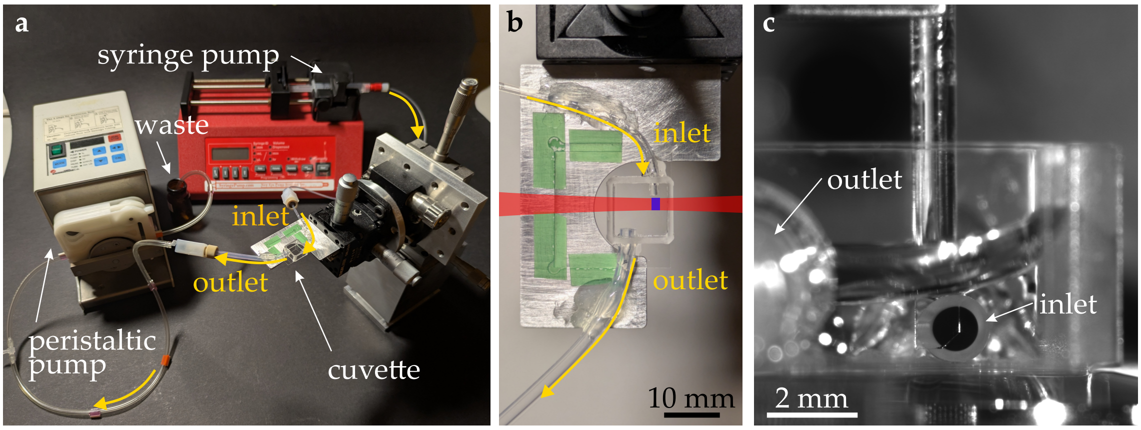

Figure 3.8: Components of the fluidics extension of LS3DP. a Photograph of all components. The photoresist is pumped via a syringe pump to the open cuvette. To level the liquid in the cuvette, a peristaltic pump connected to the outlet port vacuums excess photoresist. With this, a steady photoresist flow while printing is achieved. **b** Top-down photograph of the cuvette. For visualization, the light-sheet beam path and the projection beam path (out-of-plane) are highlighted in red and blue, respectively. **c** Side-view photograph of the assembly installed into the LS3DP setup. The printing substrate is located right in front of the inlet port.

the bottom of the cuvette. If the liquid level increases above the opening, a negative pressure is generated, and excess liquid is vacuumed from the cuvette. If the liquid level decreases again, less liquid is vacuumed. By setting the peristaltic pump to a sufficiently high pump rate, excess photoresist is continuously vacuumed, maintaining a steady liquid level.

Volume Flow Rates and Linear Velocities

Further questions are, which volume flow rates and linear velocities of the photoresist exchange are necessary. The print plane in LS3DP spans an area of approximately 160 µm × 90 µm. Typical print jobs for a single print field take hundreds of milliseconds. For stitching several print fields together, proximity effects and undesired out-of-focus polymerization effects became apparent in the past. As an example, at a linear velocity of $100\,\mu\mathrm{m\,s^{-1}}$, the resist at the print plane is exchanged after a few print fields are stitched together, which should be sufficient for the application.

These linear flow velocities inside the volume near the print plane are, however, different from the flow rates in the tubing. Furthermore, boundary conditions apply at the tube walls as well as at the cuvette's and the substrate's surfaces, creating a spatially varying flow velocity profile. At these interfaces, a no-slip boundary condition commonly applies, i.e, the liquid's linear velocity vanishes at the boundary. Under this assumption, the spatial flow profile inside a circular tube is an axis-symmetric parabola: $v(r) \propto r^2$.

To mathematically describe the laminar flow through a tubing of circular cross-section further, the Hagen-Poiseuille equation can be applied [135]. This connects the pressure difference of input and output port Δp to the resulting volume flow rate $\mathrm{d}V/\mathrm{d}t$. Considering the radius r and length l of the tubing as well as the viscosity η of the liquid, the equation reads as follows:

$$\frac{\mathrm{d}V}{\mathrm{d}t} = \frac{\pi r^4}{8\eta l}\Delta p. \tag{3.1}$$

This equation holds for laminar flow. The validity of this assumption can be assessed by calculating the Reynolds number, which is dependent on the liquid as well as the tubing parameters. For light-sheet 3D printing, the monomeric molecule dipentaerythritol hexaacrylate (DPEHA) has been mainly used so far. The viscosity of DPEHA is rather large at $\eta_{\mathrm{DPEHA}} \approx 6\,\mathrm{Pa\,s}$ (vendor specification), which is six times larger compared to PETA ($\eta_{\mathrm{PETA}} \approx 1\,\mathrm{Pa\,s}$) [136], and 6000 times larger compared to water [137]. Based on the Reynolds number, the assumption of a laminar flow is well fulfilled for the monomers employed [138].

To connect the desired linear velocities inside the cuvette to the pressures and, therefore, volume flow rates set to the pump, considering the special geometry of the presented fluidics chamber, finite-element calculations are performed. These are done using the CFD module of Comsol Multiphysics [139]. The cuvette and the substrate are modeled in 3D with no-slip boundary conditions set. A fully-developed, laminar flow is assumed with a flow rate set to the inlet, while the outlet is assumed to be open, i.e., no difference pressure restricting the fluid flow. To achieve linear velocities in the desired order of $100\,\mu\mathrm{m\,s^{-1}}$, (average) linear velocities of approximately $6\,\mathrm{mm\,s^{-1}}$ should be applied to the tubing. For an inner diameter of 1 mm, this translates to a volume flow rate of approximately $300\,\mu\mathrm{L\,min^{-1}}$. The large difference in linear velocities inside the tubing and at the print plane is connected to the small height in between the cuvette's bottom and the printing substrate, where boundary conditions restrict the fluid flow. Furthermore, the linear velocity drops as soon as the cross-section largely increases from the tube to the cuvette. To reduce these effects, the inlet tube is placed as close as possible to the print plane.

Taking the desired volume flow rates of $300\,\mu\mathrm{L\,min^{-1}}$ and DPEHA as the used monomer of the highest viscosity, one can calculate the necessary pressure differences according to the Hagen-Poiseuille equation for different tubing parameters. In all cases, one wants to keep the length of the tubing as short as possible. This not only reduces the pressure differences needed, but it also reduces the photoresist volume needed for initially filling the cuvette (swept volume). The tubing path from the pump to the fluidics chamber could be shortened to around 50 cm. The inner diameter strongly influences the pressure differences needed for a certain volume flow rate, such that lower pressures are needed for larger diameters. However, this increases the swept volume. Furthermore, larger diameters reduce the linear velocity at a constant volume flow rate as the cross-sectional area changes. A trade-off is chosen at an inner diameter of 1 mm, where standard fluidic components are readily available. With these parameters, pressure differences of $\Delta p \approx 6\,\text{bar}$ are needed for pumping DPEHA, whereas differences of only $\Delta p \approx 1\,\text{bar}$ are needed for PETA. Both can be supplied by the syringe pump used.

At the outlet port, tubing of a larger diameter is used, as the linear velocities as well as the swept volume are not of concern here. Using tubes of 2.54 mm inner diameter and 50 cm length and taking DPEHA as an example, pressure differences of only $\Delta p \approx 0.15\,\text{bar}$ are needed.

The total swept volume of photoresist needed is calculated as the sum of initially filling the tubing and the cuvette prior to printing, and the total volume flowing through the cuvette while printing. Filling the system requires around 700 µL of photoresist. Assuming print jobs of clearly less than a minute duration, this adds some hundreds of microliters, summing it to around 1 mL. Although this is not negligible when trying to upscale the process to large structures, it should be mentioned that all the components of the photoresist are rather inexpensive, commercially available chemicals.

For printing experiments, the peristaltic pump connected to the outlet port is always on, while the syringe pump connected to the inlet port is PC-controlled during printing.

Printed Structures

To benchmark the effect of the fluidics extension on the LS3DP process, printing experiments were performed with and without a continuous photoresist flow for two different photoresist compositions. As a test structure, the benchy boat [140] is chosen, a widespread test structure for 3D printing. In 2SA 3D printing in general, as well as in LS3DP, printing dense structures such as the benchy boats is particularly challenging due to pronounced dose accumulation effects arising [24, 26]. The two resist compositions used here for benchmarking LS3DP are PRA and PRC, following the nomenclature introduced in Table 3.1. Their single difference is the monomer, which is the less viscous monomer PETA in PRA, compared to the more viscous monomer DPEHA in PRC. So far, only DPEHA has been extensively used for LS3DP, as it has shown better printing results compared to less viscous monomers like TMPTA. Referring to the threshold contrast introduced in section 3.2, less viscous monomers increase the threshold contrast, judging from focus-scanning experiments [44]. In LS3DP, higher viscosity photoresists have,

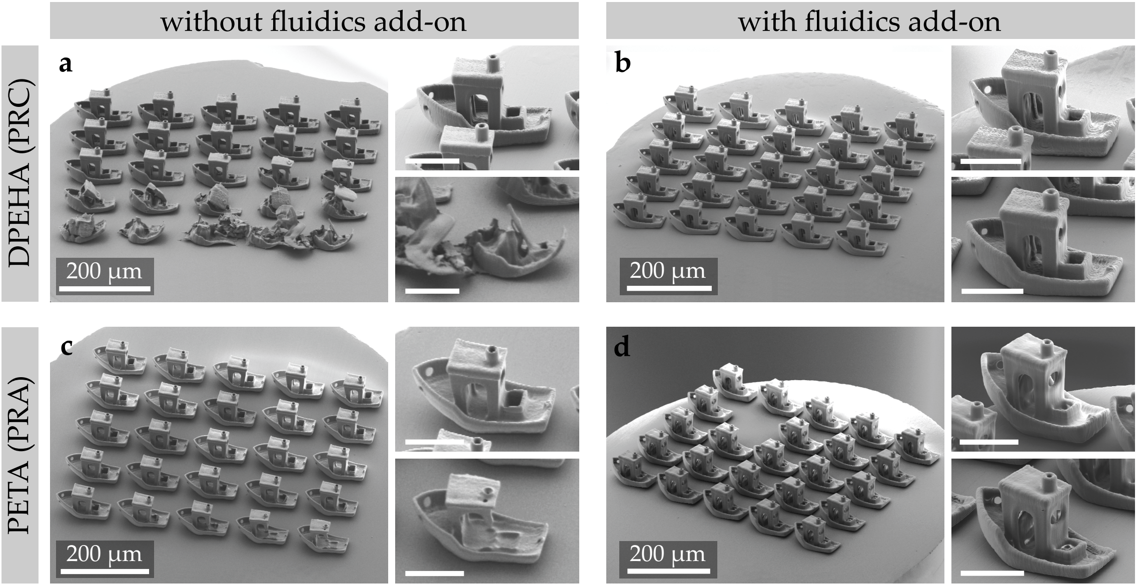

Figure 3.9: SEM images of a series of benchy boats printed by LS3DP with and without the fluidics addition. All inset scale bars are 50 µm long. The printing of one boat takes 288 ms, while the printing of the fleet of 25 boats stitched together takes 15 s. The overhead time is due to stage movements, including run-up times. **a, b** Using PRC, a significant influence of the in-situ resist exchange by the fluidics addition can be seen, achieving a constant printing quality also for rather extended prints. **c, d** Using the less viscous photoresist PRA, less improvement due to the fluidics addition is apparent. Still, a decreasing printing quality can be seen without the fluidics addition (insets of panel c).

however, shown better performance despite the lower threshold contrast. This can be explained by the simultaneous shift of the sigmoid-shaped curve towards overall lower laser powers as well as a longer intrinsic polymerization time constant, reducing aberrations due to slower refractive index changes while printing [26]. In combination with the fluidics add-on, less viscous photoresists offer the advantage of achieving higher flow rates at the same pressure difference. This is why the so far less explored photoresist PRA is added to the comparison.

SEM images of the results are shown in Figure 3.9. In all cases, 25 benchy boats were printed sequentially, with each benchy boat covering one print field. The printing time per benchy boat was 288 µs. The 25 boats were stitched together by moving the sample laterally using the two voice-coil-actuated translation stages. The total print time was 15 s, where the overhead time was due to stage movements. In all panels of Figure 3.9, the first printed boat is shown on the top left, while the boat printed last is shown on the bottom right. The printing was performed row-by-row, starting on the left for all rows. The top insets show close-ups of the boat printed first, while the bottom insets show close-ups of the boats printed last.

Looking at panel a, which shows the printing of a highly viscous resist without the fluidics, the quality of the printed structure decreases as the printing proceeds. This observation is mainly attributed to material starting to polymerize inside the cuvette in the projection beam path, which causes light scattering, rendering printing impossible at some point. It should be noted that this is somewhat different from proximity effects arising close to the printed structure, eventually in combination with an effective nonlinearity of less than two in 2SA. Still, both are caused by dose accumulation effects, the main cause of which is a depletion of quencher molecules, and as a consequence, a one-photon-triggered polymerization reaction in synergistic two-color 2SA. Using the fluidics extension, the oligomers formed by one-photon-triggered polymerization should be washed away before forming a solid polymer. At the same time, quencher molecules are delivered again, increasing the threshold for a one-photon-triggered polymerization.

Results with the fluidics extension are shown in Figure 3.9b, again using PRC. The volume flow rate for this experiment was set to $300\,\mu\mathrm{L\,min^{-1}}$. It can be seen that no noticeable degradation of the printing quality is visible for the example of 25 benchy boats. Using the mentioned process parameters, the total number or volume of structures printed is increased using the developed fluidics solution. Still, it should be noted that, also in this case, polymerized material started to show up in out-of-focus regions. This indicates that the build volume is increased but still limited due to dose accumulation effects.

Using the less viscous monomer PETA as part of the photoresist PRA, the results without and with the fluidics extension are shown in Figure 3.9c and d. Already without the fluidics, a more stable printing quality can be seen across the fleet of 25 benchy boats compared to the higher viscosity resist. Looking at the last printed boat in the bottom inset of panel c, parts of the boat's cabin are missing as a potential result of light scattering at the polymerized material. This observation is similar to PRC, where the cabin also collapsed first. The less viscous monomer already causes less out-of-focus polymerized material, however, at the expense of higher laser powers. With the fluidics extension, again a stable printing quality can be seen in Figure 3.9d, while in this case no polymerized material is observed inside the cuvette. It should be noted that the volume flow rate is increased to $900\,\mu\mathrm{L\,min^{-1}}$ for PRA.

Discussion

The fluidics extension presented could address one issue raised in chapter 3.2: the build volume of LS3DP, which is effectively limited by the photoresist. Still, there are two main drawbacks that will be explained in the following.

First, the resist flow during printing can cause printing artifacts itself. While for the shown example of dense structures of limited height, the benefits outweigh, this is not the case for tall and fragile structures. If the glass rod is raised, the linear velocity of the liquid at the printing plane increases, such that the upper parts of the printed structure are more affected by the fluidics. This causes parts to bend or swim away before they are properly connected to the rest of the structure. In principle, such effects could be reduced by adjusting the flow rate while printing. However, this not only adds further complexity but is also only partially helpful, since the response time for adjusting the flow rate is limited.

The second drawback is connected to the no-slip boundary condition of a vanishing linear velocity at the liquid-solid interface. This concerns the cuvette-photoresist interfaces as well as the substrate-photoresist interface. As, due to one-photon absorption, the undesired out-of-focus polymerization starts to build up at the cuvette-photoresist interface, one would like to have an increased instead of decreased flow velocity in this region. This problem could, however, be partly solved by a refined cuvette design in the future. A flow cell presented by Stüwe et al. [132] features flow guiding blades and additional inlets to increase the fluid flow near the interfaces while maintaining a flat flow profile in the volume. However, their flow cell is on a larger scale. Additionally, the boundary condition, of course, remains.

In summary, although the fluidics extension does not resolve the source of the out-of-focus polymerization, it minimizes the symptoms in certain cases. However, long-term efforts to reduce one-color-triggered polymerization effects should likewise focus on the development of improved photoresist compositions.

3.4 AN OPTICAL ELEMENT FOR POWER-EFFICIENT GENERATION OF A LIGHT SHEET

As discussed in section 3.2, it is beneficial to use as high red laser powers as available when relying on the photoresists currently at hand, since the threshold contrast increases with the red laser power. Of course, experimental limitations are imposed by the available laser sources at the desired wavelengths, as well as by the maximum power transmitted through the objective lens, the cuvette, and the glass rod. Besides efforts to develop new photoresist compositions, it is therefore advisable to increase the power efficiency of the light-sheet beam path. This aims at two topics: first, the transmission of the light-sheet beam path should be increased. This can be accomplished by reducing the number of optical components. Second, the uniformity of the light sheet at the focal plane should be increased. This means the cross-section should closely resemble a rectangular profile, with steep edges and a flat center. With this, the total laser power required can be reduced, as the laser power needed is largely determined by the area of lowest intensity in the print plane.

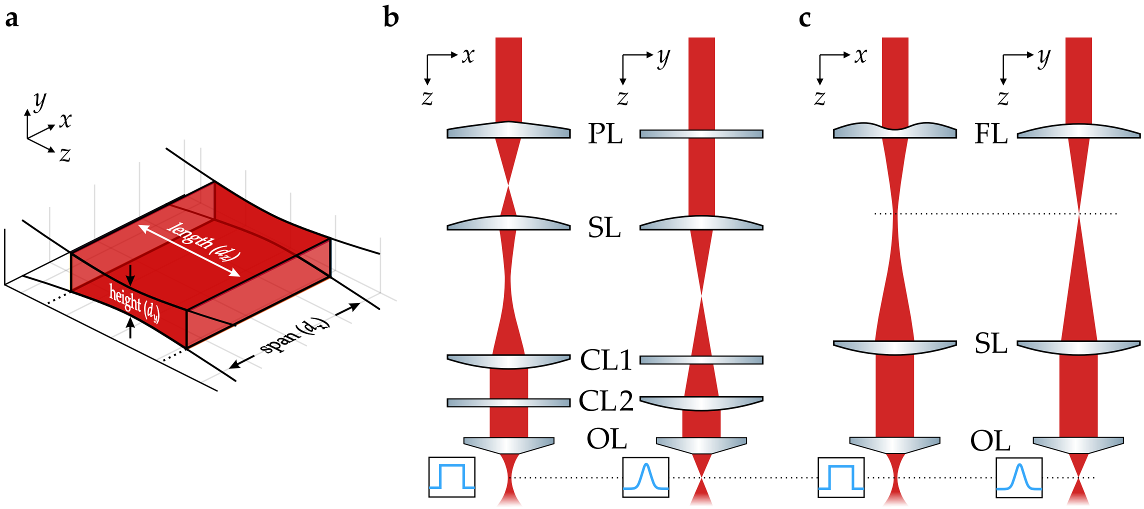

Figure 3.10: Schematic of the light-sheet beam path. a Illustration of the coordinate system as used throughout this section. **b** Components of the light-sheet beam path using a Powell lens (PL). The beam path is illustrated via two projections on the xz- as well as the yz-plane. **c** Components of the light-sheet beam path when using a freeform lens (FL). Since both lateral directions are affected by the freeform lens, no pair of cylindrical lenses is needed in this configuration. Further abbreviations used are: spherical lens (SL), cylindrical lens (CL), and objective lens (OL). Panel a is adapted from [44] while panels b and c are adapted from [141].

Along these lines, a freeform lens has been designed, manufactured via 3D laser printing, and tested for its optical performance. The experimental work presented in this section was started by the author and continued by Yvonne Schätzle in the scope of her Master's thesis [141], while the simulations were mainly carried out by the author. A part of the data analysis framework is the result of a collaborative effort by Jannis Weinacker, Sebastian Kalt, Pascal Kiefer, and the author, and is published in [121].

Design of the Optical Element

Throughout this section, I will use the coordinate system and nomenclature of the light-sheet span, height, and width as illustrated in Figure 3.10. The components of the light-sheet beam path using a Powell lens, as already explained in section 3.1, are illustrated in Figure 3.10b. Since the Powell lens has an aspheric height profile in x-direction but no height variation in y-direction, the laser beam shape is only affected in one dimension. Therefore, a set of cylindrical lenses is needed to shape the beam such that a flat top profile is generated in the focal plane of the objective lens. At the same time, a diffraction-limited focus is obtained in the orthogonal direction at the same z-plane. Using a freeform lens with a 2D spatially varying height profile, no additional cylindrical lenses are needed, as indicated in Figure 3.10b. The targeted light-sheet cross-section is formed at an intermediate plane, the focal plane of the freeform lens, and is imaged to the print plane via a spherical lens and the objective lens. This reduces complexity, increases power efficiency, and offers flexibility in light-sheet dimensions and profile design.

The freeform lens design process was performed separately for the height profile in x- and y-direction. This exploited the symmetry of the problem and reduced computational effort significantly. In x-direction, a Gaussian profile at $z = 0$ was transformed into a flat-top profile at $z = f_{\mathrm{FL}}$. The profile to accomplish this was calculated by means of an iterative angular spectrum propagation (IASP) [142–144]. Doing so, the input wave with a Gaussian amplitude profile was propagated to the desired focal plane at $f_{\mathrm{FL}} = 50\,\mathrm{mm}$. The propagation function used assumed a paraxial approximation. At f_{FL}, the amplitude was exchanged with the desired flat-top amplitude function while the phase was kept. A backpropagation was performed, after which again the phase was kept and the amplitude was replaced by the input Gaussian amplitude profile. After a fixed number of iterations, the calculation was stopped. As a target profile, a continuous profile parametrized by a higher-order Gaussian function has been found preferable to a step function. The comparison of input, design, and output can be seen in Figure 3.11a.

To examine the full beam path in a simulative approach, one-dimensional angular spectrum propagation simulations were performed. The results are shown in Figure 3.11b-d. In panel b, the full beam path is shown. Please note the largely different scales of the x- and z-axis and the saturated color scale for better visibility. A zoom-in near the focal plane of the objective lens is shown in panel c. For LS3DP, not only the profile at one position, but also over a distance matching the cross-section of the projection beam path is important. In the current implementation, this sets an area of 160 µm in x- and 90 µm in y-direction. While the freeform lens is designed for a specified span of 160 µm, the length is not taken into account in the design process. Still, it should be analyzed. Therefore, three cross-sections are shown in Figure 3.11d at the positions indicated by the colored lines in panel c. A sufficient uniformity can be seen.

In the orthogonal y-direction, the freeform lens was designed as a parabolic phase profile with a focal length of $f_{\mathrm{FL}} = 50\,\mathrm{mm}$. Illustrations of this simulation are given in [141]. Finally, the profiles in both lateral directions were extruded and added.

Fabrication by 3D Laser Printing

The design of the 2D optical element is shown in Figure 3.12a. The side length was chosen to be 2.2 mm to adequately cover the outskirts of the Gaussian input profile. Fabrication of the freeform lens was performed by means of 3D laser printing

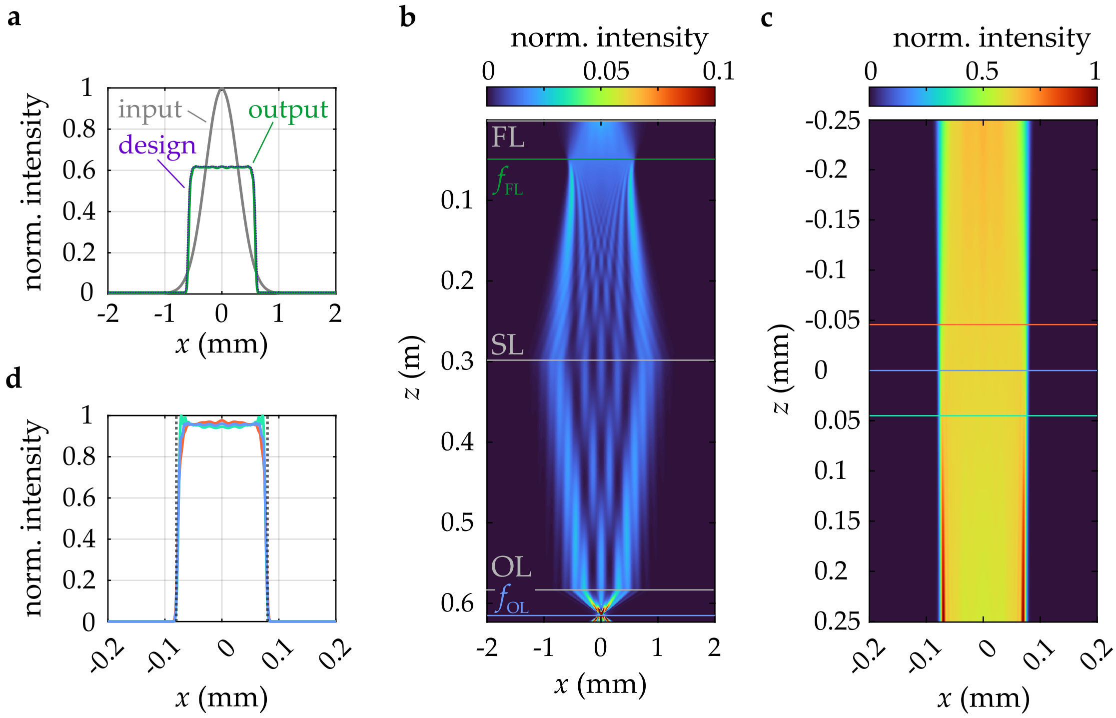

Figure 3.11: One-dimensional optics simulation of the designed light-sheet beam path. **a** Comparison of input, design, and output. The input refers to the plane of the freeform lens, where a Gaussian beam is incident. The design and output profile refer to the focal plane of the freeform lens. **b** Full optical path consisting of the freeform lens (FL), a spherical lens (SL), and an objective lens (OL). The intensity color scale is drawn saturated for better visibility. **c** Optical path near the focal plane of the objective lens. The colored lines indicate the desired light-sheet length of 90 µm. **d** Cross-sectional views of the flat-top profiles at locations indicated by the colored lines in panel c.

using a Nanoscribe QuantumX and the medium feature set, i.e., a 25×/NA0.8 objective lens and the photoresist IP-S. This allows for a dynamic adaptation of the voxel size in order to achieve smooth surfaces as needed for optical elements [83], a process called two-photon grayscale lithography (2GL). Initial fabrication efforts were carried out by the author, while more extensive parametric sweeps and optimizations were performed by Yvonne Schätzle [141]. There, additional parameter sets for optimizing the printed structures are compared. The printed structure shown in Figure 3.12b is the result of such parametric comparisons and was printed by Yvonne Schätzle. The height profile was measured by confocal optical microscopy. To ease the visual comparison of the height profile of the design and the printed freeform lens, the difference between both height profiles is depicted in Figure 3.12c. The obtained structure is the result of an iterative pre-compensation routine in which the printing design is iteratively optimized

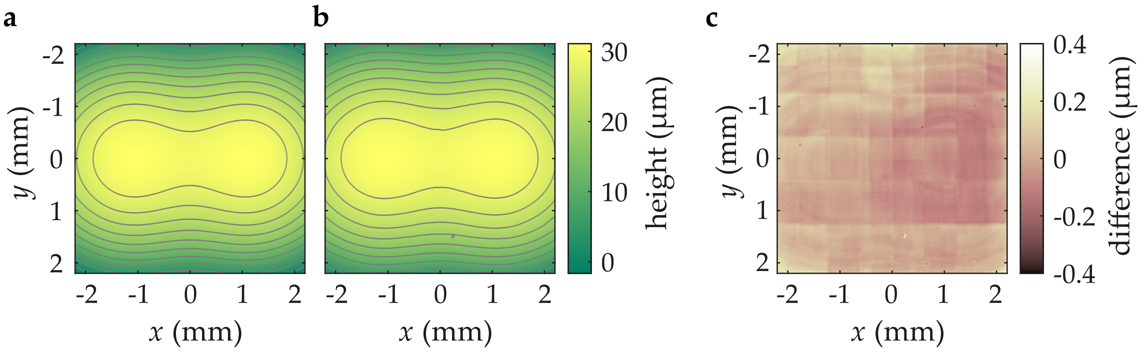

Figure 3.12: Comparison of height profiles of the designed optical element and the printed optical element. **a** The designed optical element. **b** Height profile of the 3D laser printed optical element measured by confocal-optical microscopy. The contour lines serve as a guide to the eye. **c** Difference between the height profiles shown in panels a and b. The printed structure is the result of two pre-compensation cycles as described in [121]. The measurements were performed by Yvonne Schätzle [141].

based on the printing results. Two of such iteration cycles were performed for the structure shown in Figure 3.12c. The programmatic routine for pre-compensation based on confocal-optical micrographs of the printed structure has been developed by Jannis Weinacker, Pascal Kiefer, Sebastian Kalt, and the author as a result of several projects on fabricating micro-optical components by 2GL. The routine is published in Ref. [121] and is available as an open-source software tool [145]. Details on the pre-compensation routine can be found in [41, 141, 146].

Optical Performance

Finally, the optical performance of the fabricated freeform lens was investigated. For this, the beam of the 660 nm laser source incorporated into LS3DP (see section 3.1) was guided to a dedicated characterization setup. In the focal plane of the freeform lens, a complementary metal-oxide-semiconductor (CMOS) camera was mounted on a motorized 1D translation stage to automatically measure slices of the light sheet at different z-positions. Maximum intensity projections to the xz- and yz-plane of the light-sheet generated by the freeform lens are depicted in Figure 3.13a and b. Along the x-direction, a flat-top profile is generated, while along the y-direction, the light is focused. A 1D cut at $y = z = 0$ is shown in 3.13c. It can be seen that intensity variations are still present, lowering the optical performance of the fabricated structure compared to the simulation. Especially, a peak at the right edge while there is a dip at the left edge lowers the uniformity across the light-sheet span.

Comparing the presented result to the result of the implementation using a Powell lens, the latter still yields a better uniformity. A detailed comparison, with dedi-

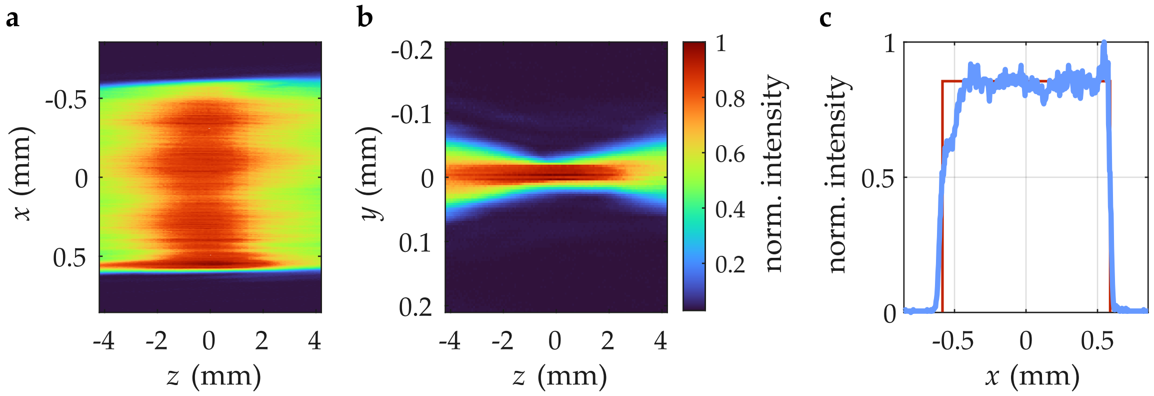

Figure 3.13: Optical measurements for benchmarking the printed freeform lens. All the measurements were performed in the focal plane of the freeform lens using a CMOS camera and a motorized translation stage. **a** Maximum intensity projection to the xz-plane. **b** Maximum intensity projection to the yz-plane. **c** Intensity cross-section at $y = z = 0$. As a visual comparison, an ideal rectangular profile is shown in the background. The measurements were performed by Yvonne Schätzle [141].

cated figures of merit introduced and compared, can be found in [141]. Therefore, the freeform lens was not implemented into the LS3DP setup at this stage. Still, a programmatic routine of the design and fabrication of optical elements was implemented within this project. The presented approach might be of future use in applications where commercial components are not suitable. This could be the case due to size restrictions or if no uniform, but a differently shaped illumination profile is desired.

3.5 CONCLUDING REMARKS

As is the case for several continuous layer-by-layer 3D printing techniques, light-sheet 3D laser microprinting inherently aims for and achieves high printing rates of up to 7×10^6 voxels s^{-1} using the setup presented here, originally built by Vincent Hahn [26]. As it is also the case for several photopolymerization 3D printing approaches, the photoresist development is as important as the development of the apparatus. The initial development of LS3DP and the synergistic two-color two-step-absorption photoresists are consequently linked. Following these initial results, this chapter assessed the potential for further development of LS3DP and two-color 2SA photoresists.

It becomes clear quickly that the photoresist is the predominant source of current limitations. An undesired one-photon-triggered polymerization reaction is present, leading to dose accumulation and limiting the build volume. Furthermore, high laser intensities are needed for the second absorption step. In collaboration with chemists, the development of novel photoresist formulations is ongoing but, unfortunately, has not led to improvements so far. The main scope of this thesis is technological development. Doing so, two main approaches have been pursued: the implementation of a fluidics add-on to increase the build volume, and the design and fabrication of a freeform lens to generate the light sheet power-efficiently. Using the fluidics chamber presented in section 3.3, printing is performed in a steady stream of fresh photoresist. Therefore, oligomers are removed and quencher molecules are delivered. This hinders dose accumulation and increases the printer's build volume. Still, the improvement is dependent on the structure to be printed. While large improvements could be obtained for dense structures and viscous photoresists, this was not the case for fragile structures and less viscous photoresists. There, the fluidics addition introduced an additional complication, the parameters of which had to be tuned to achieve sufficient printing results.

Second, a freeform lens has been designed and fabricated. With this, the number of optical elements in the light-sheet beam path can be reduced, thereby reducing complexity and increasing power efficiency. Furthermore, a uniform light sheet effectively reduces the required laser power. While the optical design yields encouraging results, the experiment lags behind. Fabrication artifacts potentially cause diffraction and interference effects, which easily add non-uniformities to the desired flat-top profile. While the specific optical element was not implemented into LS3DP, the design, as well as the iterative fabrication routine, has been proven successful. The latter, a collaborative effort among different people and applications, is published alongside two examples of optical elements generating custom laser focus distributions in Ref. [121].

Future efforts should primarily focus on investigating the photoresist as the underlying source of its limitations. The current LS3DP approach is tailored to the biacetyl-based photoresist. Significant improvements may only come with novel photoresist formulations. If this were successful and dose accumulation effects were reduced, large-scale microstructures could be fabricated in seconds without any changes to the setup.

Chapter 4

4 METHODOLOGY FOR PARALLELIZING ONE-COLOR 2SA 3D LASER PRINTING

In this chapter, the attention will be drawn to one-color two-step-absorption 3D laser nanoprinting and ways of parallelization thereof. Therefore, the target is to increase the print speeds while still relying on a compact and cost-effective laser source and overall setup. I will first point out why a multi-focus parallelization is a suitable method to pursue this target, followed by a comparison of methods to implement such an approach. The worked-out methodology will comprise dynamic multi-focus printing based on computational holography using micromirror-based spatial light modulators. On this basis, approaches to conduct 3D holographic focus scanning are discussed, and routines for the computation of holograms are introduced.

4.1 INCREASING PRINT RATES IN TWO-STEP-ABSORPTION 3D PRINTING

With the aim of increasing print rates and lowering print times, several possibilities show up. When thinking of the simplest but widespread case of scanning a single laser focus throughout the volume, print rates are increased by increasing the focus scan velocity. Furthermore, print rates can be increased by implementing parallelization approaches, therefore polymerizing several voxels at a time. These include multi-focus, layer-by-layer, and volumetric 3D printing techniques. All measures come at the expense of an increase in the necessary laser power. The consideration of the power budget is therefore essential. For a fixed nonlinearity, e.g., for $N = 2$ in the case of two-photon absorption, it is advantageous to increase the focus scan velocity up to technological limits before implementing parallelization approaches. This is because the necessary laser power scales linearly with the number of voxels polymerized in parallel (K), but scales with the N-th root of the focus scan velocity v [43]:

$$P \propto K \sqrt[N]{v} \tag{4.1}$$

Increasing the focus scan velocity and, therefore, the print rate by a factor of 100 only increases the necessary laser power by a factor of 10.
Considering two-step absorption, this argument is, however, impaired by a decreasing nonlinearity for higher focus scan velocities [24]. Therefore, an upper limit is posed to the focus scan velocity as well as the print rates for single-focus scanning. Connected to the focus scan velocity is the exposure time per voxel. From rate-equation calculations of a three-level system, as introduced in section 2.3, it can be shown that the exposure time t_{exp} should remain well above the intermediate state lifetime τ to maintain a nonlinear photoinitiation [44]. This condition should still be treated with caution, since the nonlinearity varies gradually and no single-valued upper bound can be stated. It is nonetheless vital to be aware of the magnitudes involved: Taking an intermediate-state lifetime of $\tau \approx 80\,\mu\text{s}$ for a benzil-based photoresist, a transition from a nonlinear to a linear relationship is present for focus scan velocities in the order of hundreds of micrometers per second [24]. This fits the typically used focus scan velocities for benzil-based photoresists of $v = 1\,\text{mm}\,\text{s}^{-1}$ [24, 25, 27] and the maximum used focus scan velocities of $v = 4\,\text{mm}\,\text{s}^{-1}$ [24].
Increasing the focus scan velocity above these values could be done by decreasing the intermediate-state lifetime. When sticking to benzil as the photoinitiator, this can be achieved by increasing the concentration of the quencher molecules. However, the typically used concentrations of up to 50 mM are already near the solubility limit of BTPOS in PETA. Therefore, no large improvements can be expected unless significant efforts are made to develop completely novel photoresist formulations.
For 2SA 3D printing, parallelization approaches are consequently an advisable

route to increase print rates since physical and chemical limits are reached before reaching technological limits of single focus scanning. Furthermore, 2SA starts with the inherent advantage of drastically reduced laser powers compared to 2PP. For a competitive 3D printing approach, this advantage should also be kept for a parallelized printing approach, which therefore should still rely on compact cw laser sources.

4.2 BEAM-SPLITTING AND BEAM-STEERING APPROACHES

Parallelized 3D laser printing, as discussed in this work, refers to the simultaneous polymerization of more than one voxel. This comprises multiple distinct voxels as well as dense patterns, as in layer-by-layer approaches. However, printing dense patterns simultaneously significantly lowers the resolution along the optical axis, as outlined in section 2.2. Different approaches circumvent this issue by introducing a highly absorbing one-photon-absorption photoresist, such as stereolithography and variants thereof [95, 109], or by introducing a synergistic two-color photoresist, such as LS3DP [26, 47]. When using one-color 2SA, a multi-focus parallelization is advantageous over a layer-by-layer approach, as it maintains the complete freedom to print the desired structures. Therefore, this section aims to compare different beam-splitting and beam-steering approaches for multi-focus 3D laser printing in the context of two-step absorption.

4.2.1 Static vs. Dynamic Approaches

The first design choice is between a static and a dynamic beam-splitting and beam-steering approach. In static approaches, a fixed multi-focus pattern is generated and scanned across the print field while the positions of the foci remain constant with respect to each other. In a dynamic approach, the focus pattern is changed during printing. A visual illustration of these two different approaches is shown in Figure 4.1. This further implies that static approaches typically require two separate components for beam splitting and beam steering. In a dynamic approach, beam splitting and beam steering are often combined into a single device.
Static multi-focus patterns can be created by diffractive optical elements (DOEs) [29, 148], refractive multi-lens arrays [149, 150], or a combination thereof [84]. Doing so, beam splitting at high laser power efficiencies above 90 % is possible [41, 44]. The beam splitting, however, has to be combined with separate devices, such as galvanometric mirrors [29, 84], polygon scanners [151], or electro- or acousto-optical deflectors [152], for beam scanning. This approach reaches its full advantage for highly power-critical applications, like multi-focus multi-photon 3D laser printing

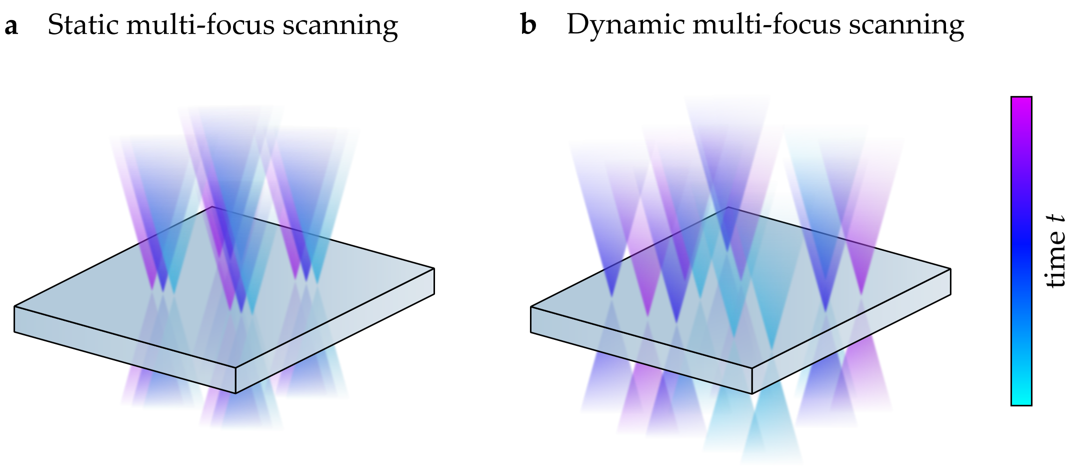

Figure 4.1: Illustration of static and dynamic multi-focus scanning approaches. a In a static approach, a fixed focus array is scanned across the print plane. **b** In a dynamic approach, the focus pattern is changed during printing at a certain refresh rate. Using dynamic approaches, the beam splitting and beam steering can be accomplished by a single device. The differently colored cones illustrate focus positions at different times t. Figure adapted from [147].

[84], where the fabrication of many identical particles or large periodic structures is targeted. When aiming at non-periodic structures, the benefit of a static beam-splitting approach is lower compared to a dynamic approach.

Using dynamic approaches, the focus pattern can change in the number and the individual position of each focus at a certain refresh rate during printing. Often, the intensity of each laser focus can be controlled as well. For non-periodic structures, the multi-focus parallelization maintains its advantage in printing rates. At the same time, a static approach needs to be restricted to a single focus in such cases, lowering its parallelization advantage. However, for combined dynamic beam splitting and beam steering, active electro-optical devices are necessary, which often entail lower power efficiency than, e.g., specifically tailored DOEs [41, 44]. Considering the application of two-step absorption, low single-focus laser powers well below 1 mW are typically used. This reduces the priority of the power efficiency consideration. More importantly, 2SA is best suited for 3D printing relatively small volumes exhibiting high spatial resolution. Furthermore, the usage of compact cw laser sources allows for compact implementations of the whole setup. For these reasons, a dynamic approach is chosen, enabling print speed gains for almost arbitrary structures in a setup that combines beam splitting and beam steering into a single device.

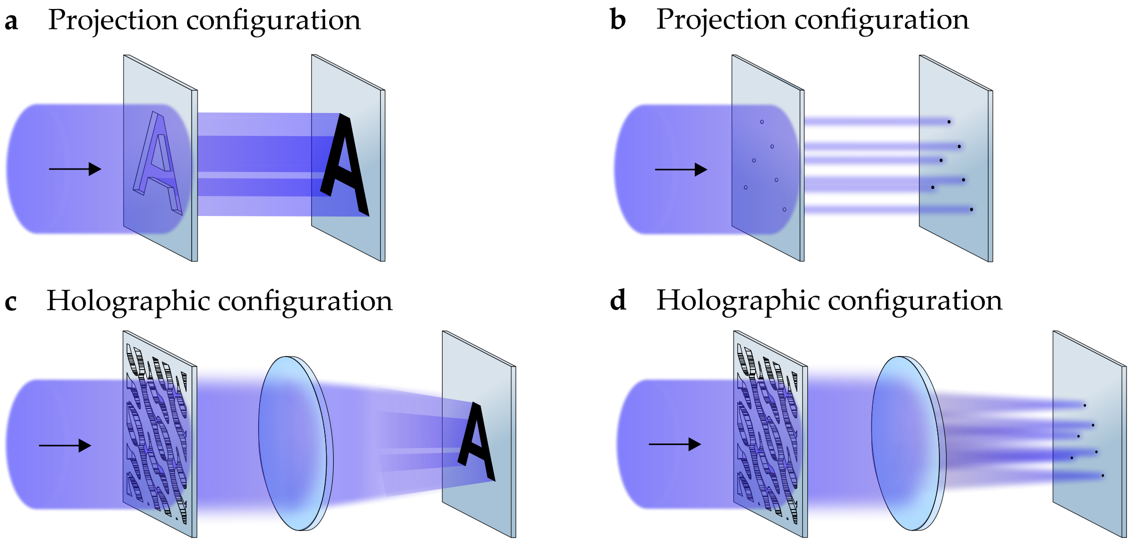

Figure 4.2: Schematic comparison of the direct imaging of a dynamic mask (projection configuration) and a diffractive beam-splitting approach (holographic configuration). **a** For dense patterns, a considerable fraction of the light incident on the dynamic mask is transmitted. **b** For sparse patterns, only a small fraction is transmitted, rendering the power efficiency very low. Note that in a 3D printing application, the mask would be imaged and demagnified via, e.g., two lenses, which are not shown for simplicity. **c** Diffractive beam splitting considering dense patterns. **d** Diffractive beam splitting considering sparse patterns. The power efficiency is much less dependent on the pattern's fill factor. Figure adapted from [147].

4.2.2 Projection vs. Holographic Configuration

The next consideration is the implementation of a dynamic multi-focus printing approach. Among the simplest, straightforward implementations is the direct imaging of a display to the print plane. This projection configuration is schematically illustrated in Figure 4.2a and b for the two cases of a dense and a sparse 2D pattern. The display acts as a dynamic mask, transmitting only certain areas while blocking the rest of the laser beam. It becomes immediately apparent that the power efficiency can be very low, especially in the case of sparse multi-focus distributions. Consider the example of a display of 10^6 pixels and a target distribution of 10 foci. The power efficiency is as low as 10^{-5}, since each pixel corresponds to one focus. Even when grouping, e.g., 10 pixels to one focus, the power efficiency is only 10^{-4}. Despite the higher power budget in 2SA due to the availability of cw laser sources, such low power efficiencies would require watt-class lasers, contradicting the overall goal of compact and affordable 3D laser printers using 2SA.

An alternative is to place a spatial light modulating device in the Fourier plane of a microscope objective lens [80, 94, 153–156]. In the context of this work, I will refer to this approach as a holographic configuration. A certain (dynamic) diffractive optical element modulates the amplitude and/or phase of the light such that the desired intensity pattern is created in the focal plane of a Fourier-transforming lens. This is schematically illustrated in Figure 4.2c and d. It is important to note that, in this configuration, the transmission of light through the modulating device is largely independent of the target pattern's fill factor. This is especially favorable for sparse patterns, as considered in this work.

The power efficiency of the holographic configuration, however, is directly linked to the modulation principle employed. This connects to the choice of modulating device: amplitude-only, phase-only, or combined phase-and-amplitude modulators at different modulation depths (i.e., different numbers of addressable levels). In all cases, the power efficiency is higher than the simple numerical example for direct imaging, so a holographic configuration for dynamic beam splitting is chosen.

4.2.3 *The Choice of the Device*

Widespread commercially available devices for spatial light modulation include liquid-crystal-on-silicon spatial light modulators (LC-SLMs) and digital micromirror devices (DMDs) [157]. A schematic comparison of their operation principles is depicted in Figure 4.3a and b.

The active component of LC-SLMs is a layer of liquid crystal molecules. These are embedded between a transparent front window and pixelated electrodes, conveniently manufactured on a complementary metal-oxide-semiconductor (CMOS) processed substrate. Liquid crystals are anisotropic molecules that align in a single preferred direction when no voltage is applied to the electrodes. Applying a voltage changes the orientation of the liquid crystal molecules and thus the refractive index of the cell. This changes the optical path length, and a spatially varying phase delay is applied. Therefore, LC-SLMs can operate as multi-level phase-only modulators.

DMDs consist of an array of movable aluminum micromirrors, mounted on actuator electronics, and integrated into a CMOS process. They are therefore considered a micro-electro-mechanical system (MEMS). Applying voltages to the actuator electrodes generates electrostatic forces, thereby causing the micromirror to move. A single DMD cell is a multi-layered device comprising hinges and support posts to achieve fast, reliable movements. Typically, the micromirrors switch between two distinct states. Therefore, light reflected from the micromirrors is directed in only two separate directions, rendering the DMD a binary amplitude modulator. These two configurations are considered the "on" and the "off" states. DMDs find widespread commercial applications in projectors, projection-based 3D printing, and the automotive industry [158, 159].

In addition to these standard devices, a new class of devices is emerging that builds on the DMD's principle of movable micromirrors as well as on its manufacturing

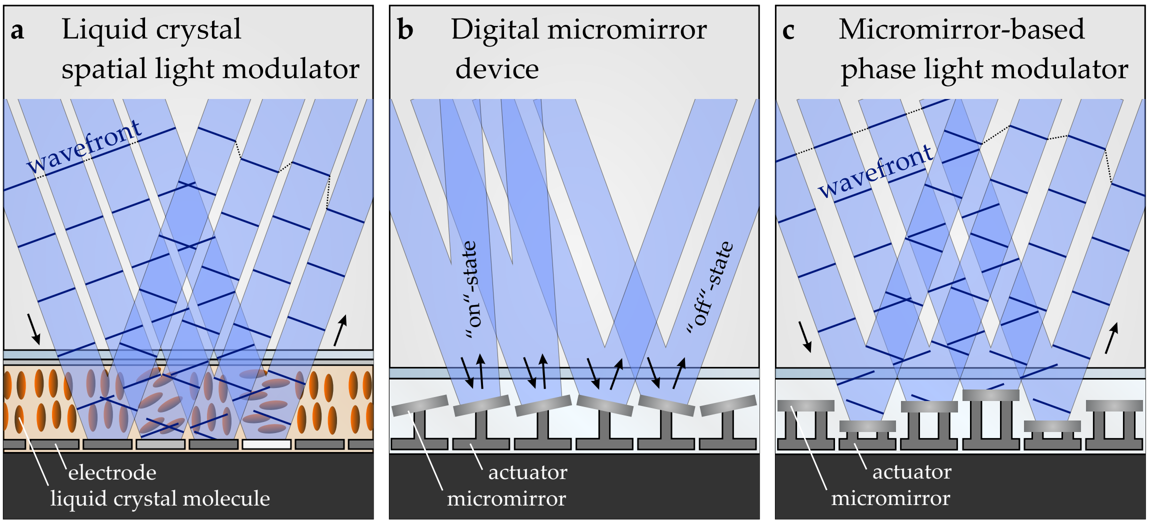

Figure 4.3: Illustration of the operation principle of LC-SLMs, DMDs, and PLMs. **a** The active layer of an LC-SLM consists of liquid crystal molecules sandwiched between electrodes. When a voltage is applied, the molecular orientation changes, altering the refractive index and thereby inducing phase modulation. **b** DMDs consist of a layer of movable aluminum micromirrors, which can be switched via electrostatic forces between two states, where light is reflected in two separate directions. DMDs are, therefore, binary amplitude modulators. **c** Micromirror-based phase light modulators allow for switching each individual micromirror between typically 16 different height levels while remaining flat with respect to the substrate. They therefore allow for phase-only modulation of the reflected light by spatially varying the phase delay.

process [160]. These are micromirror-based phase light modulators, synonymously also called piston-mode phase light modulators or PLMs in short. As the name implies, these devices offer phase-only modulation. This is achieved by driving the micromirrors to different height levels while remaining flat with respect to the substrate surface. Therefore, a spatially varying phase difference and thus a wavefront modulation is achieved. The operation principle is further illustrated in Figure 4.3c. However, at the time the research was conducted, PLMs were not commercially available. Only lately, pre-production and therefore prototype devices became available [161]. As such, some sacrifices regarding the device quality stemming from not fully matured manufacturing processes have to be made when working with these devices. These include the mirror flatness, therefore surface quality, the height level accuracy, as well as the achievable refresh rates and switching times [161, 162]. All of these current caveats are, however, subject to potential improvements in the future.

Considering the application of a dynamic holographic beam splitting, several parameters have to be taken into account to choose the best-suited device. These include the modulation rate, the laser power efficiency, the pixel size and number, as well as the device cost.

LC-SLMs are typically operated at refresh rates of 60 Hz or 120 Hz as these are standard refresh rates for projectors and displays [163, 164]. The limiting factor of an LC-SLM is, however, the time it takes the liquid crystal molecules to rearrange. These response times are typically in the range of 10 ms down to 0.6 ms for high-end devices, which translates to refresh rates of up to 1400 Hz [165–167]. DMDs in projector applications are also often linked to refresh rates of 60 Hz or 120 Hz [158]. However, the micromirror switching rates are significantly higher since a grayscale amplitude modulation, as needed for projector applications, is provided by a time-averaged on-off movement. At a typical modulation depth of 24 bit, the micromirror switching rate is already in the kilohertz range in consumer products. The minimum time it takes a micromirror to move and settle is around 10 µs [168]. Since the micromirrors are only driven between two end-positions restricted by physical barriers and no "free-floating" state has to be addressed, these move and settling times are significantly smaller compared to LC-SLMs. Current high-end DMD devices operate at modulation rates of up to 32 kHz [169]. DMDs in the mid-range as well as in the high-end segment can therefore be considered as being faster than LC-SLMs by a factor of ≈ 20. For PLMs, as the technology is not fully developed yet and different "free-floating" height levels have to be reliably addressed, the modulation rates are currently lower compared to DMDs with maximum modulation rates of up to 5.6 kHz and typical modulation rates of 1440 Hz using a video input [161]. Still, PLMs already operate at higher rates compared to LC-SLMs.

When comparing laser power efficiency, two factors must be considered: the device efficiency and the hologram efficiency. The device efficiency accounts for absorption, reflection, and diffraction losses within the device itself and is therefore largely dependent on the wavelength used. The main contribution for LC-SLMs at 405 nm is absorption, while the main contribution for DMDs and PLMs is diffraction [157], which will be discussed in more detail in section 5.1.2 and 6.2. The hologram efficiency shows further differences: LC-SLMs and PLMs, as phase-only modulators, can directly display multi-level phase holograms, with theoretical hologram efficiencies of 98.7 % assuming 16-level phase-only modulation [170]. For binary amplitude-modulating DMDs, the restriction to an "on" or "off" state significantly reduces hologram efficiency by introducing a strong zeroth-order component that must be blocked. The hologram efficiency is therefore only 10.1 % at maximum [170, 171].

Other parameters, such as pixel size and number, are comparable, with typical pixel numbers in the order of 10^6 and pixel sizes of 10 µm or less. The device cost favors the DMD, with complete modules priced around 1000 € and single DMD chips priced at only 200 € or less [158]. While current PLM pre-production devices have a higher price tag of around 2500 €, they are still considered cheaper than

Table 4.1: Comparison of LC-SLMs, DMDs, and PLMs considering print rates in dynamic multi-focus 3D printing based on two-step absorption. Quantities following an arrow are derived from other quantities given in the table. Devices in the mid-range segment are assumed with the efficiency values averaged across different devices [158, 163, 165]. The hologram efficiency assumed the theoretical maximum based on the modulation depth [170]. In all cases, a video input with therefore rather low modulation rates is assumed. The polymerization threshold refers to a one-color 2SA resist containing benzil and BTPOS dissolved in PETA, measured at 405 nm laser wavelength (PR1 in Ref. [24]). In the last row, the printing of a structure with a fill factor (FF) of 20 % across the print field is assumed.

	LC-SLM	DMD	PLM
device efficiency	80 %	40 %	70 %
hologram efficiency	98.7 %	10.1 %	98.7 %
→ combined efficiency	79 %	4 %	69 %
modulation rate	60 Hz	1440 Hz	1440 Hz
→ exposure time	16.7 ms	0.6 ms	0.6 ms
polymerization threshold	40 µW	200 µW	200 µW
→ # parallel voxels (400 mW laser source)	7896	80	1382
→ voxel distance (across 10^4 µm^2)	1.1 µm	12.5 µm	2.7 µm
→ # parallel voxels at d_{min}	1111	80	1111
→ # voxels s^{-1} at d_{min}	0.67×10^5	1.15×10^5	1.6×10^6
→ # voxels s^{-1} at d_{min} and FF = 20 %	0.13×10^5	1.15×10^5	3.2×10^5

typical LC-SLM devices [172, 173].

As a summary of the above comparison, micromirror-based devices such as widespread DMDs and emerging PLMs provide higher modulation rates while being less power efficient compared to LC-SLMs. For multi-focus 2SA 3D printing, this implies that using DMDs, a lower number of voxels can be polymerized in parallel, while patterns can be changed faster. An approximate numeric example comparing the different devices is given in Table 4.1. In all cases of LC-SLMs, DMDs, and PLMs, the exposure time assumed is still well above the intermediate state lifetime of 2SA photoinitiator molecules, as discussed in section 2.3.3. When distributing a larger number of voxels across a given area, the distance between them becomes smaller. If the distance gets too small, interference effects lower the print quality significantly [29, 80, 174, 175]. For the numbers given in Table 4.1, a minimum distance between neighboring voxels of $d_{\mathrm{min}} = 3\,\mu\mathrm{m}$ is assumed to circumvent detrimental interference effects. Furthermore, considering that 2SA is best suited for structures of small filling factors, the number of voxels polymerized in parallel is significantly reduced compared to the maximum. Although not an inherent property of the device, this fact significantly reduces the maximum achievable print rate with LC-SLMs, leading to the selection of micromirror-based devices for the presented application.

Two versions of a 3D laser nanoprinting setup are designed, built, and evaluated in the scope of this thesis. The first version, presented in chapter 5, uses an off-the-shelf available DMD for dynamic multi-focus printing. Based on the knowledge gained in this project and driven by the recent availability of pre-production devices, a second version is developed using a PLM and presented in chapter 6.

4.3 MULTI-FOCUS HOLOGRAPHIC LASER BEAM SCANNING

With the introduction of the holographic configuration based on micromirror devices, as worked out in the last section, the following will capture the calculation of the holographic patterns to be displayed on the device. In all cases, a 2D phase or amplitude pattern must be calculated to generate the desired multi-focus intensity distribution in the print volume. The primary target of this work is multi-focus 3D printing within a single plane, which can also be scanned in the axial direction via the holograms. Holograms generating continuous and/or volumetric intensity distributions are possible and can be exploited for "single-shot" 3D laser printing [116, 176], but will not be explained in detail in this section. Still, the same concepts of course also apply in this case. For the sake of simplicity, I want to split the discussion into several parts, comprising first 3D single focus scanning, which will be expanded to holographic multi-focus generation afterward.

4.3.1 3D Holographic Focus Scanning

In the most abstract configuration, the phase at the entrance pupil of the objective lens is assumed to be flat when no adaptive optical device is incorporated, and to be modulated by the adaptive optical device. This modulation should cause a focus to be deflected from the nominal focus point and positioned at predefined locations of the image volume. The basic geometry is illustrated in Figure 4.4a with the adaptive optical elements not altering the phase. Thus, the light gets focused to the nominal focus. Please note that the length scales are not to scale in this sketch. In a practical implementation, the adaptive optical device, which is a DMD or PLM in the present work, cannot be placed right in the entrance pupil of the objective lens, but can be relayed to this plane via two additional lenses.

For laterally shifting the focal spot in the image plane, a linear phase ramp has to be applied across the pupil plane. This adds a transverse spatial frequency to the wavefront. In other words, the wavefront gets tilted. This wavefront tilt translates into a lateral shift in the focal plane of the objective lens. Figure 4.4b illustrates this

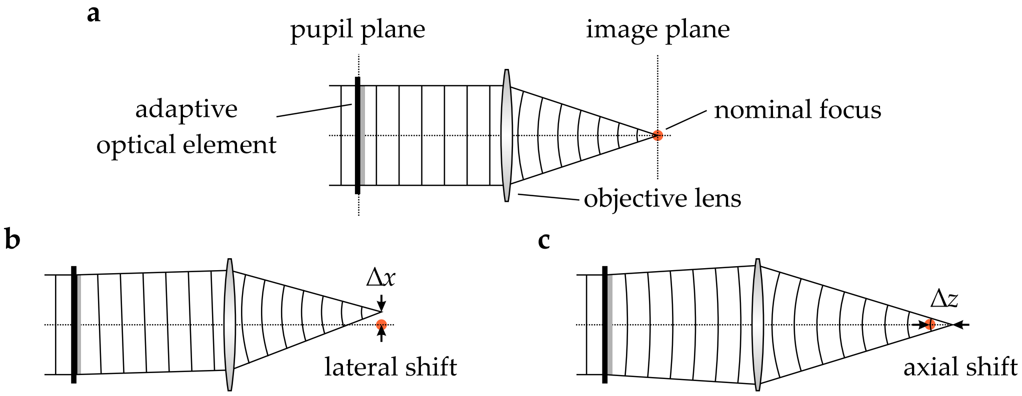

Figure 4.4: Sketch of the basic principle of holographic beam steering in the image plane via a phase modulation in the pupil plane. a If no phase modulation is applied, the light is directed to the nominal focus position on the optical axis. **b** When applying a linear phase ramp, light is deflected away from the optical axis, resulting in a lateral shift Δx. **c** When applying a curved defocus phase, the focal position is shifted along the optical axis, resulting in an axial shift Δz. Note that the distances and angles are not to scale. Furthermore, a real high-NA objective lens is a multi-lens device with the pupil plane located within it, which is omitted for clarity. Adapted from [177] with permission (© 2013 Informa UK Limited).

situation in a 1D case, shifting the focus laterally by Δx. The phase profile $\varphi(x_\mathrm{P}, y_\mathrm{P})$ to apply at the pupil plane to achieve lateral displacements of Δx and Δy in the image plane reads as

$$\varphi(x_\mathrm{P}, y_\mathrm{P}) = \frac{2\pi}{\lambda f_\mathrm{Obj}} \left(x_\mathrm{P} \Delta x + y_\mathrm{P} \Delta y \right) . \tag{4.2}$$

Here, the focal length f_Obj refers to the effective focal length of the objective lens and can be obtained by dividing the focal length of the standard tube lens of the objective lens manufacturer by the nominal magnification. For the case of a 100× Leica objective lens with a tube lens standard of $f_\mathrm{TL} = 200\,\mathrm{mm}$ this leads to: $f_\mathrm{Obj} = 200\,\mathrm{mm}/100 = 2\,\mathrm{mm}$.

For axial scanning of the focal position, a curved defocus phase must be applied. This is schematically illustrated in Figure 4.4c. However, care must be taken in the case of a high numerical aperture [178–180], as is typically employed in 3D laser nanoprinting. In this case, the phase profile can be derived from the optical path length difference of spherical waves emitted from the nominal focus and spherical waves emitted from the shifted focus [181, 182]. Considering a geometry fulfilling the sine condition, the path difference of each, the nominal focus, and the shifted focus, to the same point on the reference sphere needs to be calculated. From the path difference at the reference sphere and by invoking the sine condition, the phase profile in the pupil plane can be calculated. A detailed derivation can be

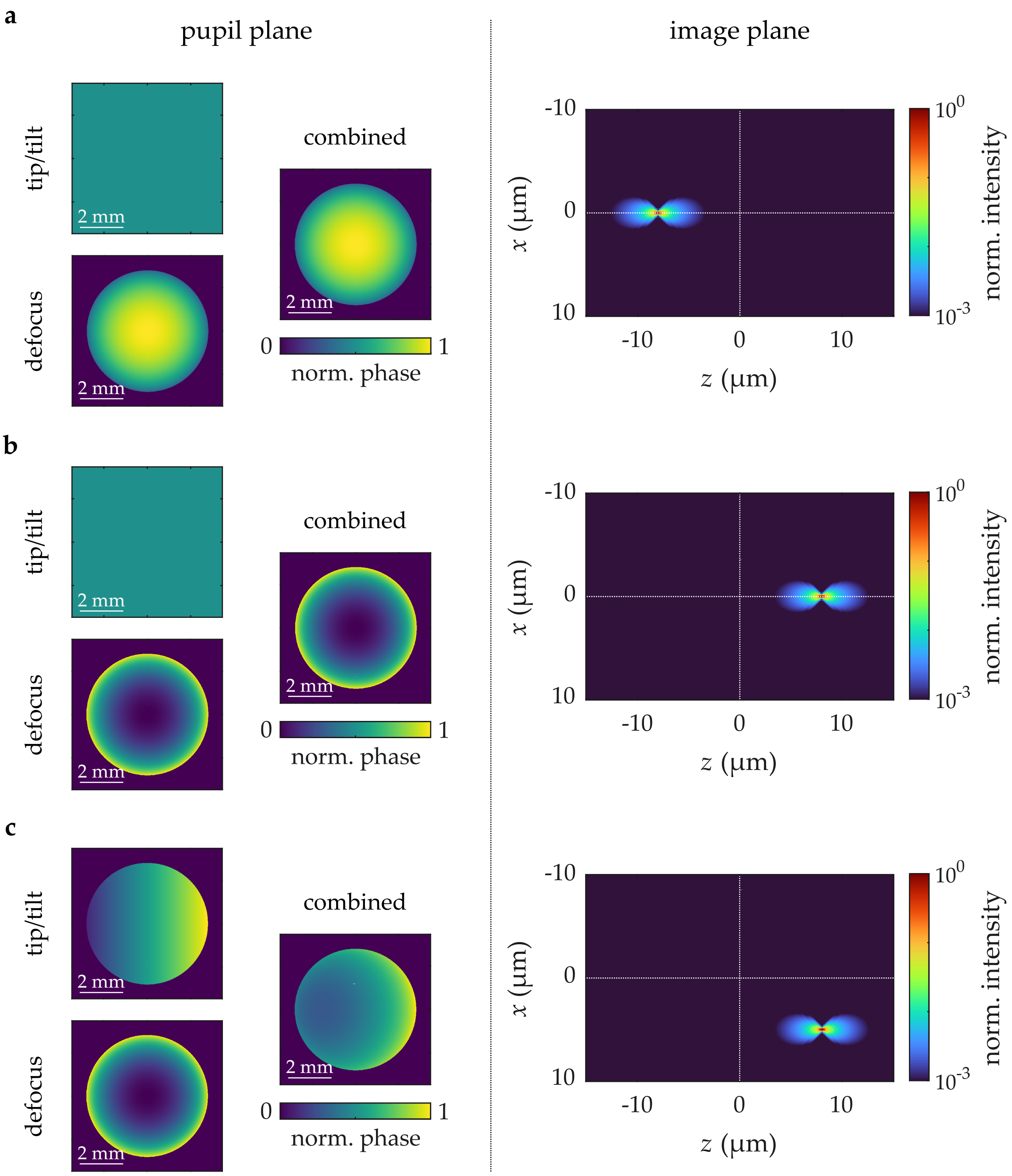

Figure 4.5: Calculation of focus position shifts for different phase patterns applied. **a** A converging defocus phase according to equation 4.3 is applied. No additional linear phase ramp, therefore no tip/tilt phase is applied. The axial focus shift is set to $\Delta z = -8\,\mu\mathrm{m}$. The optical system assumes a Leica 100×/NA1.4 objective lens, a wavelength of $\lambda = 405\,\mathrm{nm}$, and a Gaussian amplitude distribution at the pupil plane. **b** Applying a diverging phase, the focus is shifted further away from the objective lens. **c** With the defocus phase of panel b and an additional tip/tilt phase, the focus is shifted laterally by $\Delta x = 5\,\mu\mathrm{m}$ in addition to the axial shift.

found in Ref. [181]. Under the further assumption of small focus shifts compared to the objective lens's focal length, the phase profile to be applied at the pupil plane to shift the focus position axially by Δz in the image plane then reads as [181]

$$\varphi(x_\mathrm{P}, y_\mathrm{P}) = -\frac{2\pi n}{\lambda}\Delta z\sqrt{1 - \frac{x_\mathrm{P}^2 + y_\mathrm{P}^2}{f_\mathrm{Obj}^2 n^2}}. \tag{4.3}$$

n is the refractive index of the immersion medium, when present.

Simulations to illustrate the above formulas are shown in Figure 4.5. There, a pure phase modulation in the entrance pupil of an objective lens (100×/NA1.4) is assumed. Therefore, the entrance pupil radius calculates to $f_\mathrm{Obj} \cdot \mathrm{NA} = 2\,\mathrm{mm} \cdot 1.4 = 2.8\,\mathrm{mm}$, to which the phase and amplitude are restricted. The scalar field at the nominal focal plane is obtained via a Fourier transform. Planes above and beneath the focal plane are calculated via an angular spectrum propagation, without assuming a paraxial approximation [179]. In Figure 4.5a, no phase ramp is applied, but a converging defocus phase according to equation 4.3. Therefore, the focus shifts towards the objective lens (negative z-values) while maintaining its diffraction-limited shape. The opposite is illustrated in Figure 4.5b, where the distance of the focus from the objective lens is increased by applying a diverging phase profile. In Figure 4.5c, this is combined with a linear phase ramp deflecting the focus in x-direction, in addition to the shift in axial direction. In all cases, the shifts are small compared to the focal length of the objective lens so that the above formulas can be applied and a diffraction-limited focus is maintained. In reality, the adaptive optical element introduces further limitations, which are discussed in detail in Ref. [177] and which will be briefly addressed in section 5.1.4.

The formulas above are given in Cartesian coordinates and assuming real-world length scales, as these are conveniently matched to the pixel dimensions of adaptive optical devices and, of course, to the experiment. Often the defocus phase is given using a normalized pupil radius ρ with $\rho^2 = (x^2 + y^2)/(f_\mathrm{Obj}^2 \mathrm{NA}^2)$. Applying this and the definition $\mathrm{NA} = n \sin\alpha$, with the maximum acceptance angle α of the objective lens, the defocus phase reads as [180]

$$\varphi(\rho) = -\frac{2\pi n}{\lambda}\Delta z\sqrt{1 - \rho^2 \sin^2\alpha}. \tag{4.4}$$

A Taylor expansion assuming small $\rho \sin\alpha$, therefore lower numerical apertures, can be calculated:

$$\varphi(\rho) \approx -\frac{2\pi n}{\lambda}\Delta z\left(1 - \frac{1}{2}\rho^2\sin^2\alpha - \frac{1}{8}\rho^4\sin^4\alpha - \frac{1}{16}\rho^6\sin^6\alpha - O(\rho^8)\right) \tag{4.5}$$

With this, it can be seen that the focus quality is reduced by introducing spherical

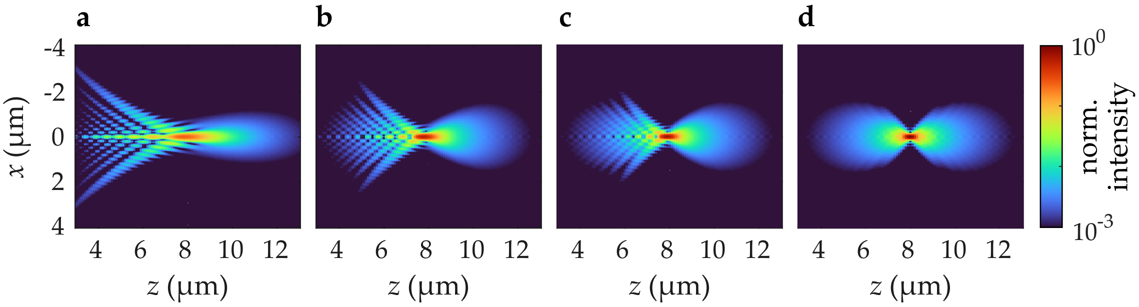

Figure 4.6: Focus calculations when applying axial shifts according to equation 4.5. In all panels, the focal position is shifted axially by approximately 8 µm. The same optical setup as in Figure 4.5 applies. In panel **a**, terms up to the ρ^2-order are considered. Spherical aberrations show up in the focus calculation for this case. In panels **b** and **c**, terms up to the ρ^6- and ρ^{10}-order are considered, such that spherical aberration effects are reduced. In panel **d**, equation 4.3 is considered as a comparison with no approximation applied.

aberrations when relying on only the quadratic phase term, as it is often done [80, 153, 183]. These aberrations have a greater effect for larger numerical apertures and increasing focus shifts. An axially shifted focus, when taking the approximation of equation 4.5 up to different polynomial orders, is shown in Figure 4.6. In panel a, only the quadratic term is incorporated, leading to clear spherical aberrations and a reduction of the maximum intensity, which is shown normalized to the non-shifted case. In Figure 4.6b, terms up to the order of ρ^6 are taken into account, while in Figure 4.6c, terms up to the order of ρ^{10} are considered. In panel d, the non-approximated case is shown. When increasing the polynomial order, the aberration effects are reduced.

The calculations shown assume a perfectly aplanatic, aberration-free optical system and make no restrictions on the phase response of the phase modulating device. In the experiment, however, additional aberrations are inevitably introduced. These originate from non-ideal optical components, imperfections of the phase modulator, and refractive-index mismatches of the different materials close to the print plane. Since it is cumbersome to model all of these effects, a more pragmatic, system-adapted approach is chosen in the experiment to achieve a sufficient quality, especially while axially scanning the focus. In doing so, the axial phase mask is expressed as a weighted sum of Zernike polynomials. The coefficients are optimized empirically to maximize the focal intensity at the desired axial position. This strategy provides a flexible basis that approximates the ideal high-NA defocus phase and compensates for system-specific aberrations. Experimental results of this approach are presented in section 6.2.4.

The above description of steering one focus to the desired location can be further expanded to multiple foci. To do so, the complex fields containing the phase patterns of each deflected focus are added, and the phase of the resulting field is extracted:

$$\varphi = \arg\left(\sum_i A_i \exp(\mathrm{i}\varphi_i)\right) \tag{4.6}$$

For each focus i, the relative amplitude can be controlled by the weight factor A_i. This direct method for the calculation of holograms generating multi-focus patterns is often referred to as the superposition of gratings and lenses method [184, 185]. Although simple and straightforward, this approach may result in limited uniformity of the foci in the image plane and unwanted ghost foci, thereby limiting diffraction efficiency. This is especially the case for highly symmetric patterns, like periodic focus arrays [185]. In these cases, iterative phase retrieval algorithms are used to refine the phase pattern.

4.3.2 Phase Retrieval Algorithms for Hologram Calculation

To calculate the phase hologram of a multi-focus pattern, the desired intensity distribution is given as the input. The task is therefore to recover the unknown phase of a complex optical field when only intensity information is available. For this purpose, iterative phase retrieval algorithms such as the Gerchberg-Saxton (GS) algorithm can be used [186]. The general implementation serving the calculation of phase holograms is illustrated in Figure 4.7, when following the red arrow on the left side. Starting at the top left, the calculation is initialized by setting the complex-valued optical field $u_{\mathrm{in}} = A_{\mathrm{in}} \exp(\mathrm{i}\varphi_{\mathrm{in}})$. If known, the amplitude can be initialized with the experimentally present amplitude profile. In practice, mostly the distinction between a Gaussian and a uniform illumination profile is made. The phase pattern is mostly initialized to be random, but can be optimized for specific target patterns [187]. Via a Fourier transform, the optical field is propagated to the Fourier or image plane at which the desired pattern should be created. While the phase information is kept, the amplitude is replaced by the target amplitude. When performing an optional weighting step, the target amplitude is modified depending on the ratio of the present and the target amplitude. If doing so, the whole algorithm is often referred to as a weighted Gerchberg-Saxton algorithm [184]. In the next step, the optical field is back-propagated to the hologram plane via an inverse Fourier transform. If the quality of the amplitude at the image plane (A_{out}) is sufficient, the phase at the hologram plane (φ_{H}) can be taken as the holographic pattern, and the calculation stops. If this is not the case, an iterative procedure starts, where again the phase is guided through while the amplitude is replaced by the original input amplitude.

The briefly introduced Gerchberg-Saxton algorithm is one of the most common routines for designing computer-generated holograms. In the present work, it has

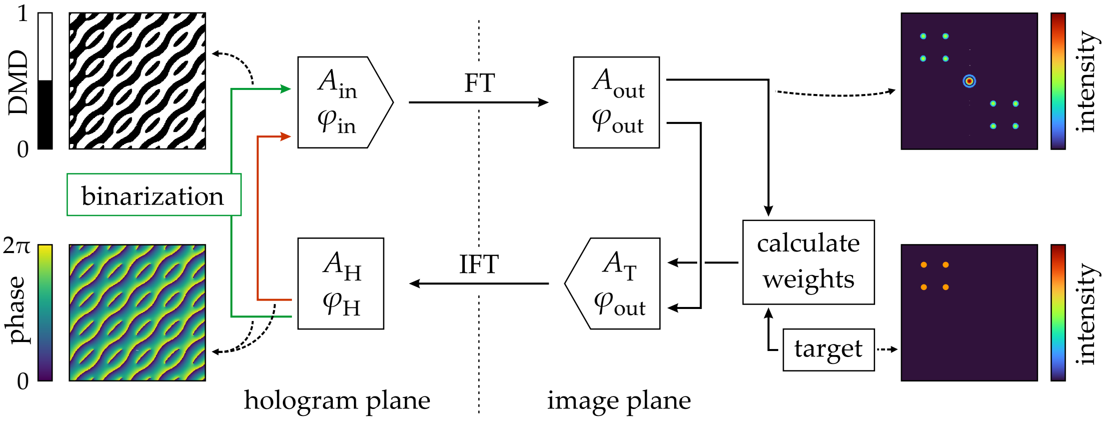

Figure 4.7: Schematic of a weighted Gerchberg-Saxton algorithm, which is one representative of iterative phase retrieval algorithms. The algorithm starts at the top left with an input amplitude A_{in} and phase φ_{in}, of which the phase can be random, and the amplitude resembles the experimental conditions. Following a Fourier transform (FT) to the image plane, the amplitude A_{out} is compared with the target amplitude A_{T}, and weight factors are set accordingly. The phase φ_{out} is kept. An inverse Fourier transform (IFT) back to the hologram plane follows. The phase φ_{H} at this plane corresponds to the holographic pattern. In one implementation, following the red arrow, the phase is always guided through, and binarization to amplitude holograms is performed outside the loop [184]. In another implementation, following the green arrow, a binarization step to obtain binary amplitude holograms is performed within the loop [183, 188].

been used to design multi-focus arrays primarily used for alignment and evaluation purposes of the experimental setup, as, e.g., shown in sections 5.1.5 and 6.2.4. When calculating the holograms for printing 3D structures, not only the quality of the holographic pattern, but also the computational time is of concern. The 3D structures to be printed consist of up to 10^5 holograms, which must be calculated before printing. Conveniently, structures with the most distinct exposure steps are consequently printed using the fewest foci in parallel. This gets down to one focus in a single-focus mode, mimicking conventional single-focus scanning. In this case, the holographic pattern is again a phase ramp, deflecting this one spot as introduced at the beginning of this section. For a small number of foci per pattern, the iterative refinement is not essential to achieve sufficient focus uniformity. This is especially the case for, already slightly, non-periodic arrangements of multiple foci [185], which is the dominant situation for the multi-focus prints performed. The number of iterations can therefore be drastically reduced to a direct calculation, as schematically shown in Figure 4.8. This approach essentially yields the same quality of the focus patterns as the calculation presented in section 4.3.1. In fact, the inverse Fourier transform performed with discrete spots, therefore delta-function-like targets, yields a superposition of phase ramps as previously

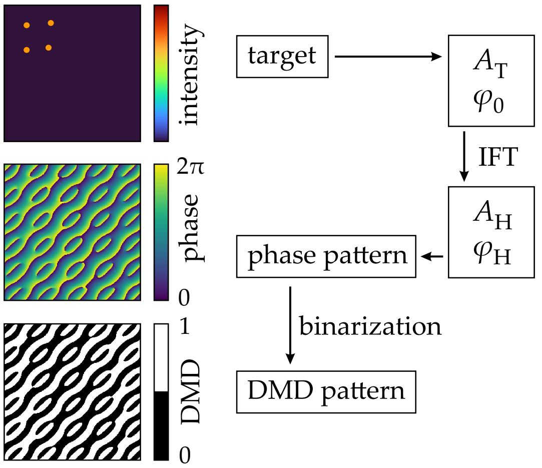

Figure 4.8: Schematic of a simplified hologram calculation routine. Starting from the target amplitude A_T, an inverse Fourier transform (IFT) is performed to get the phase hologram φ_H, which can be further binarized to an amplitude hologram afterward. This approach is computationally less expensive compared to an iterative one, but at the expense of focus uniformity and diffraction efficiency.

introduced. However, it should be noted that the IFT-based calculation restricts the addressable focus positions to the grid discretization in the image plane. Still, this direct calculation approach is used for most of the 3D printing experiments in this work, since it is conveniently implemented alongside the iterative calculation. Optimized calculation approaches better adapted to specific needs, whether to reduce computational time or improve focus uniformity, could be implemented in the future.

4.3.3 *Discretization to Binary Amplitude Holograms*

This general description holds true for calculating phase holograms, which can be displayed on LC-SLMs, PLMs, or transferred to a height profile and manufactured as DOEs. Using a DMD, a binary amplitude modulation has to be applied. To do so, the phase modulation needs to be encoded into a binary amplitude pattern. This can be done within the iterative GS algorithm, where a binarization step can be introduced, as indicated via the green arrow path in Figure 4.7. Alternatively, the transformation of a phase hologram to an amplitude hologram can be done after the calculation of the phase hologram is finalized. To do so, the phase hologram is transformed to a binary amplitude hologram by calculating [153]

$$H(x_H, y_H) = \frac{1}{2} + \frac{1}{2}\,\mathrm{sign}\left(\cos\left(\frac{2\pi}{\lambda f}(x_H \Delta x + y_H \Delta y) + \varphi_H(x_H, y_H)\right)\right). \tag{4.7}$$

This binarization is often referred to as the Lee hologram encoding [80, 153, 189]. Spatial coordinates x_H and y_H refer to the hologram plane, such that $\varphi_H(x, y)$ is the phase hologram to be displayed. Δx and Δy add lateral shifts in the image plane and therefore deflect the generated pattern off-center as the optical axis is obstructed by a large zeroth-order contribution. This can, however, also be accomplished by designing the target amplitude distribution to be off-center, such that the

additional phase ramp can be ignored in this case. The sign-function outputs either $+1$ or -1, depending on its argument being either positive or negative. Therefore, the final binary amplitude hologram $H(x_\mathrm{H}, y_\mathrm{H})$ can only take values of either 1 or 0, translating to the micromirrors being either in the "on" or "off" state.
Coming along with binary amplitude holography is a limited diffraction efficiency and, therefore, laser power efficiency of the entire 3D printing approach. For a binary amplitude grating of 50 % duty cycle, a maximum of $1/\pi^2 \approx 10.1\,\%$ of the incident laser power is diffracted into the, e.g., $+1^\mathrm{st}$ diffraction order [171, 189, 190]. To set this into comparison to phase holography: There, a binary phase hologram already allows for $4/\pi^2 \approx 40.5\,\%$ power efficiency. For multi-level phase holograms, this theoretical efficiency quickly rises and approaches 98.7 % for a 16-level phase hologram [170]. Clearly, applying binary amplitude holograms drastically limits the laser power efficiency. However, this limitation was already taken into account in the discussion about beam splitting and beam steering approaches outlined in section 4.2.

The methodology described in this chapter aimed at setting the framework for the experimental setup design and setup evaluation, which will be explained in the upcoming two chapters in more detail. In chapter 5, a first version of the setup based on commercially available DMDs and therefore binary amplitude holography is presented. Following this, chapter 6 discusses a second version of a 3D printing setup using micromirror-based phase-only modulators and their adaptation for 2SA 3D laser nanoprinting.

Chapter 5

5

A DMD-BASED SETUP FOR DYNAMIC MULTI-FOCUS 2SA 3D LASER PRINTING

With the framework of parallelizing one-color two-step-absorption 3D laser nanoprinting set, this chapter will discuss the experimental implementation of the aforementioned approach. In doing so, I will present the development rationale and the experimental realization of the 3D printing setup. This primarily covers the peculiarities in trying to perform holographic beam-splitting and beam-steering using digital micromirror devices for 3D printing. The printing performance is benchmarked by printing several test structures. This is followed by a section on spatiotemporal proximity effects, the consideration of which is important to optimize 2SA 3D printing results, and which is an application where the presented approach provided further understanding of the 2SA 3D printing process. The results presented in this chapter were already published in [96].

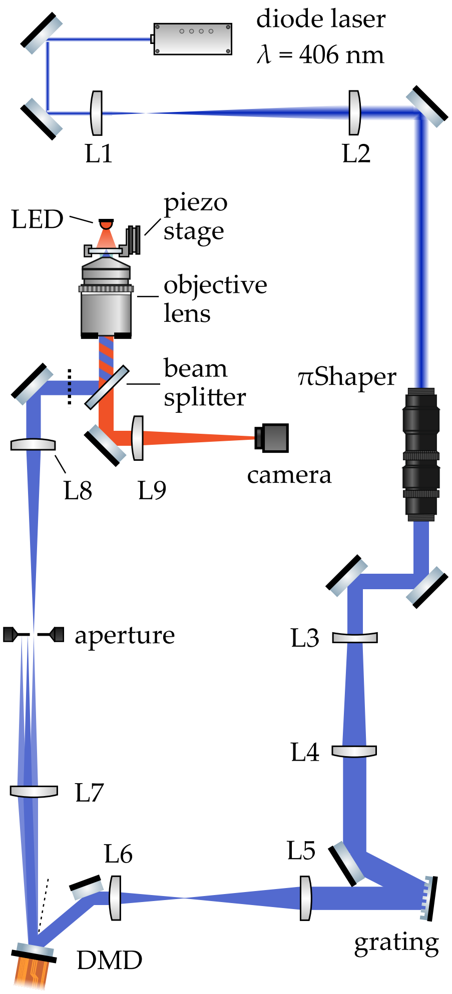

Figure 5.1: Scheme of the optical setup built for parallelized one-color two-step-absorption 3D laser nanoprinting. The light emitted from a diode laser (Toptica IBeam smart) is expanded to fill the entrance pupil of a refractive beam homogenizer (AdlOptica πShaper 6-6). From there, the laser beam is further expanded towards a diffraction grating, incorporated into the beam path to pre-compensate angular dispersion effects introduced by the DMD. The beam is then imaged to a DMD (Texas Instruments DLP4500) onto which computer-generated holograms are displayed. In the focal plane of lens L7, the desired multi-focus distribution is generated alongside a zeroth order, which is blocked by an aperture. The focus distribution is imaged and demagnified to the print plane via lens L8 and a microscope objective lens (Leica 100× / NA1.4-0.7). The dashed line indicates a coordinate system flip. Beam splitting and steering are solely done via the DMD in a holographic configuration. Slicing of the print is performed via a piezoelectric stage (PI Q-545.140). For in-situ monitoring of the printing process, the sample is illuminated by a red-light LED and imaged to a camera sensor. The scheme is not to scale and adapted from [96] under CC BY 4.0.

5.1 THE DESIGN OF THE 3D PRINTING SETUP

Based on the discussion held and the conclusions drawn from it in the preceding chapter, a setup was constructed from scratch, with a DMD in a holographic configuration serving as the core component. In the following, the optical beam path, the experimental evaluation, and the software implementation are explained.

5.1.1 *Components of the Setup*

In Figure 5.1, a schematic of the optical setup is shown. As a laser source, a compact diode laser with a maximum output power of 400 mW is used (Toptica IBeam smart 405). The laser beam emitted is circular and collimated at a beam diameter of $d_{1/e^2} = 1.25\,\mathrm{mm}$. While the center wavelength is at $\lambda = 406\,\mathrm{nm}$ at medium

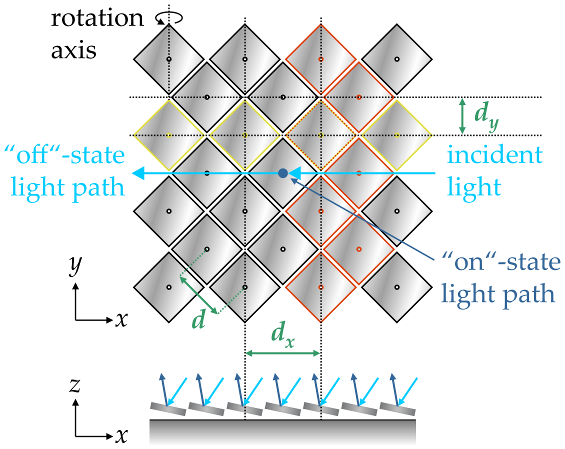

Figure 5.2: Schematic of the pixel layout of the DMD. Square pixels of $d = 7.6\,\mu\text{m}$ pixel pitch are rotated around their diagonal by ±12°. Via the red and yellow framed micromirrors, the addressing of rows and columns is indicated. Therefore, the effective pixel pitch in the x and y directions is different. In the shown configuration, the "on"-state light would leave the paper plane along its normal. This pixel layout is often referred to as "diamond" layout [158]. Figure adapted from [192] (© 2022 Optica Publishing Group).

output powers, it is not stabilized and changes depending on the output power. The spectral width of the emitted light is around $\Delta\lambda_{\text{FWHM}} = 1\,\text{nm}$.

The laser beam is expanded via a telescope consisting of two achromatic doublet lenses ($f_{\text{L1}} = 45\,\text{mm}$, $f_{\text{L2}} = 200\,\text{mm}$) to fill the entrance pupil of a πShaper (AdlOptica πShaper 6-6 VIS). This refractive device transforms a laser beam with a Gaussian intensity profile at the input into a uniform, flat-top beam at the output, while maintaining its circular shape with high power efficiency [191]. The πShaper is incorporated into the beam path to ease the hologram calculation using a uniform illumination profile [187] and to increase the power efficiency without losing power from the outskirts of a Gaussian intensity profile.

Following the πShaper, the beam is further expanded by a Galilean telescope consisting of lenses L3 ($f_{\text{L3}} = -150\,\text{mm}$) and L4 ($f_{\text{L4}} = 200\,\text{mm}$). It should be noted that for the best uniformity of the laser beam, the πShaper's output should be $4f$-imaged via a Keplerian telescope, which is not done here due to size restrictions. The distances are, however, kept short to largely maintain the uniform beam profile.

Next, a blazed diffraction grating (Edmund Optics #48-460, $600\,\text{grooves}\,\text{mm}^{-1}$, 400 nm blaze wavelength) is placed in the beam path to pre-compensate angular dispersion effects introduced by the pixelated surface of the DMD in combination with the finite spectral width of the laser source. To accomplish this, the focal lengths of the lenses L5 ($f_{\text{L5}} = 150\,\text{mm}$) and L6 ($f_{\text{L6}} = 80\,\text{mm}$) have to be matched to the diffractive properties of the grating and the DMD. A more detailed explanation will be given in section 5.1.3.

The telescope, consisting of L5 and L6, further demagnifies the laser beam to prevent overillumination of the DMD's active area. The DMD chip (Texas Instruments DLP4500) consists of 912×1140 pixels arranged in an array of $d = 7.6\,\mu\text{m}$ pixel pitch. Due to the hologram being designed as quadratic, only 912×912 pixels are used. The array of square pixels is arranged such that its edges are 45° rotated with respect to an axis parallel to the optical table. An illustration of the DMD's so-called "diamond" pixel layout is shown in Figure 5.2. Each individual micromirror rotates $+12^\circ$ or -12° around the shown rotation axis to address the "on" or "off" state. Due to the special addressing of rows and columns, as illustrate in Figure 5.2, the pixel pitches in x- and y-direction are different and calculate to $d_x = d \cdot \sqrt{2} = 10.8\,\mu\text{m}$ and $d_y = d/\sqrt{2} = 5.4\,\mu\text{m}$. Therefore, the side lengths of the DMD's active area are calculated to $l_x = 912 \cdot d_x = 9.85\,\text{mm}$ and $l_y = 912 \cdot d_y = 4.92\,\text{mm}$. The DMD chip is mounted on an evaluation module (EKB E4500MKII). Due to the small pixel size, the DMD acts as a 2D blazed diffraction grating, independent of the pattern displayed on the device. Therefore, the incident and diffraction angles are chosen such that the diffraction efficiency is maximized. Further details are given in the dedicated section 5.1.2 below.

From the DMD onward, the optical beam path is further illustrated in Figure 5.3. There, cross-sectional intensity plots are shown as a result of Fourier-optical simulations. In panel a, the intensity at a plane right after the DMD is shown, with the DMD's active area highlighted by a white rectangle. The DMD displays a binary holographic pattern generating a focus distribution of 10 foci, which is multiplied by the incident wave. Due to the different incident and diffraction angles, the intensity pattern is elliptical from the DMD onward. It should be noted that the blaze angle of the DMD's micromirror array and the particular "diamond" layout are, however, not taken into account. The ellipticity is therefore just added to the illumination profile. In the focal plane of lens L7 ($f_{\text{L7}} = 125\,\text{mm}$), the Fourier transform of the wave leaving the DMD is generated and shown in Figure 5.3b. On the optical axis, a strong zeroth-order contribution is apparent. Left and right, the $+1^{\text{st}}$ and -1^{st} orders are shown carrying the designed focus pattern of 10 foci as an example. For better visibility, each focus as well as the zeroth order is displayed 5× magnified. Since only one of the first diffraction orders can be used for multi-focus, random-access beam scanning, a rectangular aperture is placed in this plane, transmitting only the area indicated by the white rectangle. This area is finally imaged and demagnified via lens L8 ($f_{\text{L8}} = 150\,\text{mm}$) and the objective lens (Leica HCX PL APO 100×/1.4-0.7 Oil CS) to the print plane. In between these planes, at the entrance pupil of the objective lens, a spatially filtered image of the beam at the DMD is generated. This is shown in Figure 5.3c alongside a white circle illustrating the objective lens' entrance pupil of 5.6 mm diameter. In the print plane (Figure 5.3), the area transmitted through the rectangular aperture is demagnified by a factor of 75 and again indicated by a white rectangle.

Beam splitting and beam scanning are performed solely in a holographic configuration using the DMD. The slicing of the structure in this setup is performed by moving the sample using a piezoelectric inertia stage (PI Q545.140). Scanning

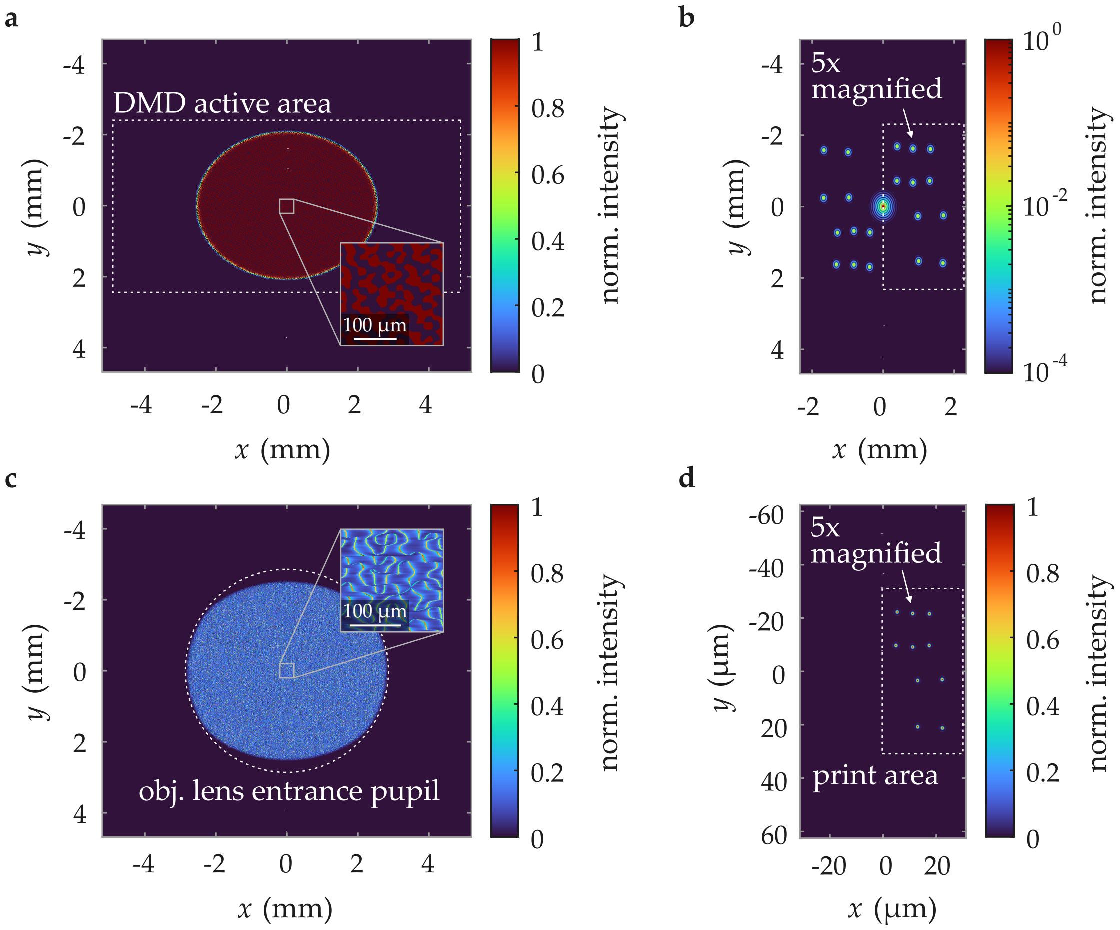

Figure 5.3: Simulated intensity profiles at different planes of the 3D laser printing setup. **a** At a plane right after the DMD, the binary hologram is multiplied with the uniform illumination profile. The DMD's active area is indicated via the dashed rectangle. **b** In the focal plane of lens L7, the Fourier transform of the holographic pattern is generated. This is a designed focus distribution of 10 foci, which repeats left and right a zeroth order in the center. Only the -1^{st} order is transmitted through a rectangular aperture. For better visibility, all foci are drawn 5× magnified. **c** At the entrance pupil of the objective lens (indicated via the dashed circle), the spatially filtered hologram displayed on the DMD is visible. **d** In the print plane, the Fourier transform of the spatially filtered hologram is generated. This is consistent with the imaging of the focus pattern transmitted through the aperture, as shown in panel b. Adapted from [96] under CC BY 4.0.

the focus in axial direction via the holograms is possible and has already been introduced in section 4.3, but is not incorporated in this first setup version, as additional effort for optimizing the defocus phase is necessary. Nonetheless, I will come back to this in a second version of the setup, as explained in chapter 6. Coarse lateral movement of the sample is done via two linear screw-drive stages (Aerotech ATS50).

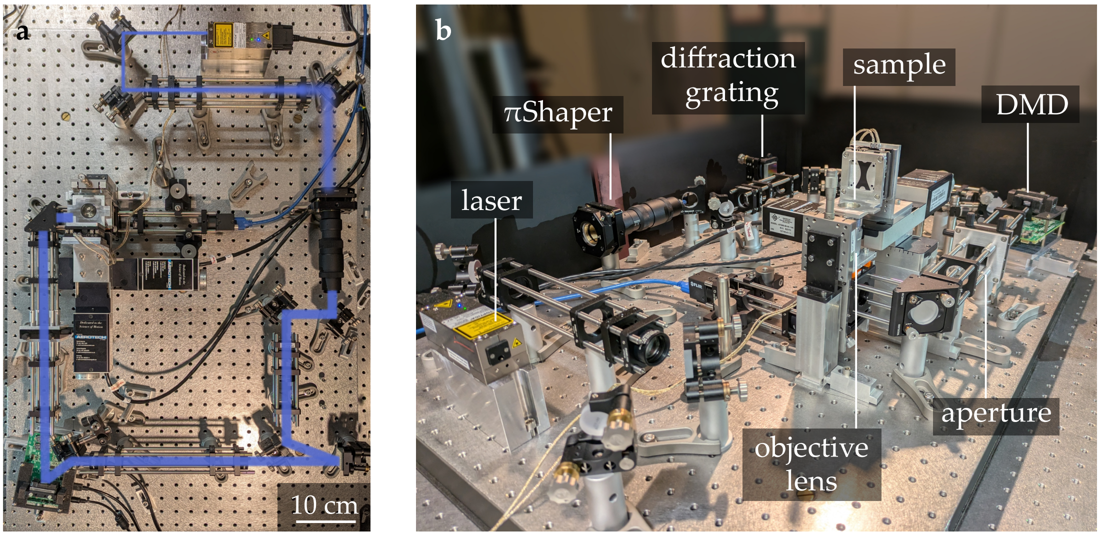

Figure 5.4: Photographs of the 3D laser printing setup. a Top-down view including a schematically overlaid laser beam path, corresponding to the drawing shown in Figure 5.1. **b** Angled view with all main components labeled.

For in-situ monitoring of the printing, the sample is illuminated by a red-light LED (Thorlabs M625L4) and imaged via the objective lens and lens L9 ($f_{\mathrm{L9}} = 150\,\mathrm{mm}$) onto a CMOS camera sensor (FLIR BFS-U3-50S5M-C). For separating the laser and the camera beam path, a dichroic mirror (Thorlabs DMLP505) is introduced. The printing is solely performed in an oil-immersion configuration. Interface finding is done by monitoring the reflection off the sample on the camera.

In Figure 5.4, photographs of the home-built 3D laser printing setup are shown. In the top-down view, as depicted in panel a, the laser beam path is schematically highlighted via a blue overlay. Panel b shows an angled view with all main components labeled.

5.1.2 Diffractive Properties of the DMD

Using DMDs in a holographic configuration, there are two overlaid diffraction gratings: one is the designed holographic pattern, e.g., for generating an array of foci. Second, since the DMD consists of a large number of separate micromirrors, the diffraction properties of the DMD itself must be taken into account. This requires the angular dispersion compensation and poses limitations to the power efficiency.

In Figure 5.5, the DMD is schematically shown as a 1D blazed grating to illustrate the relevant angles. In the "on" state, the micromirrors are tilted by $\gamma = +12^\circ$ with

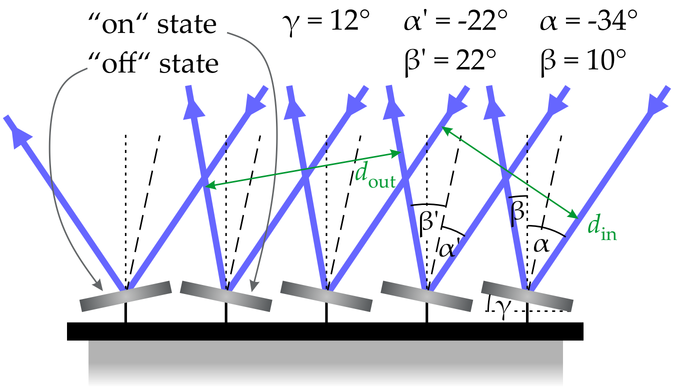

Figure 5.5: Scheme showing the DMD as a 1D blazed grating. The angles of the incident and diffracted light fulfill the blazing condition. Therefore, the diffraction angle, which fulfills the grating equation, matches the specular reflected light of each micromirror for the "on" state pixels. Adapted from [96] under CC BY 4.0.

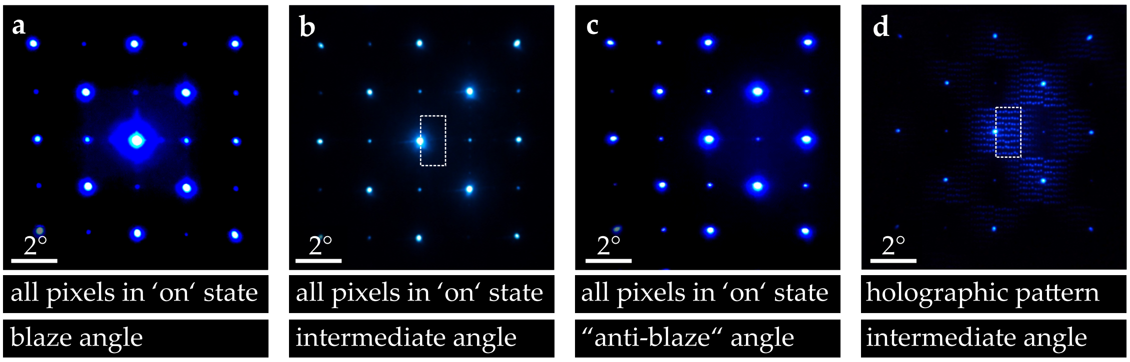

all pixels in ‘on‘ state
blaze angle

all pixels in ‘on‘ state
intermediate angle

all pixels in ‘on‘ state
“anti-blaze“ angle

holographic pattern
intermediate angle

Figure 5.6: Diffraction patterns at different incident angles and displayed images. The light reflected off the DMD is focused onto a screen and photographed. **a-c** All pixels are in the "on" state. The incident angle is varied from a blazed to an anti-blazed configuration, as well as a setting in between, as in the printing setup. **d** When displaying a hologram, the intensity peak is centered around the holographic pattern. The dashed rectangle indicates the area that would be transmitted through the rectangular aperture. Adapted from [96] under CC BY 4.0.

respect to the DMD plane. In the configuration shown, the blazing condition is fulfilled for a diffraction order of $m = -5$. This should not be confused with the first diffraction order of the holographic pattern. The blazing condition is fulfilled since the specular reflection at the individual micromirrors ($\alpha' = -\beta'$) matches a diffraction angle resulting from the grating equation ($m\lambda = \frac{d_x}{2}(\sin\alpha + \sin\beta)$). This causes an envelope function to be centered at a diffraction order m, maximizing its intensity and decreasing the intensity of the other diffraction orders. Therefore, the power efficiency drastically decreases if the blazing condition is not fulfilled, and the experimental choice of the angles is very limited.

The micromirrors only rotate along one axis. It is therefore sufficient to address the diffractive properties in a 1D scheme. But the DMD is still a 2D diffraction grating, although the blazing condition in the orthogonal direction is fulfilled for the trivial case of normal incidence. Different 2D diffraction patterns at varying incident angles α are shown in Figure 5.6. In panels a-c, all the pixels of the DMD are in the "on" state. Photographs were taken when focusing the light reflected off the DMD onto a screen via a lens of $f = 200\,\mathrm{mm}$. Therefore, the experimental configuration was slightly different from the actual printing setup, and the photographs serve primarily for visualization purposes. In panel a, the blazing condition is fulfilled, with an intensity envelope centered at the middle diffraction order. Changing the incident angle by around 2°, the envelope shifts in between two diffraction orders (panel b). When the incident angle is further changed, the anti-blaze condition is met with four diffraction orders of equal intensity. In fact, for the printing setup, fulfilling the blazing condition is not the best case, since the envelope would be centered on the hologram's zeroth order. The angle is therefore slightly changed, as shown in 5.6b and d. There, the area that would be transmitted through the rectangular aperture is indicated via a dashed rectangle, and the angles are chosen such that the diffraction envelope's maximum is in the center of the print area.

When fulfilling these criteria, the DMD's diffraction still causes two drawbacks: due to the diffraction envelope, the intensity of the foci changes depending on their location in the print area. This, however, can be corrected for via the holographic pattern. Since the diffraction envelope spans several diffraction orders, as can be seen in Figure 5.6d, where the focus pattern repeats multiple times, the laser power efficiency still decreases. The total device efficiency (including absorption losses) is measured as 38 %.

5.1.3 *Angular Dispersion Compensation*

In Figure 5.7, measurements are shown of the focus shape with and without the compensation grating (see Figure 5.1), clearly indicating the necessity as well as the success of angular dispersion compensation. These measurements were taken at an output power of 100 mW from the laser, achieved by focusing the laser beam onto a CMOS sensor located in the focal plane of lens L7. While panel a shows the compensated configuration, panels b and c show a distorted focus when either the diffraction grating or the DMD is replaced by a mirror. In doing so, either a positive or negative angular dispersion is introduced. The spatially separated maxima in Figure 5.7b and c resemble the spectral emission profile of the laser source.

To compensate for the angular dispersion, the properties of the grating as well as the focal lengths of lenses L5 and L6 have to be matched to the diffractive properties of the DMD. Following the derivation outlined in Ref. [193], the grating equation

$$m\lambda = d(\sin\alpha + \sin\beta) \tag{5.1}$$

is differentiated to get the angular dispersion

$$\partial\beta/\partial\lambda = \frac{m}{d\cos\beta}. \tag{5.2}$$

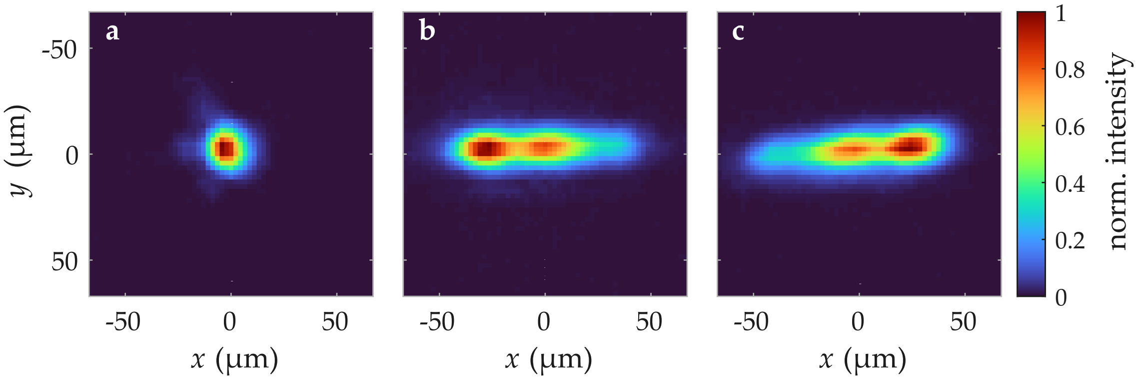

Figure 5.7: Images of a single focus with and without the angular dispersion compensating grating. The images are taken by focusing the laser beam onto a camera located at a plane conjugate to the rectangular aperture. All pixels of the DMD are set to the "on" state. **a** The blazed grating and the DMD are included in the beam path. **b** The DMD is included in the beam path, while the blazed grating is replaced by a mirror. **c** Vice versa, the blazed grating is included in the beam path, while a mirror replaces the DMD. Adapted from [96] under CC BY 4.0.

In these equations, m refers to the diffraction order, d to the grating period, and α and β to the incident and diffraction angles as shown in Figure 5.5. To compensate for the angular dispersion of the DMD, an intentional angular dispersion of $\Delta_\mathrm{D} = m_\mathrm{D}/(d_\mathrm{D}\cos\alpha_\mathrm{D})$ has to be incident onto the DMD. This has to be provided by the angular dispersion of the grating: $\Delta_\mathrm{G} = m_\mathrm{G}/(d_\mathrm{G}\cos\beta_\mathrm{G})$. Here, the specific angular dispersion values are written as Δ_i, where subscript D refers to the DMD, while subscript G refers to parameters of the grating. To ease the matching, the angular dispersion of the grating can be (de-)magnified by carefully choosing the focal lengths of lenses L5 and L6. When further assuming small angular dispersion values, this reads as

$$\Delta_\mathrm{G}\frac{f_\mathrm{L5}}{f_\mathrm{L6}} = \Delta_\mathrm{D}. \tag{5.3}$$

The parameters to be considered are as follows: For the grating, the period is $d_\mathrm{G} = 1.67\,\mu\mathrm{m}$, the diffraction order is $m_\mathrm{G} = 1$, and the diffraction angle is set to $\beta_\mathrm{G} \approx 14°$. For the DMD, the respective parameters are: $d_\mathrm{D} = 5.4\,\mu\mathrm{m}$, $m_\mathrm{D} = -5$, $\alpha_\mathrm{D} \approx -34°$. Considering these parameters, the focal lengths relaying the two diffractive components should fulfill $f_\mathrm{L6} = 0.55 \cdot f_\mathrm{L5}$. Therefore, the lenses are chosen such that $f_\mathrm{L5} = 150\,\mathrm{mm}$ and $f_\mathrm{L6} = 80\,\mathrm{mm}$, which approximates the desired ratio at $f_\mathrm{L6}/f_\mathrm{L5} = 0.53$.

5.1.4 Design Parameters and Power Efficiency

Several design parameters and the restrictions they imply have already been addressed. These include the angular orientation of the DMD to maximize the power efficiency, as well as the choice of the diffraction grating and adjacent lenses to minimize the angular dispersion. These and other parameters are linked to each other, such that they cannot be chosen independently, and trade-offs are necessary.

If a particular grating is chosen, the choice of which is limited to common grating constants like $600\,\mathrm{grooves\,mm^{-1}}$ in the present case, the power efficiency constrains the angular placement. Therefore, the diffraction order and the incident and diffraction angles should be kept small. The associated angular dispersion is then rather small and has to be magnified by the lenses L5 and L6, as stated above. This demagnifies the beam diameter from the grating to the DMD by a factor of almost two. At the DMD, the laser beam should neither overfill nor largely underfill the active area. Therefore, the beam is already expanded in front of the grating only to accommodate the following demagnification. Leaving the πShaper with 6 mm beam diameter, this gets magnified to 8 mm at the grating and again demagnified to around 4.3 mm at the DMD. Due to the non-equal incident and diffraction angles of the grating as well as the DMD, the laser beam leaving the DMD is elliptical, such that the beam size is 4.3 mm in y- and 5.4 mm in x-direction.
The choice of the lenses L7, L8, and the objective lens again needs to fulfill several criteria. As the objective lens, a high-NA, high-magnification microscope objective lens is chosen to make use of the resolution advantage 2SA 3D laser printing at 405 nm wavelength has over commercial 2PP at around 790 nm. With the chosen lens, the entrance pupil of the objective lens is restricted to 5.6 mm. This constrains the magnification between the DMD and the objective lens to fully illuminate, but not overilluminate, the objective lens's entrance pupil.

Furthermore, the choice of the DMD in combination with the optics afterward defines the maximum scan range and the minimum step size achievable in the holographic configuration. With the pixel pitches of the DMD of $d_{\mathrm{D},x} = 10.8\,\mu\mathrm{m}$ and $d_{\mathrm{D},y} = 5.4\,\mu\mathrm{m}$, the derivation again starts with the grating equation $m\lambda = d(\sin\alpha + \sin\beta)$. Since this discussion, which is similar to the one outlined in [194], can be separated from the diffractive properties of the DMD array itself, normal incidence is assumed ($\alpha = 0$). Diffraction angles β are with respect to the optical axis leaving the DMD. The small, but finite angle of the DMD placement with respect to this axis of around 10° is further neglected. In the focal plane of lens L7, the spatial separation x of the beam to the optical axis is $x = f_{\mathrm{L7}} \tan\beta$. Combining this with the grating equation leads to

$$x = f_{\mathrm{L7}} \tan\left(\arcsin\left(\frac{m\lambda}{d}\right)\right). \tag{5.4}$$

Assuming small angles β, this simply approximates to

$$x \approx f_{\mathrm{L7}} \frac{m\lambda}{d}. \tag{5.5}$$

For the holographic pattern, $m = \pm 1$, where $m = 1$ is chosen for simplicity. The minimum grating period, corresponding to the maximum diffraction angle and therefore the maximum scan range, is $d_{\mathrm{min}} = 2d_{\mathrm{D},i}$, for either the x- or y-direction. This corresponds to a pattern of adjacent "black" and "white" pixels. The maximum scan range in the focal plane of lens L7, therefore, reads as

$$x_{\mathrm{max}} \approx f_{\mathrm{L7}} \frac{\lambda}{2\, d_{\mathrm{D},x}} \quad \text{and} \quad y_{\mathrm{max}} \approx f_{\mathrm{L7}} \frac{\lambda}{2\, d_{\mathrm{D},y}}. \tag{5.6}$$

As the maximum scan range in the print plane is of main interest, the demagnification of lens L8 and the objective lens (with effective focal length $f_{\mathrm{obj}} = 2\,\mathrm{mm}$) has to be considered, leading to

$$x_{\mathrm{max}} \approx \frac{f_{\mathrm{L7}} f_{\mathrm{obj}}}{f_{\mathrm{L8}}} \frac{\lambda}{2\, d_{\mathrm{D},x}} \quad \text{and} \quad y_{\mathrm{max}} \approx \frac{f_{\mathrm{L7}} f_{\mathrm{obj}}}{f_{\mathrm{L8}}} \frac{\lambda}{2\, d_{\mathrm{D},y}}. \tag{5.7}$$

Another question is about the step size in the print plane, i.e., the minimum distance between two foci as controlled by the holographic pattern. In 3D laser printing, this parameter, mainly for neighboring lines, is commonly referred to as "hatching". Therefore, the minimum step size should be in the range of typical hatching parameters to be able to print connected instead of dashed line patterns. For the optics used, values of 100 nm are targeted [24, 41]. Following the discussion on the hologram calculation and for the present computational implementation, as explained in section 4.3, a computation via a Fourier transform is implemented. This, however, limits the number of addressable locations along each lateral direction in the Fourier plane to the same number of $n = 912$, as of the DMD used. The maximum scan range can be distributed into equally spaced steps such that the step size Δx reads as [194]

$$\Delta x \approx \frac{f_{\mathrm{L7}} f_{\mathrm{obj}}}{f_{\mathrm{L8}}} \frac{\lambda}{n\, d_{\mathrm{D},x}} \quad \text{and} \quad \Delta y \approx \frac{f_{\mathrm{L7}} f_{\mathrm{obj}}}{f_{\mathrm{L8}}} \frac{\lambda}{n\, d_{\mathrm{D},y}}. \tag{5.8}$$

Suppose finer lateral shifts of the focus distribution are needed. In that case, they are possible by adjusting the lateral shifts Δx and Δy of equation 4.7, with the limitation of changing the grating period by only one pixel.

Taking the above-stated formulas, the focus deflection parameters in the print plane can be calculated. With the focal lengths as used in the experiment, this leads to total accessible print field of $2x_{\mathrm{max}} = 62.5\,\mu\mathrm{m}$ and $2y_{\mathrm{max}} = 125\,\mu\mathrm{m}$ and minimum step sizes of $\Delta x = 68.5\,\mathrm{nm}$ and $\Delta y = 137\,\mathrm{nm}$. For the total accessible print field,

the maximum scan range is doubled since positive and negative directions can be addressed. However, only part of this is usable for a random-access focus scanning. As already shown in Figure 5.3b, a mirror image of the focus pattern generated as the $+1^{\mathrm{st}}$ order is generated in the -1^{st} order, such that only one of these diffraction orders is used and the other one gets blocked. Furthermore, part of the accessible scanning range in y-direction is obscured by higher diffraction orders generated by the DMD's pixelated surface, as can be seen in Figure 5.6d. Taking all this into account, the used print field is limited to $x_{\max} = 31.25\,\mu\mathrm{m}$ and $y_{\max} = 62.5\,\mu\mathrm{m}$. Structures of larger size can be printed by stitching several print fields together. This can be achieved by either moving the sample or by moving the print field within the field of view of the objective lens. The latter could be implemented, e.g., via motorized mirrors in front of the objective lens. In the presented setup version, however, such measures are not implemented, and all demonstrated structures fit into one print field.
By this derivation, it can be seen that the focal lengths of the lenses L7 and L8 are critical in defining the maximum scan range and the minimum step size. However, they still need to be matched to the constraint of proper imaging of the DMD pattern onto the objective lens entrance pupil. This is largely fulfilled at the chosen focal lengths of $f_{\mathrm{L7}} = 125\,\mathrm{mm}$ and $f_{\mathrm{L8}} = 150\,\mathrm{mm}$, where the circular entrance pupil is slightly overilluminated in x- and slightly underilluminated in y-direction (see Figure 5.3c). Still, a trade-off is made in that the DMD's active area is not fully illuminated, resulting in a slight reduction in the uniformity of the multi-focus patterns.

Another parameter, which of course should be as high as possible, is the laser power efficiency of the setup. In section 4.2, this was already addressed when discussing the different components and approaches chosen. In this paragraph, I want to summarize these parts, as they collectively result in a significant power loss across the beam path. When starting at 100 % out of the laser, the laser power incident on the DMD drops already to 34 %. This is mainly connected to the limited power efficiency of the diffraction grating, which is around 65 %, as well as the number of optical components used. Although the lenses used are anti-reflection coated, a power loss is still noticeable at the used wavelength of 406 nm. The device efficiency of the DMD was already mentioned in section 5.1.2. It comprises the diffraction efficiency, the fill factor, as well as absorption losses, and adds up to 38 %. The main conceptual contribution is the power efficiency of binary amplitude holograms, which can be calculated to be 10.1 % at maximum. All this combined leads to a power efficiency at the entrance pupil of the objective lens of around 1.3 %. Depending on the holographic pattern, this value can change slightly. Measured values of, e.g., a pattern of 64 foci correspond to a power efficiency of 1.1 %. Despite the efforts undertaken, power efficiency remains a clear drawback and conceptual limitation of the chosen approach of binary amplitude holography.

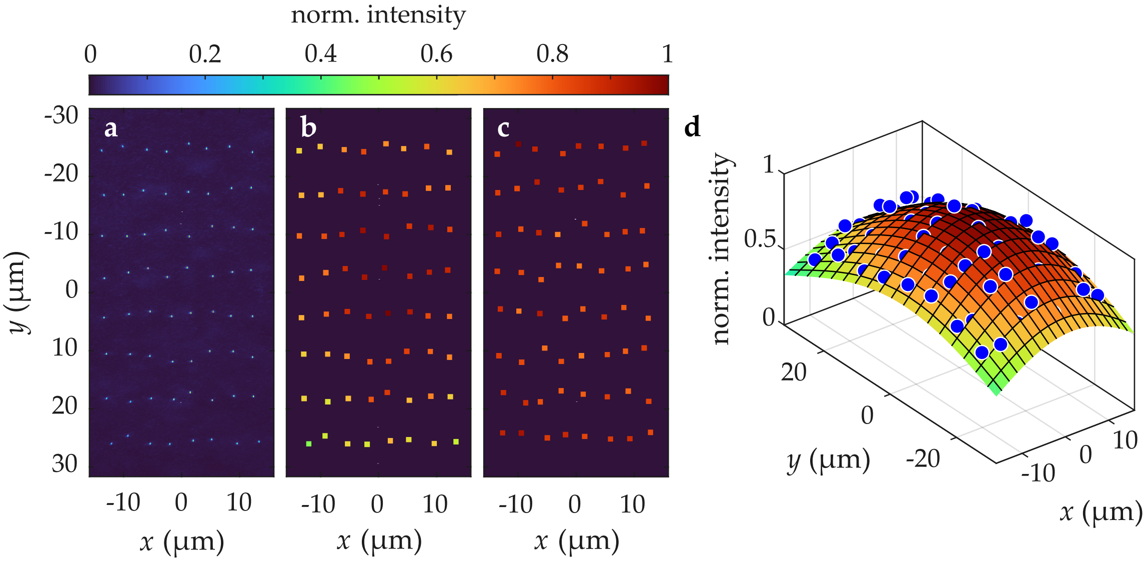

Figure 5.8: Microscopic images for evaluating the focus uniformity across the print field. The data shown in all panels is taken by imaging the reflection of the focus array of a glass-monomer interface at the print plane by the camera as shown in Figure 5.1. **a** False-color plot of the raw data of a focus pattern of 64 foci scattered across the print field. **b** To evaluate the relative optical power of each focus, the intensity values around the center of each focus are summed. A decrease in the summed intensity towards the edges is clearly visible, connected to the diffraction envelope caused by the micromirror array. **c** This can be corrected for by adjusting the amplitude of each focus in the calculation of the hologram. A more uniform focus pattern results. **d** To get the correction values, the data shown in panel b is fitted as a product of sinc-functions. Adapted from [96] under CC BY 4.0.

5.1.5 *Evaluation of the Focus Quality and Focus Uniformity*

In the following, the quality and uniformity of the focus distributions should be assessed experimentally. This was done based on focus patterns consisting of 64 individual foci. These were arranged in an 8 × 8 grid to distribute them evenly across the print field, but the locations are slightly randomized. This helps in continuously evaluating slightly different patterns, so the discussion is not based on a single pattern. Furthermore, non-periodic focus distributions have been shown to ease the calculation by requiring fewer iterations of a weighted GS algorithm or even allowing direct calculations [185].
In Figure 5.8, images are shown which were taken with and at the position of the camera as shown in Figure 5.1. The focus pattern is therefore reflected off the top surface of a glass coverslip, which was covered with the monomer PETA. A small fraction of the reflected light is then transmitted through the dichroic mirror and

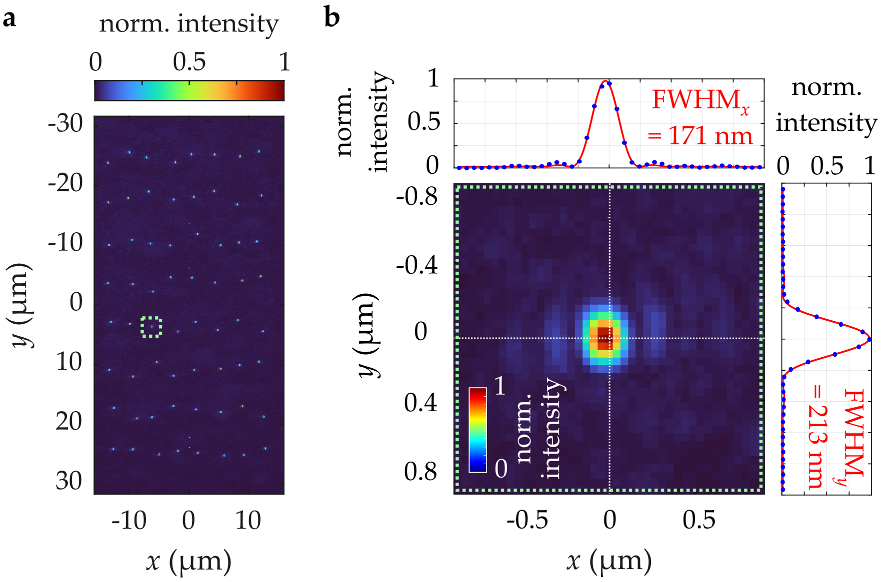

Figure 5.9: Microscopic images for evaluating the focus quality. The data set shown corresponds to the data depicted in Figure 5.8c. **a** Image of an array of 64 foci reflected from the glass-monomer interface at the print plane. **b** Zoom-in to one exemplary focus highlighted by the green rectangle in panel a. Airy functions are fitted to the 1D cuts through the center position, allowing a coarse estimation of the focus quality. The ellipticity of the foci corresponds to the elliptic beam profile at the entrance pupil. Adapted from [96] under CC BY 4.0.

imaged onto the camera, giving a reflection-mode microscopic image of the focus array in the print plane. In Figure 5.1a, the image of the focus array is shown, spanning almost the entire print field. For evaluating the uniformity of the focus array, the center position of each focus was detected, and the intensity values of an area of 24 pixels × 24 pixels around the center were summed up to evaluate the optical power of each focus.

This is shown in Figure 5.8b. Squares are drawn at the position of each individual focus, color-coded with the summed intensity values. While the laser power of the foci is highest in the center of the print field, it drops towards the corners. This can be explained by the diffractive properties of the DMD, as outlined in section 5.1.2. To still achieve a more uniform power distribution across the print field, the non-uniformity can be compensated for via the design of the focus distributions and, therefore, the holographic pattern. In doing so, each focus in the hologram calculation is assigned a different scaling factor, resulting in a different relative amplitude value.

The outcome of this is shown in Figure 5.8c, again following the same measurement and evaluation routine as before. It can be seen that the summed intensity values are more uniformly distributed, with the drop towards the edges of the

print field being removed. Still, some non-uniformity remains, which was found to be linked to the underillumination of the DMD array and to differences between the illumination profile used in the calculation and that present in the experiment. However, the non-uniformity is on an acceptable scale. It was further found to change depending on the pattern. Therefore, it slightly averages during the 3D printing process, where a large number of holograms are displayed.
In Figure 5.8d, the fit procedure of the experimental data to get an analytic expression for the correction map is illustrated. Based on the diffractive properties of the quadratic micromirrors, a product of sinc-functions is fitted to the experimental data. The correction map can then be applied to every target amplitude pattern.

Besides the focus array uniformity, the focus quality of individual foci is evaluated similarly, such that a microscopic image is taken of the foci reflected from the glass-monomer interface. The micrograph of the distribution of 64 foci is depicted in Figure 5.9a. The data shown corresponds to the evaluated focus distribution with the already applied correction map, as shown in Figure 5.8c. A zoom-in to one focus is shown in Figure 5.9b. Intensity values along the white dashed lines through the center of the focus are shown above and to the right of the 2D plot. Airy functions are fitted to these 1D cuts, from which full-width-at-half-maximum (FWHM) values of the central maximum of 171 nm in $x-$ and 213 nm in y-direction are extracted. This ellipticity corresponds to the ellipticity of the illumination at the entrance pupil of the objective lens. It should be noted that for a proper investigation of the point-spread function (PSF) in the print plane, more elaborate methods exist and should be used. These include, e.g., the spatially dependent evaluation of the back-reflected laser light from small gold nanoparticles [35]. However, such a method would require additional equipment integrated into the setup, such as fine lateral translation of the sample. Still, the investigation of images of reflected foci provides helpful guidance for both initial and everyday alignment.

5.1.6 From the 3D Design to the Stack of Holograms

Up to this point, the optics as well as the calculation of the holograms from a target (multi-)focus distribution have been explained. Still missing is the step for splitting and distributing a 3D structure into a set of multi-focus patterns. While being a simple task for an array of equal structures, this can become a non-trivial task when multi-focus printing a single structure or an array of non-periodic structures. This section explains the procedure for getting from a 3D design to the set of holograms needed for printing. For this, the schematic flowchart depicted in Figure 5.10 helps in illustrating the discussion.
It starts with a 3D design, as shown in panel a. The 3D design is sliced into a number of 2D layers, each with a specific slicing distance (panel b). In the

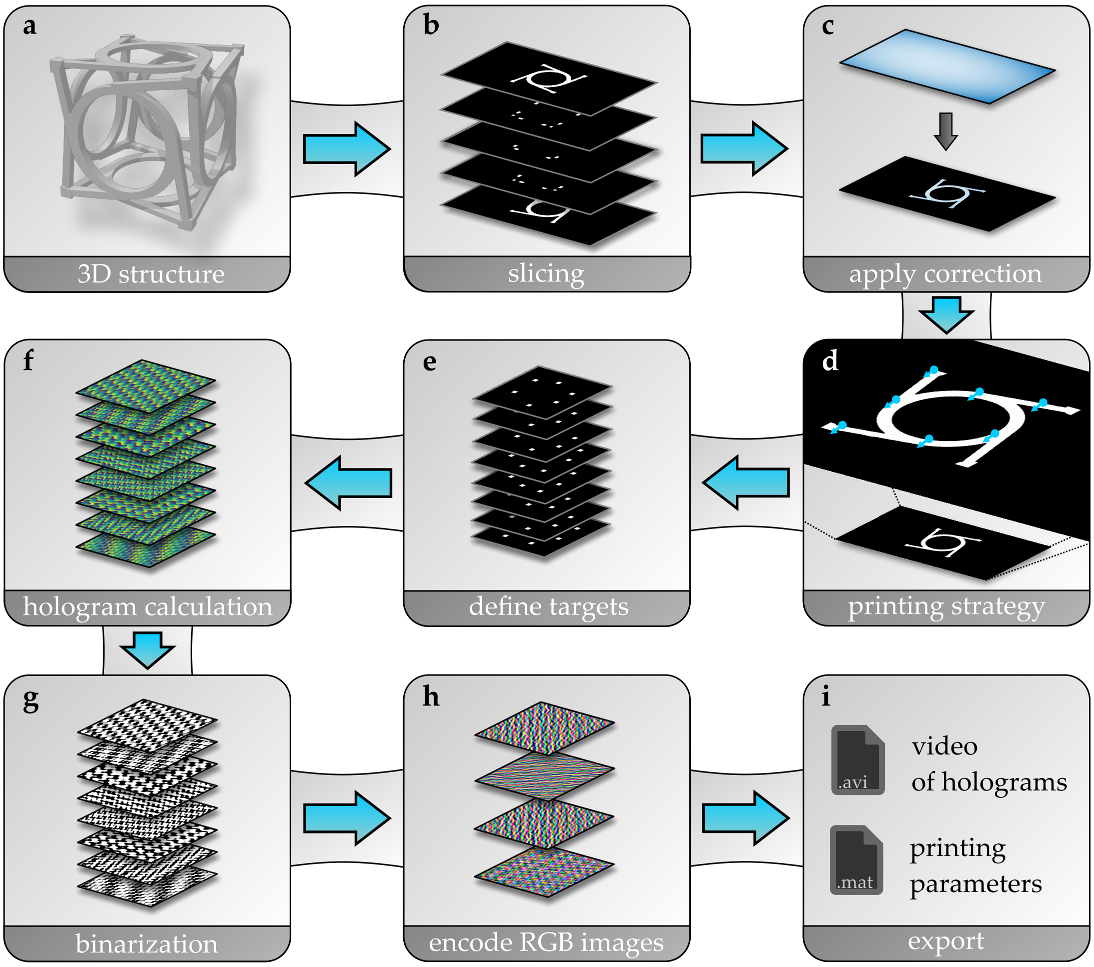

Figure 5.10: Flowchart of the process of calculating a set of holograms starting from a 3D design structure. Taking the 3D design (**a**), it is first sliced into a number of 2D layers (**b**). Following this, the relative optical power of each focus within one plane can be adjusted (**c**) to correct for, e.g., diffraction effects of the DMD. A printing strategy defines how to split a single layer into a series of focus patterns (**d**). These amplitude target arrays (**e**) serve as input to the hologram calculation (**f**). The resulting phase patterns are binarized to binary amplitude holograms (**g**). Finally, the binary patterns are encoded as RGB images (**h**) and exported as a single video file, along with a file containing relevant printing information (**i**). The respective numbers of slices in the different panels is for illustration purposes only and not to scale.

present case, typical slicing distances of 200 nm are chosen. Furthermore, the 2D layers are discretized such that the addressable focus positions are matched to the desired total size. Due to the pixel layout of the specific DMD used, which results in different pixel pitches in the two lateral directions, the addressable focus positions are also unequal distances apart. Therefore, the design appears stretched or compressed in one direction if matched to the addressable focus positions. For

the sake of clarity, this is left away in Figure 5.10.
At this stage, different corrections can be applied to the 2D layers, as indicated in panel c. As previously mentioned, the correction for the diffraction envelope is implied by the DMD's pixelated surface. Further corrections could include a structure-dependent pre-compensation of proximity effects. This is applied to some structures that have been printed and will be explained in the respective section.
Next, each 2D layer is represented as a sum of focus patterns. I will also refer to this as the printing strategy (panel d). For this step of the distribution to focus patterns, certain restrictions apply. First and foremost, the number of foci that can be illuminated simultaneously, assuming a fixed exposure time, is limited by the available laser power. In the shown implementation, this limit is reached at a focus number of around 30. Second, there is the restriction of a minimum distance of simultaneously illuminated foci of a few micrometers [80, 175]. If the focus-to-focus distance is reduced, interference effects begin to appear in the printed structure, reducing printing quality. This, depending on the structure, often reduces the maximum number of foci that can be illuminated simultaneously. Additionally, the temporal sequence is a third parameter defining the printing strategy. In general, the printing strategy comprises each rule that defines the relationship between temporally consecutive exposures. Referring to the printing, e.g., a multi-line scanning can be targeted as well as a totally random sequence. A discussion on the effect different temporal sequences have on the printed structure will follow in section 5.3. Furthermore, the target of only small changes of consecutive holograms could be another such rule, which was, however, not restricted in this work. As a result of the mentioned restrictions, various focus patterns will cover an unequal number of foci per pattern, resulting in changes in the laser power at each focus. While this could be compensated for by synchronously modulating the laser source, the approach of adding foci outside the area transmitted through the rectangular aperture was chosen. Thereby, no additional synchronization effort is necessary.
Panel e illustrates the full set of focus patterns, stacked as a 3D array and input into the hologram calculation as described in section 4.3. The result is a stack of continuous-phase holograms that already match the DMD's discretization, 912 × 912 pixels (panel f). Following this, the holograms are binarized to binary amplitude holograms according to the approach of Lee holograms, again as explained in section 4.3.3. When implementing the binarization within the iterative hologram calculation, the steps of hologram calculation and binarization are combined.
The stack of binary amplitude holograms is finally encoded into 8 bit RGB images and saved as a single video file containing the holograms of the full 3D structure. The reason for this is to ease the data transfer from the computer to the DMD controller board, as explained in more detail in the following section. Alongside the video file, a file containing all printing parameters for the movement of the z-axis stage and the laser control is exported.

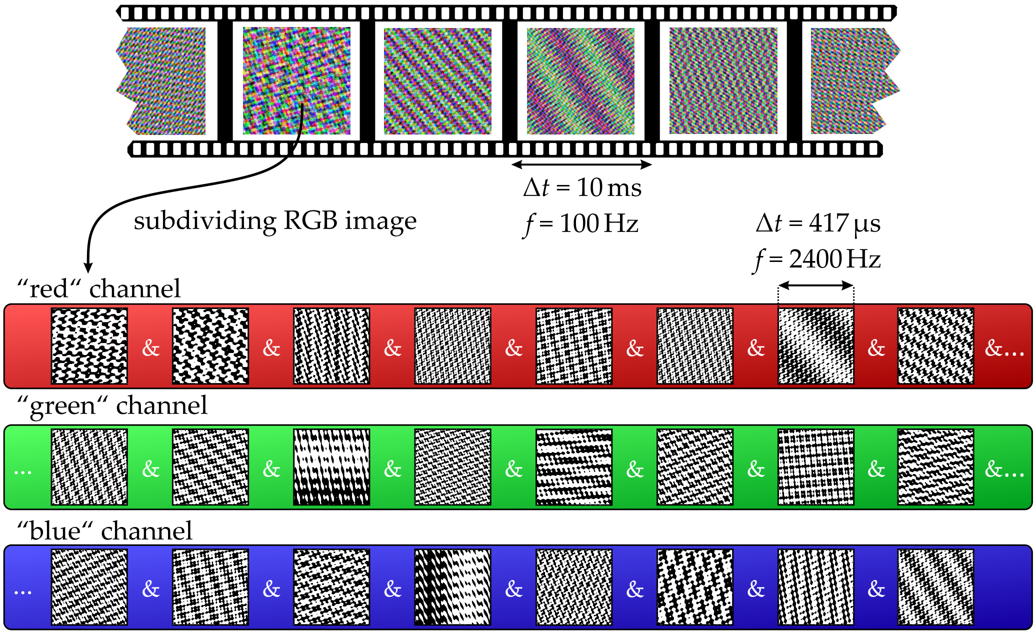

Figure 5.11: Illustration of the data transfer during 3D printing via a video stream. The film roll on top symbolizes the video stream at a frame rate of 100 Hz at maximum. Since each frame transferred is, however, encoded as an 8 bit RGB image, 24 binary holograms can be transferred simultaneously and scheduled sequentially by the DMD controller, which is illustrated at the bottom. Adapted from [96] under CC BY 4.0.

5.1.7 *Electronics and Software*

As already mentioned, the holograms are assembled altogether as a single video file. In doing so, one does not rely on the internal memory of the DMD to store the patterns. This internal memory is very limited for low-cost devices and is not able to reload patterns at the rate of displaying them [168]. High-end DMDs offer larger internal memory and faster reloading [195], but at often significantly higher cost. In the developed approach, I utilize one of the main and widespread use cases of DMDs: streaming a video signal. The hardware and software implementation is therefore not restricted to a specific, costly DMD.

The DMD is connected to a computer via HDMI (High-Definition Multimedia Interface). Therefore, the DMD serves as a second screen for the operating system and is recognized as such. As a standard, frame rates of 60 Hz are often chosen for the display refresh rate. Experimentally, a stable connection at up to 100 Hz could be achieved. At this frame rate of the video signal, the vertical synchronization (VSYNC) signal, which serves as the primary trigger input to the DMD controller, is provided. It should, however, not be confused with the patterning rate of the holograms and therefore with the exposure time of every single hologram and focus. This is higher because between each VSYNC signal, several holograms are transferred to the DMD and displayed sequentially.

This is due to the encoding of 24 binary holograms into a single 24 bit color depth, i.e., an 8 bit RGB (red-green-blue) image. One such image is transferred to the DMD every 10 ms, corresponding to 100 Hz. The DMD controller then unpacks the 24 bit color image and displays a sequence of 1 bit holograms. Each hologram is therefore displayed for 417 µs, corresponding to a patterning rate of 2400 Hz. This decoding approach is schematically illustrated in Figure 5.11.

Using the presented video-stream approach, several pitfalls arise. First, it must be ensured that video playback is pixel-accurate. This is often not the case with consumer electronics, because lossy compression or "image quality enhancement" algorithms alter information at the pixel level. Such algorithms must be disabled at any stage in the video stream pipeline, as the holographic pattern would change in an uncontrolled manner. This further means that the stored and displayed video is uncompressed. The data rate during playback that must be maintained is around 2.5 Gbit s^{-1}, which is still well within the specifications of modern computer equipment.

Video playback is handled by VLC media player, an open-source solution that offers extensive customization options to achieve a pixel-accurate video stream. But it is still high-level software. Therefore, frames being dropped or displayed twice may still occur, primarily due to interruptions from the operating system, rather than the video player or DMD itself. The relative occurrence of these artifacts has been assessed experimentally and is found to be on the order of 0.4 %. For the presented approach, where each 2D layer is composed of several focus patterns, the loss of some of them is bearable. A refined software solution could still be implemented, where the graphics card can be directly addressed via interfaces such as DirectX, Vulkan, or OpenGL [196, 197].

5.2 EVALUATION OF THE PRINTING PERFORMANCE

The 3D laser printing setup presented above enables versatile printing, allowing the number and location of multiple foci to be individually addressed. The following illustrates the printing of various performance test structures, which impose different demands on the printing process. Additionally, numerous printing strategies and parameter sets are selected. The comparison of the various test structures enables a discussion of the capabilities and limitations of the printing approach. The printing parameters and details on the printing strategies associated with the structures shown in this section can be found in Appendix A.2.

In Figure 5.12, a gallery of scanning-electron micrographs is shown demonstrating the multi-focus printing of different test structures. All structures shown were

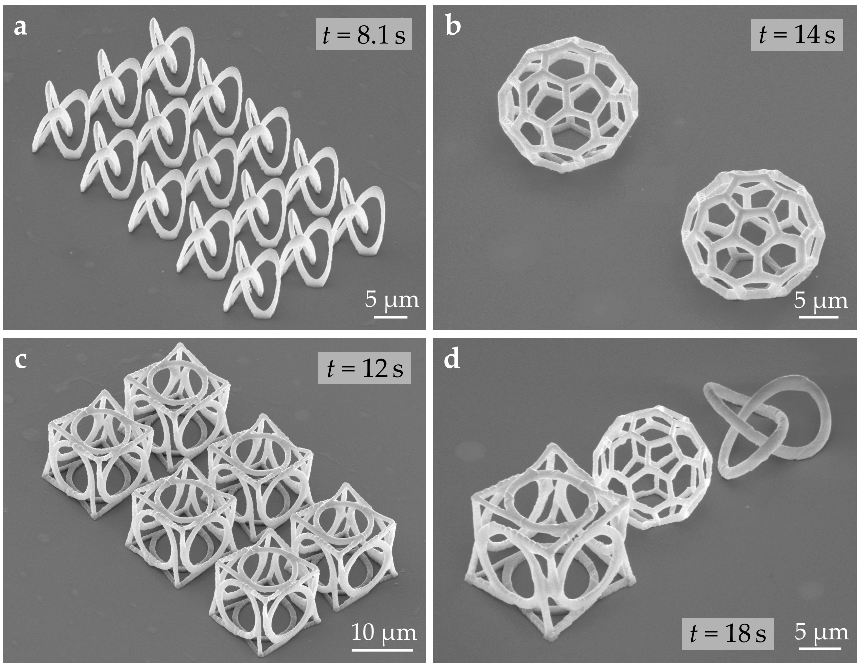

Figure 5.12: Gallery of SEM images of structures printed using the presented dynamic multi-focus setup. **a** 15 trefoil knot structures were printed in parallel using up to 31 foci in a print time of 8.1 s. This translates into a print rate of 61500 voxels s^{-1}. **b** Two buckyballs were printed in 14 s using up to 8 foci in parallel (15000 voxels s^{-1}). **c** Six unit cells of a chiral metamaterial structure were printed using 24 foci in parallel in a print time of 12 s (51000 voxels s^{-1}). **d** demonstrates the printing of three entirely different structures in parallel using up to 15 foci (13500 voxels s^{-1}). Adapted from [96] under CC BY 4.0.

printed using the photoresist PR1, following the nomenclature of table A.1. In Figure 5.12a, 15 trefoil knot structures were printed using up to 31 foci in parallel. The number of foci stated always refers to the maximum number, which can be lower for certain sparse layers of the structure. The shown structures, which have a nominal lateral side length of 10 µm, span almost the full reachable print field of around 31 µm × 62 µm. Therefore, the structures aid in evaluating the uniformity of printed structures across the print field. This is found to be acceptable, which confirms the corrections applied as discussed in section 5.1.5. The laser power used to print the trefoil knot structures is almost at the maximum output power of the laser, which translates into a power per voxel of about 142 µW. For these structures, the power limit of the setup is therefore reached, which prevents the use of a larger number of foci.

Evaluating the print rate is commonly performed in terms of voxels s^{-1} [86]. In focus-scanning approaches, the linear scan velocity is thereby divided by the average of the lateral and axial voxel size to determine the print rate [29]. For the

presented setup, a random-access scanning can be performed, where entirely different and independent patterns can be exposed with every single hologram. For this case, the determination of a linear scan velocity is less meaningful. But the total number of exposures, where each exposure leads to one voxel, either connected or disconnected to other voxels, is known. Hence, the total number of exposures is divided by the total print time to calculate the print rate in units of voxels s^{-1}. By taking the total print time, a mean print rate for a particular structure is derived. It is important to note that this also comprises effects like a reduced number of foci for certain layers, as well as run-up or settling times of devices used in the setup. Especially, the run-up and settling times of moving parts of 3D laser printing setups add an overhead to the print time and therefore lower the mean printing rate [152]. This is because of the non-negligible moments of inertia of macroscopic moving parts such as galvanometric mirrors or piezoelectric stages. Therefore, the mentioned run-up and settling movements are necessary to follow a trajectory at a constant speed to reach the best printing results. The presented setup comes with the advantage of no macroscopic moving parts. Still, the DMD's micromirrors are physically moving aluminum plates, which are, in comparison, very small and lightweight. Settling times of the individual micromirrors are in the order of a few microseconds and therefore around two orders of magnitude smaller compared to the exposure time of each hologram [168, 190]. For the printing process, no extra time is therefore allocated to let the moving parts settle. It should be mentioned that this is also the case for the piezoelectric stage employed for slicing the structure. This adds slicing artifacts, which are, however, found to be minor and therefore acceptable.
For the print shown in Figure 5.12a, a print rate of 61500 voxels s^{-1} can be derived, following a total number of exposures of around $5 \cdot 10^5$ and a print time of 8.1 s. This comes close to the peak printing rate, assuming the same photoresist system and structure to be printed, hence, assuming the same maximum number of foci of 31. At 2400 Hz, the peak print rate where every pattern would contain 31 foci would therefore calculate to 74400 voxels s^{-1}.

SEM images of further printed test structures are shown in Figure 5.12b-d. In panel b, two 18 µm bucky balls were printed in 14 s using up to 8 foci in parallel, resulting in a print rate of 15000 voxels s^{-1}. Panel c shows the printing of six unit cells of a chiral metamaterial structure [198]. The total printing time is 12 s, therefore 2 s per unit cell for the structures of 12 µm side length each. This structure was printed employing up to 24 foci in parallel at a print rate of 51000 voxels s^{-1}. Each layer of the structure is divided into 24 equal parts, such that each focus performs a line-scan-like movement across one quarter of one unit cell. Taking this printing strategy, slight stitching seams are visible where the individual print areas touch. Finally, panel d displays the printing of entirely different structures in parallel, demonstrating the full freedom of a dynamic multi-focus beam splitting and scan-

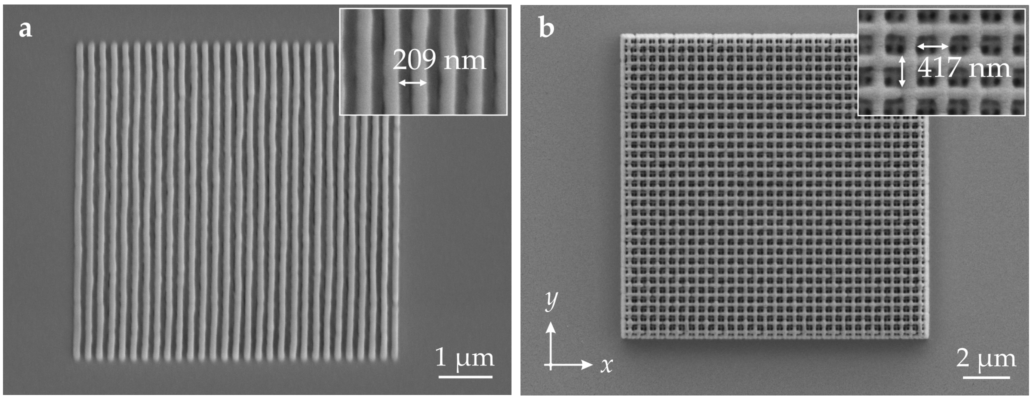

Figure 5.13: SEM images of 2D line gratings and 3D woodpile structures. Both structures are printed in single-focus mode, therefore using only one focus per hologram. **a** 2D line gratings with a measured line-to-line distance of 209 nm are still well resolved. **b** The same holds true for 3D woodpile structures at a lateral periodicity of 417 nm and an axial periodicity of 590 nm. Adapted from [96] under CC BY 4.0.

ning. The three structures are printed in 18 s with up to 15 foci in parallel. Still, the print rate calculates to only 13500 voxels s^{-1}, since the number of foci was reduced towards the top to still maintain a minimum focus distance.
For the printed structures shown in Figure 5.12c and d, a grayscale exposure profile is applied to pre-compensate for proximity effects. This follows an approach developed for synergistic two-color 2SA and used in light-sheet 3D printing [26]. Doing so, the intensity is decreased in dense regions where proximity effects appear the most. This is done by filtering the 3D binary structure with a 3D Gaussian kernel. Sharp edges of the structure are maintained by multiplying the unedited 3D structure by the filtered one. The grayscale values obtained encode the relative intensities of different foci. No additional changes to the laser source output power are needed.

Common test structures for assessment of the printing resolution are 2D line gratings and 3D woodpile photonic crystals [24, 32]. Such performance tests are shown in Figure 5.13. The structures shown were printed in single-focus mode. Therefore, the holographic pattern is a single amplitude grating at a certain periodicity and rotation. Employing only a single focus, the print quality has been shown to improve, of course, at the expense of printing time. Still, the experiments discussed in this paragraph aim at resolution rather than speed. Therefore, the effects of multiple foci are excluded from the discussion. In panel a, line gratings with measured line-to-line distances of 209 nm are shown. No effects of connected lines are visible at this spacing. Experiments at a smaller line-to-line distance of 140 nm, however, showed lines merged together. In panel b, a woodpile structure at a lateral periodicity of 417 nm and an axial periodicity of 590 nm is shown. Again, while

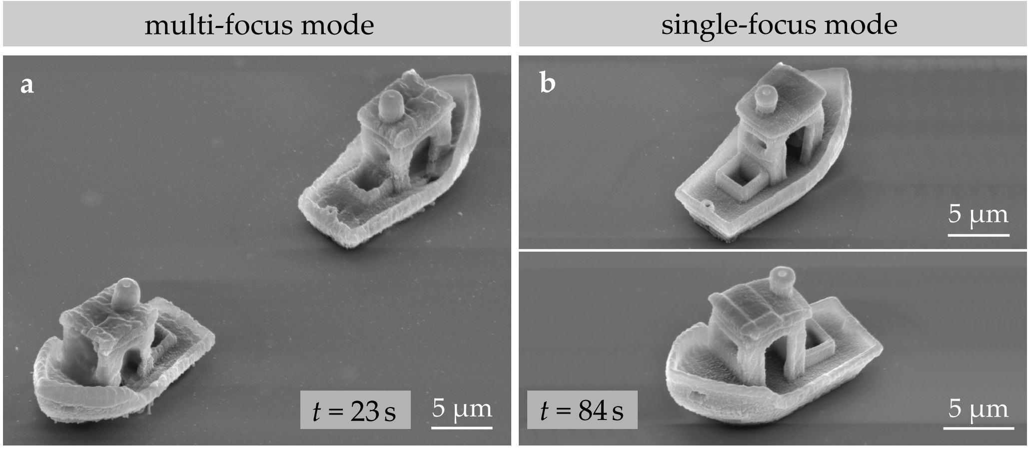

Figure 5.14: SEM images of benchy boats printed using different numbers of foci. Benchy boats are a common test structure in 3D printing and serve as an example for a structure of a larger filling fraction. **a** Two boats were printed in parallel using up to 15 foci in a print time of 23 s (17300 voxels s^{-1}). **b** A single boat was printed in a single-focus mode and is shown from two perspectives. The total print time is 84 s (2400 voxels s^{-1}). Adapted from [96] under CC BY 4.0.

this structure appears to be well resolved, woodpile structures at a smaller lateral periodicity of 280 nm showed visible proximity effects. It should be noted that the periodicities experimentally assessed correspond to discrete steps as discussed in section 5.1.4. Periodicities in between those tested would still be accessible when changing the computational routine. In general, the resolution tests shown aid in alignment and evaluation of the setup, but are not pushed to their limits. This would include extended parameter sweeps, proximity pre-compensation [44], as well as the implementation of a solid experimental assessment of the focus quality. All these, however, were not employed for the sake of simplicity. Therefore, the structures shown exhibit a slightly worse resolution compared to previous results on two-step absorption 3D printing employing single-focus scanning [24, 25]. Besides the reasons mentioned, this can further be attributed to side maxima and higher diffraction orders of the foci in the print plane, which give rise to additional proximity effects.

The structures shown in Figure 5.14 provide an example of the printing of dense structures with a larger filling fraction. This example is the well-known benchy boat, a common test structure in 3D printing across all kinds of approaches [140]. While the boat's hull shows a filling fraction of close to 100 %, fine and hollow features such as the cabin need to be printed on top of it. In Figure 5.14a, the printing of two boats in parallel using up to 15 foci in a print time of 23 s is shown. The printing parameters are therefore comparable to those of the structures shown in Figure 5.12.

However, the print fidelity is worse in comparison to those structures. A decent print quality can still be achieved when lowering the number of foci employed in parallel, eventually down to one focus as shown in Figure 5.14b. There, one boat is printed in a total print time of 84 s, and is shown from two perspectives. In this case, the cabin is nicely reproduced, while it suffers from proximity effects in the case shown in panel a. Structures of high filling fractions, as shown in this example, are particularly challenging for 2SA 3D printing [44]. As also indicated by the present results, this is potentially connected to the quencher molecules as essential ingredients to the photoresist mixture. These might be (partly) consumed during the printing process, such that the nonlinearity of the photoinitiation process decreases and dose accumulates in the printing volume. Diffusion processes are necessary to restore the original quencher concentration locally. Therefore, limitations are set in terms of the exposed volume per unit time. The filling fraction of the structure is then another parameter needed to choose the best printing strategy, specifically in terms of the maximum number of foci. It should be noted that no extended experiments have been performed to assess the maximum number of foci still maintaining a good structure quality for this particular example. Furthermore, one might argue about the effects the holographic pattern has on the structural quality for an increasing number of foci. Such effects are present, arising in additional unwanted "ghost" foci and a reduced uniformity of the exposures compared to a single-focus scan. Still, as demonstrated in Figure 5.12, a decent structure quality is achieved also for a larger number of foci as employed in Figure 5.14a. For this reason, a significant contribution to the results shown in Figure 5.14 is attributed to the photoresist.

By showing a gallery of performance test structures, the capabilities of the home-built 3D laser printing setup have been demonstrated. The printing of 3D structures at up to 61500 voxels s^{-1} using 31 foci in parallel is successfully shown. However, the characteristics of 2SA require a careful adaptation of the print parameters to the structure to be printed. This comes along with an additional degree of freedom that the developed setup offers: the distribution of the exposures in space and time. The effects of this will be further discussed in the next section.

5.3 SPATIOTEMPORAL PROXIMITY EFFECTS

5.3.1 *Introduction to Spatiotemporal Proximity Effects*

Under the term of spatiotemporal proximity effects, I will refer to proximity, therefore dose accumulation effects, which are dependent on spatial and temporal parameters. The spatial parameters are first and foremost the print design. The surrounding of one point of interest, therefore, has a different influence on the polymerization at that point depending on the print design, hence the term proximity effect. Such effects were already introduced in section 2.2 when discussing the fundamentals of photopolymerization 3D printing, as these are essential in understanding the resolution limitations of 3D laser printing.

I briefly want to recall the accumulation model introduced there: The crucial point is that light exposures of the photoresist, which can be converted to a deposited dose, add up. Although individual exposures might be below the polymerization threshold, their sum is such that the material gets polymerized. This model holds true for different photoinitiation processes, i.e., for two-photon absorption as well as for two-step absorption. An important simplification is, however, that all exposures are treated equally, regardless of their temporal sequence or the time difference between them.

This simplification is acceptable when discussing effects of the nonlinearity exponent [43] as well as when performing qualitative dose simulations for comparison with experiment [41]. However, the simplification breaks down when looking at long exposure times and/or fine features close to the resolution limit [45, 199]. Doing so, effects like the diffusion of photoinitiator and quencher molecules, such as oxygen, have to be considered. These effects are time-dependent, which leads to the observation and investigation of spatiotemporal proximity effects.

In the special case of parallelized 2SA 3D printing, as presented in this work, the discussion about spatiotemporal proximity effects is further motivated by several factors that differ from those of focus-scanning 2PP. First, due to the finite lifetime of the intermediate state, which ranges from tens to hundreds of microseconds, temporal effects of the printing sequence are expected to have a larger influence on the photoinitiation process. Second, quite large quencher molecules are an essential ingredient of the photoresist. The diffusion of these is therefore also important for the printing result. Third, different pathways of radical generation exist with different resulting nonlinearity exponents. Depending on the local parameters in the reaction volume, either pathway is preferred. These local parameters, such as the concentrations of the molecules, experience time-dependent changes. Combining these points, complicated reaction-diffusion kinetics are involved in 2SA 3D printing, which are expected to render spatiotemporal proximity effects important across a wide range of printing conditions.

Besides the factors related to the photoresist, a fourth factor related to the setup can be identified: As already discussed in the last section, the dynamic multi-focus approach naturally raises the question of how to utilize and benefit from this additional degree of freedom, which is not present in focus-scanning approaches.

5.3.2 *Experimental Investigation*

The systematic experimental investigation of spatial and spatiotemporal proximity effects is mainly motivated by the wish to push 3D laser printing capabilities further. When trying to print fine features in less time, proximity effects often pose limitations. Understanding proximity effects might therefore help in overcoming them.

When specifically talking about spatiotemporal proximity effects, the time dependence of printing parameters is investigated. In focus scanning approaches, probably the most low-level investigation is the dependence of the polymerization threshold on the exposure time of single-point exposures. In doing so, different regimes with different dependencies show up. Remarkably, a regime exists where the polymerization threshold remains constant when changing the exposure time, which is commonly attributed to the diffusion of oxygen [45]. Furthermore, the broadening of structural elements depending on time delays during printing has been investigated to define suitable printing conditions for the structures targeted [200, 201]. Moving on to random-access (multi-focus) approaches, Waller et al. [199] investigated the broadening of printed lines depending on different printing strategies and time delays. They, as well as many others, concluded that diffusion effects play a major role in the explanation of their observations.

As two-step absorption is still a novel photoinitiation mechanism for 3D laser printing, no systematic investigation of proximity effects has been performed so far. Nonetheless, they are of significance, as was observed in printing experiments [24, 27] and have been discussed in the previous section. The experiments performed in the scope of this thesis mainly aim at comparing different printing strategies, i.e., different temporal sequences of laser exposures for the same design structure. To cover the extreme cases of random-access scanning, the printing strategy of what I will refer to as the "ordered temporal sequence" is compared with a "random temporal sequence". Taking the first, a focus-scan is mimicked, while the exposures are randomly shuffled to arrive at the latter. The randomization is only performed within one layer, since the slicing is not conducted via the holograms.

In Figure 5.15, the result of printing one unit cell of a chiral metamaterial structure is shown using either of the already mentioned ordered or random temporal sequences. The printing was done using PETA as the monomer and in single-focus mode. The schematics depicted on top of the SEM images illustrate the temporal sequences for the example of one of the bottom layers of the structure. The color encodes the timestamp of the laser exposure for each point in space. In the SEM images, clear differences can be seen regarding the surface structure of the two structures. While the ordered sequence leads to a uniform surface, a grainy surface texture is apparent for the random sequence. This indicates a spatially varying polymerization threshold on the order of single voxels.

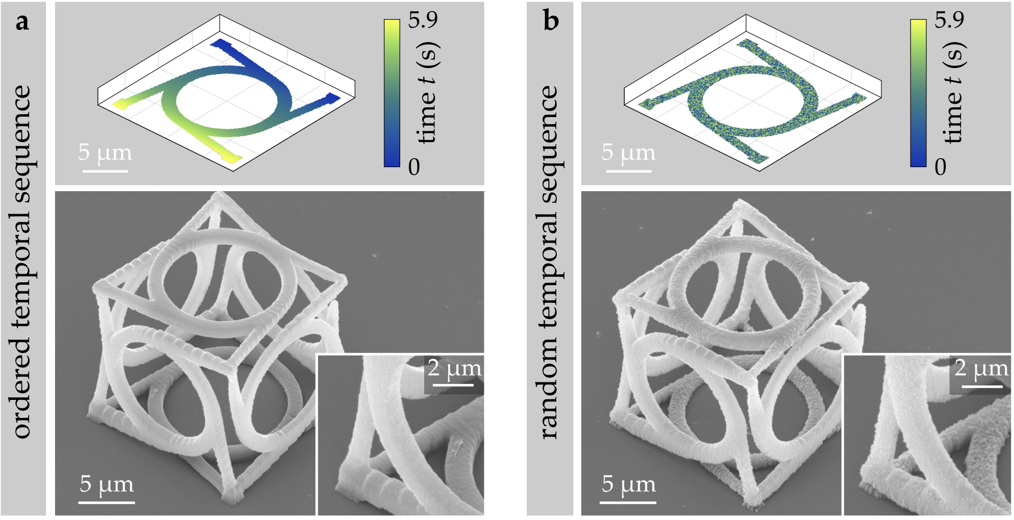

Figure 5.15: SEM images of chiral metamaterial unit cells printed with different temporal sequences. The employed sequences are either ordered (**a**), therefore mimicking a line scan or random (**b**) within one plane. For both cases, the sequence is illustrated in the top row for one exemplary layer with the time stamp for each single exposure encoded via the color. In the SEM images in the bottom row, differences between the temporal sequences, mainly in terms of the surface texture, can be seen. Adapted from [96] under CC BY 4.0.

For a more simplified investigation, differently sized square planes composed of only one layer were printed. The different lateral sizes lead to different average time delays between neighboring exposures for the case of the random sequence, while they stay the same for the ordered sequence. In Figure 5.16, results are shown for the printing of planes of 14 µm as well as 3.5 µm side length. Taking the first, the print time was 8.3 s, while it was only 0.55 s for the smaller structure. As in the previous example, a rather uniform surface structure compared to a grainy one results. Looking at the random sequence, almost disconnected single voxels are visible around the edges of the printed plane, while larger "grains" form towards the center. However, overall, less material seems to polymerize, taking into account the random sequence, which is in accordance with a larger local and spatially varying polymerization threshold. In the insets, the smaller printed planes are shown at the same magnification with qualitatively the same result, but with fewer differences when comparing edges to the center.

From these experimental observations, one would clearly prefer maintaining an ordered focus sequence. Besides the experiments in single-focus mode, experiments in multi-focus mode qualitatively yield the same, although less pronounced, differences. However, no systematic comparison has been performed. In general, the average time difference of neighboring exposures can be identified as the main governing parameter. As a result of these experiments, an ordered temporal se-

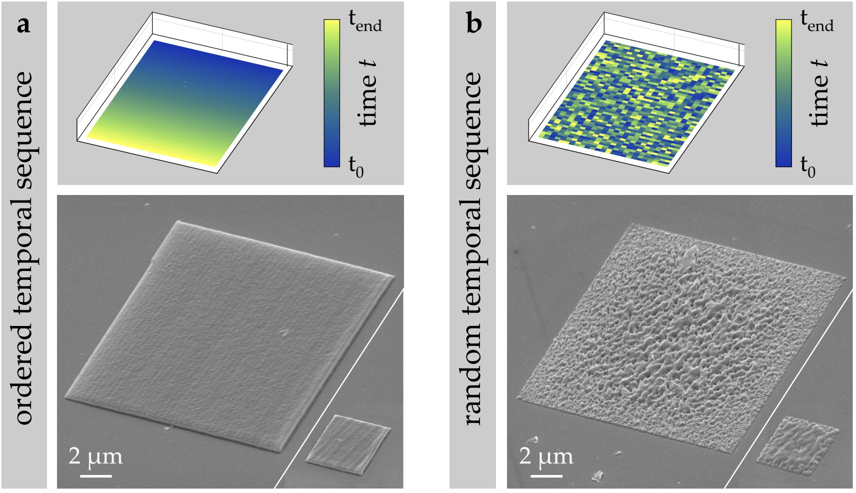

Figure 5.16: Comparison between ordered and random temporal sequence for differently sized planes. The top row illustrates the sequence, while in the bottom row, SEM images are shown. Clear differences between the ordered (**a**) and the random (**b**) sequence are visible with a non-uniform surface texture for the random sequence and distinct polymerized voxels visible towards the edges. The print time for the larger planes is $t_{\text{end}} = 8.3\,\text{s}$, while the print time for the smaller planes is only $t_{\text{end}} = 0.55\,\text{s}$. Adapted from [96] under CC BY 4.0.

quence is tried to ensure for single- as well as for multi-focus prints. A simple implementation to reach this is to distribute each layer into a grid, with each focus scanning across one part of the grid. This, however, does not optimize for a minimum print time. Further approaches could therefore include a k-means algorithm for equally sized areas [202]. An overview across the print strategies employed for the prints shown is provided in Appendix A.2.

5.3.3 Calculation via a Rate-Equation-Based Dose Simulation

Besides choosing the best-fitting printing strategy, the investigation of spatiotemporal proximity effects allows for further insights into the reaction-diffusion kinetics of the printing process. This, at the same time, motivates a comparison with computational approaches with the goal of a refined dose simulation beyond a simple accumulation model. This has been pursued and will be explained in the following. As the unique part of 2SA 3D printing is the photoinitiation process, special attention is paid to this. Hahn et al. already set up rate-equation calculations to model the photoinitiation process [24, 26, 44]. The rate-equation model developed therein also provides the basis for the dose simulation presented in this work. A reaction scheme of this model is shown in Figure 5.17. It covers the photoinitiator as well as

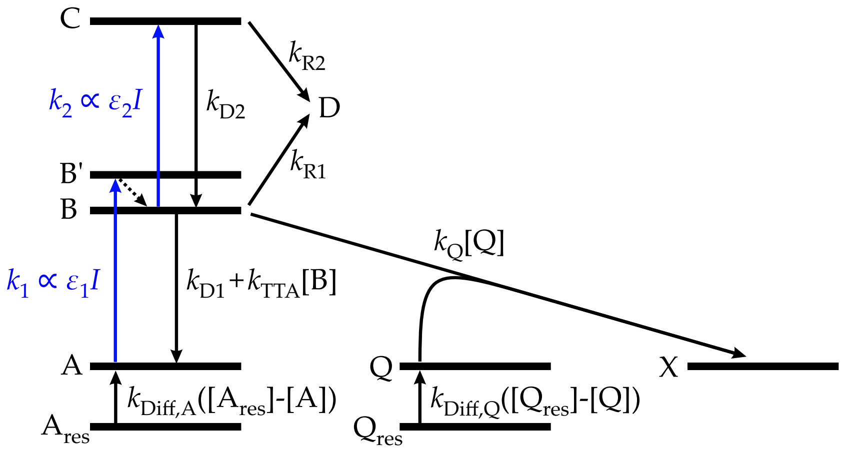

Figure 5.17: Sketch of the reaction scheme as used for the rate-equation calculations. The scheme is based on [26] and includes two subsequent absorptions from a photoinitiator's ground state A to excited states B and C, governed by the rates k_1 and k_2. Radicals generated are identified by the level D, which can be populated from both B and C. Irreversible scavenging reactions are taken into account in the inert state X. Several reversible decay pathways are furthermore considered. Photoinitiator and quencher molecules are replenished from infinite reservoirs A_{res} and Q_{res}. Adapted from [26, 96] under CC BY 4.0.

the quencher molecules in a simplified manner.

Initially, at a time stamp of zero, the states A, Q, A_{res} and Q_{res} are populated at a concentration of $[A]_0 = [A_{res}]_0 = 100\,\text{mM}$ and $[Q]_0 = [Q_{res}]_0 = 50\,\text{mM}$. This resembles the photoresist PRA in Appendix A.1. A and Q are the ground states of the photoinitiator and the quencher, respectively. From the ground state A, the photoinitiator molecules can get excited to state B′ via the absorption of laser light of intensity I. From there, the molecule quickly relaxes to state B, resembling the intermediate state of two-step absorption. A second absorption process can therefore excite the molecule further to state C. From this state, radicals are generated at the rate k_{R2}. Generated radicals accumulate in state D, which we assume to be proportional to the accumulated dose. Besides this 2SA photoinitiation pathway, several decay pathways as well as a one-photon photoinitiation pathway (k_{R1}) are accounted for. From the intermediate state B, a reversible unimolecular (k_{D1}) as well as a bimolecular decay via triplet-triplet annihilation (k_{TTA}) is considered [53]. Furthermore, state B can be depopulated in an irreversible bimolecular quenching reaction with quencher molecules from state Q. In the model, only a single quenching is assumed, which is the additional quencher molecule BTPOS, as it is assumed to govern the reaction [44]. The quenching reaction ends at an inert state X.

The states A_{res} and Q_{res} approximate the surroundings of the reaction volume by assuming an infinite reservoir of photoinitiator and quencher molecules. While this assumption may fail for extended printing experiments, it should hold true for the

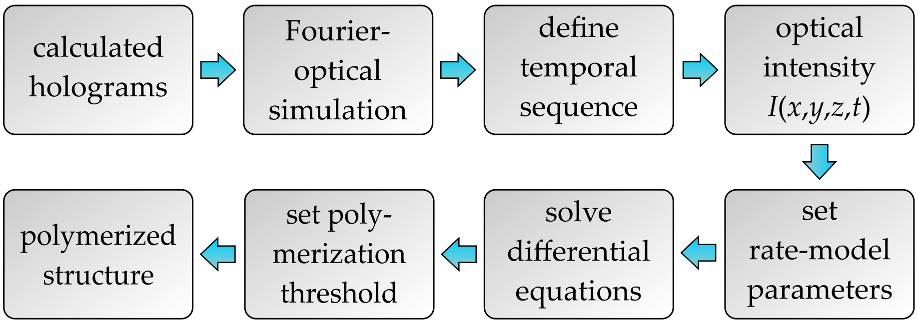

Figure 5.18: Flowchart of the rate-equation-based dose simulation. The holograms are propagated to several layers close to the print plane via a Fourier-optical simulation. With a defined temporal sequence, one gets the spatiotemporal intensity $I(x, y, z, t)$ in the print volume. Following the definition of all rate coefficients, the set of differential equations is numerically solved. As the population of the radical level is assumed to be proportional to the dose deposited, setting a threshold allows for a representation of the polymerized structure. Adapted from [96] under CC BY 4.0.

printing of small structures, compared to the structure size, in a large photoresist droplet. In-diffusion processes from the surrounding are treated in a simplified, and therefore approximate manner, via a rate proportional to the difference of the population of the ground states A and Q and the infinite reservoirs A_{res} and Q_{res}. This approximate description of spatial diffusion is made to arrive at reasonable computation times. In fact, the full description via a set of partial differential equations in three spatial dimensions and time would be orders of magnitude more demanding numerically. For this reason, many studies simplify spatial diffusion processes in different manners [45, 118, 199].

Based on the described reaction scheme, a rate-equation-based dose simulation was set up, as illustrated by the flowchart depicted in Figure 5.18. Due to computational limitations and given the current implementation, the dose simulation is so far only used to compare with small printed structures, such as the printed planes in the inset of Figure 5.16. Conceptually, it is, however, not limited to such structures. The computational routine starts with the set of calculated holograms for printing a certain structure. Using Fourier optics, the stack of holograms is imaged to the print plane following the same computational routine as used in Figure 5.3. From the print plane, the focus patterns are further propagated to different planes above the focal plane. The result is a 4D tensor $I(x, y, z, n)$ containing the intensity at different locations in and near the print plane for all N holograms. Afterward, the temporal sequence is defined such that each hologram, therefore each laser exposure n, is associated with a certain time interval between t_0 and t_{end}. The duration of each interval corresponds to the patterning rate of the DMD and calculates to $t_{\mathrm{exp}} = 417\,\mu\mathrm{s}$. Therefore, the data now refers to $I(x, y, z, t)$ and is input to the rate-equation model.

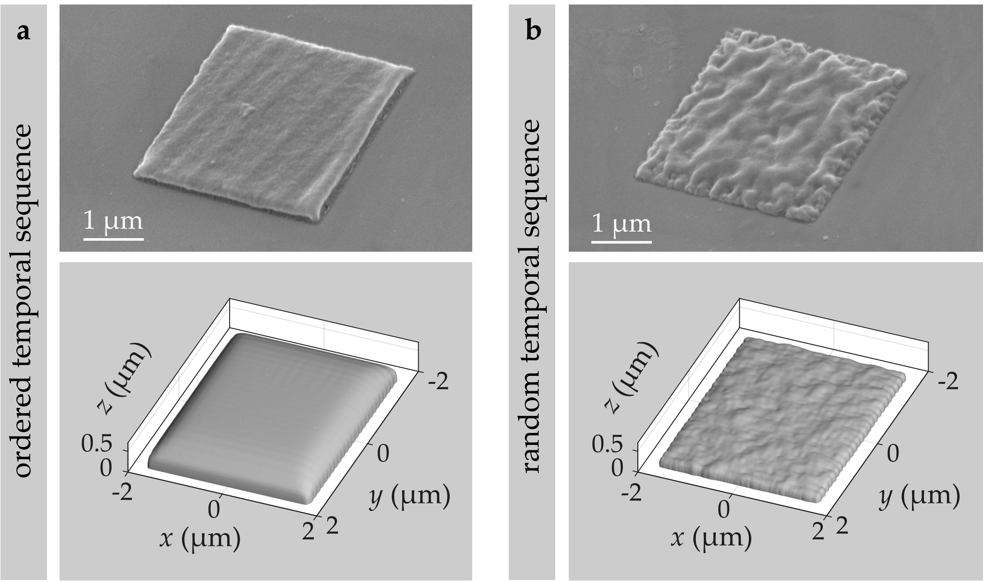

Figure 5.19: Comparison of two temporal sequences in experiment and simulation. The SEM images refer to the smaller printed planes as already shown in Figure 5.16, where the temporal sequence is also illustrated. The simulated structures result from the described dose simulation. Comparing experiment with simulation, a qualitative agreement can be seen, such that different degrees of polymerization as well as surface textures are reproduced. Adapted from [96] under CC BY 4.0.

Accompanying the space- and time-dependent intensity values, all parameters of the rate equations need to be set. The different rate coefficients are either taken from literature or manually set to best fit the experimental observations. A table containing the parameters is provided in Appendix A.3. With the coefficients set, the system of differential equations is independently solved for every point in space via the "ode23t" solver built into MATLAB. Finally, a polymerization threshold value is set to the population of level D as $[\mathrm{D}]_{\mathrm{th}} = 0.1[\mathrm{A}]_0$ [44]. The binarized population is then associated with the polymerized structure.

A result of the rate-equation-based dose simulation, in comparison with the experiments, is depicted in Figure 5.19. The experimental results refer to the smaller planes of 3.5 µm side length, which were already shown in Figure 5.16. For the simulation and experiment, the temporal sequence is either chosen to mimic a line scan or randomly shuffled. The simulation qualitatively coincides with the experiment. In the simulation, the random sequence clearly shows a non-uniform surface, a lower overall polymerized volume, and almost unconnected voxels towards the edges of the structure. This matches the experiment. However, the simulation of the ordered sequence shows a bulging behavior that is less pronounced in the experiment. Furthermore, the non-uniformities in the experiment when looking at

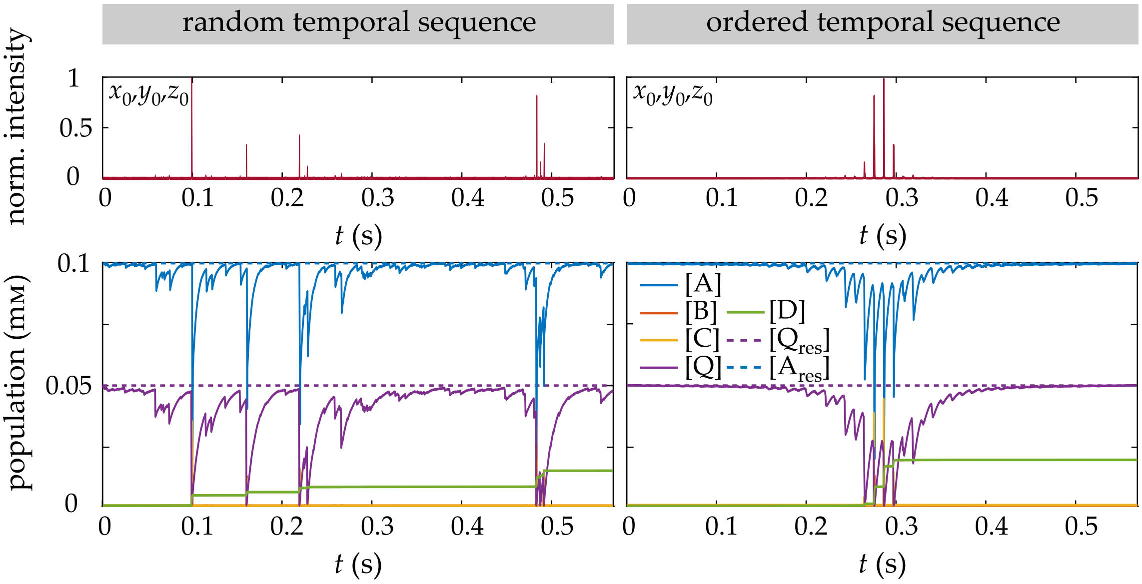

Figure 5.20: Temporal evolution of the population of different levels as resulting from the rate-equation calculations. The two columns refer to a random and an ordered temporal sequence. The top row depicts the time-dependent intensity for both sequences at one observation point ($x = y = z = 0$). In the bottom row, the population of different levels of the rate-equation model is shown. The ordered sequence leads to a higher degree of polymerization, since all absorption events are condensed to a narrow time frame in which the quencher concentration is noticeably reduced. Adapted from [96] under CC BY 4.0.

the random sequence appear to be on a larger scale compared to the simulation. The latter might be a result of the simplified treatment of spatial diffusion as well as the assumption of infinite reservoirs. Still, by performing dose simulations taking the finite lifetime of the intermediate state, as well as simplified quenching and diffusion processes into account, spatiotemporal proximity effects of 2SA photoresists can be modeled.

Further insights into the process are provided when looking at the population of the different levels as a function of time. This temporal evolution at $x = y = z = 0$ is plotted in Figure 5.20, again as a comparison of the random with the ordered sequence. In the top row, the time-dependent intensity values are plotted. These are proportional to the time-dependent coefficients k_1 and k_2. In the bottom row, the population of the respective levels of the rate-equation model is plotted in units of mM. At time intervals of a significant laser intensity near the observation point, the population of the photoinitiator's and the quencher's ground state decreases while the population of states B and C, and consequently also D, increases. Between absorption events, the populations of levels A and Q are restored through in-diffusion from their surroundings. The point of highest laser intensity refers

to the situation in which the laser directly exposes the observation point. For the ordered sequence, this is the center of a narrow time frame in which the majority of the absorption events are condensed. Interestingly, at the timestamp of direct exposure of the observation point, the populations of states A and Q are noticeably lower compared to their equilibrium populations. This is because the in-diffusion from the surrounding area, following preceding absorption events, is too slow to restore the original population, rendering the quenching process less efficient. Of course, this observation is dependent on the chosen parameters, time scales, and structure to be printed. Still, it holds true for the given examples and in comparison with the experiment. In conclusion, the less efficient quenching leads to an overall higher dose accumulation and a larger contribution of a one-photon triggered polymerization for the ordered sequence, which is undesired. On the other hand, the conditions are more consistent for different points of the structure, leading to an almost constant polymerization across the structure and a more uniform surface.
The presented simulation was developed to the point where it achieved qualitative agreement with the experiment for very simple example structures. In doing so, it already helped in investigating different printing strategies and showcasing spatiotemporal proximity effects for two-step absorption. However, the presented simulation routine still comes with several approximations and simplifications. These are the simplified treatment of diffusion processes, the manual fitting procedure of the rate coefficients, and the processes themselves, which are taken into account. A desired goal for any evolved dose simulation routine would be to exploit the predictive power to pre-compensate the printing design before printing. To achieve this, further parameter studies need to be carried out, where the high-dimensional parameter space is addressed in an automated way. As this requires increased computational effort, the main processes of the reaction scheme contributing to the photoinitiation process should be selected so that less important processes can be disposed of. Furthermore, neural networks could accelerate the computation of the differential equations.

5.4 DISCUSSION AND CONCLUSION

Of course, every newly developed 3D laser printing approach has to compete with the already existing ones. For the herein developed printing setup, this should be first done within the category of two-step-absorption 3D laser printing. The inherent benefit of 2SA 3D printing is a low single-voxel polymerization threshold and, therefore, the ability to use more affordable and compact cw lasers compared to rather expensive short-pulsed lasers for 2PP. This motivates further goals that make use of the low single-voxel polymerization threshold powers, like a massive parallelization approach. Doing so, light-sheet 3D printing offers high printing rates of up to 7×10^6 voxels s^{-1} at voxel sizes of 1.35 µm using synergistic two-color

2SA [26]. By this technique, benchy boats and an assembly of six chiral metamaterial unit cells were printed in only 288 ms and 1.4 s, respectively. However, the total dimensions of these structures were approximately seven times larger. On the other hand, a miniaturized single-focus setup can be targeted, which achieved print rates of 4.9×10^3 voxels s^{-1} at voxel sizes of around 210 nm [25]. Using this setup, the printing of a 16 µm long benchy boat and a 16 µm side length chiral metamaterial unit cell was shown at overall printing times which are comparable to the DMD-based setup using only a single focus. However, the structures presented in Ref. [25] were printed at smaller hatching and slicing values, but a four times higher linear focus velocity of $1\,\mathrm{mm\,s^{-1}}$ (in contrast to $250\,\mathrm{\mu m\,s^{-1}}$ in the present approach, as derived from the step size and the patterning rate employed). Compared to this, already a small number of foci employed in parallel offers an advantage in printing time.

The goal of the approach developed in this work was to bridge the gap between these two previous implementations of two-step-absorption 3D laser printing by circumventing their drawbacks while largely preserving their advantages. Specifically, the print rates should be increased compared to single-focus 2SA 3D printing. As outlined in section 4.1, parallelization approaches become vital due to limited single-focus scan velocities. LS3DP is already a parallelized 2SA 3D printing approach capable of steering 33000 individual foci. However, it comes with the drawback of experimental complexity, initial total laser powers of about 30 W, and a limited build volume [26]. Using the presented setup, a compact 400 mW output power laser is used to perform a dynamic multi-focus printing at print rates of up to 6.2×10^4 voxels s^{-1}. The voxel sizes, although not thoroughly investigated experimentally, are near those of single-focus 2SA printing approaches. From top-down and side-view SEM images of printed woodpile structures, approximate voxel sizes of around 270 nm can be deduced. The printing rate, therefore, falls behind LS3DP but outperforms all other two-step-absorption processes.

The herein developed approach is at the forefront of cost-effective (1+1)-photon absorption techniques. However, applications of 3D laser micro- and nanoprinting are still largely dominated by 2PP and parallelized one-photon absorption approaches, such as micro-stereolithography. Commercial instruments for 2PP operate at print rates of 2.5×10^5 voxels s^{-1} for many years already. The approach presented herein cannot compete with this at the moment. Therefore, development is still needed, and/or specific applications have to be defined.

Further development could initially involve additional steps along the same lines, utilizing the knowledge gained in this chapter. The used patterning rate of 2400 Hz is limited by the implementation of the printing as a video stream. The derived exposure times are still well above the intermediate-state lifetime, and accompanying focus velocities are below the commonly employed focus velocities for single-focus scanning in 2SA 3D printing, respectively. Therefore, higher patterning rates would be beneficial to first push the single-focus velocities to their limits, thereby reducing the number of foci and better using the power budget, as explained at the beginning of this chapter. Such DMD-based solutions are available, however, at a higher cost [195]. Further steps pursuing other goals include reducing costs by making the setup more power-efficient, thereby relying on lower total laser powers, and by incorporating a 3D holographic laser beam-scanning approach, which eliminates the need for a piezoelectric stage for slicing the structure. These steps were taken in a second version of the presented setup, largely building on the ways paved herein. While the setup described in this chapter is based on off-the-shelf, widely available DMDs, the recent availability of micromirror-based phase light modulators motivates the steps outlined. This will be discussed in the next chapter 6, at the end of which a more extensive outlook on possible further developments will be given.

Chapter 6

6 A 3D HOLOGRAPHIC BEAM SCANNING SETUP FOR 2SA 3D LASER PRINTING

In this chapter, the design and realization of a 3D laser nanoprinting setup based on novel micromirror phase light modulators and 3D holographic beam scanning is presented. It is a second version of the printing approach introduced in the previous chapter, with an emphasis on affordability and versatility of the setup. Likewise, the goal of affordable 3D laser printing is first discussed. Afterward, the design considerations are explained, details of the experiment are given, and exemplary printed structures are discussed. The chapter concludes with a summary and an outlook on further development routes.

6.1 THE GOAL OF AFFORDABLE 3D LASER NANOPRINTING

For applications requiring 3D printing capabilities with voxel sizes below 1 µm, two-photon-absorption 3D laser printing is by far the most widespread method. It has matured over almost three decades, and a commercial market of manufacturers and customers has grown, which nowadays comprises academia and industry. As it is natural for high technology, developments on the side of the tools and on the side of the applications stimulate each other, where new applications make new tools necessary and new tools inspire new application examples. This bidirectional exchange might however be held back if resources are limited, e.g., if state-of-the-art machinery is not affordable to academia, education, or small- and medium-sized enterprises.
In the optics community, several open-source projects have therefore emerged which describe and provide low-cost construction kits for microscopy [203, 204], even for elaborate techniques such as light-sheet microscopy [205]. Coming back to the specific case of 3D laser nanoprinting, commercial 3D printing devices come at a price tag on the order of several hundred thousand euros. A large cost driver is the necessary short-pulsed laser, which alone has a price of around 10^5 €. Therefore, efforts have already been made to replace commonly used titanium-sapphire solid-state lasers or erbium fiber lasers with lower-cost alternatives. Besides (1+1)-photon absorption, this includes the use of (quasi) continuous-wave lasers in combination with chemical nonlinearities of the photoresist [206], or in combination with two-photon absorption [207]. Further research is ongoing on novel short-pulsed laser sources, which are chip-scale diode lasers [208, 209]. However, these approaches are either significantly less power-efficient than (1+1)-photon absorption or are still under development. To date, (1+1)-photon absorption techniques, of which two-step absorption clearly stands out, are the most well-developed techniques for cost-effective 3D laser nanoprinting.

Two-step absorption from the beginning offered the advantage of replacing expensive, bulky short-pulsed lasers with cw lasers. Therefore, the goal of providing affordable 3D laser nanoprinting approaches was also pursued right away. This led to the demonstration of a miniaturized 3D printing setup of the size of a shoebox, containing only a minimal number of parts [25]. In this implementation, the two most costly components were first a piezoelectric inertia stage for slicing the structure by moving the objective lens axially, and second, a movable mirror based on a micro-electro-mechanical system (MEMS) used for laterally scanning the laser beam. The combination of these two devices comes at a price of around 4500 € and is the major cost driver of the overall setup. Other components, including the laser source and the objective lens, can be purchased at a price of less than 1000 € in total. However, it should be noted that some sacrifices in terms of printing resolution have to be made when choosing low-cost objective lenses [210]. Therefore, a complete 3D laser nanoprinting setup can already be built at a price tag of only a little more than 5000 €.

The present work aims at two things building on this: first, the price tag should be brought to even smaller values. In particular, only a single device will be employed for holographically scanning the laser beam in the lateral and axial directions. This cuts the cost from 4500 € to around 2200 € for a PLM prototype device or to around 1000 € for DMD devices. Furthermore, two separate devices are combined, such that the complexity of the setup is reduced. If cost is the main criterion, it could be further reduced by taking DMD assemblies out of old projectors, if needed, together with new DMD chips, at a price tag of only 100 € to 200 €. Second, affordability is not only about cost, it is also about the versatility of the setup. The presented setup, using micromirror-based phase light modulators, is by design not only capable of single-focus scanning in three spatial directions, but can be used in the way any spatial light modulator is used. This includes multi-focus printing, holographic beam shaping, as well as single-exposure 3D holographic printing [116, 196].

6.2 DESIGN AND REALIZATION OF THE SETUP FOR PARALLEL 2SA 3D PRINTING

6.2.1 *Components of the Setup*

Since the setup presented in this chapter can be seen as a second version of the dynamic multi-focus printing setup presented in the previous chapter 5, some components are identical. Besides this, many design rationales were already outlined in the previous chapter. In this section, additional or diverging design considerations are discussed in detail while references are made to previous sections wherever applicable.

A schematic of the 3D laser printing setup is shown in Figure 6.1. The laser source used is the same compact diode laser at a center wavelength of $\lambda = 406\,\mathrm{nm}$ and a maximum output power of 400 mW (Toptica IBeam smart) as used in the previous version. In the context of an affordable 3D laser nanoprinting solution, it should be noted that the laser source utilized could be readily substituted with one of a considerably lower output power and, consequently, a significantly lower cost. This is because the present laser is operated at a very low percentage of its maximum output power for the phase holography as applied in this chapter.

Following the laser source, the laser beam is expanded via a telescope consisting of two achromatic doublet lenses L1 and L2 ($f_{\mathrm{L1}} = 30\,\mathrm{mm}$, $f_{\mathrm{L2}} = 150\,\mathrm{mm}$). Via two dielectric mirrors, the laser beam is directed onto the PLM such that it is incident under a small angle of approximately 13° with respect to the PLM normal.

The PLM module used is a Texas Instruments DLP6750Q1EVM evaluation module kit for application development. The currently available modules are built on exist-

Figure 6.1: Scheme of the optical setup for 3D printing based on a PLM and 3D holographic laser beam scanning. Starting from a diode laser (Toptica IBeam smart), the laser beam is expanded via a 5× telescope consisting of the lenses L1 and L2. The expanded beam impinges onto a micromirror-based phase light modulator (Texas Instruments DLP6750), which is an adaptive optical device used for 3D holographic beam splitting and beam steering, as well as for aberration correction. The pattern displayed on the PLM is imaged to the entrance pupil of the objective lens (Leica 100×/1.4-0.7) via a 1× telescope consisting of the lenses L3 and L4. Unwanted diffraction orders are blocked via an aperture in between. The dashed line indicates a coordinate system flip. Lateral and axial translation stages are part of the setup, but are not requisite for printing. For in-situ monitoring of the printing process, the sample is illuminated by an LED and imaged by a camera.

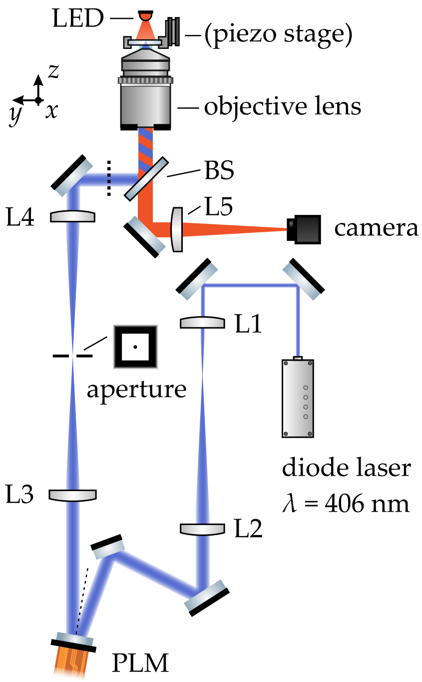

ing DMD hardware. The DLP6750, therefore, fits the same package as a DLP670S DMD chip and is controlled by a DLPLCR900 control board. The chip features an array of 1358 × 800 pixels of 10.8 µm pixel pitch. This translates into an active area of 14.7 mm × 8.6 mm. The nominal cross-sectional laser beam size at the PLM plane is 6.25 mm with the laser beam incident on the PLM at an angle of $\alpha \approx -13^\circ$. For illustration purposes, the calculated intensity as well as the phase at the plane of the DMD is shown in Figure 6.2a, with the PLM's active area highlighted. The effects of finite incident and diffraction angles are not considered in this visualization.
Following the PLM, the laser beam is relayed to the entrance pupil of the objective lens via a 1:1 imaging using the lenses L3 and L4 ($f_{\mathrm{L3}} = 125\,\mathrm{mm}$, $f_{\mathrm{L4}} = 125\,\mathrm{mm}$). In the focal plane of lens L3, the designed holographic pattern is generated. An illustration of this for a pattern of 10 distinct foci is shown in Figure 6.2b. Due to the phase-only hologram, the zeroth order is way less pronounced compared to the usage of binary amplitude holograms and the DMD. But a zeroth order is still present, which needs to be blocked to prevent dose accumulation in the print plane. The light focused to the zeroth order originates from different factors, comprising the discretization of the addressable phase levels as well as manufacturing imperfections and light reflected from the cover glass securing the PLM micromirror array. Please note that only the effect of the discretized phase levels is accounted for in the shown simulation, resulting in a substantially smaller contribution than in the experimental situation. Besides the zeroth order contribution,

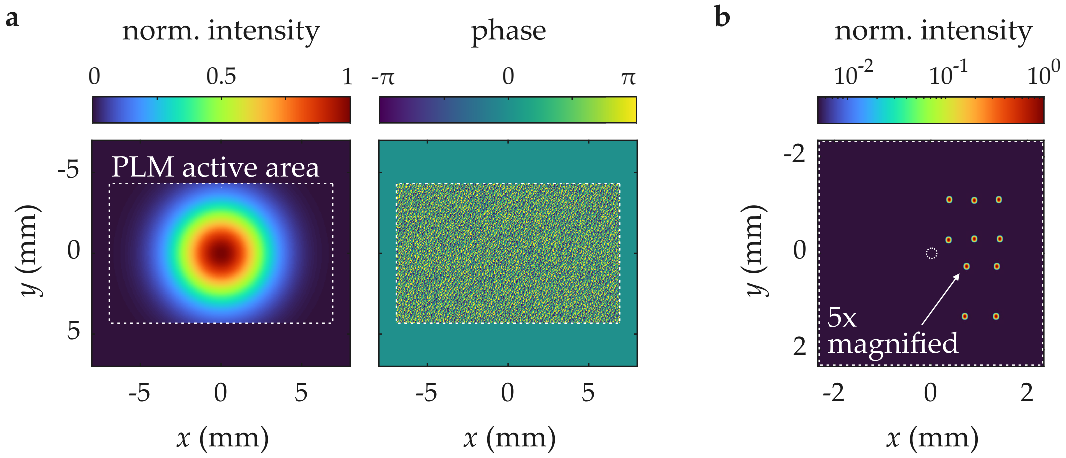

Figure 6.2: Illustrative calculations of the laser beam profile at the PLM as well as of the focus pattern generated. **a** At the PLM, a Gaussian beam is incident on the device. The PLM's active area is indicated via the white dashed rectangle. The phase of the incident beam is modulated across this area. **b** In the focal plane of lens L3, a focus pattern of 10 distinct foci is generated. For better visibility, each focus as well as the zeroth order are plotted 5× magnified in size. The dashed rectangle indicates the accessible area for beam steering, which is likewise transmitted through the aperture. The zeroth order, as indicated by the dashed circle, is blocked.

also contributions from higher diffraction orders of the PLM's pixelated array need to be blocked, similarly to the DMD (see section 5.1.2). Therefore, an aperture is assembled consisting of a precisely machined square aperture milled into a black polyvinyl chloride (PVC) slab for blocking higher diffraction orders and a positive obstruction target (Thorlabs R1D500P) for blocking the zeroth order.

The further optical setup, consisting of a dichroic mirror, the objective lens, and the illumination and camera beam path, is the same as already discussed in section 5.1.1. Therefore, a Leica HCX PL APO 100×/1.4-0.7 Oil CS objective lens is used.

In the spirit of reducing complexity and increasing the affordability of the 3D laser nanoprinting setup, the laser beam splitting and beam scanning in all three spatial directions are accomplished via the holographic patterns in this setup. This means that also axial scanning of the laser focus, as introduced in section 4.3.1, is now performed via the holograms, which was not the case for the DMD-based setup. Therefore, a piezoelectric stage for fine slicing of the structure during printing is not needed, which significantly reduces the cost of the overall setup. Still, the sample and/or the objective lens need to be positioned relative to each other, e.g., for finding the interface between the printing substrate and the photoresist. This task is, in the present case, still done via the piezoelectric stage as it is still a part of the existing setup. However, it could also be achieved by an inexpensive screw drive stage, with a potentially necessary additional fine positioning done via the holographic patterns.

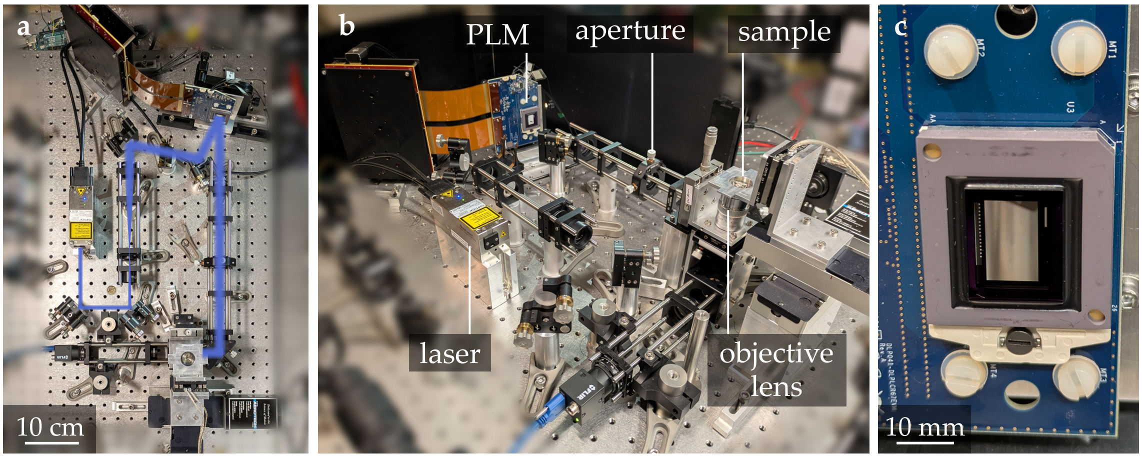

Figure 6.3: Photographs of the optical setup. a Top-down view with the optical path highlighted by the blue overlay corresponding to the scheme shown in Figure 6.1. **b** Angled view with the main components of the setup labeled. **c** Close-up of the PLM assembly. The central reflective element is a micromirror array comprising approximately one million individually addressable micromirrors.

The used PLM has a pixel pitch of 10.8 µm and a square instead of a diamond pixel layout. With these parameters and the downstream optics, the accessible print field calculates to 75 µm × 75 µm, following the same formulas as outlined in section 5.1.4. The minimum step size when relying on the discretization of the Fourier grid, as it is also done in this case, calculates to 94 nm and 59 nm in the two respective lateral dimensions. Due to the phase holography, no equally intense mirror image of the hologram in the first diffraction order is generated. Therefore, the "full" area of the first diffraction order can be used. However, since the blocked zeroth order is located in the center, the usable print field is a square with a non-accessible small circle in the middle.
Photographs of the optical setup are shown in Figure 6.3. Besides the reduction in the total number of components, the total footprint of the setup is also reduced since fewer relay telescopes are used. Although no special attention has been drawn to particularly compact individual components, the setup fits into a compact rectangular footprint of 30 cm × 60 cm.

Besides the already addressed piezoelectric stage for slicing the structure, two other components are removed compared to the setup presented in section 5.1.1: the πShaper and the diffraction grating. Due to the removal of the πShaper, a Gaussian amplitude profile is incident on the PLM. In general, a tradeoff of power efficiency when largely overilluminating the PLM's active area or a reduction in the holographic pattern quality when underilluminating the PLM's active area has to be made, which complicates for the Gaussian profile since there is no sharp edge. Based on the experience gained with the first setup version, the quality is found to be acceptable even when underilluminating the micromirror array. In conjunction with the goal of a simplified and affordable setup, the πShaper is removed, therefore also removing cost and complexity of the setup.

While the πShaper removal can be argued to be a compromise, the additional diffraction grating is not needed for the PLM-based setup. Using a DMD, the individual micromirrors are tilted with respect to the device normal, therefore acting as a blazed grating. To maximize the power efficiency, the angles of the incident and diffracted light, and therefore the diffraction order of the pixel array, have to be set accordingly. This led to a large diffraction order of $m = -5$, introducing significant angular dispersion effects (see section 5.1.3). The diffraction order considering only the micromirror array is reduced to $m = 0$ for the flat positioning of the micromirrors of the PLM, such that the pixelated array introduces no angular dispersion. Still, slight angular dispersion is introduced by the superposed holographic pattern. However, the effect of this is only minor for the present case of $m = \pm 1$ and diffraction angles centered around 13° with respect to the mirror normal.

6.2.2 *Laser Power Efficiency*

An increase in laser power efficiency is directly gained when switching from binary amplitude holograms to phase holograms, as already outlined in sections 4.2.3 and 4.3.3. While binary amplitude holograms are limited to a diffraction efficiency of around 10 %, 16-level phase holograms can, in theory, achieve diffraction efficiencies of 99 %. The parameters that experimentally limit the overall setup efficiency are described in the following.

The main device of interest when discussing the efficiency of the setup is the PLM. Its overall laser power efficiency can be divided into what I refer to as the device efficiency and the hologram efficiency. The device efficiency is the amount of light that can be used for the generation of the holographic pattern and which is focused to the zeroth order in an unpowered state of the PLM. It can therefore also be considered as the diffraction efficiency of the device. Current PLM devices achieve device efficiencies of around 70 %, which could be experimentally verified with the device at hand and at the wavelength used. Increasing the device efficiency is part of active development by the manufacturer and has increased significantly over the last years [160, 161, 211, 212]. Limiting factors are manufacturing process parameters such as the fill factor of the micromirror array, the mirror tilt, or the mirror flatness.

The experimentally accessed hologram efficiency comprises the light that is diffracted out of the zeroth order if a hologram is displayed on the PLM, compared to the optical power when including the zeroth order. This includes the efficiency of the actual calculated holograms under the limitation of the discretized addressable phase levels, as well as experimental mismatches of the real height levels of the micromirrors compared to the designed height levels. Furthermore, reflections from the cover glass and the space in between the mirrors are focused to the zeroth order, therefore part of the hologram efficiency. Another point for the time-averaged laser power efficiency is the time interval in which the micromirrors move when changing the pattern, which, to some extent, is also the case if the displayed pattern does not change. The sum of these effects leads to a hologram efficiency of 66 %, averaged across different holographic patterns.

The total power efficiency, measured in the entrance pupil of the objective lens and compared to the power out of the laser, is around 28 %. This is an averaged value for different holographic patterns used for printing, ranging from 25 % to 30 % for the examples which will be shown in section 6.2.6. In the case of steering a single focus, the efficiency largely depends on the deflection angle due to the diffraction envelope superposed on the steered focus. Therefore, values span between around 40 % close to the center to only 10 % near the edges. The remaining differences between the setup efficiency and the combination of device and hologram efficiency are attributed to losses at the different optical elements, as well as overillumination of the objective lens entrance pupil. The efficiency of the latter factors is around 68 % combined. The laser power efficiency is still more than an order of magnitude larger compared to the DMD-based setup and rivals the power efficiencies using LC-SLMs (see section 4.2.3).

6.2.3 *Encoding Phase Holograms onto PLM Devices*

As already briefly mentioned, the PLM does not allow for a continuous phase modulation but for addressing 16 different distinct phase levels, therefore for a 4 bit phase modulation. Calculated continuous phase holograms need to be discretized to match the addressable phase levels.

For the PLM, these discrete phase levels are not equally spaced, such that the relation of the displacement levels of the micromirrors to the integer phase levels is not linear. The actual relation is depicted in Figure 6.4, where experimental data provided by the manufacturer, Texas Instruments, is plotted. It can be seen that the separation of adjacent phase levels is denser for small displacements and rather sparse for large displacements. The reasons for this lie in the specific electrode layout and, therefore, the actual operating principle of how to move the micromirrors. This will be explained in a bit more detail in the following, based on resources from the manufacturer [160, 161, 211–214].

To illustrate the discussion, a schematic of a single PLM micromirror cell and its electrode layout is depicted in Figure 6.5. Underneath each micromirror, there are

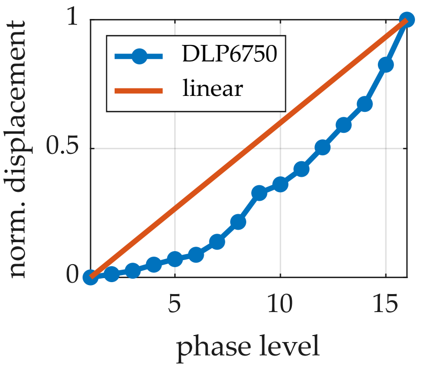

Figure 6.4: Discretized phase level map of the DLP6750 PLM. The 16 addressable micromirror displacement and therefore phase difference levels are not linearly distributed (orange line), but follow the blue data points with a finer discretization for low displacements. The data is provided by Texas Instruments [215].

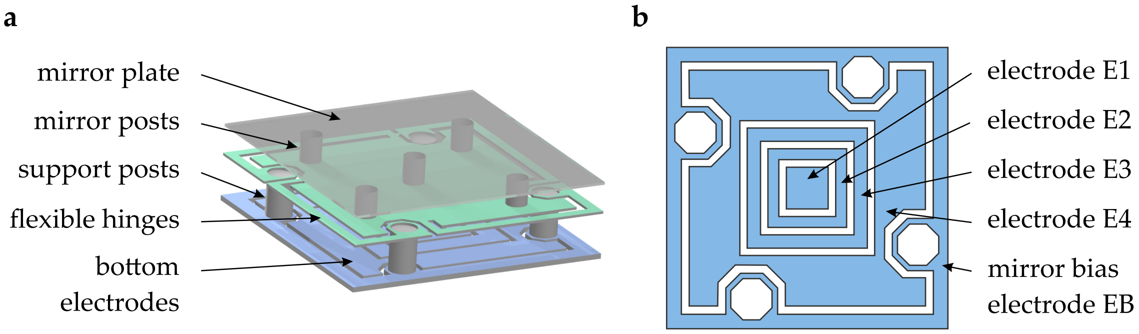

Figure 6.5: Schematic of the electrode layout of a single PLM micromirror cell. a Drawing of the main components. On top is an aluminum plate, which sits on five mirror posts. These are attached to a spring-loaded layer. Applying voltages to the bottom electrodes electrostatically attracts the spring-loaded layer, causing it to move downwards. This movement is guided by four support posts. **b** Top view drawing of the bottom electrode layout. Electrodes E1 - E4 are individually addressable for each micromirror cell, while electrode EB is set to a global value. Images redrawn based on information from [215] (panel a) and [214] (panel b).

several layers of flexible hinges and support posts, which allow the top aluminum micromirror surface to move while being restricted to a purely vertical movement. At the bottom of the micromirror cell, a layout of a total of five electrodes is manufactured. In an unpowered state, all micromirrors are in their highest position. The movement of the top plate is controlled by attractive electrostatic forces between the bottom electrodes and the top metal plate, which lowers the top plate. Of the five electrodes, four can be individually addressed for each micromirror (E1 - E4). In contrast, the fifth electrode, the mirror bias electrode (EB), is set to the same voltage for all micromirrors. The electrodes E1 - E4 are set to binary values of either 0 V or 10 V. Therefore, 16 distinct electrode voltage combinations are possible, resulting in 16 distinct displacement levels. Setting a suitable electrode layout to linearize the displacement curve and manufacturing of such are crucial parameters to be optimized by the manufacturer.

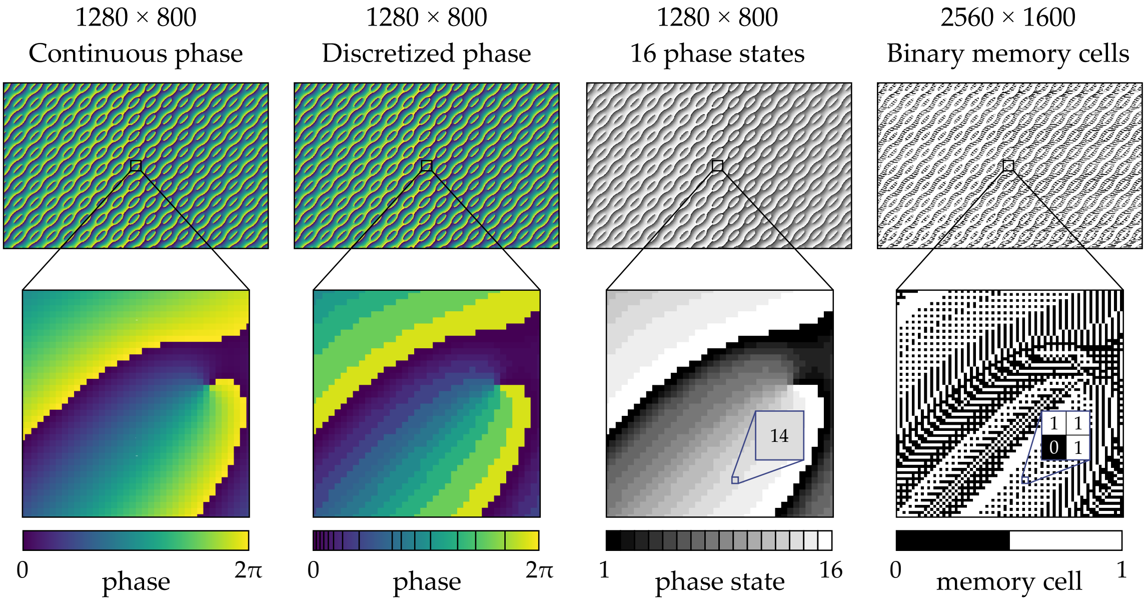

Figure 6.6: Illustration of the encoding of continuous phase holograms to the PLM's electrode states. **a** Exemplary 1280 × 800 pixel continuous phase hologram generating a 2×2 focus array wrapped at a 2π phase difference. **b** Phase map discretized to the 16 addressable phase levels of the PLM. These distinct levels are further indicated as vertical lines in the colorbar. **c** The phase map is displayed by the integer number of the phase level. **d** As each micromirror displacement is generated by four electrodes set to either 0 V or 10 V, a 2560 × 1600 pixel binary array of the memory cell status setting the electrode's voltages is calculated.

The voltage level of the mirror bias electrode can be continuously adjusted by the user based on the wavelength of the illumination. To achieve a complete phase modulation of 2π, the displacement of the micromirrors needs to change between a normalized value of 0 and $\lambda/2$. Since a phase difference of 0 or 2π leads to the same interference effects, the maximum physical displacement of the 16^{th} level is $\frac{15}{16}\lambda/2 = 190\,\text{nm}$ for the used wavelength of 405 nm. To set this maximum displacement, the mirror bias voltage is adjusted experimentally until the fraction of light in the zeroth-order hologram is reduced. The optimal voltage is 2.1 V.

With this knowledge of the operation principle of the mirror movements, the computational pipeline of encoding the continuous phase holograms to binary electrode states is shown in Figure 6.6. In panel a, a phase hologram generating an exemplary 2 × 2 focus array is shown, calculated for the used pixel count of 1280 × 800 pixels. This is mapped to the addressable 16 phase levels (panel b). In panel c, each pixel is represented by the integer number of the phase level it should address. This decimal number is finally translated into binary values that encode the voltage levels of the different electrodes. Therefore, a binary image of doubled lateral pixel numbers needs to be transferred to the PLM for display.

6.2.4 *Lateral and Axial Aberration Correction*

Adaptive optical elements like PLMs, LC-SLMs, or DMDs come with the appealing possibility of not only displaying holograms and generating focus patterns, but they also allow for aberration correction of the optical system they are incorporated in at the same time. The other side of the coin is, however, that the adaptive optical elements themselves are often one major source of aberrations that need to be corrected. This situation is present for the PLM used in this chapter. It should be noted that for the DMD-based setup presented in the previous chapter, an aberration correction would have been possible, but was found not to be necessary.

The main sources of aberrations for PLMs and DMDs are uneven surfaces. Due to the different heights at different points across the array, these effects are a source of different optical path lengths and apply a second phase modulation on top of the designed hologram. Potentially due to the not fully developed manufacturing process, these uneven surfaces are more pronounced for the PLM at hand compared to the DMD. If the surface shape is known, a phase map can be calculated, correcting for the surface shape by imposing the opposite phase delays.

With the optical setup presented in section 6.2.1, aberrations introduced by the PLM were measured by positioning a Shack-Hartmann wavefront sensor (Thorlabs WFS30-7AR/M) in the focal plane of lens L3 and setting all PLM pixels to the nominally same height level. The decompositions of the measured wavefront into Zernike polynomials were taken as the starting point for the calculation of an aberration correction phase map. The main contribution was found to be an astigmatism, which is in accordance with previous measurements of PLM-induced aberrations [160, 196].

Based on the coefficients describing the relative contribution of low-order Zernike polynomials, these coefficients were empirically optimized. To do so, the wavefront sensor was replaced by a camera, and a 6×6 focus array was holographically generated by the PLM and focused onto the camera sensor. The coefficients were adjusted such that diffraction-limited foci are obtained. These measurements are shown in Figure 6.7. In panel a, no aberration correction map was applied, leading to visibly aberrated foci as can be seen in the inset on the right-hand side. With the empirically optimized aberration correction phase map, as shown in the middle, foci were obtained with significantly reduced aberrations.

The simple procedure of empirically optimizing the coefficients of Zernike polynomials was repeated in the print plane, since additional aberrations might show up further down the optical path and when focusing through a high-NA objective lens. In the print plane, the tightly focused spots cannot be directly captured with a camera sensor. Furthermore, no elaborate PSF measurement techniques like gold bead scans are implemented into the setup. Therefore, the light reflected off a glass-

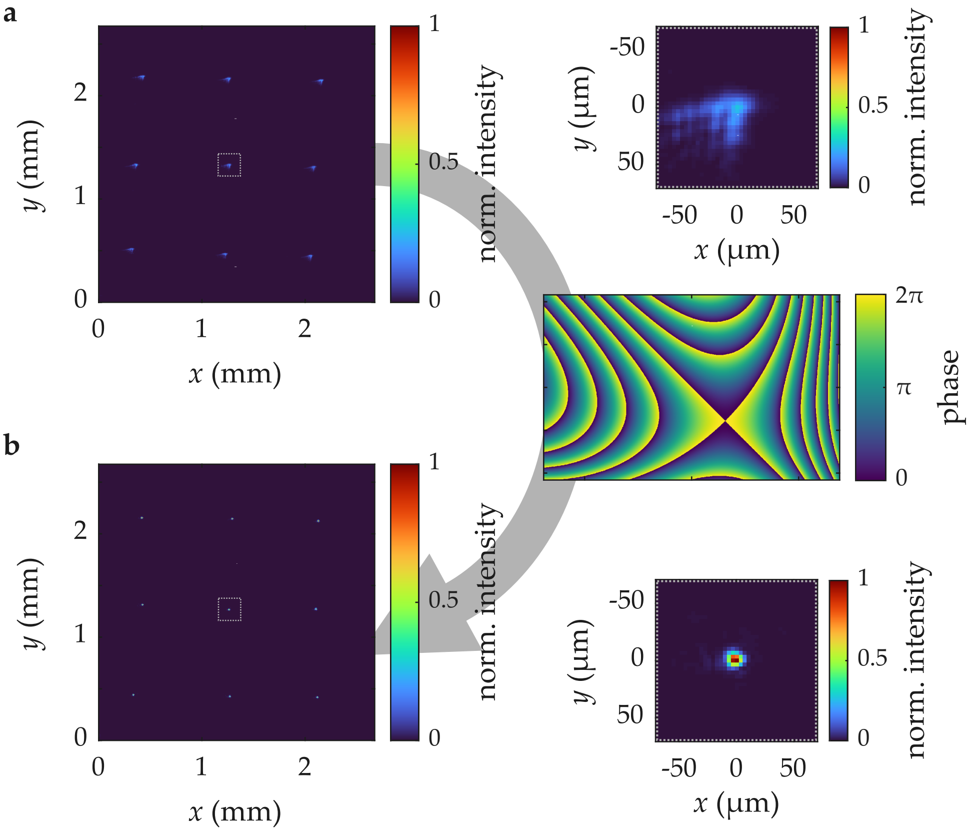

Figure 6.7: Lateral aberration correction via the PLM. A 6×6 focus array was holographically generated by the PLM and focused to a camera located in the focal plane of lens L3 (see Figure 6.1). For better visibility, only a quarter of the focus array is shown. **a** The zoom-in on the top right shows one exemplary focus out of the focus array, showing clearly visible aberrations. **b** By applying the correction phase map shown in the middle, the aberrations can be largely reduced. As seen in the zoom-in on the bottom right, an almost symmetric spot is obtained. The color scale of all intensity data shown is normalized to the same value.

monomer interface was imaged onto a camera the same way as in section 5.1.5. These imaged foci are clearly only an approximation of the real PSF shape, but can still be used as a simple characterization technique, at least for the lateral focus shape in the focal plane. Doing so, similar coefficients of Zernike polynomials were found as in the intermediate plane evaluated in Figure 6.7 with an astigmatism being the dominant contribution.

The same routine was also employed for a simple evaluation and optimization of the focus shape at different axial positions when shifting a single focus or an entire focus pattern along the optical axis. Therefore, the coefficients of the quadratic defocus term, as well as higher-order primary and secondary spherical aberration terms, were adjusted. With this, the shape and intensity of the imaged foci were optimized for axial shifts of $\Delta z = -10\,\mu\text{m}$ to $\Delta z = +10\,\mu\text{m}$. As outlined in section 4.3.1, the theoretical phase mask for axially scanning a focus in a high-NA system fulfilling the sine condition is a spherical profile. With this, the focus shape can be maintained when scanning the focus over a moderate distance. The combination of Zernike polynomials is only an approximation to this profile, but it provides several degrees of freedom for experimentally adjusting the phase profile. However, the maximum intensity and focus shape in the nominal print plane could not be restored completely when axially shifting the foci, although higher-order spherical aberration terms provide a source of improvement. The maximum intensity across the focus pattern when shifting the pattern axially by $\pm 10\,\mu\text{m}$ dropped to around 70 % of the maximum value at the nominal focal plane. In the experiment, effects such as refractive-index mismatches, imperfect optical elements, and imperfect alignment were present and were not accounted for in theory. In combination with a pragmatic, yet simple, measurement and optimization routine, the discrepancies are understandable and could be reduced by using proper PSF measurements and automated optimization algorithms. For the initial printing experiments conducted in this work, the Zernike polynomial coefficients were empirically determined at different axial positions and interpolated between them.

6.2.5 Electronics and Software Control

The hardware and software control of the PLM-based setup is largely the same as for the DMD-based setup presented in chapter 5. This includes the computational pipeline of how to get from the 3D design to the stack of holograms, as explained in section 5.1.6 as well as the electronics and the software of the printing setup itself, as explained in section 5.1.7. Nonetheless, some changes and different parameters are present, which will be explained in this section.

In the calculation of the holograms, additional steps are performed for mapping the phase holograms to the PLM's electrode addresses, which increases computational effort. On the other hand, no binarization of phase holograms to binary amplitude holograms is necessary. Since the arrays to be transferred - the electrode mappings - are still binary, the same solution of assembling 24 binary images into a single 8 bit RGB image can be maintained. Therefore, a stack of holograms needed for printing is stored as a single video file and displayed via the same software framework as discussed in 5.1.7.

Some care has to be taken with the data rates. As the information per pixel increases from 1 bit to 4 bit, while the total number of pixels stays roughly the same, the file sizes increase by a factor of approximately four. With the firmware currently available, the PLM's video frame rate is limited to 60 Hz, compared to 100 Hz, which could be reliably achieved with the DMD. Patterning rates using the PLM

are therefore 1440 Hz, such that the data rate for a 1280×800 pixel array calculates to 5.9 Gbit s^{-1}. It is found that also at this data rate, the fraction of delayed or missed frames during the video playback is acceptably low.
A second change concerns the time frame in which new patterns are to be displayed on the PLM and the micromirrors move. During this time, which is some tens of microseconds, light is directed towards the zeroth order as well as to random positions within the print field. To not suffer from additional dose accumulation effects, the laser is triggered by the PLM and turned off during these refresh times. Applying this procedure, the laser power efficiency being measured as an average across many frames, is further reduced by the time period the laser is turned off, which is around $70\,\mu\mathrm{s}/694\,\mu\mathrm{s} = 0.1$.

6.2.6 Printing Performance

To showcase the printing performance and to further evaluate the developed setup, 3D test structures were printed similarly to those presented in section 5.2. As the setup presented in this chapter has been developed up to a proof-of-principle status with a larger goal set on affordability and versatility, no extended quantitative printing experiments have been performed up to now.
Nonetheless, SEM images of a gallery of test structures are shown in Figure 6.8. It should be emphasized that all four examples presented were printed solely by holographically steering the light via the PLM in all three spatial directions without the need for macroscopic moving parts during printing.

To achieve the best printing results, some adjustments in terms of printing parameters and preparation of the print design were made, which will be explained before discussing the printing results in more detail. This includes an adjustment for a non-uniform intensity distribution of the foci throughout the print field as a direct result of the diffractive nature of the PLM's pixelated array. Here, the generally same argumentation holds as for the explanation of the diffraction envelope and the correction applied in the case of the DMD (see section 5.1.5). However, for the DMD-based printing setup, diffraction envelope corrections were only necessary if a large fraction of the printing field was used, since the diffraction envelope maximum can be aligned with the print field center by selecting appropriate angles. This is in contrast to the PLM, where the maximum of the diffraction envelope cannot be steered with respect to the print field, since all micromirrors remain flat with respect to the substrate. Therefore, the maximum aligns with the blocked zeroth order, and the diffraction envelope is more noticeable. To circumvent this, an additional focus was intentionally placed close to the zeroth order, therefore blocked by the aperture, carrying some laser light. By adjusting the relative strength of the foci, a uniform printing focus intensity throughout the print field can be

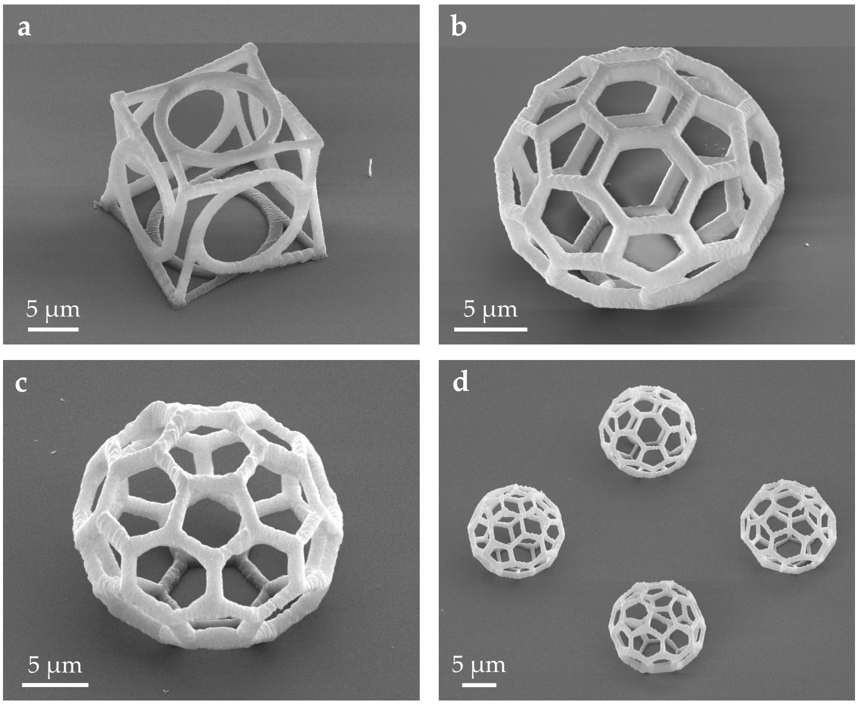

Figure 6.8: SEM images of structures printed for testing the performance of the developed 3D laser printing setup. a A unit cell of a chiral metamaterial was printed by holographically scanning a single laser focus in all three spatial directions. With laser power corrections applied as described in the main text, a similar printing performance is achieved compared to using a piezoelectric stage for slicing the structure. **b** By holographically scanning a single focus, but without further laser power corrections, a bucky ball structure was printed. **c** The shown bucky ball structure was printed using five foci in parallel and holographic beam scanning. **d** Four bucky ball structures were printed in parallel in a total print time of 5.5 s using up to 16 foci in parallel, translating to a print rate of 16400 voxels s^{-1}. Only 7 mW of laser power out of the laser is needed for printing the structure in panel d.

achieved. Of course, this correction comes at the expense of reduced laser power efficiency by a factor equal to the diffraction envelope's intensity drop. This drops to values of up to 20 % of its maximum intensity at the edges of the print field. A second adjustment made concerns the laser power set for different slices of the printed structure. Based on the simplified focus measurements performed, the voxel size increases with larger axial shifts away from the nominal focal plane. To adapt the printing parameters in this regard, the laser power can be increased with increasing axial shifts. This maintains the peak intensity at the expense of a larger voxel size and therefore reduced resolution. This adaption is made for the structures shown in Figure 6.8a and c.

With this said, I want to discuss the printed test structures. Further information

on printing parameters and printing strategies can be found in Appendix A.2. In Figure 6.8a, a single unit cell of a chiral metamaterial with side lengths of 16 µm is shown. The printing was performed in a single focus mode at a total print time of 123 s, such that the patterning rate directly translates into the print rate of 1440 voxels s^{-1} for this example. With the already mentioned adjustment of the laser power in axial direction, the laser power at the objective lens entrance pupil spans a range of 84 µW to 170 µW with an averaged power efficiency of the setup of around 30 %. It should be noted that the laser power adjustment made for the structure shown is partly due to the axially varying voxel dimension and also helps reduce proximity effects in the middle layers of the structure. Similar adjustments were also made for the structures discussed in section 5.2. A comparison of the laser powers required for printing the same structure at the same patterning rate (Figure 6.8a and 5.15a) reveals that the PLM-based setup requires a 14- to 28-fold lower laser power compared to the DMD-based setup.
Another example of printing in a single focus mode is shown in Figure 6.8b. A bucky ball structure was printed again at 1440 voxels s^{-1} in a total print time of 80 s with a laser power of 380 µW incident on the PLM. In this case, no laser power adjustments are made, neither in the lateral nor in the axial direction. This showcases that the mentioned adjustments help in achieving the best printing results, but their necessity is largely dependent on the complexity of the structure design.
Figures 6.8c and d illustrate printing using multiple foci in parallel. In panel c, the same bucky ball structure was printed using five foci in parallel at an average print rate of 6000 voxels s^{-1}, such that the total printing time was reduced to 19 s. In this example, laser power adjustments were made in lateral and axial directions. The axial adjustments, with a factor of 1.25 increase in the laser power, are, however, significantly lower than in the example shown in panel a, where a factor of 2 was applied. This can be explained by the fact that proximity-effect corrections for the bucky ball structure are less of a concern than for the metamaterial unit cell.
In a last example shown in Figure 6.8d, a larger fraction of the accessible print field is used by printing four bucky ball structures in parallel using up to 16 foci at a time. This translates to a print rate of 16400 voxels s^{-1} in this example. The four structures were aligned such that the blocked zeroth-order location is in the center. As special emphasis is placed on the total print time, the rod sizes were reduced and the slicing distance was slightly increased for the shown example, resulting in a total print time of only 5.5 s for the four structures.

The printed structures are currently only some selected examples to evaluate the 3D printing performance and to identify crucial parameters to take care of. Neither the laser power budget nor the print field size is currently pushed to their limits, as was done for the examples printed using the DMD-based setup (see section 5.2). Therefore, routes for future development of the designed and built setup will be discussed in the next section.

6.3 Discussion and Outlook

In the introductory part of this chapter, I motivated the printing setup developed herein with the goal of affordable 3D laser nanoprinting. I furthermore defined this task as achieving not only a cost-effective but also a versatile 3D printing setup. This led to the implementation of 3D holographic multi-focus scanning, made possible by emerging micromirror-based phase light modulators. Alongside the goal of affordable 3D laser printing, these novel PLM devices were evaluated for their use in 3D laser nanoprinting applications, with both benefits and challenges highlighted. Ways of further increasing the printing capability of the presented setup, exceeding proof-of-principle printing tests, and further pursuing the mentioned goals will be discussed in the following.

Besides the shown examples, straightforward next steps could include identifying application examples where the benefits of a random-access 3D laser scanning can be fully utilized. Often, 3D printing is immediately thought of as a layer-by-layer approach, where slicing a structure is performed as a first step in preparing the printing. However, when printing, e.g., diagonal rods and trusses, run-up and settling times add a significant overhead in a layer-by-layer printing using galvanometric mirrors and piezoelectric stages. In a 3D scanning approach, such structures can be directly printed along their long axis, allowing for an optimized printing strategy that reduces print time and slicing artifacts.
To further speed up the printing, the distinct focus patterns could be extended to larger continuous structures polymerized at a time. So far, only patterns of foci, which are targeted to be at a diffraction-limited size, were holographically generated in the depicted examples. However, as not every part of a design structure requires the best possible resolution, voxels can be grouped, effectively increasing the voxel size. Such tuning of the voxel size, although by different means, was already proven successful in two-photon grayscale lithography [83]. Of course, this has to be accompanied by a computational routine that distributes the design structure into "macro-voxels", which are then the targets of a hologram calculation step. In doing so, the axial resolution needs to be considered, as extended lateral structures will also exhibit a larger axial extent. Furthermore, targeted smooth holographic patterns might suffer from interference effects, and therefore speckle patterns, which need to be reduced to obtain a sufficient surface quality [153]. As a dynamic voxel tuning still relies on a design addressing only a single layer per hologram, it can readily be implemented into the hologram calculation routine.
With a fast phase modulator at hand, one is, however, not limited to a single z-plane per exposure. The print speed and versatility of the setup can be further increased by either generating multi-focus patterns with foci in different z-planes or by even shaping the complete 3D optical field in the print plane via a single hologram displayed on the PLM. Clearly, these steps also need additional computational

effort in calculating the desired phase hologram, and/or restrictions to the design which can be printed might be necessary [176, 216–219].
These two discussed outlook topics mainly aim at increasing printing speeds and exploring further printing approaches based on the developed setup, rather than reducing cost. Therefore, the laser power needed understandably increases when polymerizing a larger volume per unit time, assuming the intensity remains the same. With the current setup incorporating a 400 mW output power laser, which is not selected for its low cost, but rather for providing a versatile test bed, a large power budget is still available for these kinds of improvements. The structures shown in Figure 6.8 were printed only using between 0.12 % and 1.75 % of the available laser power.
Since the aforementioned printing strategies are not limited to 2SA 3D printing, they can also be implemented using 2PP or other photoinitiation mechanisms if suitable laser sources are incorporated.

When shifting the focus from increasing print speeds to reducing the cost of the setup and increasing affordability, the different components of the setup need to be assessed one by one. Single laser diodes can be purchased at a very low cost if the user performs laser beam collimation and cleanup instead of purchasing an all-in-one solution. Doing so, laser diodes at 405 nm can be purchased at 1 €/mW, to give a rough estimate [220]. Optical components such as lenses and mirrors are not the main cost driver, but the cost could be further reduced by relying on plastic lenses and metallic mirrors, if needed. The PLM as a pre-production device is already cheaper compared to the assembly of a MEMS mirror and a piezoelectric stage, as incorporated in a previous cost-effective 3D laser nanoprinting setup [25]. As the PLM technology largely builds on the well-established and large-scale DMD manufacturing process, further cost reduction could be anticipated in the future. The objective lens was already addressed in section 6.1, as there is a large span between low-cost and high-cost devices of a factor of more than 10. A lower-cost objective lens comes at the expense of slightly worse optical and printing quality, as shown in Ref. [25]. There, decisions must be made based on the specific application.

With the presented setup at hand and the evaluation of PLM devices for 3D laser nanoprinting, the routes are now set for further development. In doing so, the unique advantages of 2SA can be exploited to reduce cost, the dynamic phase modulators incorporated can be used to potentially print an entire volumetric structure at once, or both approaches could be eventually combined.

7

Chapter 7

CONCLUSIONS AND OUTLOOK

In this thesis, I explored several avenues for advancing parallelized two-step-absorption 3D laser micro- and nanoprinting. This comprises work in the field of light-sheet 3D laser microprinting via a synergistic two-color two-step absorption, as well as the development and realization of novel approaches for parallelizing one-color two-step-absorption 3D laser printing. In the following, I will summarize the main findings, discuss the most important conclusions, and give an outlook for possible future work on this topic.

In chapter 2, I started by introducing the general concept, workflow, and chemistry of photopolymerization 3D laser printing. This included an explanation of the importance of nonlinear photoinitiation and dose accumulation in 3D laser printing, concepts I revisited several times in this work. I went on with introducing two-step absorption as an alternative photoinitiation path to the commonly employed two-photon absorption. I pointed out the advantages of 2SA, as well as current challenges and limitations. Furthermore, the two current best-performing photoinitiator molecules and their underlying photochemistry were introduced. These are benzil for one-color 2SA and biacetyl for synergistic two-color 2SA. I concluded the chapter by briefly reviewing different implementations of 3D laser printing, which serve as sources of inspiration for its technological development.

In chapter 3, I introduced light-sheet 3D laser microprinting based on synergistic two-color 2SA, as well as the dedicated setup for this printing approach originally developed by Hahn et al. [26]. In the following, I analyzed current challenges hindering the application of LS3DP and identified development opportunities to bridge this gap. Identified topics are mainly the photoresist's ingredient molecules, which are prone to unwanted side reactions, leading to, e.g., a limited build volume and increased laser power requirements for the LS3DP printing approach. While work on the photoinitiator molecules themselves was carried out in collaboration with chemists [27, 124], the work presented herein focused on technological measures to mitigate the photoresist's flaws. These include the realization of a fluidics chamber to deliver a steady stream of fresh photoresist during printing. In doing so, the printing quality of extended print jobs could be improved. Additionally, a freeform lens for power-efficient light-sheet generation was demonstrated as a proof-of-principle experiment. Although it did not outperform the current light-sheet generation, it demonstrated competitive performance and could be of future use in LS3DP.

In chapter 4, I switched gears from LS3DP and two-color 2SA to one-color 2SA and parallelization methods for increased print speeds. In doing so, I discussed a dynamic multi-focus approach using micromirror-based spatial light modulators as a suitable route, since single-focus scan speeds are limited by the photoinitiator's intermediate-state lifetime. To lay the foundation, I further outlined the methodologies for 3D holographic laser beam steering and beam splitting, and explained computational approaches for calculating computer-generated holograms on a general basis.

Based on this methodology, in chapter 5, I discussed in detail the design and implementation of a dynamic multi-focus printing setup for 2SA based on DMDs and computational holography. This included the optical setup, which was built from scratch, in which the diffractive properties of the DMD, as well as measures to compensate for angular dispersion effects, were carefully considered. In addition, the computational routine for transferring a 3D structure to a stack of holograms was outlined. The setup built allowed the demonstration of printing 3D structures at up to 61500 voxels s^{-1} using 31 foci in parallel, while relying on a compact cw diode laser. This exceeds all other 3D printing approaches based on one-color two-step absorption. Furthermore, the dynamic multi-focus approach allows for changing the focus number, the focus distribution, and each focus's individual laser power at kilohertz rates. Furthermore, spatiotemporal proximity effects were introduced in the particular context of 2SA 3D printing. How they affect the printing quality was examined in printing experiments and via a rate-equation-based dose simulation. In this regard, the printing strategy has been adapted for different structures to achieve the best possible printing results.

In chapter 6, a second version of a dynamic multi-focus printing approach was realized. This relied on micromirror-based phase light modulators, an emerging class of MEMS-based spatial light modulators that allow phase modulation at kilohertz rates at an affordable cost. Likewise, the goal was set to demonstrate an affordable 3D laser nanoprinting setup based on PLMs as the single device for achieving 3D holographic beam steering. The designed and built setup, therefore, only needs a laser source, the PLM, an objective lens, and a camera, besides lenses and mirrors, for 3D laser nanoprinting. The cost of the employed PLM is already lower compared to the combination of, e.g., a steerable mirror and a piezoelectric stage, and might be reduced in the future when PLMs fully enter the commercial market. Furthermore, due to phase modulation, the laser power efficiency increased by approximately 20× compared to the DMD-based printing setup. After evaluating PLMs for suitability for 3D laser nanoprinting, e.g., by implementing a correction for their distorted surfaces, the printing performance was investigated. In doing so, the printing of single- and multi-focus test structures was demonstrated at print rates of up to 16000 voxels s^{-1}, but only using 7 mW of cw laser light out of the laser source and a solely holographic beam steering without macroscopic moving parts. These proof-of-principle experiments provide a powerful and versatile test bed for further developments.

OUTLOOK

Two-step absorption, as a novel photoinitiation mechanism for 3D laser micro- and nanoprinting, has attracted considerable attention since its first report less than five years ago [24]. It started from the beginning with low laser power consumption, enabling the use of compact cw lasers and, understandably, raising expectations for inexpensive, compact, and largely parallelized 3D laser printing. The present work might fall into a consolidation phase, where initial strategies are refined and novel routes are sought based on the knowledge gained. Possible future steps should comprise a potentially long-term effort of trying to gain an understanding of the photochemical process, as well as an application-oriented search for suitable combinations of specific printing approaches and applications made possible by these.
Apart from the close relation to 2SA, I adapted novel holographic printing approaches based on micromirror spatial light modulators for 3D laser micro- and nanoprinting, where only a few approaches are reported in the literature [80, 156, 193], and none have been reported using two-step absorption and/or the recently emerging PLMs. Therefore, this outlook section should also include further development strategies utilizing these approaches, which may be independent of the photoinitiation mechanism employed.
As some specific next steps were already discussed in the last sections of the chapters 3, 5, and 6, these will only be briefly revisited here.

The random-access 3D holographic laser-scanning capability adopted for micromirror-based spatial light modulators can be further expanded immediately using the presented setup. This can span different levels of computational complexity, and approaches need to be chosen based on the demonstrative application in mind.
Often, it is immediately thought of as a layer-by-layer approach, but the present 3D printing setup is not limited to this. Diagonal rods and trusses, or 3D curved voxel lines, can be printed without any additional restrictions compared to layer-by-layer focus-scanning. Clearly, such an adaptation of the printing strategy is most beneficial for applications that currently suffer from printing artifacts and/or large overhead times for positioning galvanometric mirrors and piezoelectric stages in conventional approaches.

Furthermore, dynamic voxel tuning could be implemented, grouping voxels into "macro-voxels" in regions of the structure that do not require the highest achievable resolution. By doing so, the print rates could be further increased.
Going even a step further, an entire 3D structure could be encoded in a single hologram and exposed and polymerized in a single exposure step. Clearly, one crucial part is the calculation of the mentioned holographic pattern to shape the 3D light field in the print volume. This might restrict the 3D structure to be printed to specific designs, and/or require computational effort to calculate the hologram. Of course, the laser power requirement increases as the number of voxels polymerized at a time increases. It should be noted, however, that, since the extinction is rather low for the photoresists employed, the laser power requirement does not increase significantly when going from layer-by-layer polymerization to volume polymerization, since only a minor fraction of the light is absorbed. With the setup and, e.g., benzil-based photoresists at hand, the polymerization of volumes with a side length of tens of micrometers is possible in less than a second. With another concern being dose-accumulation effects in 2SA photoinitiation, there are challenges to address, but overcoming them might yield large gains in print rates.

Current implementations of 2SA 3D printing still lack a "killer application" that demonstrates a clear advantage over conventional 3D laser nanoprinting. For the large number of applications, current 2SA approaches are not able to provide the needed print quality across a large build volume at satisfactory print speeds. Therefore, the significantly lower device cost is not convincing enough. For application-oriented use, either niche applications have to be defined or the quality has to be increased while maintaining the cost advantage.
Such niche applications could include cases where one can gain an advantage from the increased resolution offered by 2SA approaches at 405 nm compared to typical 2PP at around 800 nm, such as for specialized applications in optics and photonics. Other such niches might likewise be hybrid devices, combining 2PP with 2SA and a suitable photoresist, or the incorporation of 3D laser printing functionality into laser-scanning microscopes. And of course, affordability is a major criterion for research groups exploring the application of 3D laser printing, or for educational facilities. In this regard, the foundation was set within this work for even further cost reduction by combining the 3D beam steering into a single device.
As already addressed several times, the main factor limiting improvement in terms of printing performance, as defined, is the photoresist. This has, however, turned out to be difficult to address, largely due to the vast parameter space of molecules and printing parameters. So far, screening photoinitiator candidates started from the proven 2SA initiators benzil and biacetyl, and drawing a map of structurally similar compounds. These molecules need to be synthesized and experimentally investigated so that a working initiator molecule is found or at least conclusions can be drawn, aiming to understand the relationship between chemical structure,

photophysical properties, and printing performance. This procedure takes a lot of resources. Therefore, computational efforts are ongoing to reproduce experimental results and potentially predict suitable molecules, which could guide experimental screening [221]. Furthermore, analytical and quantitative experiments to better understand the photoinitiation and quenching mechanisms are a widely debated approach. Such experiments could provide insight into reaction products and reveal rates of different processes, allowing important and less important pathways to be weighted. However, it is not clear how to perform such experiments while maintaining printing conditions, which require strongly focused lasers and produce only tiny amounts of reaction products. If this route is pursued, a clear research question must be posed and an experiment designed to answer it.
While this dilemma is still present, the routes already taken within this thesis to mitigate dose accumulation effects of present photoresists could be expanded. With the fluidics addition for LS3DP introduced in section 3.3, advantages and disadvantages were already discussed. Some disadvantages are related to the special geometry of LS3DP. However, a fluidics addition might also be useful to reduce dose accumulation effects in one-color 2SA printing. In this case, the geometrical restrictions of LS3DP are relaxed, allowing already reported and partially commercially available solutions to be incorporated, thereby increasing the build volume.

I began this thesis by outlining the impact of 3D printing on manufacturing and innovation cycles. In fact, often only a small number of parts of a whole product are 3D printed. These parts are still so important that it is worth optimizing their manufacturing, as the sum of many small optimizations makes a competitive product. I want to conclude by taking this as a metaphor. Within the large field of 3D laser micro- and nanoprinting, this work addressed specialized challenges and successfully demonstrated the proof-of-concept of new printing approaches. I hope that the sum of these contributions to the field of 3D laser micro- and nanoprinting is valuable, supporting the exploration of novel printing techniques and applications.

Appendix A

APPENDIX

A.1 PHOTORESIST COMPOSITIONS AND PHOTOINITIATOR MOLECULES

Table A.1: Description of photoresist (PR) compositions as used in this work. Each resist consists of monomer, photoinitiator (PI), and quencher (Q) molecules. Following the composition of PRi, different photoinitiators are compared. Experimental details regarding the photoresist mixture are given in the respective references.

resist	monomer	photoinitiator	c_{PI} (mM)	quencher	c_{Q} (mM)	source
PRA	PETA	biacetyl	110	TEMPO	11	[44]
PRB	TMPTA	biacetyl	110	TEMPO	11	[44]
PRC	DPEHA	biacetyl	110	TEMPO	11	[44]
PRi	PETA	(varying)	100	TEMPO	50	[27]
PR1	PETA	benzil	100	BTPOS	50	[24, 96]
PR3	TMPTA	benzil	100	BTPOS	50	[24, 96]

Table A.2: Full names of the photoinitiator molecules as stated in Figure 3.6 [27, 124].

abbreviation	full name
1-NT	1,2-Di(naphthalen-1-yl)ethane-1,2-dione
BBZ	1,4-Bisbenzil
F2BZ	4,4′-Difluorobenzil
HD	3,4-Hexanedione
B1-1	1-(4-Fluorophenyl)-2-phenylethane-1,2-dione
B1-2	1-(4-Chlorophenyl)-2-phenyl-ethane-1,2-dione
B1-5	1-Phenyl-2-(p-tolyl)ethane-1,2-dione
B2-1	1-(3-Fluorophenyl)-2-phenyl-ethane-1,2-dione
B2-2	1-(3,5-Dimethylphenyl)-2-phenyl-ethane-1,2-dione
B2-3	1,2-Bis(3,5-difluorophenyl)ethane-1,2-dione
B2-5	1,2-Bis(3-fluorophenyl)ethane-1,2-dione
B3-1	1-[3-(2-Oxo-2-phenyl-acetyl)phenyl]-2-phenyl-ethane-1,2-dione
B3-4	2,2′-(1,3-Phenylene)bis(1-(3-fluorophenyl)ethane-1,2-dione)
B4-3	1-(4-Methylphenyl)-2-[4-[2-(4-methylphenyl)-1,2-dioxoethyl]phenyl]ethane-1,2-dione
BA	2,3-Butanedione

A.2 PRINTING PARAMETERS

The specific printing parameters for the structures presented in this work are detailed in table A.3 for the structures shown in chapter 5, as well as in table A.5 for the structures shown in chapter 6. Information regarding the photoresist composition can be found in table A.1. The following part will elaborate on the computational procedures used to define the exposure sequence and to mitigate dose-accumulation effects. This includes the methodology for generating sequences of multi-focus distributions, which we term the printing strategy (PS), and the algorithm for pre-compensating proximity effects (PC).

A.2.1 Printing Strategies

I. Automated multi-line tiling: For each layer of the structure, the exposure area is automatically enclosed within a bounding box. This area is then partitioned into a set of rectangular tiles, with a defined minimum side length to ensure a minimum separation between adjacent foci. Each tile is printed using a line-scan path with a single focus. The dimensions of these tiles are dynamically adjusted based on the total number of tiles, which must not exceed a predefined maximum number of available foci. When a tile requires fewer exposure points than others, dummy foci are placed outside the build area. This ensures that the total number of foci, and thus the laser power per focus, remains constant throughout the exposure of a single multi-focus pattern. Drawbacks of this strategy include visible stitching seams and its lack of optimization for the highest print rate.

II. Iterative distance-based grouping: This algorithm begins by compiling a single list of all exposure coordinates for a given layer, initially arranged for a line-scan trajectory. An iterative procedure then groups these coordinates into discrete multi-focus distributions. For each distribution, a set of coordinates is selected, ensuring that the Euclidean distance between any two points in the set exceeds a predefined minimum threshold. Points that do not meet this criterion are temporarily rejected. The process is repeated on the set of rejected coordinates until all exposure points have been assigned to a multi-focus distribution. This method partially preserves the character of a multi-line scan because of the initial coordinate ordering. As with the previous method, dummy foci are added to distributions that do not utilize the maximum available number of foci. Drawbacks of this strategy include partly random scanning, which reduces surface quality, and the large number of single-focus exposures if no sacrifice is made in the minimum distance.

Table A.3: Printing parameters for all printed structures shown in chapter 5. The first column refers to the Figure number. The laser power P_{voxel} refers to the power per voxel at the entrance pupil of the objective lens. The total laser power at the entrance pupil is therefore P_{voxel} × number of foci. P_{laser} is the total laser power out of the laser. "PR" refers to the photoresist as given in table A.1. "PS" refers to the printing strategy as outlined below. "PC" refers to the proximity correction as outlined below. "LP_{ax}" states the factor by which the laser power was changed for different layers of the structure, if such a correction was applied.

#	print time (s)	P_{voxel} (µW)	P_{laser} (mW)	update rate (Hz)	slicing (nm)	number of foci	PR	PS	PC	LP_{ax}
5.12 a	8.1	150	380	2400	200	31	PR1	II	no	-
5.12 b	14	133	85	2400	200	8	PR1	III	no	-
5.12 c	12	180	360	2400	200	24	PR1	III	yes	-
5.12 d	18	133	160	2400	200	15	PR1	I	yes	-
5.13 a	0.52	140	18	2400	-	1	PR1	IV	-	-
5.13 b	60	186	18	1440	148	1	PR3	IV	-	0.71
5.14 a	23	193	230	2400	200	15	PR3	II	yes	0.61
5.14 b	84	220	18	2400	200	1	PR3	IV	-	-
5.15 a	125	100	8	1440	200	1	PR1	IV	-	-
5.15 b	125	125	10	1440	200	1	PR1	V	-	-
5.16 a1	8.3	250	20	2400	-	1	PR1	IV	-	-
5.16 a2	0.55	225	18	2400	-	1	PR1	IV	-	-
5.16 b1	8.3	250	20	2400	-	1	PR1	V	-	-
5.16 b2	0.55	225	18	2400	-	1	PR1	V	-	-

III. Manual multi-line tiling: This approach is analogous to the automated tiling method described above. However, the rectangular tiles are defined manually and remain uniform across all layers of the structure.

IV. Single-focus ordered scanning: This mimics a conventional line-scan approach in which a single laser focus scans the exposure pattern of each layer along a line-by-line trajectory.

V. Single-focus random scanning: The exposure points within each layer are addressed in a randomized sequence rather than an ordered path [23].

Table A.4: Printing parameters for all printed structures shown in chapter 6. The first column refers to the Figure number. The laser power P_{voxel} refers to the power per voxel at the entrance pupil of the objective lens. The total laser power at the entrance pupil is therefore $P_{\mathrm{voxel}} \times$ number of foci. P_{laser} is the total laser power out of the laser and transmitted through an NG3 absorptive filter with a measured transmittance of 4.4 %. "PR" refers to the photoresist as given in table A.1. "PS" refers to the printing strategy as outlined below. "PC" refers to the proximity correction as outlined below. "$\mathrm{LP}_{\mathrm{ax}}$" states the factor by which the laser power was changed for different layers of the structure, if such a correction was applied.

#	print time (s)	P_{voxel} (µW)	P_{laser} (mW)	update rate (Hz)	slicing (nm)	number of foci	PR	PS	PC	$\mathrm{LP}_{\mathrm{ax}}$
6.8 a	123	170	0.53	1440	200	1	PR1	IV	no	0.5
6.8 b	80	135	0.4	1440	200	1	PR1	IV	no	-
6.8 c	19	116	1.65	1440	200	5	PR1	II	no	0.8
6.8 d	5.5	131	7	1440	235	16	PR1	III	no	-

A.2.2 Pre-Compensation of Proximity Effects

To reduce over-exposure and subsequent feature distortion inside densely patterned regions, a pre-compensation algorithm based on the approach by Hahn et al. [26] was employed. This procedure adjusts the exposure dose computationally based on local feature density.

The algorithm starts by slicing and discretizing the 3D model of the target structure into a series of binary 2D images, with a typical slicing distance of 200 nm. These slices are then assembled into a 3D array, which is subsequently filtered by convolution with a 3D Gaussian kernel. The standard deviation values for the Gaussian kernel were determined empirically through a trial-and-error process to get the best printing results.

Next, a correction mask is generated by inverting the filtered 3D array. This mask is then multiplied element-wise with the original, unfiltered array. This step effectively restores the intended sharp edges of the structure, which were blurred by the convolution operation. The final output is a series of 2D grayscale images that serve as the input target to the hologram calculation. The grayscale value at each coordinate directly modulates the relative intensity of the corresponding laser focus in a multi-focus pattern. This process selectively decreases the applied intensity in dense regions of the structure, thereby preventing detrimental proximity effects and improving overall fabrication fidelity [23].

A.3 PARAMETERS OF THE RATE-EQUATION-BASED DOSE SIMULATION

Table A.5: Rate coefficients as used in the rate-equation calculations discussed in section 5.3. Sources of the values are given in the third column. The fitting refers to a manual comparison of the simulated results with the experiment (see Figure 5.16). R refers to the ideal-gas constant, $T = 296\,\mathrm{K} = 23\,°\mathrm{C}$ is the temperature set. As PETA is the monomer used, the viscosity η is set to $\eta = 1\,\mathrm{Pa\,s}$. The diffusion-limited bimolecular rates are calculated to be $6 \times 10^6\,\mathrm{s}^{-1}$. The extinction coefficients of benzil in the ground and excited state are $\varepsilon_1 = 41\,\mathrm{M}^{-1}\,\mathrm{cm}^{-1}$ and $\varepsilon_2 = 3400\,\mathrm{M}^{-1}\,\mathrm{cm}^{-1}$, respectively. The pre-factor of $1.92\,\mathrm{mol}^{-1}\,\mathrm{J}^{-1}\,\mathrm{m}^{-1}$ is added for unit conversion from a molar decadic extinction coefficient to an absorption cross section. From the laser power ($P = 150\,\mu\mathrm{W}$) and the laser focus's FWHM of 170 nm, the intensity values are calculated. Therefore, these are in the same regime as the experimental values.

coefficient	value	source
k_{R2}	$3 \times 10^2\,\mathrm{s}^{-1}$	fit
k_{R1}	$3 \times 10^2\,\mathrm{s}^{-1}$	fit
k_{D2}	$1 \times 10^6\,\mathrm{s}^{-1}$	based on [26]
k_{D1}	$1.25 \times 10^4\,\mathrm{s}^{-1}$	based on [24]
k_{TTA}	$8000RT/3\eta$	diffusion limited [26]
k_{Q}	$8000RT/3\eta$	diffusion limited [26]
$k_{\mathrm{Diff,A}}$	$2 \times 10^2\,\mathrm{s}^{-1}$	fit, based on [59]
$k_{\mathrm{Diff,Q}}$	$1 \times 10^2\,\mathrm{s}^{-1}$	fit, based on [59]
k_1	$1.92\,\mathrm{mol}^{-1}\,\mathrm{J}^{-1}\,\mathrm{m}^{-1} \cdot 0.1 \cdot \varepsilon_1 \lambda I(t)$	fit, based on [26]
k_2	$1.92\,\mathrm{mol}^{-1}\,\mathrm{J}^{-1}\,\mathrm{m}^{-1} \cdot \varepsilon_2 \lambda I(t)$	based on [26]

BIBLIOGRAPHY

[1] I. Gibson, D. Rosen, B. Stucker, and M. Khorasani, *Additive Manufacturing Technologies* (Springer International Publishing, Cham, 2021) (cited on page 3).

[2] ASTM International, *Wohlers Report 2025 shows 9.1% AM industry growth*, (2025) `https://www.astm.org/news/press-releases/wohlers-report-2025` (visited on 10/10/2025) (cited on page 3).

[3] Siemens AG, *Die Zukunft ist 3D: Additive Fertigung bei Siemens*, (2025) `https://www.siemens.com/de/de/unternehmen/stories/forschung-technologien/additivefertigung/additive-fertigung.html` (visited on 10/10/2025) (cited on page 3).

[4] TRUMPF SE + Co. KG, *What industries use 3D printing*, (2025) `https://www.trumpf.com/en_CA/newsroom/stories/what-industries-use-3d-printing/` (visited on 10/10/2025) (cited on page 3).

[5] Authentise, *From Buzz to Business: How Airbus, Bugatti & Adidas Use AM in 2025*, (2025) `https://www.authentise.com/post/from-buzz-to-business-how-airbus-bugatti-adidas-use-am-in-2025` (visited on 10/10/2025) (cited on page 3).

[6] Eos GmbH, *Medizinische Innovationen fördern: Industrieller 3D-Druck für die Medizintechnik*, (2025) `https://www.eos.info/de/industrien/medizintechnik` (visited on 10/10/2025) (cited on page 3).

[7] H. B. Mamo, M. Adamiak, and A. Kunwar, "3D printed biomedical devices and their applications: A review on state-of-the-art technologies, existing challenges, and future perspectives", Journal of the Mechanical Behavior of Biomedical Materials **143**, 105930 (2023) (cited on page 3).

[8] D. Zielke, *Mikrosysteme* (Springer Berlin Heidelberg, Berlin, Heidelberg, 2025) (cited on page 3).

[9] Y. Wang, M.-H. Chi, J. J.-C. Lou, and C.-Z. Chen, eds., *Handbook of Integrated Circuit Industry* (Springer Nature Singapore, Singapore, 2024) (cited on page 3).

[10] S. O'Halloran, A. Pandit, A. Heise, and A. Kellett, "Two-Photon Polymerization: Fundamentals, Materials, and Chemical Modification Strategies", Advanced Science **10**, 1–18 (2023) (cited on pages 3, 4, 9).

[11] T. Baldacchini, *Three-Dimensional Microfabrication Using Two-photon Polymerization*, edited by T. Baldacchini (William Andrew, 2016) (cited on pages 3, 4, 9, 11, 16).

[12] P. Somers, A. Münchinger, S. Maruo, C. Moser, X. Xu, and M. Wegener, "The physics of 3D printing with light", Nature Reviews Physics **6**, 99–113 (2023) (cited on pages 3, 32).

[13] G. Zyla and M. Farsari, "Frontiers of Laser-Based 3D Printing: A Perspective on Multi-Photon Lithography", Laser & Photonics Reviews **18** (2024) (cited on pages 4, 28, 32).

[14] S. Maruo, O. Nakamura, and S. Kawata, "Three-dimensional microfabrication with two-photon-absorbed photopolymerization", Optics Letters **22**, 132 (1997) (cited on pages 4, 16, 17, 28).

[15] A. K. Nguyen and R. J. Narayan, "Two-photon polymerization for biological applications", Materials Today **20**, 314–322 (2017) (cited on pages 4, 32).

[16] G. Weisgrab, O. Guillaume, Z. Guo, P. Heimel, P. Slezak, A. Poot, D. Grijpma, and A. Ovsianikov, "3D Printing of large-scale and highly porous biodegradable tissue engineering scaffolds from poly(trimethylene-carbonate) using two-photon-polymerization", Biofabrication **12**, 045036 (2020) (cited on page 4).

[17] F. Colombo, M. Taale, F. Taheri, M. Villiou, T. Debatin, G. Dulatahu, P. Kollenz, M. Schmidt, C. Schlagheck, J. Wittbrodt, and C. Selhuber-Unkel, "Two-Photon Laser Printing to Mechanically Stimulate Multicellular Systems in 3D", Advanced Functional Materials **34** (2024) (cited on page 4).

[18] S. Yu, Q. Du, C. R. Mendonca, L. Ranno, T. Gu, and J. Hu, "Two-photon lithography for integrated photonic packaging", Light: Advanced Manufacturing **4**, 1 (2023) (cited on page 4).

[19] T. Gissibl, S. Thiele, A. Herkommer, and H. Giessen, "Two-photon direct laser writing of ultracompact multi-lens objectives", Nature Photonics **10**, 554–560 (2016) (cited on page 4).

[20] H. Wang, W. Zhang, D. Ladika, H. Yu, D. Gailevičius, H. Wang, C.-F. Pan, P. N. S. Nair, Y. Ke, T. Mori, J. Y. E. Chan, Q. Ruan, M. Farsari, M. Malinauskas, S. Juodkazis, M. Gu, and J. K. W. Yang, "Two-Photon Polymerization Lithography for Optics and Photonics: Fundamentals, Materials, Technologies, and Applications", Advanced Functional Materials **33**, 1–51 (2023) (cited on pages 4, 28, 32).

[21] O. M. Young, X. Xu, S. Sarker, and R. D. Sochol, "Direct laser writing-enabled 3D printing strategies for microfluidic applications", Lab on a Chip **24**, 2371–2396 (2024) (cited on page 4).

[22] S. Grebenyuk, A. R. Abdel Fattah, M. Kumar, B. Toprakhisar, G. Rustandi, A. Vananroye, I. Salmon, C. Verfaillie, M. Grillo, and A. Ranga, “Large-scale perfused tissues via synthetic 3D soft microfluidics”, Nature Communications **14**, 193 (2023) (cited on page 4).

[23] The preceding paragraphs of this section were partly formulated with the help of AI tools such as OpenAI ChatGPT GPT-5 and Google Gemini 2.5 Pro (cited on pages 4, 138, 139).

[24] V. Hahn, T. Messer, N. M. Bojanowski, E. R. Curticean, I. Wacker, R. R. Schröder, E. Blasco, and M. Wegener, “Two-step absorption instead of two-photon absorption in 3D nanoprinting”, Nature Photonics **15**, 932–938 (2021) (cited on pages 4, 11, 16–19, 21–23, 27, 29, 47, 58, 65, 85, 96, 97, 100, 102, 131, 136, 140).

[25] T. Messer, M. Hippe, J. Gao, A. Naber, and M. Wegener, “A shoe-box-sized 3D laser nanoprinter based on two-step absorption”, Light: Advanced Manufacturing **5**, 269 (2024) (cited on pages 4, 26, 27, 29, 58, 97, 108, 112, 128).

[26] V. Hahn, P. Rietz, F. Hermann, P. Müller, C. Barner-Kowollik, T. Schlöder, W. Wenzel, E. Blasco, and M. Wegener, “Light-sheet 3D microprinting via two-colour two-step absorption”, Nature Photonics **16**, 784–791 (2022) (cited on pages 4, 5, 17, 20, 24–26, 31–34, 36, 38–42, 47, 48, 55, 59, 96, 102, 103, 108, 129, 139, 140).

[27] N. M. Bojanowski, A. Vranic, V. Hahn, P. Rietz, T. Messer, J. Brückel, C. Barner-Kowollik, E. Blasco, S. Bräse, and M. Wegener, “Search for Alternative Two-Step-Absorption Photoinitiators for 3D Laser Nanoprinting”, Advanced Functional Materials **33**, 2212482 (2023) (cited on pages 4, 21, 27, 29, 39–41, 58, 100, 129, 136).

[28] V. Hahn, F. Mayer, M. Thiel, and M. Wegener, “3-D Laser Nanoprinting”, Optics and Photonics News **30**, 28 (2019) (cited on pages 4, 5, 20, 25, 31).

[29] V. Hahn, P. Kiefer, T. Frenzel, J. Qu, E. Blasco, C. Barner-Kowollik, and M. Wegener, “Rapid Assembly of Small Materials Building Blocks (Voxels) into Large Functional 3D Metamaterials”, Advanced Functional Materials **30**, 1907795 (2020) (cited on pages 8, 27–29, 59, 65, 94).

[30] L. Li and J. T. Fourkas, “Multiphoton polymerization”, Materials Today **10**, 30–37 (2007) (cited on page 8).

[31] T. Bückmann, N. Stenger, M. Kadic, J. Kaschke, A. Frölich, T. Kennerknecht, C. Eberl, M. Thiel, and M. Wegener, “Tailored 3D Mechanical Metamaterials Made by Dip-in Direct-Laser-Writing Optical Lithography”, Advanced Materials **24**, 2710–2714 (2012) (cited on page 8).

[32] J. Fischer and M. Wegener, “Three-dimensional direct laser writing inspired by stimulated-emission-depletion microscopy [Invited]”, Optical Materials Express **1**, 614 (2011) (cited on pages 8, 13, 21, 32, 96).

[33] B. E. Kelly, I. Bhattacharya, H. Heidari, M. Shusteff, C. M. Spadaccini, and H. K. Taylor, “Volumetric additive manufacturing via tomographic reconstruction”, Science **363**, 1075–1079 (2019) (cited on pages 9, 31, 32).

[34] T. Frenzel, “On 3D Chiral Mechanical Metamaterials”, PhD thesis (Karlsruhe Institute of Technology (KIT), 2020) (cited on page 9).

[35] J. Fischer, “Three-dimensional optical lithography beyond the diffraction limit”, PhD thesis (Karlsruhe Institute of Technology (KIT), 2012) (cited on pages 9, 12, 14, 15, 89).

[36] M. Hippler, “3D Laser Lithography of Stimuli-Responsive Hydrogels”, PhD thesis (Karlsruhe Institute of Technology (KIT), 2020) (cited on page 10).

[37] T. N. Eren, J. Liang, J. L. G. Schneider, M. Wegener, J. Bauer, K. Ehrmann, F. Feist, and C. Barner-Kowollik, “Soft and Stiff 3D Microstructures by Step-Growth Photopolymerization Using a Single Photoresin and Multi-Photon Laser Printing”, Advanced Functional Materials (2025) (cited on page 9).

[38] B. Tieke, *Makromolekulare Chemie: Eine Einführung*, 3rd ed. (Wiley, Hoboken, 2014) (cited on page 9).

[39] W. A. Green, *Industrial Photoinitiators* (CRC Press, Apr. 2010) (cited on page 10).

[40] A. S. v. d. Nes, L. Billy, S. F. Pereira, and J. J. M. Braat, “Calculation of the vectorial field distribution in a stratified focal region of a high numerical aperture imaging system”, Optics Express **12**, 1281 (2004) (cited on page 12).

[41] P. Kiefer, “On Next-Generation Multi-Focus 3D Laser Printing”, PhD thesis (Karlsruhe Institute of Technology (KIT), 2023) (cited on pages 12, 13, 54, 59, 60, 85, 99).

[42] J. Fischer and M. Wegener, “Three-dimensional optical laser lithography beyond the diffraction limit”, Laser & Photonics Reviews **7**, 22–44 (2013) (cited on pages 11, 12, 14, 21).

[43] P. Kiefer, V. Hahn, M. Nardi, L. Yang, E. Blasco, C. Barner-Kowollik, and M. Wegener, “Sensitive Photoresists for Rapid Multiphoton 3D Laser Micro- and Nanoprinting”, Advanced Optical Materials **8**, 2000895 (2020) (cited on pages 11, 12, 28, 58, 99).

[44] V. Hahn, “On 3D Laser Micro- and Nanoprinting:Faster, Finer, and More Affordable”, PhD thesis (Karlsruhe Institute of Technology, 2022) (cited on pages 13, 15, 17, 19, 21, 23, 24, 26, 27, 34–40, 47, 51, 58–60, 97, 98, 102, 103, 105, 136).

[45] L. Yang, A. Münchinger, M. Kadic, V. Hahn, F. Mayer, E. Blasco, C. Barner-Kowollik, and M. Wegener, "On the Schwarzschild Effect in 3D Two-Photon Laser Lithography", Advanced Optical Materials **7** (2019) (cited on pages 13, 99, 100, 104).

[46] M. Göppert-Mayer, "Über Elementarakte mit zwei Quantensprüngen", Annalen der Physik **401**, 273–294 (1931) (cited on page 16).

[47] M. Regehly, Y. Garmshausen, M. Reuter, N. F. König, E. Israel, D. P. Kelly, C. Y. Chou, K. Koch, B. Asfari, and S. Hecht, "Xolography for linear volumetric 3D printing", Nature **588**, 620–624 (2020) (cited on pages 20, 31, 59).

[48] R. E. Schwerzel, V. E. Wood, V. D. McGinniss, and C. M. Verber, "Three-Dimensional Photochemical Machining With Lasers", in Applications of Lasers to Industrial Chemistry, Vol. 0458, edited by R. L. Woodin and A. Kaldor, May 1984 (May 1984), p. 90 (cited on pages 20, 25).

[49] V. Hahn, N. M. Bojanowski, P. Rietz, F. Feist, M. Kozlowska, W. Wenzel, E. Blasco, S. Bräse, C. Barner-Kowollik, and M. Wegener, "Challenges and Opportunities in 3D Laser Printing Based on (1 + 1)-Photon Absorption", ACS Photonics **10**, 24–33 (2023) (cited on pages 21, 29, 30).

[50] J. P. Fouassier and J. Lalevée, "One-Component Photoinitiating Systems", in *Photoinitiators for Polymer Synthesis* (Wiley, July 2012), pp. 127–197 (cited on pages 21, 22).

[51] C. J. Brown and R. Sadanaga, "The crystal structure of benzil", Acta Crystallographica **18**, 158–164 (1965) (cited on page 22).

[52] W. G. McGimpsey and J. C. Scaiano, "A two-photon study of the "reluctant" Norrish type I reaction of benzil", Journal of the American Chemical Society **109**, 2179–2181 (1987) (cited on page 22).

[53] T.-S. Fang, R. E. Brown, C. L. Kwan, and L. A. Singer, "Photophysical studies on benzil. Time resolution of the prompt and delayed emissions and a photokinetic study indicating deactivation of the triplet by reversible exciplex formation", The Journal of Physical Chemistry **82**, 2489–2496 (1978) (cited on pages 22, 103).

[54] A. A. Lamola and G. S. Hammond, "Mechanisms of Photochemical Reactions in Solution. XXXIII. Intersystem Crossing Efficiencies", The Journal of Chemical Physics **43**, 2129–2135 (1965) (cited on page 22).

[55] N. J. Turro, *Molecular Photochemistry* (1967) (cited on pages 22, 23, 25).

[56] T. Cáceres, M. Encinas, and E. Lissi, "Photocleavage of benzil", Journal of Photochemistry **27**, 109–114 (1984) (cited on page 22).

[57] L. Flamigni, F. Barigelletti, S. Dellonte, and G. Orlandi, "Photophysical properties of benzil in solution: triplet state deactivation pathways", Journal of Photochemistry **21**, 237–244 (1983) (cited on pages 22, 23).

[58] M. Mukai, S. Yamauchi, and N. Hirota, "A time-resolved EPR study of one- and two-photon processes in the photochemical reactions of benzil", The Journal of Physical Chemistry **93**, 4411–4413 (1989) (cited on page 22).

[59] J. B. Mueller, J. Fischer, F. Mayer, M. Kadic, and M. Wegener, "Polymerization Kinetics in Three-Dimensional Direct Laser Writing", Advanced Materials **26**, 6566–6571 (2014) (cited on pages 23, 140).

[60] C. Decker and A. D. Jenkins, "Kinetic approach of oxygen inhibition in ultraviolet- and laser-induced polymerizations", Macromolecules **18**, 1241–1244 (1985) (cited on page 23).

[61] P. Gijsman, "A review on the mechanism of action and applicability of Hindered Amine Stabilizers", Polymer Degradation and Stability **145**, 2–10 (2017) (cited on page 23).

[62] R. B. Grubbs, "Nitroxide-Mediated Radical Polymerization: Limitations and Versatility", Polymer Reviews **51**, 104–137 (2011) (cited on page 23).

[63] A. S. Tatikolov, P. P. Levin, T. A. Kokrashvili, and V. A. Kuz'min, "Quenching of the triplet states of carbonyl compounds by nitroxyl radicals", Bulletin of the Academy of Sciences of the USSR Division of Chemical Science **32**, 465–468 (1983) (cited on page 24).

[64] L. J. Johnston, M. Tencer, and J. C. Scaiano, "Evidence for hydrogen transfer in the photochemistry of 2,2,6,6-tetramethylpiperidine N-oxyl", The Journal of Organic Chemistry **51**, 2806–2808 (1986) (cited on page 24).

[65] A. Singh, A. R. Scott, and F. Sopchyshyn, "Flash photolysis of camphorquinone and biacetyl", Journal of Physical Chemistry **73**, 2633–2643 (1969) (cited on pages 24, 25).

[66] R. Bensasson and E. J. Land, "Triplet-triplet extinction coefficients via energy transfer", Transactions of the Faraday Society **67**, 1904 (1971) (cited on pages 24, 25).

[67] G. A. Burdock, *Fenaroli's Handbook of Flavor Ingredients* (CRC Press, Dec. 2004) (cited on pages 24, 25).

[68] K. Eriks, T. D. Hayden, S. H. Yang, and I. Y. Chan, "Crystal and molecular structure of biacetyl (2,3-butanedione), (H3CCO)2, at -12 and -100.degree.C", Journal of the American Chemical Society **105**, 3940–3942 (1983) (cited on page 25).

[69] P. Harber, K. Saechao, and C. Boomus, "Diacetyl-Induced Lung Disease", Toxicological Reviews **25**, 261–272 (2006) (cited on page 25).

[70] H. L. J. Bäckström, K. Sandros, J.-E. Lindgren, E. Varde, and G. Westin, "Transfer of Triplet State Energy in Fluid Solutions. I. Sensitized Phosphorescence and Its Application to the Determination of Triplet State Lifetimes.", Acta Chemica Scandinavica **14**, 48–62 (1960) (cited on page 25).

[71] J. W. Sidman and D. S. McClure, "Electronic and Vibrational States of Biacetyl and Biacetyl-d 6 . II. Vibrational States 1", Journal of the American Chemical Society **77**, 6471–6474 (1955) (cited on page 25).

[72] A. Horowitz and J. G. Calvert, "Emission studies of the mechanism of gaseous biacetyl photolysis at 3450, 3650, 3880, and 4358 a and 28°C", International Journal of Chemical Kinetics **4**, 207–227 (1972) (cited on page 25).

[73] H. L. J. Bäckström, K. Sandros, H. Haraldsen, A. Grönvall, B. Zaar, and E. Diczfalusy, "The Quenching of the Long-lived Fluorescence of Biacetyl in Solution.", Acta Chemica Scandinavica **12**, 823–832 (1958) (cited on page 25).

[74] J. C. Scaiano, "Intermolecular photoreductions of ketones", Journal of Photochemistry **2**, 81–118 (1973) (cited on page 25).

[75] S. M. Wolf, "Applied Photochemistry for Multicolor Photolithography", PhD thesis (University of Maryland, 2019) (cited on page 25).

[76] C. C. Badcock, H. W. Sidebottom, J. G. Calvert, B. R. Rabe, and E. K. Damon, "Triplet-triplet annihilation reaction in biacetyl vapor excited at 4365 Ang and 25.deg.", Journal of the American Chemical Society **94**, 19–24 (1972) (cited on page 25).

[77] C. Richard, M. Bouchy, J. C. Andre, and M. Niclause, "Radiationless transitions between excited singlet states of biacetyl", International Journal of Chemical Kinetics **10**, 213–226 (1978) (cited on page 25).

[78] M. Almgren, "The natural phosphorescence lifetime of biacetyl and benzil in fluid solution", Photochemistry and Photobiology **6**, 829–840 (1967) (cited on page 25).

[79] P. Somers, Z. Liang, J. E. Johnson, B. W. Boudouris, L. Pan, and X. Xu, "Rapid, continuous projection multi-photon 3D printing enabled by spatiotemporal focusing of femtosecond pulses", Light: Science & Applications **10**, 199 (2021) (cited on pages 26, 29, 32).

[80] W. Ouyang, X. Xu, W. Lu, N. Zhao, F. Han, and S.-C. Chen, "Ultrafast 3D nanofabrication via digital holography", Nature Communications **14**, 1716 (2023) (cited on pages 26, 29, 61, 65, 70, 73, 91, 131).

[81] J. B. Mueller, J. Fischer, Y. J. Mange, T. Nann, and M. Wegener, "In-situ local temperature measurement during three-dimensional direct laser writing", Applied Physics Letters **103** (2013) (cited on page 27).

[82] J. Fischer, J. B. Mueller, J. Kaschke, T. J. A. Wolf, A.-N. Unterreiner, and M. Wegener, “Three-dimensional multi-photon direct laser writing with variable repetition rate”, Optics Express **21**, 26244 (2013) (cited on page 27).

[83] Nanoscribe GmbH & Co. KG, *Introducing Two-Photon Grayscale Lithography (White paper)* (cited on pages 27, 29, 53, 127).

[84] P. Kiefer, V. Hahn, S. Kalt, Q. Sun, Y. M. Eggeler, and M. Wegener, “A multi-photon (7 × 7)-focus 3D laser printer based on a 3D-printed diffractive optical element and a 3D-printed multi-lens array”, Light: Advanced Manufacturing **4**, 1 (2024) (cited on pages 27–29, 59, 60).

[85] J. H. Strickler and W. W. Webb, “Two-photon excitation in laser scanning fluorescence microscopy”, in , Vol. 1398, edited by R. L. Antos and A. J. Krisiloff (Apr. 1991), pp. 107–118 (cited on page 28).

[86] Karlsruher Institut für Technologie, *Comparing 3D Printers: Speed vs. Voxel Size*, `https://3dprintingspeed.aph.kit.edu/` (visited on 10/17/2025) (cited on pages 28, 94).

[87] A. Münchinger, V. Hahn, D. Beutel, S. Woska, J. Monti, C. Rockstuhl, E. Blasco, and M. Wegener, “Multi-Photon 4D Printing of Complex Liquid Crystalline Microstructures by In Situ Alignment Using Electric Fields”, Advanced Materials Technologies **7** (2022) (cited on page 28).

[88] M. Hippler, E. Blasco, J. Qu, M. Tanaka, C. Barner-Kowollik, M. Wegener, and M. Bastmeyer, “Controlling the shape of 3D microstructures by temperature and light”, Nature Communications **10**, 232 (2019) (cited on page 28).

[89] P. Mainik, C. A. Spiegel, and E. Blasco, “Recent Advances in Multi-Photon 3D Laser Printing: Active Materials and Applications”, Advanced Materials **36** (2024) (cited on page 28).

[90] L. Yang, H. Hu, A. Scholz, F. Feist, G. Cadilha Marques, S. Kraus, N. M. Bojanowski, E. Blasco, C. Barner-Kowollik, J. Aghassi-Hagmann, and M. Wegener, “Laser printed microelectronics”, Nature Communications **14**, 1103 (2023) (cited on page 28).

[91] F. Kotz, A. S. Quick, P. Risch, T. Martin, T. Hoose, M. Thiel, D. Helmer, and B. E. Rapp, “Two-Photon Polymerization of Nanocomposites for the Fabrication of Transparent Fused Silica Glass Microstructures”, Advanced Materials **33** (2021) (cited on page 28).

[92] J. Bauer, C. Crook, and T. Baldacchini, “A sinterless, low-temperature route to 3D print nanoscale optical-grade glass”, Science **380**, 960–966 (2023) (cited on page 28).

[93] S. K. Saha, D. Wang, V. H. Nguyen, Y. Chang, J. S. Oakdale, and S.-C. Chen, “Scalable submicrometer additive manufacturing”, Science **366**, 105–109 (2019) (cited on page 29).

[94] L. Yang, J. Li, Y. Hu, C. Zhang, Z. Lao, W. Huang, and J. Chu, “Projection two-photon polymerization using a spatial light modulator”, Optics Communications **331**, 82–86 (2014) (cited on pages 29, 61).

[95] H. Taylor, “Rapid 3D-printing method could be used on space missions”, Nature **634**, 1061–1062 (2024) (cited on pages 29–31, 59).

[96] P. Rietz, P. Somers, S. Kalt, J. L. G. Schneider, P. Kiefer, and M. Wegener, “Dynamic Multi-Focus 3D Laser Nanoprinting Based on Two-Step Absorption and Computational Holography”, Laser & Photonics Reviews **19**, 1–11 (2025) (cited on pages 29, 75, 76, 79, 81, 83, 87, 88, 92, 94, 96, 97, 101–106, 136).

[97] X. Liu, C. Ding, X. Gao, X. Shen, M. Tang, Z. Yang, L. Xu, C. Kuang, and X. Liu, “High-resolution 3D nanoprinting based on two-step absorption via an integrated fiber-coupled laser diode”, Optics Letters **48**, 4300 (2023) (cited on page 29).

[98] J. Lu, L. Xu, M. Luo, J. Wen, Y. Bian, Z. Yang, D. Zhu, X. Shen, C. Ding, C. Kuang, and X. Liu, “Parallel direct laser writing method based on optical fiber array”, Optics & Laser Technology **186**, 112738 (2025) (cited on page 29).

[99] J. Zhu, Q. Zhang, T. Yang, Y. Liu, and R. Liu, “3D printing of multi-scalable structures via high penetration near-infrared photopolymerization”, Nature Communications **11**, 3462 (2020) (cited on page 30).

[100] Q. Zhang, A. Boniface, V. K. Parashar, M. A. M. Gijs, and C. Moser, “Multiphoton polymerization using upconversion nanoparticles for tunable feature-size printing”, Nanophotonics **12**, 1527–1536 (2023) (cited on page 30).

[101] Y. Chen, J. Zhang, X. Liu, S. Wang, J. Tao, Y. Huang, W. Wu, Y. Li, K. Zhou, X. Wei, S. Chen, X. Li, X. Xu, L. Cardon, Z. Qian, and M. Gou, “Noninvasive in vivo 3D bioprinting”, Science Advances **6**, 1–10 (2020) (cited on page 30).

[102] S. Li, K. Li, C. Yi, X. Gao, and Z. Gan, “Cascade upconversion: a strategy enabling four-photon lithography in weak light intensity”, Nature Communications **16**, 6449 (2025) (cited on page 30).

[103] D. K. Limberg, J.-H. Kang, and R. C. Hayward, “Triplet–Triplet Annihilation Photopolymerization for High-Resolution 3D Printing”, Journal of the American Chemical Society **144**, 5226–5232 (2022) (cited on page 30).

[104] S. N. Sanders, T. H. Schloemer, M. K. Gangishetty, D. Anderson, M. Seitz, A. O. Gallegos, R. C. Stokes, and D. N. Congreve, “Triplet fusion upconversion nanocapsules for volumetric 3D printing”, Nature **604**, 474–478 (2022) (cited on page 30).

[105] N. Awwad, A. T. Bui, E. O. Danilov, and F. N. Castellano, "Visible-Light-Initiated Free-Radical Polymerization by Homomolecular Triplet-Triplet Annihilation", Chem **6**, 3071–3085 (2020) (cited on page 30).

[106] Q. Zhou, H.-C. Yen, Q. Lan, A. O. Gallegos, M. Hu, K. Frohna, H. Niese, D. Lin, N. Murrietta, P. Narayanan, T. H. Schloemer, L. Pucurimay, S. Fernández, M. Seitz, and D. N. Congreve, *Low Power, Scalable Nanofabrication via Photon Upconversion*, 2025 (cited on page 30).

[107] C. W. Hull, "Apparatur for Production of Three-Dimensional Objects by Stereolithography", US4575330A (3D Systems Inc, Aug. 8, 1984) (cited on page 30).

[108] X. Zheng, J. Deotte, M. P. Alonso, G. R. Farquar, T. H. Weisgraber, S. Gemberling, H. Lee, N. Fang, and C. M. Spadaccini, "Design and optimization of a light-emitting diode projection micro-stereolithography three-dimensional manufacturing system", Review of Scientific Instruments **83** (2012) (cited on page 31).

[109] J. R. Tumbleston, D. Shirvanyants, N. Ermoshkin, R. Janusziewicz, A. R. Johnson, D. Kelly, K. Chen, R. Pinschmidt, J. P. Rolland, A. Ermoshkin, E. T. Samulski, and J. M. DeSimone, "Continuous liquid interface production of 3D objects", Science **347**, 1349–1352 (2015) (cited on pages 31, 59).

[110] K. Hsiao, B. J. Lee, T. Samuelsen, G. Lipkowitz, J. M. Kronenfeld, D. Ilyn, A. Shih, M. T. Dulay, L. Tate, E. S. G. Shaqfeh, and J. M. DeSimone, "Single-digit-micrometer-resolution continuous liquid interface production", Science Advances **8**, eabq2846 (2022) (cited on page 31).

[111] J. M. Kronenfeld, L. Rother, M. A. Saccone, M. T. Dulay, and J. M. DeSimone, "Roll-to-roll, high-resolution 3D printing of shape-specific particles", Nature **627**, 306–312 (2024) (cited on page 31).

[112] C. Vidler, M. Halwes, K. Kolesnik, P. Segeritz, M. Mail, A. J. Barlow, E. M. Koehl, A. Ramakrishnan, L. M. Caballero Aguilar, D. R. Nisbet, D. J. Scott, D. E. Heath, K. B. Crozier, and D. J. Collins, "Dynamic interface printing", Nature **634**, 1096–1102 (2024) (cited on page 31).

[113] D. Loterie, P. Delrot, and C. Moser, "High-resolution tomographic volumetric additive manufacturing", Nature Communications **11**, 1–6 (2020) (cited on page 31).

[114] M. Campbell, D. N. Sharp, M. T. Harrison, R. G. Denning, and A. J. Turberfield, "Fabrication of photonic crystals for the visible spectrum by holographic lithography", Nature **404**, 53–56 (2000) (cited on page 32).

[115] Y. K. Pang, J. C. W. Lee, H. F. Lee, W. Y. Tam, C. T. Chan, and P. Sheng, "Chiral microstructures (spirals) fabrication by holographic lithography", Optics Express **13**, 7615 (2005) (cited on page 32).

[116] P. Somers, S. Koch, P. Kiefer, M. L. Meretska, and M. Wegener, "Holographic multi-photon 3D laser nanoprinting – at the speed of light: opinion", Optical Materials Express **14**, 2370 (2024) (cited on pages 32, 66, 113).

[117] J. E. Johnson, I. R. Jamil, L. Pan, G. Lin, and X. Xu, "Bayesian optimization with Gaussian-process-based active machine learning for improvement of geometric accuracy in projection multi-photon 3D printing", Light: Science & Applications **14**, 56 (2025) (cited on page 32).

[118] N. Lang, S. Enns, J. Hering, and G. V. Freymann, "Towards efficient structure prediction and pre-compensation in multi-photon lithography: publisher's note", Optics Express **30**, 45302 (2022) (cited on pages 32, 104).

[119] T. Alletzhäusser, R. Zvagelsky, S. Kalt, P. Friederich, and M. Wegener, "In-situ optical tomographic reconstruction during 3D laser microprinting using deep learning", in Laser 3D Manufacturing XII, edited by H. Helvajian, B. Gu, and H. Chen (Mar. 2025), p. 2 (cited on pages 32, 38).

[120] I. Powell, "Design of a laser beam line expander", Applied Optics **26**, 3705 (1987) (cited on page 35).

[121] J. Weinacker, S. Kalt, P. Kiefer, P. Rietz, and M. Wegener, "On Iterative Pre-Compensation of 3D Laser-Printed Micro-Optical Components Using Confocal-Optical Microscopy", Advanced Functional Materials **2309356**, 1–12 (2023) (cited on pages 38, 51, 54, 56).

[122] J. E. Johnson, Y. Chen, and X. Xu, "Model for polymerization and self-deactivation in two-photon nanolithography", Optics Express **30**, 26824 (2022) (cited on page 38).

[123] S. De Giuseppe, "Über die Simulation des Lightsheet 3D Mikrodrucks", Bachelor's thesis (Karlsruher Institut für Technologie (KIT), 2022) (cited on page 38).

[124] A. Vranić, S. Wulff, P. Rietz, J. L. G. Schneider, S. Abou El Mirate, M. Wegener, and S. Bräse, "Novel Photoinitiators for Two-Step Absorption-Based 3D Laser Nanoprinting: From Molecular Design to Printing Behavior", ChemPhotoChem **10**, e202500337 (2026) (cited on pages 40, 41, 129, 136).

[125] F. Mayer, S. Richter, J. Westhauser, E. Blasco, C. Barner-Kowollik, and M. Wegener, "Multimaterial 3D laser microprinting using an integrated microfluidic system", Science Advances **5**, 1–7 (2019) (cited on page 43).

[126] G. Lipkowitz, T. Samuelsen, K. Hsiao, B. Lee, M. T. Dulay, I. Coates, H. Lin, W. Pan, G. Toth, L. Tate, E. S. G. Shaqfeh, and J. M. DeSimone, "Injection continuous liquid interface production of 3D objects", Science Advances **8**, 1349–1352 (2022) (cited on page 43).

[127] P. Yemulwar, F. Rajabasadi, T. Saxena, M. H. Wong, J. Zscheile, and R. Kirchner, “Flow dynamics of multi-material exchange in two-photon absorption 3D printing”, in Laser 3D Manufacturing XII, edited by H. Helvajian, B. Gu, and H. Chen (Mar. 2025), p. 1 (cited on page 43).

[128] L. Stüwe, M. Geiger, F. Röllgen, T. Heinze, M. Reuter, M. Wessling, S. Hecht, and J. Linkhorst, “Continuous Volumetric 3D Printing: Xolography in Flow”, Advanced Materials **36**, 287–288 (2024) (cited on page 43).

[129] S. C. Laza, M. Polo, A. A. R. Neves, R. Cingolani, A. Camposeo, and D. Pisignano, “Two-Photon Continuous Flow Lithography”, Advanced Materials **24**, 1304–1308 (2012) (cited on page 43).

[130] D. Dendukuri, S. S. Gu, D. C. Pregibon, T. A. Hatton, and P. S. Doyle, “Stop-flow lithography in a microfluidic device”, Lab on a Chip **7**, 818 (2007) (cited on page 43).

[131] D. Dendukuri, D. C. Pregibon, J. Collins, T. A. Hatton, and P. S. Doyle, “Continuous-flow lithography for high-throughput microparticle synthesis”, Nature Materials **5**, 365–369 (2006) (cited on page 43).

[132] L. Stüwe, M. Geiger, F. Röllgen, T. Heinze, M. Reuter, M. Wessling, S. Hecht, and J. Linkhorst, “Continuous Volumetric 3D Printing: Xolography in Flow”, Advanced Materials **13**, 287–288 (2023) (cited on pages 43, 50).

[133] D. Han, C. Yang, N. X. Fang, and H. Lee, “Rapid multi-material 3D printing with projection micro-stereolithography using dynamic fluidic control”, Additive Manufacturing **27**, 606–615 (2019) (cited on page 43).

[134] R. Kirchner, J. Knorr, and J. Zscheile, *Heteromerge GmbH*, `https://www.heteromerge.com` (visited on 10/17/2025) (cited on page 43).

[135] P. J. Pritchard and J. C. Leylegian, *Fox and McDonald’s Introduction to Fluid Mechanics* (John Wiley & Sons, Inc., 2011), p. 899 (cited on page 46).

[136] T. Hanemann and K. Honnef, “Optical and Thermomechanical Properties of Doped Polyfunctional Acrylate Copolymers”, Polymers **10**, 337 (2018) (cited on page 46).

[137] W. M. Haynes, D. R. Lide, and T. J. Bruno, eds., *CRC Handbook of Chemistry and Physics* (CRC Press, June 2016) (cited on page 46).

[138] J. Rotta, “Experimenteller Beitrag zur Entstehung turbulenter Strömung im Rohr”, Ingenieur-Archiv **24**, 258–281 (1956) (cited on page 46).

[139] Comsol, *CFD Module User’s Guide*, 2017 (cited on page 46).

[140] Creative Tools, *#3DBenchy*, (2025) `https://www.3dbenchy.com/` (visited on 10/17/2025) (cited on pages 47, 97).

[141] Y. Schätzle, “Design und Herstellung von diffraktiven optischen Elementen zur Erzeugung eines Lichtblattes”, Master's thesis (Karlsruher Institut für Technologie (KIT), 2023) (cited on pages 51–55).

[142] D. Pi, J. Liu, and Y. Wang, “Optimized Iterative Algorithm to Generate Computer-Generated Holograms Based on the Intermediate Angular-Spectrum Method”, IEEE Photonics Journal **14**, 1–5 (2022) (cited on page 52).

[143] S. Mellin and G. Nordin, “Limits of scalar diffraction theory and an iterative angular spectrum algorithm for finite aperture diffractive optical element design”, Optics Express **8**, 705 (2001) (cited on page 52).

[144] S. H. Kazemi, M. M. Mirsalehi, and A. R. Attari, “Comparison of iterative angular spectrum and optimal rotation angle methods in designing beam-fanners”, Optics Express **17**, 14825 (2009) (cited on page 52).

[145] J. Weinacker, S. Kalt, P. Kiefer, P. Rietz, and M. Wegener, *Quandalf program (online)*, (2023) `https://gitlab.kit.edu/kit/aph/AGW/quandalf` (visited on 08/29/2025) (cited on page 54).

[146] J. Weinacker, “Micro-Optical Elements used for Single-Molecule Raman Spectroscopy and as Scintillators”, PhD thesis (Karlsruhe Institute of Technology, 2024) (cited on page 54).

[147] P. Rietz, P. Somers, S. Kalt, P. Kiefer, J. L. G. Schneider, and M. Wegener, “Parallelized two-step-absorption 3D laser nanoprinting via computational holography using a digital micromirror device”, in Laser 3D Manufacturing XII, edited by H. Helvajian, B. Gu, and H. Chen (Mar. 2025), p. 12 (cited on pages 60, 61).

[148] C. Maibohm, O. F. Silvestre, J. Borme, M. Sinou, K. Heggarty, and J. B. Nieder, “Multi-beam two-photon polymerization for fast large area 3D periodic structure fabrication for bioapplications”, Scientific Reports **10**, 8740 (2020) (cited on page 59).

[149] J.-i. Kato, N. Takeyasu, Y. Adachi, H.-B. Sun, and S. Kawata, “Multiple-spot parallel processing for laser micronanofabrication”, Applied Physics Letters **86**, 044102 (2005) (cited on page 59).

[150] S. Matsuo, S. Juodkazis, and H. Misawa, “Femtosecond laser microfabrication of periodic structures using a microlens array”, Applied Physics A **80**, 683–685 (2005) (cited on page 59).

[151] C. Rensch, S. Hell, M. v. Schickfus, and S. Hunklinger, “Laser scanner for direct writing lithography”, Applied Optics **28**, 3754 (1989) (cited on page 59).

[152] B. J. Jiao, F. Chen, Y. Liu, X. Fan, S. Zeng, Q. Dong, L. Deng, H. Gao, and W. Xiong, "Acousto-optic Scanning Spatial-switching Multiphoton Lithography", International Journal of Extreme Manufacturing **5**, 035008 (2023) (cited on pages 59, 95).

[153] M. I. Álvarez-Castaño, A. G. Madsen, J. Madrid-Wolff, V. Sgarminato, A. Boniface, J. Glückstad, and C. Moser, "Holographic tomographic volumetric additive manufacturing", Nature Communications **16**, 1551 (2025) (cited on pages 61, 70, 73, 127).

[154] E. H. Waller, M. Renner, and G. von Freymann, "Active aberration- and point-spread-function control in direct laser writing", Optics Express **20**, 24949 (2012) (cited on page 61).

[155] L. Zhang, C. Wang, C. Zhang, Y. Xue, Z. Ye, L. Xu, Y. Hu, J. Li, J. Chu, and D. Wu, "High-Throughput Two-Photon 3D Printing Enabled by Holographic Multi-Foci High-Speed Scanning", Nano Letters **24**, 2671–2679 (2024) (cited on page 61).

[156] Z. Fan, C. Wang, Z. Ye, L. Zhang, C. Zhang, D. Pan, Y. Hu, J. Chu, and D. Wu, "Independent and parallel 3D scanning method based on holographically shifted femtosecond multi-foci", Optics Letters **50**, 6782 (2025) (cited on pages 61, 131).

[157] G. Gauthier, T. A. Bell, A. B. Stilgoe, M. Baker, H. Rubinsztein-Dunlop, and T. W. Neely, "Dynamic high-resolution optical trapping of ultracold atoms", in *Advances in Atomic, Molecular and Optical Physics*, Vol. 70 (2021), pp. 1–101 (cited on pages 62, 64).

[158] Texas Instruments Inc., *Texas Instruments DLP Technology*, (2025) `https://www.ti.com/product-category/dlp-products/overview.html` (visited on 09/03/2025) (cited on pages 62, 64, 65, 77).

[159] Audi AG, *The DMD technology of the digital matrix LED headlights*, (2025) `https://www.audi-mediacenter.com/en/videos/video/the-dmd-technology-of-the-digital-matrix-led-headlights-animation-5831` (visited on 09/18/2025) (cited on page 62).

[160] T. A. Bartlett, B. C. McDonald, and J. Hall, "Adapting Texas Instruments DLP technology to demonstrate a phase spatial light modulator", in Emerging Digital Micromirror Device Based Systems and Applications XI, Vol. 10932, edited by M. R. Douglass, B. L. Lee, and J. Ehmke (Mar. 2019), p. 27 (cited on pages 63, 117, 118, 121).

[161] G. Orr, T. Byrum, M. Worrall, Z. Walker, W. McDonald, K. Oberascher, D. Doane, N. Gilly, S. O'Brien, P. Oden, and J. Hall, "High-volume production test methodology and parametrics of the Texas Instruments Phase Light Modulator (PLM)", in Emerging Digital Micromirror Device Based Systems and Applications XVII, Vol. 13383, edited by B. L. Lee and A. Lyubarsky (Mar. 2025), p. 4 (cited on pages 63, 64, 117, 118).

[162] B. Ouyang, S. Gong, T. Lawrence, and J. Hall, "Evaluating Texas instruments Phase Light Modulator (PLM)", in Ocean Sensing and Monitoring XIV, Vol. 12118, edited by W. " Hou and L. J. Mullen, Figure 2 (May 2022), p. 18 (cited on page 63).

[163] HOLOEYE Photonics AG, *Holoeye PLUTO-2.1 LCOS Spatial Light Modulator*, (2025) `https://holoeye.com/products/spatial-light-modulators/pluto-2-1-lcos-phase-only-refl/` (visited on 09/03/2025) (cited on pages 64, 65).

[164] Meadowlark Optics Inc., *Meadowlark Optics 1920 x 1200 Spatial Light Modulator*, (2025) `https://www.meadowlark.com/shop/slms/1920-x-1200-spatial-light-modulator/` (visited on 09/03/2025) (cited on page 64).

[165] Hamamatsu Photonics K.K., *Hamamatsu X15213-01*, (2025) `https://www.hamamatsu.com/eu/en/product/optical-components/lcos-slm/wide_wavelength_bandwidth_type/X15213-01.html` (visited on 09/03/2025) (cited on pages 64, 65).

[166] Meadowlark Optics Inc., *Meadowlark Optics 1024 x 1024 Spatial Light Modulator*, (2025) `https://www.meadowlark.com/shop/slms/1024-x-1024-spatial-light-modulator/` (visited on 09/03/2025) (cited on page 64).

[167] Laser 2000 (UK) Limited, *Understanding the jargon of LCOS Spatial Light Modulators (SLMs)*, (2025) `https://photonics.laser2000.co.uk/blogs/understanding-the-jargon-of-lcos-spatial-light-modulators-slms/` (visited on 09/03/2025) (cited on page 64).

[168] Texas Instruments Inc., *Texas Instruments DLP4500 .45 WXGA DMD*, (2025) `https://www.ti.com/product/de-de/DLP4500` (visited on 10/17/2025) (cited on pages 64, 92, 95).

[169] Texas Instruments Inc., *Texas Instruments DLP7000UV*, (2025) `https://www.ti.com/product/DLP7000UV` (visited on 09/03/2025) (cited on page 64).

[170] J. W. Goodman, *Introduction to Fourier Optics* (McGraw-Hill, 1996) (cited on pages 64, 65, 74).

[171] D. Stuart and A. Kuhn, "Single-atom trapping and transport in DMD-controlled optical tweezers", New Journal of Physics **20**, 023013 (2018) (cited on pages 64, 74).

[172] Hamamatsu Photonics K.K., *Hamamatsu X13267*, (2025) `https://hamamatsu.su/media/index/?type=catalog&id=115` (visited on 10/04/2025) (cited on page 65).

[173] Thorlabs Inc., *Thorlabs Exulus Series*, (2025) `https://www.thorlabs.com/newgrouppage9.cfm?objectgroup_id=10378` (visited on 10/04/2025) (cited on page 65).

[174] A. Egner and S. W. Hell, "Time multiplexing and parallelization in multifocal multiphoton microscopy", Journal of the Optical Society of America A **17**, 1192 (2000) (cited on page 65).

[175] C. Arnoux, L. A. Pérez-Covarrubias, A. Khaldi, Q. Carlier, P. L. Baldeck, K. Heggarty, A. Banyasz, and C. Monnereau, "Understanding and overcoming proximity effects in multi-spot two-photon direct laser writing", Additive Manufacturing **49**, 102491 (2022) (cited on pages 65, 91).

[176] D. Yang, L. Liu, Q. Gong, and Y. Li, "Rapid Two-Photon Polymerization of an Arbitrary 3D Microstructure with 3D Focal Field Engineering", Macromolecular Rapid Communications **40** (2019) (cited on pages 66, 128).

[177] P. S. Salter, Z. Iqbal, and M. J. Booth, "Analysis of the Three-Dimensional Focal Positioning Capability of Adaptive Optic Elements", International Journal of Optomechatronics **7**, 1–14 (2013) (cited on pages 67, 69).

[178] C. J. R. Sheppard, "High-aperture beams", Journal of the Optical Society of America A **18**, 1579 (2001) (cited on page 67).

[179] L. Novotny and B. Hecht, *Principles of Nano-Optics*, 2nd (Cambridge University Press, Cambridge, 2012) (cited on pages 67, 69).

[180] A. Jesacher and M. J. Booth, "Parallel direct laser writing in three dimensions with spatially dependent aberration correction", Optics Express **18**, 21090 (2010) (cited on pages 67, 69).

[181] E. Botcherby, R. Juškaitis, M. Booth, and T. Wilson, "An optical technique for remote focusing in microscopy", Optics Communications **281**, 880–887 (2008) (cited on pages 67, 69).

[182] M. Bawart, M. A. May, T. Öttl, C. Roider, S. Bernet, M. Schmidt, M. Ritsch-Marte, and A. Jesacher, "Diffractive tunable lens for remote focusing in high-NA optical systems", Optics Express **28**, 26336 (2020) (cited on page 67).

[183] N. Holland, D. Stuart, O. Barter, and A. Kuhn, "Benchmarking modern algorithms to holographically create optical tweezers for laser-cooled atoms", Journal of Modern Optics **65**, 2133–2141 (2018) (cited on pages 70, 72).

[184] R. Di Leonardo, F. Ianni, and G. Ruocco, "Computer generation of optimal holograms for optical trap arrays", Optics Express **15**, 1913 (2007) (cited on pages 71, 72).

[185] J. E. Curtis, C. H. Schmitz, and J. P. Spatz, “Symmetry dependence of holograms for optical trapping”, Optics Letters **30**, 2086 (2005) (cited on pages 71, 72, 87).

[186] B. R. W. Gerchberg and W. O. Saxton, “A Practical Algorithm for the Determination of Phase from Image and Diffraction Plane Pictures”, Optik **35**, 237–246 (1972) (cited on page 71).

[187] H. Pang, W. Liu, A. Cao, and Q. Deng, “Speckle-reduced holographic beam shaping with modified Gerchberg–Saxton algorithm”, Optics Communications **433**, 44–51 (2019) (cited on pages 71, 77).

[188] D. Chan, S. G. Narasimhan, and M. O’Toole, “Holocurtains: Programming Light Curtains via Binary Holography”, in 2022 IEEE/CVF Conference on Computer Vision and Pattern Recognition (CVPR), Vol. 2022-June (June 2022), pp. 17865–17874 (cited on page 72).

[189] W.-H. Lee, “Binary Synthetic Holograms”, Applied Optics **13**, 1677 (1974) (cited on pages 73, 74).

[190] P. Zupancic, P. M. Preiss, R. Ma, A. Lukin, M. Eric Tai, M. Rispoli, R. Islam, and M. Greiner, “Ultra-precise holographic beam shaping for microscopic quantum control”, Optics Express **24**, 13881 (2016) (cited on pages 74, 95).

[191] A. Laskin and V. Laskin, “Imaging techniques with refractive beam shaping optics”, in , edited by A. Forbes and T. E. Lizotte (Oct. 2012), 84900J (cited on page 77).

[192] M.-J. Deng, Y.-Y. Zhao, Z.-X. Liang, J.-T. Chen, Y. Zhang, and X.-M. Duan, “Maximizing energy utilization in DMD-based projection lithography”, Optics Express **30**, 4692 (2022) (cited on page 77).

[193] Q. Geng, D. Wang, P. Chen, and S. C. Chen, “Ultrafast multi-focus 3-D nano-fabrication based on two-photon polymerization”, Nature Communications **10**, 1–7 (2019) (cited on pages 82, 131).

[194] Q. Geng, C. Gu, J. Cheng, and S.-c. Chen, “Digital micromirror device-based two-photon microscopy for three-dimensional and random-access imaging”, Optica **4**, 674 (2017) (cited on pages 84, 85).

[195] ViALUX Messtechnik + Bildverarbeitung GmbH, *High Performance DLP Subsystems*, (2025) `https://www.vialux.de/ViALUX-Website/dlp-subsystems_v-modules_chipsets.html` (visited on 06/10/2025) (cited on pages 92, 109).

[196] J. C. A. Rocha, T. Wright, U. G. Būtaitė, J. Carpenter, G. S. D. Gordon, and D. B. Phillips, “Fast and light-efficient wavefront shaping with a MEMS phase-only light modulator”, Optics Express **32**, 43300 (2024) (cited on pages 93, 113, 121).

[197] M. I. Álvarez-Castaño, Y. Pu, and C. Moser, *High Light-Efficiency Holographic Tomographic Volumetric Additive Manufacturing using a MEMS-based Phase-only Light Modulator*, (2025) `https://arxiv.org/abs/2506.02578` (cited on page 93).

[198] T. Frenzel, M. Kadic, and M. Wegener, "Three-dimensional mechanical metamaterials with a twist", Science **358**, 1072–1074 (2017) (cited on page 95).

[199] E. Waller and G. Von Freymann, "Spatio-Temporal Proximity Characteristics in 3D μ-Printing via Multi-Photon Absorption", Polymers **8**, 297 (2016) (cited on pages 99, 100, 104).

[200] A. Mao, S. Fess, N. Kraiem, P. Li, Z. Wu, Q. Zhu, X. Huang, P. Fan, B. Cui, J.-F. Silvain, S. Hu, M. Anthamatten, S. P. Regan, D. Harding, and Y. Lu, "Spatiotemporal Reaction Dynamics Control in Two-Photon Polymerization for Enhancing Writing Characteristics", Advanced Materials Technologies **9** (2024) (cited on page 100).

[201] I. Drobecq, C. Bigot, O. Soppera, L. Malaquin, and B. Venzac, "Optimizing dimensional accuracy in two-photon polymerization: Influence of energy dose and proximity effects on sub-micrometric fiber structures", Additive Manufacturing **103**, 104735 (2025) (cited on page 100).

[202] Kai-Daniel Büchter, *Algorithm to generate equal-sized clusters based on k-means*, MATLAB Central File Exchange, (2025) `https://www.mathworks.com/matlabcentral/fileexchange/105445-algorithm-to-generate-equal-sized-clusters-based-on-k-means` (visited on 09/19/2025) (cited on page 102).

[203] J. T. Collins, J. Knapper, J. Stirling, J. Mduda, C. Mkindi, V. Mayagaya, G. A. Mwakajinga, P. T. Nyakyi, V. L. Sanga, D. Carbery, L. White, S. Dale, Z. Jieh Lim, J. J. Baumberg, P. Cicuta, S. McDermott, B. Vodenicharski, and R. Bowman, "Robotic microscopy for everyone: the OpenFlexure microscope", Biomedical Optics Express **11**, 2447 (2020) (cited on page 112).

[204] B. Diederich, R. Lachmann, S. Carlstedt, B. Marsikova, H. Wang, X. Uwurukundo, A. S. Mosig, and R. Heintzmann, "A versatile and customizable low-cost 3D-printed open standard for microscopic imaging", Nature Communications **11**, 5979 (2020) (cited on page 112).

[205] P. G. Pitrone, J. Schindelin, L. Stuyvenberg, S. Preibisch, M. Weber, K. W. Eliceiri, J. Huisken, and P. Tomancak, "OpenSPIM: an open-access light-sheet microscopy platform", Nature Methods **10**, 598–599 (2013) (cited on page 112).

[206] M. Thiel, J. Fischer, G. von Freymann, and M. Wegener, "Direct laser writing of three-dimensional submicron structures using a continuous-wave laser at 532 nm", Applied Physics Letters **97** (2010) (cited on page 112).

[207] P. Mueller, M. Thiel, and M. Wegener, “3D direct laser writing using a 405 nm diode laser”, Optics Letters **39**, 6847 (2014) (cited on page 112).

[208] N. Surkamp, F. Behlau, C. Plassmann, S. Wohlfeil, A. Knigge, C. Esen, A. Ostendorf, and M. R. Hofmann, “Compact diode laser-based system for multi-photon polymerization with conventional resins”, in Laser 3D Manufacturing XII, edited by H. Helvajian, B. Gu, and H. Chen (Mar. 2025), p. 4 (cited on page 112).

[209] D. Perevoznik, R. Nazir, R. Kiyan, K. Kurselis, B. Koszarna, D. T. Gryko, and B. N. Chichkov, “High-speed two-photon polymerization 3D printing with a microchip laser at its fundamental wavelength”, Optics Express **27**, 25119 (2019) (cited on page 112).

[210] T. Messer, “On 3D Laser Printing Beyond the Common – Compact Printers, Novel Materials, Special Applications”, PhD thesis (Karlsruhe Institute of Technology (KIT), 2023) (cited on page 112).

[211] T. A. Bartlett, W. C. McDonald, J. N. Hall, P. I. Oden, D. Doane, R. S. Ketchum, and T. Byrum, “Recent advances in the development of the Texas Instruments phase-only microelectromechanical systems (MEMS) spatial light modulator”, in Emerging Digital Micromirror Device Based Systems and Applications XIII, Vol. 11698, edited by B. L. Lee and J. Ehmke (Mar. 2021), p. 20 (cited on pages 117, 118).

[212] T. M. Byrum, K. Oberascher, Z. Walker, A. Lyubarsky, S. Martin, G. Orr, W. McDonald, N. Gilly, S. O’Brien, K. Taylor, W. Hamlin, P. Oden, and J. Hall, “Optimizing a micro electro mechanical system (MEMS) based phase-only light modulator (PLM) for improved system performance”, in Emerging Digital Micromirror Device Based Systems and Applications XVI, Vol. 12900, edited by B. L. Lee and J. Ehmke (Mar. 2024), p. 23 (cited on pages 117, 118).

[213] P. I. Oden, T. A. Bartlett, W. C. McDonald, J. C. Baker, and J. N. Hall, “Innovations with a massively paralleled, microelectromechanical systems (MEMS) toward piston-mode-based phase light modulator (PLM)”, in Emerging Digital Micromirror Device Based Systems and Applications XII, Vol. 11294, edited by B. L. Lee and J. Ehmke (Feb. 2020), p. 15 (cited on page 118).

[214] M. R. Douglass, J. Hall, P. Oden, and T. M. Byrum, “Reliability assessment of the Texas Instruments phase light modulator”, in Emerging Digital Micromirror Device Based Systems and Applications XIV, Vol. 12014, edited by B. L. Lee and J. Ehmke (Mar. 2022), p. 17 (cited on pages 118, 119).

[215] Texas Instruments Inc., *DLP PLM Informational*, (2025) `https://dev.ti.com/tirex/explore/node?node=A__ABHrSxvbU.7P1gFXYYDMdA__DLP-GENERAL-DEVTOOLS__FUz-xrs__LATEST` (visited on 10/13/2025) (cited on page 119).

[216] M. Plidschun, M. Zeisberger, J. Kim, T. Wieduwilt, and M. A. Schmidt, "Fiber-based 3D nano-printed holography with individually phase-engineered remote points", Scientific Reports **12**, 20920 (2022) (cited on page 128).

[217] G. Whyte and J. Courtial, "Experimental demonstration of holographic three-dimensional light shaping using a Gerchberg–Saxton algorithm", New Journal of Physics **7**, 117–117 (2005) (cited on page 128).

[218] Y. Cai, S. Yan, Z. Wang, R. Li, Y. Liang, Y. Zhou, X. Li, X. Yu, M. Lei, and B. Yao, "Rapid tilted-plane Gerchberg-Saxton algorithm for holographic optical tweezers", Optics Express **28**, 12729 (2020) (cited on page 128).

[219] Z. Qu, H. Jiang, K. Wang, Y. Liu, Y. Yang, C. Feng, X. Zhao, and J.-L. Wang, "Deep-learning-aided multi-focal hologram generation", Optics & Laser Technology **182**, 112056 (2025) (cited on page 128).

[220] Roithner Lasertechnik GmbH, *Roithner Lasertechnik Price List 03/2025*, (2025) `https://www.roithner-laser.com/pricelist.pdf` (visited on 10/07/2025) (cited on page 128).

[221] A. Mauri, "Photoinitiators in 3D laser printing : a quantum-mechanical investigation", PhD thesis (Karlsruhe Institute of Technology (KIT), 2024) (cited on page 133).

TOOLS

For the sake of integrity, I summarize the tools and software I used for the experimental work, calculations, data analysis, and the creation of this manuscript.

- MATLAB was used to write the control software of the experimental setups presented in chapters 5 and 6, to perform the hologram calculation and the rate-equation-based dose simulation, as well as for data analysis and data visualization.
- User-created MATLAB libraries, which were used, are: VLC created by Lea Strobino, 200 colormap created by Zhaoxu Liu, Fullscreen 1.1 created by Pithawat Vachiramon, and ZSimpleSyringePump created by Chenguang Zhang.
- Autodesk Inventor was used to design equipment and prepare technical drawings.
- Blender, Prusa Slicer, and DLP Slicer were used to prepare the design files for printing experiments.
- VLC Media Player using the OpenGL video output module was used as video playback software for the printing setup.
- CorelDRAW and Inkscape were used to create vector graphics and assemble multi-panel figures.
- The artificial intelligence (AI) tools OpenAI ChatGPT GPT-5 and Google Gemini 2.5 Pro were used for literature research and for the generation of MATLAB and LaTeX source code. Additionally, these tools were used to help with text formulation. An additional citation marks paragraphs where this applies.
- Grammarly and DeepL were used to correct spelling, grammar, and improve clarity.
- LaTeX was used to write this thesis, together with the LaTeX2e class template for diploma theses, based on wissdoc.cls by Roland Bless, 1996-2001, and heavily modified by Robert Schittny, 2015.

ACKNOWLEDGMENTS

Certainly, research is a collaborative effort. Likewise, the results of this thesis would not have been possible without the active work and supporting contributions of many people. I want to express my sincere gratitude to them here.

First and foremost, I would like to thank Prof. Dr. Martin Wegener for the opportunity to join his group for my PhD thesis to work on the emerging topic of two-step absorption 3D laser printing. The balance between guidance and freedom provided the essential environment for experiencing self-responsible research, while one could always rely on the insightful engagement when facing challenges.
My thanks also go to Prof. Dr. Carsten Rockstuhl for kindly agreeing to be the co-referee for this thesis.

I am deeply grateful to Dr. Vincent Hahn for introducing me to many topics related to two-step absorption and 3D laser printing. His optimism and countless ideas for new directions or problem-solving were essential at the beginning of my work and provided an important toolbox for my own projects.

My gratitude extends to Dr. Paul Somers for the same reasons of having countless ideas about routes to take and ways to resolve problems, while simultaneously spreading joy in what he is doing.

Working on the topic of two-step absorption was exciting but often challenging, and expectations might be disappointed, overshadowing the undeniable advantages. In this regard, I want to thank the people I could share this journey with, who are Dr. Vincent Hahn, Dr. Tobias Messer, Dr. Maximilian Bojanowski, Aleksandra Vranić, and Josephine Spiegelberg.

My sincere thanks go to all the current and former members of the research group I had the pleasure of working with. The collaborative, supportive, and humorous atmosphere was an experience I would not want to miss. I especially wish to acknowledge the people I spent the most time with: Dr. Sebastian Kalt, Dr. Tobias Messer, Alexander Berkes, Dr. Vincent Hahn, Dr. Pascal Kiefer, Jonathan Schneider, and Tim Alletzhäusser.

When working on novel 3D printing approaches, *the* crucial result is the printed structure. Therefore, I am grateful to the people who spent many hours with me at the SEM and revealed the truth, be it either encouraging or disappointing:

Jonathan Schneider, Dr. Sebastian Kalt, Dr. Vincent Hahn, Dr. Tobias Messer, and Tim Alletzhäusser.

A fruitful collaborative effort that emerged during my PhD time was on the precompensation routine of 3D laser-printed micro-optical components. For this joint research, I want to thank Dr. Jannis Weinacker, Dr. Sebastian Kalt, and Dr. Pascal Kiefer.

During my PhD time, I had the pleasure of supervising the Master's thesis of Yvonne Schätzle, as well as the Bachelor's thesis of Stefano De Giuseppe. I learnt a lot from you, and I hope you did likewise.

I am also very grateful to the administrative and technical staff at the Institute of Applied Physics (APH) and the Institute of Nanotechnology (INT). These include Petra Bauer, Michaela Detscher, Gloria Zanda, and Ursula Mösle from the secretaries' office at APH, as well as Patricia Jaeger, Christine Fischer, Lena Eglitis, and Felicitas Lauer from the INT.
Furthermore, I wish to thank our group's technician, Johann Westhauser, for the technical drawings and purchasing orders. My thanks also go to Michael Hippe, Helmuth Lay, and Werner Gilde from the electronics workshop for their help with defective equipment and the rapid execution of soldering tasks.
I also thank Maik Nothdurft, Mario Nusche, Frank Landhäußer, and the whole team from the mechanical workshop for their input regarding mechanical equipment and the manufacturing of many different parts over the years.

I gratefully acknowledge the Cluster of Excellence "3D Matter Made to Order" and the "HEiKA Graduate School on Functional Materials" for their funding, for the occasions where researchers from different groups were brought together, and for the opportunities for professional development.

A special thank you is owed to the people who took the time to proofread this thesis, spotting mistakes and providing valuable suggestions: Tim Alletzhäusser, Alexander Berkes, Dr. Sebastian Kalt, Jonathan Schneider, and Josephine Spiegelberg.

I also want to thank my former colleagues, Dr. Simon Woska and Lukas Rebholz, for their continued friendship and regular discussions.

Finally, I want to thank the people who are always with me and support me unconditionally. These are my family and friends, especially my parents, my grandmother, and Franziska.